# THÈSE DE DOCTORAT

de l'Université de recherche Paris Sciences et Lettres
PSL Research University

**Préparée à ESPCI Paris**

# Joint-statistics between reflected and transmitted speckle patterns: from mesoscopic correlations to information theory

**École doctorale n°564**

PHYSIQUE EN ÎLE DE FRANCE

**Spécialité** PHYSIQUE


**Nikos Fayard**
Soutenue le 02/11/2017

Dirigée par **Rémi Carminati**
et **Romain Pierrat**


**COMPOSITION DU JURY**

Bart van Tiggelen
Rapporteur

Alexey Yamilov
Rapporteur

Juan José Sáenz
Examinateur

Kevin Vynck
Examinateur

Sylvain Gigan
Président du jury

Rémi Carminati
Directeur de thèse

Romain Pierrat
Co-directeur de thèse

Philippe Adam
Invité


Institut **Langevin**
ONDES ET IMAGES

# Contents

# Chapter I

# Introduction

The understanding of the propagation of light inside different types of media is of crucial importance. Indeed it allows both to image object inside such media and/or to deliver energy or information through them. The way light propagates through homogeneous media is perfectly understood [1]. Thus it is possible to shape precisely the source of light so that the emitted signal interferes constructively in one given direction, position, and/or at a given time. Consequently, one can deliver efficiently energy or information though homogeneous media towards a specific detector or object.

When the medium of propagation gets more complex (with an optical index or equivalently a permittivity varying in space) we loose the *a priori* knowledge on the way waves propagate through it. Complex media (or equivalently scattering media) are medium with a large number of strong inhomogeneities of the optical index of refraction. Many complex media for light exist in nature, the most famous examples are clouds, fog, milk, paint or paper. All of them appear opaque when illuminated with light as we can see in Fig. I.1 in which we show a bridge in the fog.

**Figure I.1** – Photograph of a bridge in the fog.

To discuss this complex scattering phenomenon let us introduce the scalar Helmholtz equation for the electric field $E$ in a complex medium without sources:

$$\left[\Delta + \frac{\omega^2}{c^2}\epsilon(\mathbf{r},\omega)\right] E(\mathbf{r},\omega) = 0, \tag{I.1}$$

with $\omega$ the pulsation ($\omega = 2\pi/\lambda$ with $\lambda$ the wavelength in vacuum), $c$ the speed of light in vacuum, $\epsilon$ the permittivity of the medium. Note that the only difference between Eq. (I.1) and the wave equation in vacuum is the presence of $\epsilon(\mathbf{r},\omega)$. This small change in the equation contrasts with its impressive effect on the propagation of light as we can see Fig. I.1.

To give an intuitive feeling about the role of the inhomogeneities of permittivity in the scattering phenomenon, we can introduce the Lippman-Schwinger equation for the field. This exact equation

is completely equivalent to the Helmholtz equation. It reads

$$E(\mathbf{r},\omega) = E_0(\mathbf{r},\omega) + \int G_0(\mathbf{r}-\mathbf{r}')k_0^2[\epsilon(\mathbf{r}',\omega)-1]E(\mathbf{r}',\omega)\mathrm{d}\mathbf{r}' \tag{I.2}$$

with $E(\mathbf{r},\omega)$ the total field, $E_0(\mathbf{r},\omega)$ the incident field, $\epsilon(\mathbf{r},\omega)$ the permittivity of the medium and $G_0$ the free space Green function of the Helmholtz equation. The Green function $G_0(\mathbf{r}-\mathbf{r}')$ is the field response at $\mathbf{r}$ due to the presence of a source at $\mathbf{r}'$. The complex character of the scattering phenomenon is revealed by the presence of the total field on both the left hand side and inside the integral in Eq. (I.2). To give an intuitive picture of the scattering phenomenon, we can iterate Eq. (I.2) in order to express the total field as the sum of the incident field, the single scattered field, and all the possible orders of interaction with the complex medium. This is done in Eq. (I.3) and represented schematically in Fig. I.2:

$$\begin{aligned} E(\mathbf{r},\omega) = E_0(\mathbf{r},\omega) &+ \int G_0(\mathbf{r}-\mathbf{r}')k_0^2[\epsilon(\mathbf{r}',\omega)-1]E_0(\mathbf{r}',\omega)\mathrm{d}\mathbf{r}' \\ &+ \int G_0(\mathbf{r}-\mathbf{r}'')k_0^2[\epsilon(\mathbf{r}'',\omega)-1]G_0(\mathbf{r}''-\mathbf{r}')k_0^2[\epsilon(\mathbf{r}',\omega)-1]E_0(\mathbf{r}',\omega)\mathrm{d}\mathbf{r}'\mathrm{d}\mathbf{r}'' + ... \end{aligned} \tag{I.3}$$

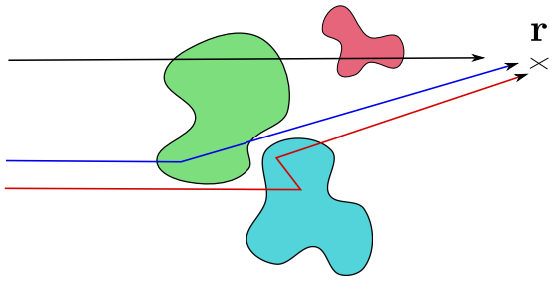


**Figure I.2** – Scheme of the scattering of a wave by a complex medium. The total field can be viewed as the sum of the incident field (black arrow), the single scattered field (blue arrow), the field scattered twice by the medium (red arrow) etc.

The presence of inhomogeneities of permittivity in the propagation medium acts as secondary sources producing fields which will interfere with the incident field, and excite the other homogeneities, and so on an so forth. If we do not know the position and the strength of the inhomogeneities, we cannot *a priori* know the value of the field at one given position. If one measures the intensity scattered by a complex medium either in reflection or in transmission, one obtains a highly contrasted intensity pattern called *speckle*. In Fig. I.3 we show a typical speckle pattern obtained from light scattering from a complex medium. In this pattern, the intensity changes from zero to one on a typical distance on the order of the wavelength [due to the complex interference phenomenon represented in Eq. (I.2)]. This prevents the efficient delivery of energy or information.

There already exist techniques allowing to focus light, for example, in transmission though a scattering medium. In the following we discuss two of these techniques: time reversal and wavefront shaping. Both are based on properties of the Helmholtz equation Eq. (I.1).

- Time reversal techniques [3, 4] are based on the fact that (for a lossless medium) if the field $E$ is a solution of Eq. (I.1), then its complex conjugate $E^*$ is solution of the same equation. Let us describe now a typical time reversal experiment. First a source at a given position excites the sample and the scattered field is measured on a surface surrounding the medium. Second, the source is removed and the conjugated field is sent back [1] from the measurement surface and

[1] Conjugating the field in the frequency domain is equivalent to time reversing it in the time domain.

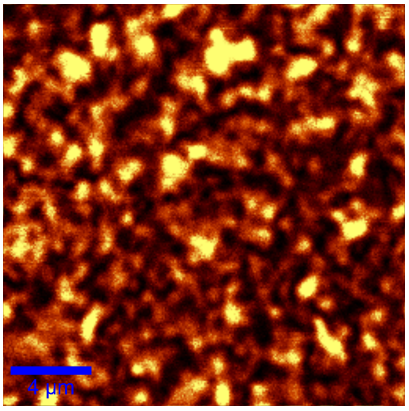


**Figure I.3** – Speckle pattern produced by the multiple scattering of light from a disordered dielectric medium. The wavelength of the Laser is $\lambda = 633\,\text{nm}$. The imaged plane is at a distance of $60\,\mu\text{m}$ from the exit surface of the sample. This image has been obtained by E. Perros in a work published in ref. [2].

eventually focuses at the position of the source. Those time reversal techniques have proven to focus monochromatic and polychromatic light efficiently even in scattering media [5] and for every type of waves [6, 7, 8]. Nonetheless they are two step techniques and need a source at the position where we want to focus the light.

- Taking advantage of the linearity of the Helmholtz equation given in Eq. (I.1), the so called wavefront shaping techniques have been proposed [9, 10, 11]. These techniques require a CCD camera placed in transmission of the scattering medium measuring the scattered field and a spatial light modulator (SLM) to shape spatially the phase of the incident field (on each pixel of the SLM). Using the transmission measurement, one can find the correctly shaped incident field to achieve focusing in transmission. These techniques have produced impressive results allowing to focus monochromatic (or polychromatic [12, 13, 14]) light at a given position, to transfer all (or none of) the energy in transmission of a thick scattering medium [15, 16, 17, 18, 19]. Nonetheless, they need a measure in transmission of the sample, which is often out of reach of the operator.

The two techniques discussed require an operation on the transmission side of the sample (whether a measurement with a CCD or a source) to overcome the effect of scattering on wave propagation. This part of the sample is out of reach in many applications. Working with reflected intensity as a feedback seems a promising option. Variants of optical coherence tomography techniques allow to detect objects inside a scattering sample retrieving the specular intensity in the reflected light using clever post processing [20, 21, 22]. Note that these methods cannot be applied when the sample is to thick (or only on its surface) since they rely on the measurement of single scattered light. Our objective is to study the feasibility of some techniques based on the measurement of the scattered light in reflection of thick samples.

To study the multiply scattered light formally, the usual approach is to study its statistical properties. Indeed, somewhat surprisingly, one observes similarities between the intensity patterns emerging from different scattering medium: average value of the intensity, etc. This means that some properties of the light can be described with a small number of parameters (*e.g.* temperature for a perfect gas). A key parameter for complex media is the scattering mean free path $\ell$. This very important quantity can be seen as the average distance between two scattering events of the light inside the medium, and its knowledge provides information on the light propagation regime inside the medium. We can compare the size of the medium $L$ with the scattering mean free path $\ell$ in order to define the following regimes of transport:

- $\lambda \ll L \ll \ell$ is the quasi-ballistic regime. In this regime the medium is transparent (there is almost no scattering event).
- $\lambda \ll L \sim \ell$ is the single scattering regime. In this regime there is approximatively as much scattered and non scattered light. One can still see through the sample.
- $\lambda \ll \ell \ll L$ is the diffusive regime[2]. In this regime all the light transmitted through the sample has been scattered many times. The sample is opaque.

Our purpose in this thesis is to study the existence of statistical links between the reflected and the transmitted scattered light in the diffusive regime as a function of $\lambda$, $\ell$, $L$ and the transverse spacing between the points $\Delta R$ (as represented in Fig. I.4). Such a statistical link between reflection and

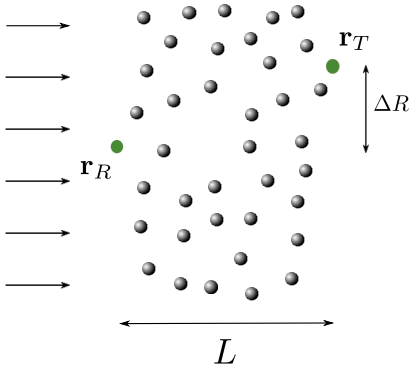


**Figure I.4** – Scheme of the typical geometry studied in this thesis. A plane wave at normal incidence illuminates a scattering medium of size $L$. The intensity is measured in transmission and in reflection and we interest ourselves to the statistical links between the intensity in $\mathbf{r}_R$ and the intensity in $\mathbf{r}_T$.

transmission could be used to image objects hidden behind a diffusive medium, or to control the light using only reflected informations.

The purpose of the first part of this thesis is to study analytically, numerically and experimentally (in collaboration with an experimental group from the University of Exeter) the existence and the properties of the intensity-intensity correlation between the reflected and the transmitted light in all the propagation regimes (in other words we study $\langle I(\mathbf{r}_R) I(\mathbf{r}_T) \rangle$ with $\langle ... \rangle$ meaning average over the disorder). Once this building block is studied, we propose a new imaging modality (named Blind Ghost Imaging) using this correlation to image an object hidden behind a thick scattering medium, requiring only one mono-pixel detector in transmission of the scattering medium.

In the second part of the thesis we study deeper statistical links between reflection and transmission building the joint probability density function between reflected and transmitted light $P\left[I(\mathbf{r}_R), I(\mathbf{r}_T)\right]$. Based on this function we study a quantity called mutual information between a large number of reflected and transmitted intensities versus the parameters of the physical system. The mutual information is a key quantity in information theory, that quantifies the statistical dependency between two sets of random variables. Eventually, we use our knowledge about the joint statistics between reflection and transmission to study the conditional average value of the transmitted intensity at one given position. This quantity could be a good observable to describe wavefront shaping experiments with reflected feedback only.

[2]In this work we do not differentiate the scattering mean free path $\ell$ and the transport mean free path $\ell^*$ because we consider point-like scatterers.

# Part I

# Intensity correlation between reflected and transmitted speckle patterns

# Chapter II

# The scattered field: a gaussian random variable?

## Table des matières

In order to introduce the purpose of this work we intend in this chapter to present the basics about the statistics of the field scattered by a disordered medium. First we present the canonical geometry studied in this thesis: the slab geometry. Second we study the one point statistics of the scattered intensity and discuss the implication of the gaussian approximation on its probability density. Third we show that in the gaussian approximation, only short-range correlation exists between intensities at different points. Eventually we show that beyond the gaussian approximation, a long-range correlation survives between two intensities at different points in transmission, and we discuss its existence between intensities observed in transmission and in reflection.

## II.1 Geometry of interest

In this section we comment about the geometry studied in this work. In Fig. II.1 we show a 2D disordered sample composed of point like scatterers [23] shined from the left with a plane wave at normal incidence. The points where we measure intensities are $\mathbf{r}_R$ and $\mathbf{r}_T$, respectively, at the entrance and exit plane of the scattering medium. The depth, denoted by $z$, is equal to 0 at the entrance plane and $L$ at the exit plane. The transverse width of the slab $W$ is kept many times larger than $L$ in all numerical calculations. The slab geometry ($W \gg L$) provides translationnal invariance properties useful for analytical calculations. The transverse distance between $\mathbf{r}_R$ and $\mathbf{r}_T$ is denoted $\Delta R$.

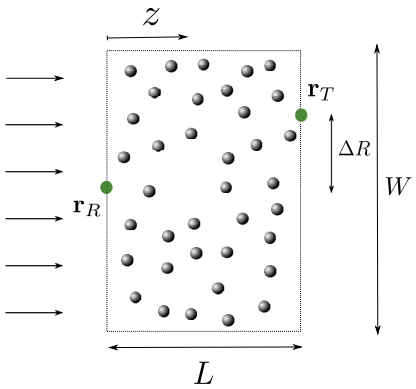


**Figure II.1** – Scheme of the geometry studied in this work. A 2D disordered sample of depth $L$ and transverse size $W \gg L$ is shined from the left at normal incidence by a plane wave.

It is important to emphasize that the results we obtain in this work are specific to this geometry. For instance if we do not shine with a plane wave but with a point source or if we do not measure intensities on the sample surface but in the far field different results can be obtained.

Another important point is that most (but not all) of the results we present are obtained for 2D random samples. The scatterers, randomly distributed over the sample, are cylinders with one direction of invariance. Dealing with TE-polarized waves, *i.e.* electric field oriented along the invariance

axis of the system, the problem reduces to the 2D scalar case. The total electric field at one point is given by the sum of the incident field $E_0$ and the scattered field $E_s$

$$E(\mathbf{r}) = E_0(\mathbf{r}) + E_s(\mathbf{r}). \tag{II.1}$$

We call reflected field the scattered field measured in reflection

$$E_R = E_s(\mathbf{r}_R) \tag{II.2}$$

and transmitted field the total field measured in transmission

$$E_T = E(\mathbf{r}_T). \tag{II.3}$$

## II.2 One point statistics in the gaussian approximation

In this section we give simple arguments that lead to the full statistics of the intensity measured at one position whether in reflection or in transmission of a scattering medium. We deal with dilute samples ($k_0\ell \gg 1$).

### II.2.1 A gaussian field

In the introduction we explained that the unknown character of the disorder upon which the wave scatters when it propagates through a complex medium makes the analysis impossible without assumptions on the nature of the disorder. The usual approach is to study statistics of the field when scattered by a disordered medium with known statistical properties.

#### Decomposition of the field over all possible scattering paths

The easiest and most direct way to access many properties of the field is to express it as a sum over all possible scattering paths in the medium

$$E(\mathbf{r}) = \sum_{\mathcal{S}} E_{\mathcal{S}}(\mathbf{r}) = \sum_{\mathcal{S}} e^{i\phi_{\mathcal{S}}(\mathbf{r})} A_{\mathcal{S}}(\mathbf{r}) \tag{II.4}$$

where $\phi_{\mathcal{S}}$ is the phase acquired during propagation along the path $\mathcal{S}$ and $A_{\mathcal{S}}$ is the amplitude of the field after propagation along $\mathcal{S}$. To define all possible paths existing into the complex medium we can label each scatterer inside the medium. If we define for instance $\mathcal{S}_1$ as the path that encounters a given ordered list of scatterers, then $\mathcal{S}_1$ will change with the positions of the scatterers in different configurations of disorder and thus the field traveling along $\mathcal{S}_1$ becomes a random variable. Under the assumption of dilute systems ($k_0\ell \gg 1$), the fields traveling along two different scattering sequences vary independently when the positions of the scatterers are changed. Thus applying the central limit theorem to the sum of all those fields, the total scattered field must be a gaussian complex random variable, see for instance ref. [24].

In order to test this we use the couple dipole method [25] to solve Maxwell equation in a 2D slab geometry composed of point like scatterers (more details about the numerical method are given in App. .3). In Fig. II.3 we plot the numerically calculated imaginary part of the transmitted field versus its real part for a large number of realizations of disorder in a thick ($b = L/\ell = 10$) and dilute ($k_0\ell = 10$) system. At first sight the transmitted field indeed looks like a gaussian random variable. The same behavior is observed for the reflected field in Fig. II.4.

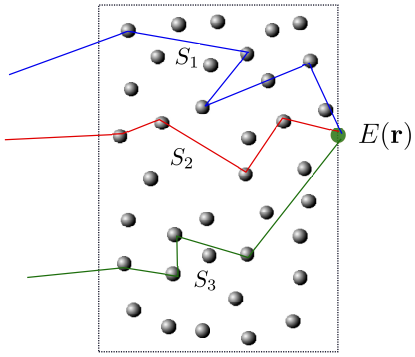


**Figure II.2** – Scheme of the decomposition of the transmitted field over three different scattering paths. The total field is the sum over all possible scattering sequences.

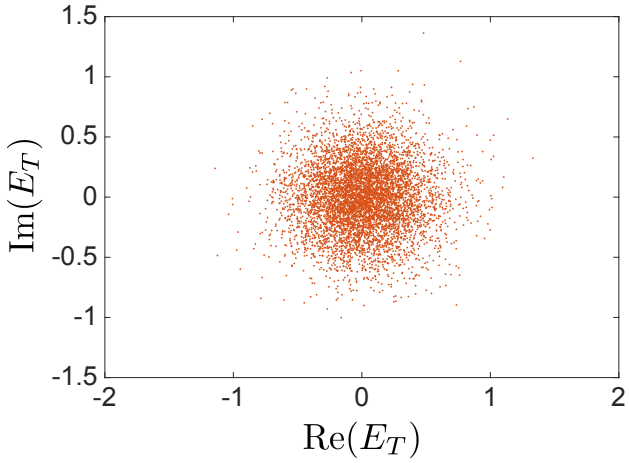


**Figure II.3** – Calculations of the transmitted field for numerous realizations ($N = 6400$) of a disorder characterized by $k_0\ell = 10$ and $b = L/\ell = 10$. The average value of the field is close to zero, and its statistics seems gaussian at first sight.

## The average value of the field

Under the assumption of dilute systems ($k_0\ell \gg 1$) the phase acquired during the propagation along one scattering path changes dramatically when the positions of the scatterers change (it varies between 0 and $2\pi$). Thus the average value of the complex random variable associated with the field following this exact scattering sequence should be vanishingly small. As a result the average value of the total scattered field is also expected to be small.

Comparing numerical calculations of the reflected and transmitted fields for two different optical thickness in Fig. II.4 we can conclude that:

- The average value of the transmitted field is large for small samples and decreases with the optical thickness $b = L/\ell$ (we will see in Sec. III that it decreases exponentially with $b/2$) while the average value of the reflected field seems small and constant [1].
- From panel (c) of Fig. II.4 in which we plot the absolute value of the average field in transmission and in reflection versus the optical thickness ($L$ varies and $\ell$ is kept constant) *we see that when* $b \gg 1$ *both the reflected and the transmitted fields have approximatively a zero average value.*

[1] Let us remind that the reflected field is defined as the scattered field measured in reflection, see Eq. (II.1).

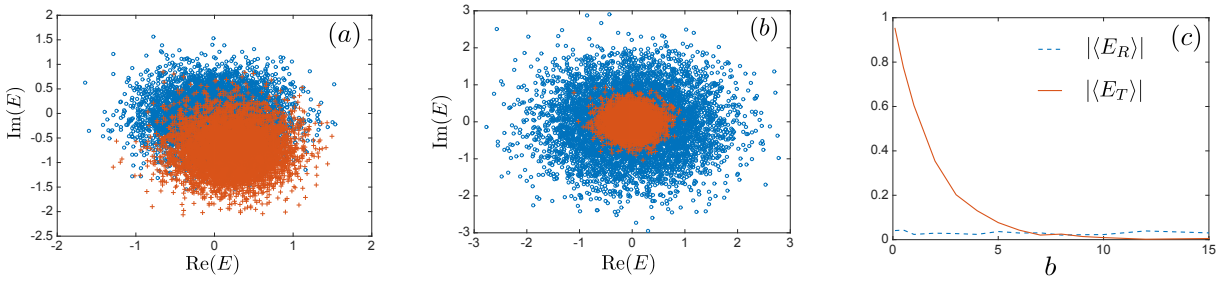


**Figure II.4** – Calculations of the transmitted field (red crosses) and the reflected field (blue circles) for numerous realizations ($N = 6400$ ) of a disorder characterized by $k_0\ell = 10$ and $b = 0.5$ [panel (a)] and $k_0\ell = 10$ and $b = 15$ [panel (b)]. In panel (c) we represent the average value of the numerically calculated transmitted field (red solid line) and of the reflected field (blue dotted line) versus the optical thickness of the sample ($L$ varies and $k_0\ell$ is kept constant equal to 10).

Let us define the fluctuating field $\delta E$ as the difference between the field and its mean value:

$$E(\mathbf{r}) = \langle E(\mathbf{r}) \rangle + \delta E(\mathbf{r}) \tag{II.5}$$

with $\langle \delta E(\mathbf{r}) \rangle = 0$ by definition[2]. From Fig. II.4 we see that the fluctuating part of the field is not negligible. In other words the field fluctuates a lot from one realization of the disorder to the other. The knowledge of the average value of the field is thus not sufficient, we have to study higher moments of the field.

## II.2.2 Intensity scattered by a complex medium

In the previous section we observed that the average value of the transmitted field decreases exponentially with the optical thickness of the scattering medium. Does this mean that the average intensity (average value of the squared modulus of the field) measured in transmission will be exponentially small as well?

### Decomposition of the intensity over pairs of scattering paths

Taking the modulus squared of Eq. (II.4) we can express the intensity as a sum over pairs of scattering paths:

$$I(\mathbf{r}) = \sum_{\mathcal{S},\mathcal{S}'} E_{\mathcal{S}}(\mathbf{r}) E^*_{\mathcal{S}'}(\mathbf{r}) = \sum_{\mathcal{S},\mathcal{S}'} e^{i[\phi_{\mathcal{S}}(\mathbf{r}) - \phi_{\mathcal{S}'}(\mathbf{r})]} A_{\mathcal{S}}(\mathbf{r}) A_{\mathcal{S}'}(\mathbf{r}) \tag{II.6}$$

where $\phi_{\mathcal{S}}$ is the phase acquired along the scattering sequence $\mathcal{S}$ and $A_{\mathcal{S}}$ is the amplitude of the field scattered along $\mathcal{S}$. Equation. (II.6) gives a clear understanding of the visual aspect speckle pattern (see Fig. II.10). Each point of the intensity pattern corresponds to a complicated interference term that can be either contructive or destructive, resulting in a pattern made of bright and dark spots.

Let us try to give a handy picture of what happens to the different pairs of fields on average over all disorder realizations. Using the same argument as that used for the average field we know that a pair of paths $\mathcal{S} \neq \mathcal{S}'$ gives on average an exponentially small contribution to the intensity. Indeed the phase difference between the field and its complex conjugate oscillates between 0 and $2\pi$ when the positions of the scatterers are changed. Nonetheless we see that when $\mathcal{S} = \mathcal{S}'$ the phases exactly

[2]Let us stress that $\delta E = \delta E_s$ since the incident field does not depend on disorder.

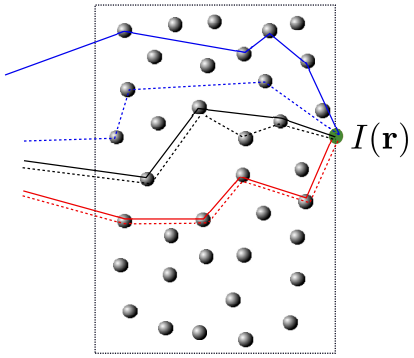


**Figure II.5** – Scheme of the decomposition of the transmitted intensity over three different pairs of scattering paths. Scatterers are represented by small spheres and each line connecting them corresponds to the propagation of the field (or its complex conjugate when dotted) into the vacuum

compensate, thus those contributions resist to the averaging process. Taking the average of the square modulus of Eq. (II.5) we can highlight the separation between those two different terms

$$\langle I(\mathbf{r})\rangle = \underbrace{|\langle E(\mathbf{r})\rangle|^2}_{I_b(\mathbf{r})} + \underbrace{\langle|\delta E(\mathbf{r})|^2\rangle}_{I_d(\mathbf{r})}. \tag{II.7}$$

The first part is called "ballistic" intensity ($I_b$) and comes from the scattering of the field and its complex conjugate by pairs of different scattering sequences while the second part is called the "diffuse" intensity ($I_d$) and comes from the scattering of the field and its complex conjugate along the same scattering sequences [26]. Equation (II.7) shows that the intensity can be split into the sum of two fundamental quantities: the squared modulus of the average field and the variance of the field.

### Ballistic and diffuse intensities, two different terms with two different scalings

In our numerical calculation we have access to the field, we can thus easily separate the two terms in Eq. (II.7).

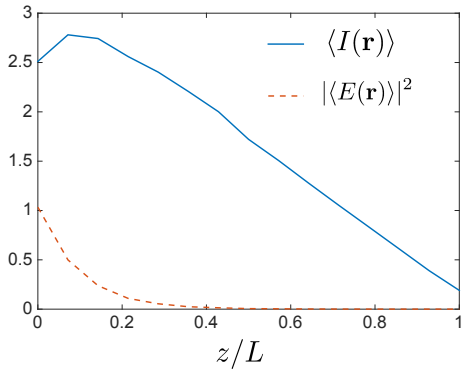


**Figure II.6** – Numerical calculation of the average intensity (blue solid line) and of the ballistic intensity (red dotted line) inside a scattering medium of parameters $k_0\ell = 10$ and $b = 10$.

In Fig. II.6 we plot the average intensity and the ballistic intensity inside the medium versus the normalized depth $z/L$. We see that the dominant process in the transport of intensity over long distances inside the scattering medium corresponds to $\langle|\delta E(\mathbf{r})|^2\rangle$. The ballistic intensity has non

zero value only close to the boundary of the medium ($z \simeq \ell$). In Sec. III we calculate explicitly those two terms. Here we focus on the fact that the diffuse intensity (variance of the field) survives at large depth while the ballistic intensity does not.

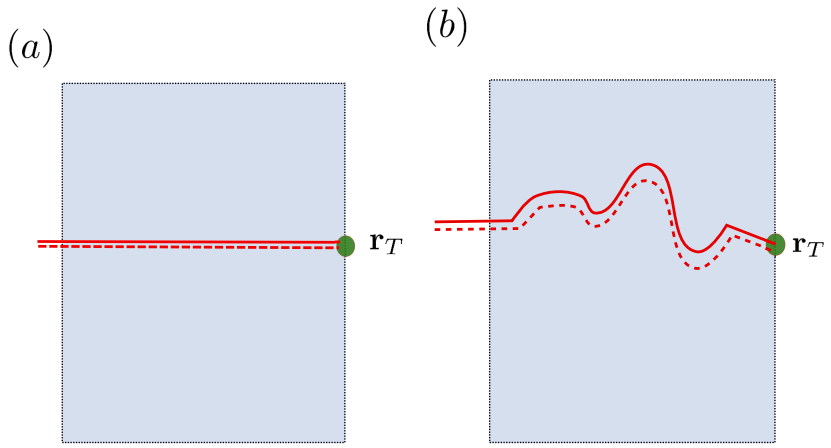


**Figure II.7** – Diagrammatic representation of Eq. (II.7). The straight line represents the propagation of the mean field. Panel (a) thus corresponds to the ballistic intensity. The twisting lines corresponds to fluctuating fields. Panel (b) thus corresponds to the diffuse intensity.

Let us here mention a few words about the diagrammatic approach used in this thesis. In this section we had the first glimpse of a quantity (the mean intensity) which can be split into two terms (ballistic intensity and diffuse intensity) with different scaling with the parameters of the system ($\ell$ and $L$). In the following we will go from mathematical expressions to diagrammatic representations (see ref. [27]). The main purpose of a diagram is that it helps us to handle decompositions of the type of Eq. (II.7) easily, and to predict the scaling of the quantity under study with the parameters of the system. For instance in Fig. II.7 we give the diagrammatic equivalent of Eq. (II.7). Panel (a) composed of two straight lines, one solid and one dashed represents the propagation of the modulus squared of the average field (ballistic intensity). Each time we find a diagram with mean fields it will decay very quickly through propagation. Panel (b) composed of two twisting lines, one solid and one dashed, represents the propagation of the variance of the field (diffuse intensity). We should keep in mind that when fields are paired during their propagation, they can travel over long distances through the sample.

### Intensity of the fluctuating field: $\widetilde{I}$

So far we have seen in Fig. II.4 that the statistics of both the transmitted and the reflected field seem *a priori* gaussian. In this section we discuss the expression of the probability density [3] of the intensity scattered by a random medium. It is known that the squared modulus of a zero mean complex random variable follows a Rayleigh law (see ref. [28] or ref. [29] for the impact of a non zero average field on the statistics of $I$). In panel (c) of Fig. II.4 we have seen that the reflected field always has a small average value, while the average value of the transmitted field seems to decrease exponentially with the optical thickness. Thus for a thick medium both the reflected and the transmitted intensity should follow Rayleigh laws. We will discuss in this thesis how the presence of a non zero first moment of the field may affect statistics. But in most cases we will discuss statistics of the centered variable $\delta E(\mathbf{r})$. This quantity is *a priori* gaussian and has by definition a zero mean value. It should follow a Rayleigh law regardless of the optical thickness of the medium. *For the*

[3] Let us remind that for gaussian random variables, the full statistics can be built from the first and second moments.

*sake of clarity we have chosen to use the notation* $\widetilde{I}$ *for the squared modulus of the fluctuating part of the field*[4] *(whose mean value is the diffuse intensity)*:

$$\widetilde{I}(\mathbf{r}) = |\delta E(\mathbf{r})|^2 \tag{II.8}$$

being aware that in general this quantity does not equal the "real" intensity $I$. Let us stress here that deviations from Rayleigh law due to the non vanishing of the mean field will be of little interest in the present work. From a statistical point of view we *center* the fields in order to enhance the sensitivity to deviations from the Rayleigh law due to the imperfect gaussian character of the field.

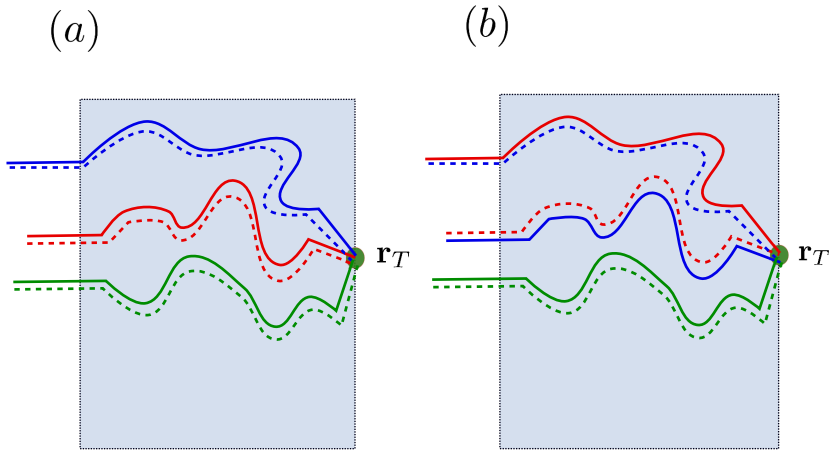


**Figure II.8** – Two different contributions to the third moment of the transmitted intensity of the fluctuating field. The various pairing give the $N!$ factor in the expression of the moments of the Rayleigh law.

### Derivation of the Rayleigh law: counting the fields

Let us briefly comment on the way we obtain the distribution of intensity. Let us remind first that if all moments of a distribution are known, we can obtain the complete distribution using

$$P(x) = \frac{1}{2\pi}\int \sum_N \frac{(ik)^N}{N!}\langle x^N\rangle \exp(-ikx)\mathrm{d}k. \tag{II.9}$$

In Eq. (II.9), $P(x)$ represents the probability density of the random variable $x$. To obtain $P(I)$ we need to obtain an expression of $\langle I^N\rangle$ for all positive $N$. Studying $\widetilde{I}$ simplifies this procedure because the only way to transport higher order moments of the centered variable through the complex medium is to pair fluctuating fields during propagation. For instance in order to express the second moment of the intensity of the fluctuating field: $\langle\widetilde{I}^2\rangle = \langle\delta E_1\delta E_1^*\delta E_2\delta E_2^*\rangle$ we use the following pairing $\langle\delta E_1\delta E_1^*\rangle\langle\delta E_2\delta E_2^*\rangle$ and $\langle\delta E_1\delta E_2^*\rangle\langle\delta E_2\delta E_1^*\rangle$. Observing that each possibility gives the square of the intensity we thus obtain $\langle\widetilde{I}^2\rangle = 2\langle\widetilde{I}\rangle^2$. Now if we repeat the procedure for a higher moment of order $N$ we have to count all the possible ways to create different pairs of field and complex conjugate given the two ensembles $\{\delta E_1, ...., \delta E_N\}$ and $\{\delta E_1^*, ...., \delta E_N^*\}$ (see refs. [28, 30, 31, 32] for more details). To create the first pair we have $N$ possibilities, the second pair $N-1$, etc. Eventually we can show that there exist $N!$ possible ways to create pairs of fields given these two ensembles leading to the important results $\langle\widetilde{I}^N\rangle = N!\langle\widetilde{I}\rangle^N$ (valid for gaussian fields). These different possibilities of pairing

[4]The presence of a $\widetilde{...}$ in Eq. (II.8) is here to stress the absence of the mean field in the quantity studied. In Eq. (II.7) $\langle I(\mathbf{r})\rangle$ corresponds the second order moment of the non-centered field while $\langle\widetilde{I}(\mathbf{r})\rangle$ is the second order moment of the centered field.

fields are represented in Fig. II.8 where two contributions of the third moment of the intensity out of six are shown.

We can now insert the expression of $\langle \widetilde{I}^N \rangle$ into Eq. (II.9) in order to obtain the Rayleigh law :

$$P(\widetilde{I}) = \frac{1}{2\pi} \int \sum_N (ik\langle \widetilde{I} \rangle)^N \exp(-ik\widetilde{I}) \mathrm{d}k = \frac{1}{\langle \widetilde{I} \rangle} \exp\left(-\frac{\widetilde{I}}{\langle \widetilde{I} \rangle}\right). \tag{II.10}$$

To obtain the right hand side in Eq. (II.10), we first calculate the sum over N, and compute the integral using the residue theorem. The expression of $P(\widetilde{I})$ in Eq. (II.10) depends on a single parameter $\langle \widetilde{I} \rangle$. In order to compare statistics of the intensity of the centered field for many different samples, the best way is to normalize $\widetilde{I}$ by its mean value. Indeed if the statistics of $\widetilde{I}$ follows a Rayleigh law, then it implies the normalized quantity $\widetilde{\mathcal{I}} = \widetilde{I}/\langle \widetilde{I} \rangle$ follows a simple negative exponential law $P(\widetilde{\mathcal{I}}) = \exp(-\widetilde{\mathcal{I}})$ that has a universal character. In Fig. II.9 we plot the numerically calculated

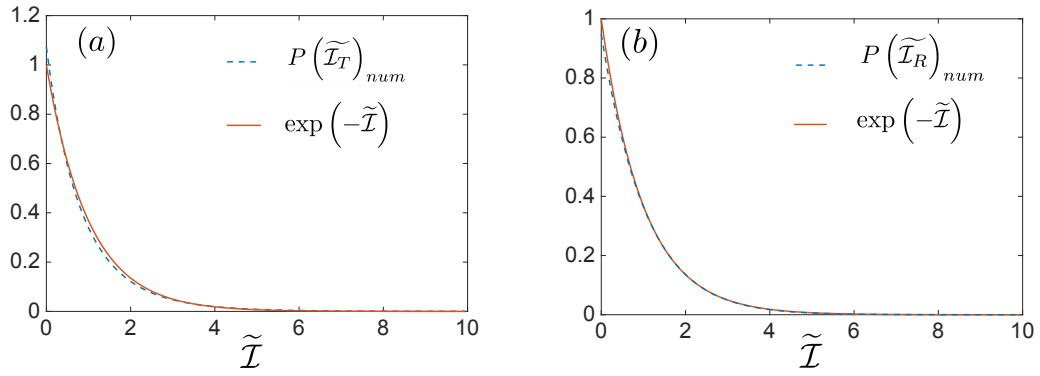


**Figure II.9** – Numerical calculation of the statistics of the normalized intensity $\widetilde{\mathcal{I}} = \widetilde{I}/\langle \widetilde{I} \rangle$ of the fluctuating fields (blue dashed line) and analytical expression of the negative exponential law (red solid line) in transmission [panel (a)] and in reflection [panel (b)] . The parameters in the simulation are $b = 8$, $k_0\ell = 10$.

distribution of the normalized intensity of the fluctuating fields in transmission (a) and in reflection (b) for a thick ($b = 8$) and dilute ($k_0\ell = 10$) sample, that we compare to the negative exponential law. Appart for some small deviations we see that the approximation of a gaussian field is relevant.

Let us conclude this subsection summarizing the assumptions that ensure a Rayleigh statistics for the intensity:

1. The field is a gaussian random variable thus all higher order moments can be built from the first and second moments.
2. The average value of the field is zero. Only its variance (average intensity) plays a role in the construction of all the moments.

Each time one of these two assumptions breaks, the Rayleigh law is no more valid for the statistics of the intensity.

### Is $\widetilde{I}$ a physical quantity?

As the reader can notice we emphasize the role of the random variable $\widetilde{I}$. Indeed, as long as the field is gaussian the statistics of $\widetilde{I}$ follows a Rayleigh law (while $I$ follows a Rayleigh law only if $\langle E \rangle = 0$). *The analysis seems simpler with centered variables, but do they have a physical meaning?* In Fig. II.4

we have seen that the mean value of the reflected field is non zero but small. Actually for diluted samples, it scales as $1/(4k_0\ell)$ which is small compared to one. The reflected field is thus almost by itself a centered random variable, and $\widetilde{I}_R \simeq I_R$. The behavior is different in transmission. Indeed in this case the average field is large for thin samples $b \simeq 1$[5] and is exponentially small when $b \gg 1$. Thus $\widetilde{I}_T$ tends to $I_T$ when the optical thickness of the sample increases.

Let us conclude by stressing that even experimentally one can measure $\widetilde{I}$, for example using off-axis illumination/detection geometry (an example will be described in Chap. IV).

## II.3 Joint-statistics in the gaussian approximation

In the previous section we discussed the probability density of $\widetilde{I}$ under the gaussian assumption for the field. We now intend to study the spatial variation of $\widetilde{I}$. When we analyze a speckle pattern (as for instance in Fig. II.10) obtained in transmission of a thick ($b \gg 1$) random medium we can see two features. First its granularity, or in other words the fact that $\widetilde{I}$ changes drastically from one point to the other. Second we see that there is a distance (typically on the order of wavelength) over which $\widetilde{I}$ seems to remain constant.

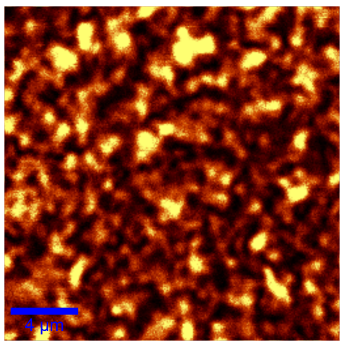


**Figure II.10** – Speckle pattern produced by the multiple scattering of light from a disordered dielectric medium. The wavelength of the Laser is $\lambda = 633\,\text{nm}$. The imaged plane is at a distance of $60\,\mu\text{m}$ from the exit surface of the sample. This image has been obtained by E. Perros in a work published in ref. [2]

### II.3.1 Short-range correlation between two speckle spots

To understand the granularity of a speckle pattern we have to study the joint-statistics between two adjacent speckle spots. Keeping in mind that the fundamental quantity in this study (the field) is a gaussian random variable, we can restrict the analysis to the spatial correlation function of the scattered fields at two different points in order to capture the $\widetilde{I}$-$\widetilde{I}$ correlation function.

[5] As we make clear in the last section of this chapter, the physical process we are interested in this thesis is the breaking down of the gaussian character of the field (importance of high order moments of the fields) and its implication for the joint-statistics between reflected and transmitted speckle patterns. We want to study this break down for various optical thicknesses (even $b \simeq 1$). Considering $\widetilde{I}$ allows us to do so getting rid of the appearance of the mean field when $b \simeq 1$.

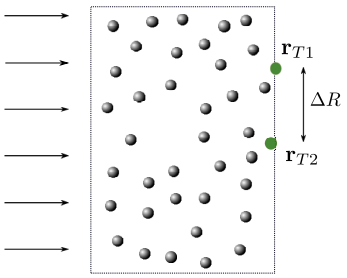


**Figure II.11** – Typical realization of the numerical experiments performed to obtain panels (a) and (c) in Fig. II.12. We shine a 2D random sample with a plane wave and measure the transmitted fields at two different positions $\mathbf{r}_{T1}$ and $\mathbf{r}_{T2}$ separated by a transverse distance $\Delta R$.

### Field-field correlation

In Fig. II.12(a), we represent the numerically calculated phase of the transmitted field at a given position versus the phase of the transmitted field at a fixed distance from the reference point as depicted in Fig. II.11 (parameters of the simulation are $b = 8$ and $k_0\ell = 10$). If the fields were not correlated we would see a random distribution of points in $[-\pi, +\pi]^2$. This is actually observed for points separated by a distance $\Delta r = 12\lambda$. For smaller distances the points tend to agregate on the diagonal of this figure, which testifies of the strong correlation between the two random variables. A different representation of the same phenomenon is given in panel (c) where we show the real part of the field at a given position versus the real part of the field at a fixed distance from this position. In panels (b) and (d) we test the field-field correlation function between points in reflection and transmission using the same two observables (a more complete study of this quantity will be presented in Chap. III).

Let us summarize the main conclusions obtained from these figures:

- For distances smaller than $\lambda$, two transmitted fields are strongly correlated, while for distances larger than $\lambda$ the correlation is lost. In this case the fields can be considered as resulting from two different realizations of the same random process.
- There is *a priori* no field-field correlation between reflection and transmission (at least in the diffusive regime with $b \gg 1$ and $k_0\ell \gg 1$).

Let us give the diagrammatic picture describing the field-field correlations. The idea is really close to that previously used to discuss the diffuse intensity. Indeed a field-field correlation is also a second order moment of the field. To find a way to propagate two fields eventually measured at two different points $\mathbf{r}_{T1}$ and $\mathbf{r}_{T2}$, we have to pair them during propagation. Nonetheless to be measured at two different points, they must separate before the exit surface as shown in Fig. II.13. This process creates short-range correlation only.

### $\widetilde{I}$-$\widetilde{I}$ correlation in the gaussian approximation: the $C_1$ correlation function

Let us now describe the $\widetilde{I}$-$\widetilde{I}$ correlation function defined as

$$C(\mathbf{r}_1, \mathbf{r}_2) = \frac{\langle \delta\widetilde{I}_1 \delta\widetilde{I}_2 \rangle}{\langle \widetilde{I}_1 \rangle \langle \widetilde{I}_2 \rangle} = \frac{\langle \delta E_1 \delta E_1^* \delta E_2 \delta E_2^* \rangle}{\langle \widetilde{I}_1 \rangle \langle \widetilde{I}_2 \rangle} - 1 \tag{II.11}$$

with $\delta\widetilde{I} = \widetilde{I} - \langle \widetilde{I} \rangle$. Keeping in mind that the fields are in first approximation gaussian random variables, we can try to express the correlation between intensities in terms of the first and second

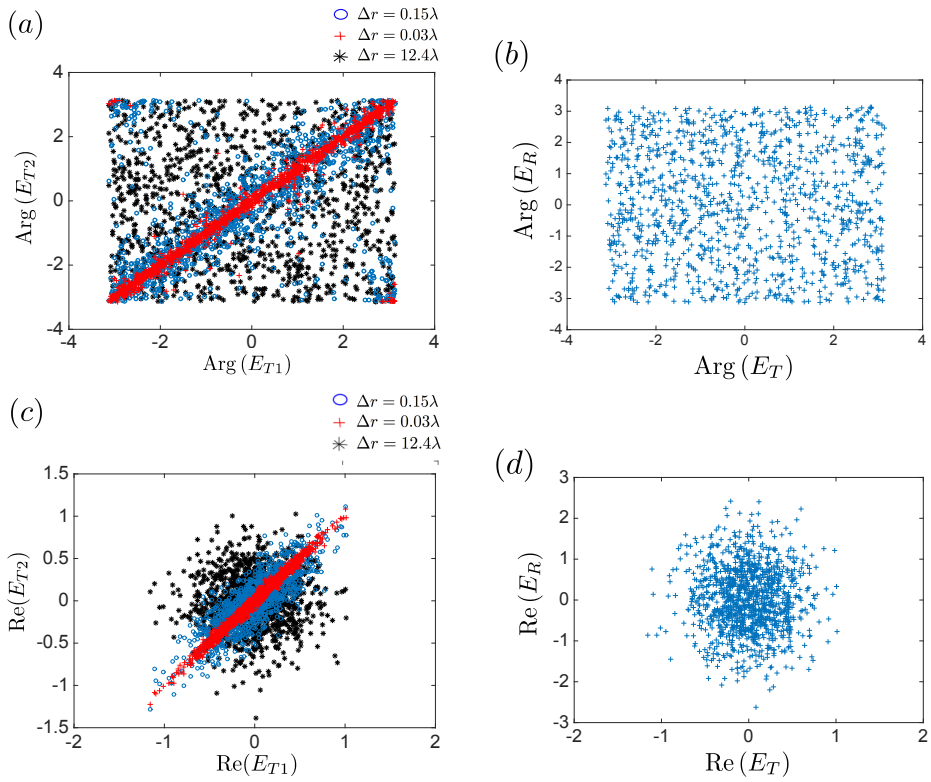


**Figure II.12** – Numerical simulation of two different observables witnessing the existence of the field-field correlations. Panel (a) represents the argument of the field measured at a distance $\Delta r$ of a reference point, versus the argument of the field measured at this reference point in transmission and for three different distances between the points. Panel (b) represents the argument of a reflected field versus the argument of a transmitted field. Panel (c) represents the real part of the field at a given distance of the reference point versus the real part of the field at the reference position in transmission of the sample and for three different distances. Panel (d) represents the same observable for the reflected and the transmitted field. The parameters of the simulations are $b = 8$ and $k_0\ell = 10$.

moments of the fields. The minus one in the expression removes the non-connected part which corresponds to the propagation of $\langle|\delta E_1|^2\rangle$ and $\langle|\delta E_2|^2\rangle$ separately. The only remaining component is the squared modulus of the field-field correlation

$$C(\mathbf{r}_1, \mathbf{r}_2) = \frac{|\langle \delta E_1 \delta E_2^* \rangle|^2}{\langle \widetilde{I}_1 \rangle \langle \widetilde{I}_2 \rangle} = C_1(\mathbf{r}_1, \mathbf{r}_2). \tag{II.12}$$

Let us stress here that Eq. (II.12) is strictly valid for two gaussian fields, which is an approximation as we will show in the next subsection. Nonetheless at this order of approximation we showed that the $\widetilde{I}$-$\widetilde{I}$ correlation is directly linked to the field-field correlation. This contribution usually dominates the intensity-intensity correlation in transmission of a thick medium, and is usually referred to as the $C_1$ correlation (see refs. [28, 33, 34]).

Equation. (II.12) together with panels (a) and (c) in Fig. II.12 shows that for distances smaller than $\lambda$, two transmitted intensities of the fluctuating fields are strongly correlated[6] while for distances larger than $\lambda$ the correlation disappears. Now let us remind that in the gaussian approximation $\langle \delta\widetilde{I}^2 \rangle = \langle \widetilde{I} \rangle^2$. Thus from one speckle spot to the other, on average the intensity fluctuates on a range

[6] We usually say that two points are in the same speckle spot (identical random variables) when their relative distances is smaller than $\lambda$.

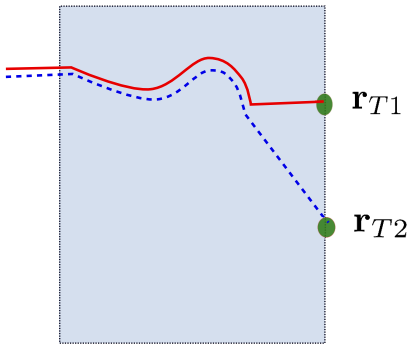


**Figure II.13** – Diagrammatic representation of the field-field correlation. The two fields propagate together and separate to end up at two different measurement points.

of the order of the average intensity. This strong fluctuation on a typical distance of $\lambda$ is responsible for the granularity of a speckle pattern (see ref. [28]) .

The diagrammatic equivalent of Eq. (II.12) is represented on Fig. II.14. We show in panel (a) the non connected part of the $\widetilde{I}$-$\widetilde{I}$ correlation and in panel (b) its component coming from the modulus squared of the field-field correlation ($C_1$).

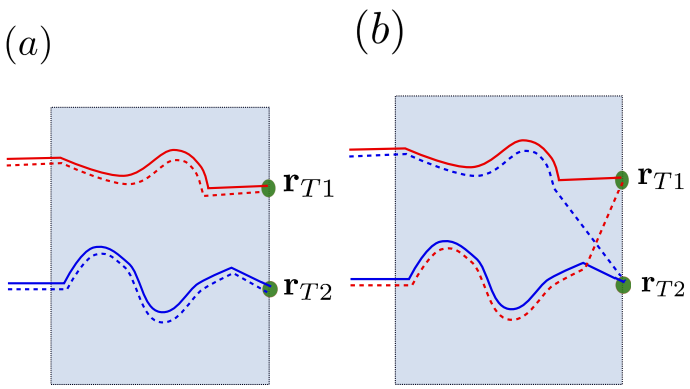


**Figure II.14** – Diagrammatic representations of the two components of the second moment of the intensity at different positions $\langle \widetilde{I}_{T1}\widetilde{I}_{T2}\rangle$ in the gaussian approximation. In panel (a) we show the non connected part of this correlation: two diffuse intensities propagate separately towards two different points $\mathbf{r}_{T1}$ and $\mathbf{r}_{T2}$. In panel (b) we show the connected contribution to the $\widetilde{I}$-$\widetilde{I}$ correlation: the two diffuse intensities exchange their partners at their very last scattering event. We recognize in this diagram the squared modulus of the field-field correlation responsible for the $C_1$ correlation function.

### II.3.2 Joint statistics between intensities of centered and correlated fields

In this section we study the impact of the existence of the field-field correlation on the joint statistics of the intensities of the fluctuating fields. The joint statistics of the normalized intensities of the fluctuating fields of two correlated gaussian random fields is given in ref. [24] and reads

$$P(\widetilde{\mathcal{I}}_1,\widetilde{\mathcal{I}}_2) = \frac{1}{1-\rho^2}\exp\left(\frac{\widetilde{\mathcal{I}}_1+\widetilde{\mathcal{I}}_2}{1-\rho^2}\right) J_0\left(\frac{2\rho\sqrt{\widetilde{\mathcal{I}}_1\widetilde{\mathcal{I}}_2}}{1-\rho^2}\right) \tag{II.13}$$

where

$$\rho = \frac{|\langle \delta E_1 \delta E_2^* \rangle|}{\sqrt{\langle \delta |E_1|^2 \rangle \langle \delta |E_2|^2 \rangle}}. \tag{II.14}$$

In this expression $J_0$ is the Bessel function of first kind and zeroth order and $\widetilde{\mathcal{I}}_1$ and $\widetilde{\mathcal{I}}_2$ are normalized intensities of the fluctuating fields.

A basic analysis of Eq. (II.13) reveals that when $\rho$ tends to 1, the joint distribution tends to agregate on the diagonal of the 2D space $(\widetilde{\mathcal{I}}_1, \widetilde{\mathcal{I}}_2)$. This tells us that when considering two points strongly correlated by the field-field correlation, the two random variables $\widetilde{\mathcal{I}}_1$ and $\widetilde{\mathcal{I}}_2$ become indentical. In the opposite regime, when $\rho$ tends to zero, we see that the two random variables become independent. Indeed $P(\widetilde{\mathcal{I}}_1, \widetilde{\mathcal{I}}_2)$ reduces to $P(\widetilde{\mathcal{I}}_1)P(\widetilde{\mathcal{I}}_2)$.

As shown in Fig. II.12, the field-field correlation function is *a priori* extremely weak between reflection and transmission (at least in the diffusive regime). Thus the $\widetilde{I}$-$\widetilde{I}$ correlation coming from the field-field correlation should be extremely small and the two random variables should be independent.

Nonetheless if we take a look at Fig. II.15 in which we plot the $\widetilde{I}$-$\widetilde{I}$ correlation in transmission (red dashed line) and the modulus squared of the field-field correlation (blue solid line) for two different regimes (panel (a) $b = 3$, $k_0\ell = 10$ and panel (b) $b = 8$, $k_0\ell = 10$) we see that the $\widetilde{I}$-$\widetilde{I}$ correlation is not exactly equal to its gaussian part $C_1$. This intriguing result will be discussed in the next section.

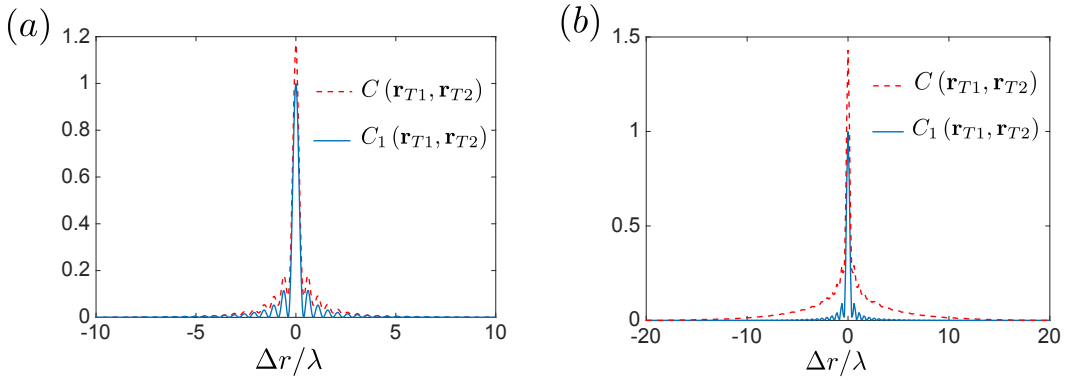


**Figure II.15** – Numerical calculation of the $C_1$ correlation (blue solid line) and $\widetilde{I}$-$\widetilde{I}$ correlation (red dotted line) in transmission for two different medium. The parameters are (a) panel $b = 3$, $k_0\ell = 10$ and (b) panel $b = 8$, $k_0\ell = 10$.

### II.3.3 Crossing of trajectories: beyond the gaussian approximation

We have seen that the field-field correlation function induces strong statistical dependency [strong difference between $P(\widetilde{\mathcal{I}}_1, \widetilde{\mathcal{I}}_2)$ and $P(\widetilde{\mathcal{I}}_1)P(\widetilde{\mathcal{I}}_2)$)] between the intensities of the fluctuating fields observed at two different points. We have also seen that *a priori*, no such field-field correlation exist between points in reflection and in transmission. Does that mean that there is no $\widetilde{I}$-$\widetilde{I}$ correlation nor statistical dependency in reflection/transmission geometry? The answer is *yes in the range of validity of Eq. (II.13) which is the gaussian model.*

Nevertheless we have seen in this chapter that the gaussian model has some flaws. First the probability densities of the transmitted and the reflected intensities of the fluctuating fields do not exactly follow Rayleigh laws as can be seen in Fig. II.9. Moreover in Fig. II.15 it seems that there is an extra contribution to the $\widetilde{I}$-$\widetilde{I}$ correlation on top of the gaussian contribution. This contribution seems to

survive through longer distances between the observation points. This observation of "long-range non-gaussian" correlation is a central issue in this thesis.

Deviations from the gaussian model have been widely studied (see refs. [35, 36, 37, 38, 39]). It is now understood that they emerge as a consequence of crossing of different trajectories inside the scattering medium (see ref. [34]). Let us remind that at the heart of the derivation of the gaussian behavior of the field is the independence of two fields following two different scattering sequences. But as can be seen in Fig. II.16, there are ways to connect two trajectories, or four fields, during their propagation. In this figure we represent two different trajectories that at some point get "close" to each other. Due to the small distances that separate the two trajectories, there is a non negligible probability that the fields exchange at this point, connecting the intensities measured at points $\mathbf{r}_{T1}$ and $\mathbf{r}_{T2}$.

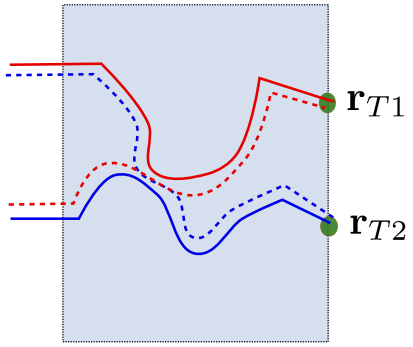


**Figure II.16** – Diagrammatic representation of one contribution of the non gaussian $\widetilde{I}$-$\widetilde{I}$ correlation between two points in transmission $\mathbf{r}_{T1}$ and $\mathbf{r}_{T2}$.

These contributions appear in the development of the $\widetilde{I}$-$\widetilde{I}$ correlation

$$\frac{\langle \delta\widetilde{I}_1 \delta\widetilde{I}_2 \rangle}{\langle \widetilde{I}_1 \rangle \langle \widetilde{I}_2 \rangle} = \frac{|\langle \delta E_1 \delta E_2^* \rangle|^2}{\langle \widetilde{I}_1 \rangle \langle \widetilde{I}_2 \rangle} + \frac{\langle \delta E_1 \delta E_1^* \delta E_2 \delta E_2^* \rangle_c}{\langle \widetilde{I}_1 \rangle \langle \widetilde{I}_2 \rangle} \tag{II.15}$$

where the additional term is the non gaussian-contribution of the intensity-intensity correlation, or connected (subscript $\langle ... \rangle_c$) part of the four-field correlation[7]. The difficulty in the study of these terms is that there is *a priori* a huge number of them because there are many ways to connect two trajectories or four fields. How to select them, and how to calculate them will be discussed in Chaps. III, IV, V and in App. .3.3

One can wonder why these terms are of interest, since they are corrections to a model that works very well in many practical situations. The answer is that when these terms are the only contribution to an observable, they deserve a complete study (see ref. [40]). In particular we demonstrate in this thesis that they are the dominant term of the $\widetilde{I}$-$\widetilde{I}$ correlation between reflection and transmission[8].

[7]This contribution is the first correction to the intensity-intensity correlation due to the non-gaussian character of the field for centered variables. Indeed the connected three fields correlation has to be paired with $\langle \delta E \rangle$ and thus gives a zero contribution.

[8]Equation. II.15 *is a milestone* because it expresses the $\widetilde{I}$-$\widetilde{I}$ correlation as the sum of the $C_1$ correlation and the connected four fields correlation. Its simplicity whatever the physical parameters of the system is the justification of our choice to study statistics of centered variables.

# Chapter III

# Correlation between reflected and transmitted intensities in the diffusive regime

## Table des matières

The purpose of this chapter is to discuss the different building blocks we need to analytically derive the expression of the intensity-intensity correlation function between reflection and transmission for a thick ($b \gg 1$) and dilute ($k_0\ell \gg 1$) medium. In this regime the average fields are negligible, thus the intensity-intensity correlation function follows directly from Eq. (II.15). We start this section by discussing the reflected and transmitted fields and their average value in a system composed of point dipoles. Then we study the average intensity and find that the diffuse intensity follows a diffusion equation whose source term is the ballistic intensity. Then we calculate the $C_1$ correlation function between reflection and transmission and find that it is exponentially decreasing with the optical thickness. Eventually we discuss the main contribution to the non-gaussian correlation between reflection and transmission, derive its analytical expression for large optical thickness, and show that it is the main contribution of the intensity-intensity correlation function between reflection and transmission.

## III.1 A discussion on mesoscopic correlations

The purpose of this introductory section is to give a brief review of different works about non-gaussian correlations for classical waves. We also want to discuss the limitations of analytical techniques used to derive these correlations.

### It started with electrons

At the beginning of the 80's, researchers in condensed matter physics discovered that micrometer size metallic wires cooled to low temperature exhibited some unexpected coherent effects like weak localization corrections to conductivity [41] or universal conductance fluctuations [42, 43, 44]. The conductance is the natural observable for electronic experiments for which it is not possible to excite or detect one channel specifically. Few years later, it was realized that classical waves (optics, acoustics, microwaves) offer many more observables to study the richness of wave transport in disordered systems. Indeed with those waves, one can excite a specific channel and observe the response in each outgoing channel.

### Classical waves: new observables

Studies of mesoscopic phenomena in optics,started in the mid 80's motivated by the unparallelled access to channel-resolved quantities. In the optical regime it became possible to measure the strong spatial variations of the intensity scattered by a medium [28], or the fact that those complicated intensity patterns shift with the angle of incidence of the laser light, provided that the change is small. This is the so called memory effect [45, 46, 47]. It is important to stress that these phenomena were impossible to observe with electrons for which only conductance can be measured [38]. Let us notice

that many of these mesoscopic effects are independent of the type of waves. Thus weak localization effects [48, 49, 50] or universal conductance fluctuations [51] have been recovered with classical waves.

### Intensity-intensity correlations

With classical waves, we can excite a disordered medium with a controlled incident wave and observe the scattering of this wave in a given direction or position in space [52]. In optics we measure intensity more easily than fields. One observable we can study is thus the correlation between intensities at two different positions or in two given directions[1]. It is also possible to mimic electronic experiments integrating either the transmitted intensity, the incoming channels, or both. Those three different types of experiments are represented schematically in Fig. III.1.

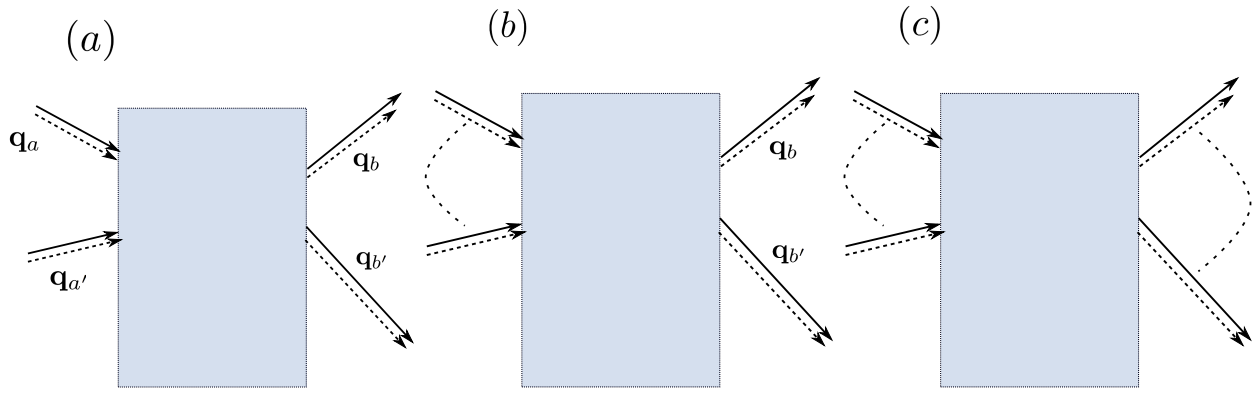


**Figure III.1** – Schematics of three different experiments used to study intensity-intensity correlation. Panel (a) corresponds to the correlation of the intensity scattered in directions $\mathbf{q}_b$ and $\mathbf{q}_{b'}$ when the medium is shined with $\mathbf{q}_a$ and $\mathbf{q}_{a'}$. Panel (b) corresponds to the correlation of the intensity scattered in directions $\mathbf{q}_b$ and $\mathbf{q}_{b'}$ for an integrated source. Panel (c) corresponds to fluctuation of the integrated intensity (equivalent of the universal conductance fluctuations for classical waves).

The dominant term of these three experiments has been given a name $C_1$, $C_2$ and $C_3$ [53]. The $C_1$ correlation is the leading term of the correlation between non integrated intensities measured at two nearby points or nearby directions [panel (a) in Fig. III.1]. The $C_2$ correlation is the leading term of the correlation between two intensities scattered in two different directions for an integrated illumination [panel (b) in Fig. III.1]. Microscopically, this term comes from the crossing of trajectories inside the medium, thus to the non gaussian behavior of light. This $C_2$ correlation is also called long-range intensity correlations. Its existence has been predicted in the end of the 80's in transmission of a thick disordered medium [54, 55, 53, 56]. First measurements of long range correlations appeared few years later in optics [57, 58] and for microwaves [59]. The $C_3$ correlation is the leading term of the fluctuation of the integrated intensity when the medium is excited with all possible channels [panel (c) in Fig III.1]. It corresponds to measurements in electronic experiments where all modes are excited when electrons enter a conductor. The $C_3$ term is thus the one responsible for the universal conductance fluctuation. Microscopically, this term comes from the crossing of trajectories twice inside the medium, thus it also contributes to the non gaussian behavior of light as represented in Fig III.2. For a review about speckle correlations see ref. [37]. Another contribution to the intensity-intensity correlation function has been introduced in 1999 as the dominant term of the intensity-intensity in two distant speckle spots produced by a point source. This contribution has been called the $C_0$ correlation [60, 61, 62, 63]. Diagrammatically it corresponds to the exchange of

[1] We can also observe the intensity in one direction or in one given position and vary the exciting fields.

four ballistic fields using one extra scatterer at the entrance of the scattering media before leaving diffusively (this contribution will be discussed in details in Chap. IV) .

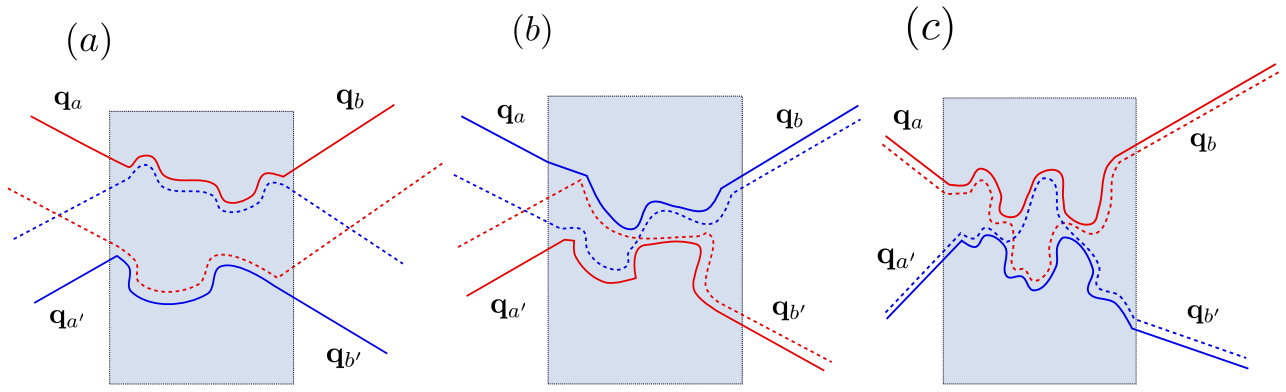


**Figure III.2** – Panel (a): leading term of the experiments represented in [panel (a) in Fig. III.1] in the diffusive regime ($C_1$). Panel (b): one of the two leading term of the experiments represented in [panel (b) in Fig. III.1] in the diffusive regime ($C_2$). Panel (c): one of the leading term of the experiments represented in [panel (c) in Fig. III.1] in the diffusive regime ($C_3$).

Comparing this splitting with that given in Chap. II

$$\frac{\langle \delta\widetilde{I}_1 \delta\widetilde{I}_2\rangle}{\langle\widetilde{I}_1\rangle\langle\widetilde{I}_2\rangle} = \frac{|\langle \delta E_1 \delta E_2^*\rangle|^2}{\langle\widetilde{I}_1\rangle\langle\widetilde{I}_2\rangle} + \frac{\langle \delta E_1 \delta E_1^* \delta E_2 \delta E_2^*\rangle_c}{\langle\widetilde{I}_1\rangle\langle\widetilde{I}_2\rangle} \tag{III.1}$$

we understand that the diagrams giving rise to $C_0$, $C_2$ or $C_3$ are all contained in $\langle \delta E_1 \delta E_1^* \delta E_2 \delta E_2^*\rangle_c$. In a nutshell, $\langle \delta E_1 \delta E_1^* \delta E_2 \delta E_2^*\rangle_c$ is a complex quantity which takes into account all possible ways to connect four fields inside the disorder medium. When a particular experiment makes one of those terms dominate the other, we can study them independently. Doing so we understand the different part of this complicated quantity $\langle \delta E_1 \delta E_1^* \delta E_2 \delta E_2^*\rangle_c$ one by one. Let us illustrate this using the example of microwave experiments [64, 65, 66]. In these measurements one has direct access to the field amplitude and phase (which is not the case in optics and in electronics). One can thus play with Eq. (II.15), measuring the $C_1$ correlation independently and have a direct access to $\langle \delta E_1 \delta E_1^* \delta E_2 \delta E_2^*\rangle_c$ (substracting $C_1$) without any integration. Doing so one managed to study carefully the exit vertex of the long-range diagrams without integration. This provided important informations about this part of the scattering sequence.

## Analytical descriptions of mesoscopic effects

Let us discuss the limitations of the analytical methods used in studies of non-gaussian correlations. First let us point out that there are two analytical approaches to calculate mesoscopic correlations: the microscopic approach (or diagrammatic) and the random matrix theory (RMT) (see refs. [67, 68]).

- Diagrams have an appealing property in providing a clear physical picture in term of scattering sequences. The shortcoming of the diagrammatic approach is that there are easy to compute only in the diffusive regime ($k_0\ell \gg 1$ and $b \gg 1$). Let us also stress that because diagrammatics is a perturbative approach, extra care must be taken when one wants to add a diagram to the model.
- The other approach, the RMT, is based on simple arguments of unitarity and time reversal symmetry, and works in all regimes. Nonetheless it is harder to give a physical interpretation

to the results and the exact form of the correlation functions cannot be obtained with this method [69, 70].

In this thesis we work with diagrammatic technique. We will thus not discuss the RMT approach in detail.

### Limitations of diagrammatic techniques

The diagrammatic method is based on the decomposition of the scattering sequences into building blocks. The knowledge of the building blocks allows us to calculate every scattering sequence. It is important to note that the diagrammatic representation in Fig. III.2 is adequate only for a thick ($b \gg 1$) and dilute ($k_0\ell \gg 1$) medium in *transmission*. Beyond this regime, we face two difficulties: the building blocks are harder to compute analytically, and additional diagrams need to be derived. Let us discuss the example of the reflection geometry. In that case it has been claimed that the usual model does not work [71]. In transmission through a thick and dilute sample, intensity-intensity correlation requires the use of a complicated object called Hikami vertex [72]. This vertex represents the exchange of partners as depicted in panel (b) in Fig. III.2. The study of the reflection geometry led to two questions:

- Is the Hikami vertex complete? As detailed in App. .3.3 this vertex considers that fields can only be scattered by impurities by pairs, and neglects for instance the possibility that four fields scatter at the same impurity.

- Is the usual decomposition of the correlation function represented in Fig. III.2 still true in the reflection configuration?

The first attempt to go to a higher order in the expression of the vertex has been presented in ref. [73]. This discussion has been followed in refs. [39, 74] in which it is shown that the higher order terms in the Hikami vertex add additional terms to the intensity-intensity correlation function. Those terms are called by the authors of ref. [39] incoherent contribution to the non-gaussian correlation. To our knowledge they have not been observed so far. These authors also tried to consider all the possible diagrams in order to represent the intensity-intensity correlation in reflection of a scattering medium [71, 75, 76, 77]. To proceed they use the radiative transfer equation to represent the propagation close to the boundaries (which is important in a reflection configuration) and consider more diagrams than in the usual approach. Indeed in the usual picture of long-range correlation given in Fig. II.16, two diffuse intensities meet inside the medium, pairs of fields exchange, and two diffuse intensities leave towards the measurements points. This contribution does not take into account, for instance, the scattering sequences where one ballistic intensity meets a diffuse intensity, exchange fields and then leave diffusively. Adding those terms is important in reflection according to ref [71].

From this discussion we see that diagrammatic techniques are not necessarily complete. New observable need to be studied to strengthen these techniques. The reflection configuration is a good example of this limitation, for which it can be safer to use RMT [78, 70, 79]. In this thesis we focus on a new configuration, namely the reflection/transmission (R/T) geometry[2]. We expect this configuration will provide new observables that will help us to improve our understanding of diagrammatic techniques.

[2]Let us stress that to our knowledge, R/T correlations have been discussed only twice before our work [80, 71].

# III.2 Average field

The first building block we need to derive the expression of the intensity-intensity correlation function in R/T is the average field.

## III.2.1 Cluster expansions for point dipoles

The total field for a given configuration of disorder can be written in operator[3] representation:

$$E = E_0 + \sum_{j=1}^{N} G_0 T_j E_0 + \sum_{j=1}^{N} \sum_{\substack{k=1 \\ k\neq j}}^{N} G_0 T_k G_0 T_j E_0 + ... \tag{III.2}$$

with $N$ the number of scatterers in the complex medium, $G_0$ the Green function of the wave equation in vacuum, $E_0$ the incident field and $T_j$ the T-matrix of particle $j$. The T-matrix takes into account all the scattering from a given particle. In the case of point dipoles it takes the form

$$T_j(\mathbf{r}', \mathbf{r}'') = \alpha(\omega) k_0^2 \delta(\mathbf{r}' - \mathbf{r}_j)\delta(\mathbf{r}'' - \mathbf{r}_j) \tag{III.3}$$

with $\alpha$ the polarizability of the particles. For resonant scatterers in 2D it takes the form

$$\alpha(\omega) = -\frac{2\Gamma}{k_0^2(\omega - \omega_0 + i\Gamma/2)} \tag{III.4}$$

where $\omega_0$ is the resonance frequency and $\Gamma$ the line width. This specific form of the polarizability fulfills the optical theorem (energy conservation).

Equation (III.2) is called the cluster expansion and has been derived in ref [27]. It decomposes the field over scattering paths of different number of scattering events. Indeed the first term of Eq. (III.2) corresponds to the incident field, while the second term corresponds to the single scattering contribution (involving all paths containing only one scattering event), etc.

## III.2.2 Dyson Equation

Equation (III.2) allows us to perform the averaging process. In the case of $N$ identical particles contained in a volume $V$, this averaging process consists in changing randomly the position of the scatterers. Taking the average of Eq. (III.2) we can write

$$\langle E \rangle = E_0 + \sum_{j=1}^{N} G_0 \langle T_j \rangle E_0 + \sum_{j=1}^{N} \sum_{\substack{k=1 \\ k\neq j}}^{N} G_0 \langle T_k G_0 T_j \rangle E_0 + ... \tag{III.5}$$

We can associate to the first term the operator $\Sigma_{\text{ISA}}$ given by

$$\Sigma_{\text{ISA}} = \sum_{j=1}^{N} \langle T_j \rangle. \tag{III.6}$$

[3]For instance the second term of Eq. (III.2) means $\int \sum_{j=1}^{N} G_0(\mathbf{r} - \mathbf{r}'')T_j(\mathbf{r}'', \mathbf{r}')E_0(\mathbf{r}')\mathrm{d}\mathbf{r}''\mathrm{d}\mathbf{r}'$.

The subscript ISA (for independent scattering approximation) mathematically means that the $T$ matrix of two different scatterers are not correlated. In the ISA the third term in Eq. (III.5) simply reads $\Sigma_{\text{ISA}} G_0 \Sigma_{\text{ISA}}$. Nonetheless if some correlations exist between two different scatterers an additional contribution can exist. We can define $\Sigma_{\text{corr}}$ as the unfactorizable part of this term as

$$\Sigma_{\text{ISA}} G_0 \Sigma_{\text{ISA}} + \Sigma_{\text{corr}} = \sum_{j=1}^{N} \sum_{\substack{k=1 \\ k \neq j}}^{N} \langle T_k G_0 T_j \rangle. \tag{III.7}$$

The same reasoning can be applied to each term of the sum in Eq. (III.5). Taking all the unfactorizable terms into account, and including them into a single quantity called *self energy* $\Sigma$

$$\Sigma = \Sigma_{\text{ISA}} + \Sigma_{\text{corr}} + ... \tag{III.8}$$

one can show that the average Green function[4] obeys the equation

$$\langle G \rangle = G_0 + G_0 \Sigma \langle G \rangle \tag{III.9}$$

known as the *Dyson equation*. Equation (III.9) is exact, the complexity of the problem being hidden in the self energy $\Sigma$. Knowing the self energy, we can obtain the expression of the average Green function transforming Eq. (III.9) into

$$\langle G(\mathbf{k}) \rangle = \left( \frac{1}{G_0(\mathbf{k})} - \Sigma(\mathbf{k}) \right)^{-1}. \tag{III.10}$$

The free space Green function can be easily calculated using Helmholtz equation in the $(\mathbf{k}, \omega)$ domain and reads $G_0(\mathbf{k}) = 1/\left(k^2 - k_0^2\right)$. Thus we can write the expression of the average Green function the following way

$$\langle G(\mathbf{k}) \rangle = \frac{1}{k^2 - k_{eff}^2} \tag{III.11}$$

with $k_{eff}^2 = k_0^2 + \Sigma(\mathbf{k})$. Let us stress that Eq. (III.11) has the exact same form as the equation $G_0$ with the simple change $k_0 \to k_{eff}$. The presence of the disordered medium can thus be represented for the average field by an effective medium with an index of refraction $n_{eff} = n + in''$ [when $\Sigma(\mathbf{k})$ is approximated by $\Sigma(\mathbf{k}_0)$]. The attenuation from scattering is the cause of the presence of the imaginary part of the index. We can link $n''$ to the scattering mean free path $n'' = 1/(2k_0\ell)$. For dilute systems composed of point scatterers the self energy has a simple expression $\Sigma \simeq \Sigma_{\text{ISA}} = \rho k_0^2 \alpha$ in terms of the polarizability and of the density of the scatterers. From Eq. (III.11) we can show that the average Green function of a disordered medium reads in real space

$$\langle G(r) \rangle = \begin{cases} (i/4)\, \mathrm{H}_0(k_{eff} r) & \text{for 2D scalar waves} \\ \dfrac{\exp\left(ik_{eff} r\right)}{4\pi r} & \text{for 3D scalar waves.} \end{cases} \tag{III.12}$$

In the 2D expression $H_0$ is the Hankel function of first kind and order zero.

### III.2.3 Average field inside a slab illuminated with a plane wave

The determination of the average Green function allows us to calculate the average field for a slab illuminated by a monochromatic plane wave. To do so we can use the propagator of the average

[4] It is the Green function of the equation followed by the average field.

field[5] which acts on the incident wave of transverse vector $\mathbf{q}_a$:

$$\begin{aligned}\langle E(\mathbf{r})\rangle_{\mathbf{q}_a} &= -2ik_a \int_S \langle G(\mathbf{r}-\mathbf{r}_1)\rangle E_0 \exp\left(-i\mathbf{q}_a.\mathbf{r}_{1,\perp}\right) \mathrm{d}\mathbf{r}_{1,\perp} \\ &= -2ik_a E_0 \int \langle G(\mathbf{k})\rangle \exp\left[i\mathbf{k}.(\mathbf{r}-\mathbf{r}_1)\right] \exp\left(-i\mathbf{q}_a.\mathbf{r}_{1,\perp}\right) \mathrm{d}\mathbf{r}_{1,\perp} \frac{\mathrm{d}\mathbf{k}}{(2\pi)^d} \\ &= -2ik_a E_0 \int \frac{\exp\left(ik_z z\right)}{k_z^2 + q_a^2 - k_{eff}^2} \exp\left(-i\mathbf{q}_a.\mathbf{r}_\perp\right) \frac{\mathrm{d}k_z}{(2\pi)} \\ &= E_0 \exp\left(ik_a z\right) \exp\left(-i\mathbf{q}_a \mathbf{r}_\perp\right)\end{aligned} \tag{III.13}$$

with $k_a = \sqrt{k_{eff}^2 - q_a^2}$ defined with a positive imaginary part (the scattered medium is defined for $0 < z < L$) and $\mathbf{r}_{1,\perp}$ the transverse component of the vector $\mathbf{r}_1$. Note that when $\mathbf{q}_a = 0$ (normal incidence)

$$\langle E(\mathbf{r})\rangle = E_0 \exp\left(i\sqrt{k_{eff}^2} z\right) \simeq E_0 \exp\left(ik_0 z\right) \exp[-z/(2\ell)] \tag{III.14}$$

## Average field in transmission

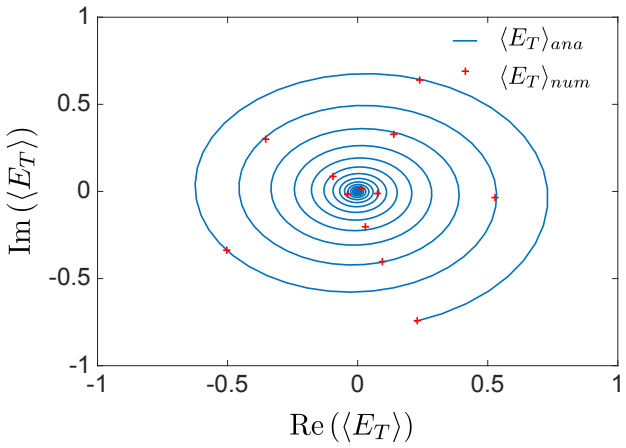


**Figure III.3** – Imaginary part of the mean field versus its real part for various optical thicknesses ($L$ varies and $k_0\ell = 10$). The blue curve corresponds to Eq. (III.14) calculated for $z \simeq L$ while the red crosses correspond to numerical calculation of the average transmitted field.

In Fig. III.3, we test the validity of Eq. (III.14). To do so we represent the imaginary part of the analytically calculated average transmitted field (blue solid line) versus its real part, varying the optical thickness of the medium (we set $k_0\ell = 10$ and we vary $L$ from $0.5\ell$ to $7\ell$). Additionally we represent the numerically calculated average transmitted fields at specific optical thicknesses (red crosses) and observe a very good agreement between analytical and numerical calculations. For a fixed mean free path, varying the optical thickness has two effects on the average transmitted field: a dephasing effect simply due to the fact that the field travels through a longer distance $L = b\ell$ when $b$ increases, and a decrease of its absolute value due to scattering. This result is in good agreement with Fig. II.4 in which we plot the numerically calculated absolute value of the transmitted average field versus the optical thickness, and observe an exponential behavior.

[5] As for free-space propagation, we will state that the propagator for the field between two parallel plane is linked to the derivative along the normal direction of the average Green function [81].

### Average field in reflection

In reflection the discussion becomes different. We defined the reflected field as the scattered field measured in reflection, a quantity which does not follow the same equation as the total field. An easy way to discuss the scaling of the average reflected field is to consider that it is created by reflections on the boundaries of the effective medium[6]. For dilute samples we can show that $\epsilon_{eff} = 1 + \rho\alpha$ thus $n_{eff} = \sqrt{\epsilon_{eff}} \simeq 1 + i/(2k_0\ell)$. From the value of $n_{eff}$ we can calculate the transmission and reflection factors at the different interfaces (for instance the reflection factor at the first interface is $r = (1 - n_{eff})/(n_{eff} + 1) \simeq (-i)/[4k_0\ell]$). Taking into account all the multiple reflection we obtain

$$\langle E_R \rangle = rE_0 \left( 1 - \frac{t_1 t_2 \exp[2ik_{eff}L]}{1 + r^2 \exp[2ik_{eff}L]} \right) \simeq \frac{-iE_0}{4k_0\ell}. \tag{III.15}$$

The last equality is more and more accurate as the optical thickness increases (since it shows that the Fabry-Perot effect becomes negligible). In Fig. III.4 we plot the absolute value of the numerically calculated average reflected field (for optical thicknesses varying from 2 to 5) versus $k_0\ell$, and the analytically calculated absolute value of the average reflected field in the limit $b \to \infty$ (thus using the right-hand side of Eq. III.15). We find a good agreement between numerics and analytics. Let us stress that the oscillating terms coming from the Fabry-Perot effect at the boundaries of the effective medium can be well described by the analytical formula and becomes negligible when $b$ increases due to extinction of the average field. The important point is that for all optical thicknesses $|\langle E_R \rangle| \propto E_0/(k_0\ell)$ and is thus a small quantity.

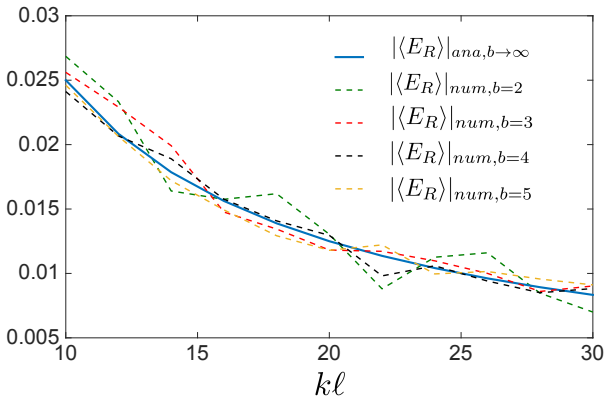


**Figure III.4** – Modulus of the average reflected field versus the parameter $k_0\ell$. The blue solid line corresponds to the analytical calculation taking only into account the reflection at the first boundary $z = 0$ [right hand side of Eq. (III.15)], thus corresponding to the limiting case $b \to \infty$. The dashed lines corresponds to numerical calculation of the absolute value of the average reflected field for optical thicknesses from 2 to 5.

## III.3 Average intensity

In the previous section, we were interested in the average field in reflection and transmission. We have seen that the average transmitted field is exponentially decreasing with the optical thickness of the medium, and that the average field in reflection scales with the small parameter $1/(k_0\ell)$. Let us now study the second moment of the fields in reflection and in transmission.

[6]For the average transmitted field we did not take those terms into account because they are sub-leading. In the remaining part of this work we neglect the boundaries of the effective medium.

### III.3.1 Bethe-Salpeter equation

Let us multiply Eq. (III.2) by its complex conjugate (taken at two different positions) and take the average value of the resulting equation. Doing so, we can cast the averaged equation in the following closed form, known as the *Bethe-Salpeter* equation

$$\langle E(\mathbf{r})E^*(\mathbf{r}')\rangle = \langle E(\mathbf{r})\rangle\langle E^*(\mathbf{r}')\rangle + \int \langle G(\mathbf{r},\mathbf{r}_3)\rangle\langle G^*(\mathbf{r}',\mathbf{r}_4)\rangle\, \mathrm{U}(\mathbf{r}_4,\mathbf{r}_3,\mathbf{r}_2,\mathbf{r}_1)\langle E(\mathbf{r}_2)E^*(\mathbf{r}_1)\rangle \mathrm{d}\mathbf{r}_1 d\mathbf{r}_2 d\mathbf{r}_3 d\mathbf{r}_4. \quad \text{(III.16)}$$

The first term comes from the non correlated propagation of the field and its complex conjugate, and the second term takes into account all the possible way to correlate two fields. Equation. (III.16) is the exact equivalent of Dyson equation for the moment of order two of the field. It is an exact equation, all the complexity of the problem is contained in the vertex operator $\mathrm{U}(\mathbf{r}_4,\mathbf{r}_3,\mathbf{r}_2,\mathbf{r}_1)$ (which can be written in terms of the T-matrix). The idea is the same as for the self energy. We can express U as the sum of different terms:

$$\mathrm{U} = \mathrm{U}_{\text{ladder}} + \mathrm{U}_{\text{corr}} + ... \quad \text{(III.17)}$$

For diluted systems, the dominant term to first order in $(k_0\ell)^{-1}$ is given by $\mathrm{U}_{\text{ladder}}$:

$$\mathrm{U}_{\text{ladder}} = \sum_{j=1}^{N} \langle T_j T_j^* \rangle = \gamma\delta(\mathbf{r}_1-\mathbf{r}_2)\delta(\mathbf{r}_3-\mathbf{r}_2)\delta(\mathbf{r}_4-\mathbf{r}_3) \quad \text{(III.18)}$$

$\gamma = \rho k_0^4 |\alpha|^2$ being the average weight of an interaction with the disorder, and is equal to

$$\gamma = \begin{cases} \dfrac{4k_0}{\ell} & \text{for 2D scalar waves} \\ \dfrac{4\pi}{\ell} & \text{for 3D scalar waves.} \end{cases} \quad \text{(III.19)}$$

Inserting Eq. (III.18) into Eq. (III.16) we obtain the expression of the field-field correlation function in the ladder approximation:

$$\langle E(\mathbf{r})E^*(\mathbf{r}')\rangle = \langle E(\mathbf{r})\rangle\langle E^*(\mathbf{r}')\rangle + \gamma \int \langle G(\mathbf{r},\mathbf{r}_1)\rangle\langle G^*(\mathbf{r}',\mathbf{r}_1)\rangle\langle E(\mathbf{r}_1)E^*(\mathbf{r}_1)\rangle \mathrm{d}\mathbf{r}_1. \quad \text{(III.20)}$$

Equation (III.20) is hard to use in this form since it is a recursive equation (the second order moment is expressed as an integral of itself). Let us define the ladder operator by

$$\mathrm{L}(\mathbf{r}_1,\mathbf{r}_2) = \gamma\delta(\mathbf{r}_1-\mathbf{r}_2) + \gamma \int |\langle G(\mathbf{r}_2,\mathbf{r}_3)\rangle|^2\, \mathrm{L}(\mathbf{r}_3,\mathbf{r}_1)\mathrm{d}\mathbf{r}_3. \quad \text{(III.21)}$$

This allows us to rewrite the second moment of the field in terms of the first moment in the form

$$\langle E(\mathbf{r})E^*(\mathbf{r}')\rangle = \langle E(\mathbf{r})\rangle\langle E^*(\mathbf{r}')\rangle + \int \langle G(\mathbf{r},\mathbf{r}_2)\rangle\langle G^*(\mathbf{r}',\mathbf{r}_2)\rangle\, \mathrm{L}(\mathbf{r}_1,\mathbf{r}_2)\langle E(\mathbf{r}_1)\rangle\langle E^*(\mathbf{r}_1)\rangle \mathrm{d}\mathbf{r}_1 \mathrm{d}\mathbf{r}_2. \quad \text{(III.22)}$$

Let us discuss Eq. (III.22) and Eq. (III.21). Together they give a nice picture of the propagation of the second order moment of the field. Indeed, looking at Eq. (III.22), we see that the second moment is composed of two terms. The first term consists in the product of the first moment (average fields that propagate separately). We know that this part is decreasing exponentially with the optical thickness in transmission. The second term describes the propagation of two mean fields up to a point where they start to travel together (scattered by the same impurities), which we represent mathematically with the operator ladder $\mathrm{L}(\mathbf{r}_1,\mathbf{r}_2)$. One can see by iterating Eq. (III.21) that the ladder operating from $\mathbf{r}_1$ to $\mathbf{r}_2$ takes into account all scattering processes where the field and its complex conjugate are scattered once, twice, or any number of times as long as they do it together from $\mathbf{r}_1$ to $\mathbf{r}_2$. The final part of the propagation is done from $\mathbf{r}_2$ to the observation points $\mathbf{r}$ and $\mathbf{r}'$ through the average Green functions.

### III.3.2 A diffusion equation for the "diffuse" intensity

We have seen in the introduction that for a thick medium, the diffuse intensity (which coincides with the second term in Eq. (III.22) taken at $\mathbf{r} = \mathbf{r}'$) decreases slowly compared to the ballistic intensity. This implies that the ladder operator should decrease more slowly than the absolute value of the mean Green function. Taking this into account in Eq. (III.21), we can show that the ladder operator follows a diffusion equation

$$\Delta_{\mathbf{r}_1} \mathrm{L}(\mathbf{r}_1, \mathbf{r}_2) = -\frac{d\gamma}{\ell^2}\delta(\mathbf{r}_1 - \mathbf{r}_2) \tag{III.23}$$

with $d$ the dimension of the problem. Taking the Laplacian of the expression of the diffuse intensity given by the second term in the right hand side of Eq. (III.22), we can show that:

$$-\frac{\ell^2}{d}\Delta\langle|\delta E(\mathbf{r})|^2\rangle = |\langle E(\mathbf{r})\rangle|^2 \tag{III.24}$$

in which we remind that $\langle|\delta E(\mathbf{r})|^2\rangle = I_d(\mathbf{r})$. Taking into account that, for a plane-wave incident on the slab at normal incidence we have $|\langle E(\mathbf{r})\rangle|^2 = I_0 \exp(-z/\ell)$ we can show that

$$\langle I(z)\rangle = \frac{dI_0(1 + z_0/\ell)}{L + 2z_0}(L + z_0 - z) - (d-1)I_0 \exp\left(-\frac{z}{\ell}\right) \tag{III.25}$$

with $\langle I(z)\rangle = \underbrace{|\langle E(\mathbf{r})\rangle|^2}_{I_b(\mathbf{r})} + \underbrace{\langle|\delta E(\mathbf{r})|^2\rangle}_{I_d(\mathbf{r})}$ and $z_0$ the so called *extrapolation length* [82, 83] given by

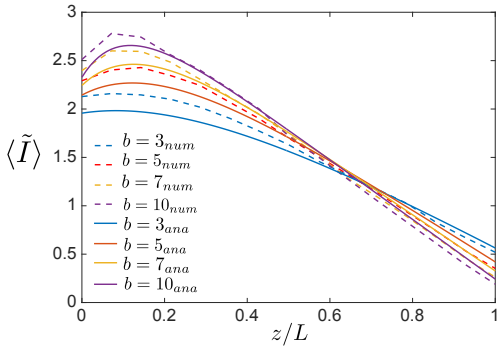


**Figure III.5** – Numerical and analytical calculations of the average intensity $\langle I\rangle$ versus the depth inside the medium normalized by $L$ for various optical thicknesses ($L$ varies and $k_0\ell = 10$).

$$z_0 = \begin{cases} \dfrac{\pi\ell}{4} & \text{for 2D scalar waves} \\ \dfrac{2\ell}{3} & \text{for 3D scalar waves.} \end{cases} \tag{III.26}$$

In Fig. III.5 we plot the numerical and analytical calculations of the average intensity $\langle I\rangle$ versus the depth inside the medium normalized by $L$ for various optical thicknesses. There are two regimes of depths for all curves. For $z \leq \ell$, the ballistic light couples into the scattering medium while for $z \gg \ell$ there is no more ballistic intensity into the medium. This part of the curves ($z \gg \ell$) has a linear decay characteristic of the diffusive regime. Let us define

$$\langle I_T\rangle = \langle I(\mathbf{r}_T)\rangle \tag{III.27}$$

and

$$\langle I_R\rangle = |\langle E_R\rangle|^2 + I_d(\mathbf{r}_R). \tag{III.28}$$

We stress that $\langle I_R\rangle \neq \langle I(\mathbf{r}_R)\rangle = |\langle E(\mathbf{r}_R)\rangle|^2 + I_d(\mathbf{r}_R)$ because of the difference of average fields in the two expressions. From the two previous subsections we have $\langle I_T\rangle \simeq I_d(\mathbf{r}_T)$ when $b \gg 1$ and $\langle I_R\rangle \simeq I_d(\mathbf{r}_R)$ when $k_0\ell \gg 1$. In the diffusive regime ($b \gg 1$ and $k_0\ell \gg 1$) the average intensities in reflection and in transmission are thus equal to their diffuse components.

### III.3.3 The ladder operator for a slab

We have seen in the previous subsection that the ladder operator is at the heart of the derivation of the diffusion equation for the diffuse intensity. This operator propagates pairs of fields diffusively, and can thus be directly used to calculate the diffuse intensity at a given position. It is one of the building blocks we need to calculate more advanced observables in the diagrammatic approach. Let us remind that the slab is invariant along its transverse direction. The ladder operator has thus the property

$$\mathrm{L}(\mathbf{r}_1,\mathbf{r}_2) = \mathrm{L}(z_1,z_2,\mathbf{r}_{1,\perp}-\mathbf{r}_{2,\perp}) = \int \mathrm{L}(z_1,z_2,\mathbf{q})\exp[i\mathbf{q}.(\mathbf{r}_{1,\perp}-\mathbf{r}_{2,\perp})]\frac{\mathrm{d}\mathbf{q}}{(2\pi)^{d-1}}. \tag{III.29}$$

as represented in Fig. III.6. We obtain

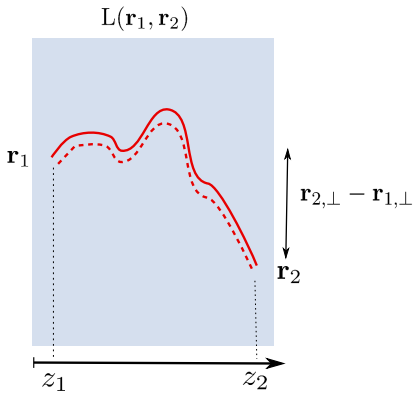


**Figure III.6** – Schema of the ladder operator propagating a pair of fields from point $\mathbf{r}_1$ to point $\mathbf{r}_2$. In the slab geometry the ladder operator only depends on $(z_1, z_2, \mathbf{r}_{2,\perp}-\mathbf{r}_{1,\perp})$

$$\mathrm{L}(z_1,z_2,\mathbf{q}) = \frac{d\gamma}{\ell^2 q}\frac{\mathrm{sh}[q\,(z_<+z_0)]\,\mathrm{sh}[q\,(L+z_0-z_>)]}{\mathrm{sh}[q\,(L+2z_0)]} \tag{III.30}$$

where $z_< = \min(z_1,z_2)$ and $z_> = \max(z_1,z_2)$.

#### An example of use of the ladder operator: the diffuse intensity

Knowing the ladder expression we can access the diffuse intensity by writing:

$$\begin{aligned}\langle|\delta E_T|^2\rangle &= \int |\langle E(\mathbf{r}_1)\rangle|^2\,\mathrm{L}(\mathbf{r}_1,\mathbf{r}_2)|\langle G(\mathbf{r}_T-\mathbf{r}_2)\rangle|^2\mathrm{d}\mathbf{r}_1\mathrm{d}\mathbf{r}_2 \\ &\simeq \int |\langle E(z_1)\rangle|^2\,\mathrm{L}(z_1,L,\mathbf{r}_{T,\perp}-\mathbf{r}_{1,\perp})|\langle G(\mathbf{r}_T-\mathbf{r}_2)\rangle|^2\mathrm{d}\mathbf{r}_1\mathrm{d}\mathbf{r}_2.\end{aligned} \tag{III.31}$$

To go from the first to the second line, we use the fact that the ladder operator follows a diffusion equation whose characteristic size is $L$, while the absolute value of the average Green function

decreases on a typical scale of order $\ell$. We thus make the approximation $\mathbf{r}_2 \simeq \mathbf{r}_T$ in the expression of the ladder which allows us to disconnect the integrations over $\mathbf{r}_1$ and $\mathbf{r}_2$. Using the fact that $\int |\langle G(\mathbf{r}_T - \mathbf{r}_2)\rangle|^2 \mathrm{d}\mathbf{r}_2 = 1/\gamma$ we can write

$$\langle |\delta E_T|^2 \rangle \simeq \frac{1}{\gamma} \int_0^L |\langle E(z_1)\rangle|^2 \, \mathrm{L}(z_1, L, \mathbf{q} = 0) \mathrm{d}z_1 \tag{III.32}$$

Moreover we have $\int \exp(-z/\ell) f(z) \mathrm{d}z \simeq \ell f(\ell)$ since $f$ does not vary on the scale of $\ell$ so that we can write $\langle |\delta E_T|^2 \rangle$ in the following way:

$$\begin{aligned} \langle |\delta E_T|^2 \rangle &\simeq \frac{\ell}{\gamma} \mathrm{L}(\ell, L, \mathbf{q} = 0) \\ &\simeq \frac{dI_0(1 + \frac{z_0}{\ell})z_0}{L + 2z_0}. \end{aligned} \tag{III.33}$$

We recover Eq. (III.25) in the limit $b \gg 1$ in which we can neglect the exponential contribution to the diffuse intensity.

Let us now detail the diagrammatic representation we gave for the diffuse intensity in Fig. II.7, comparing it with Eq. (III.31). In panel (b) in Fig. II.7, we represent the diffuse intensity, and see that at the beginning of the propagation we use straight lines. This corresponds to the coupling to the ladder operator using $|\langle E(\mathbf{r}_1)\rangle|^2$ in Eq. (III.31). The twisting lines corresponds to $\mathrm{L}(\mathbf{r}_1, \mathbf{r}_2)$ and the straight lines at the final part corresponds to $|\langle G(\mathbf{r}_T - \mathbf{r}_2)\rangle|^2$.

The derivation of the ladder operator and the average fields allows us to calculate all diagrams representing scattering sequences in the Gaussian approximation (since both tools represent properly the diffusive behavior of the light in the complex medium).

## III.4 $C_1$ correlation

The ladder operator introduced in the previous section is a powerful tool to study wave propagation in a complex medium. Indeed, as discussed in Chap. II, most of the statistics of the fields is governed by its diffusive behavior, which is described by the ladder operator. With this operator we can calculate connected quantities of order two (non factorizable moments of two fields). For instance in the previous section we have derived the expressions of $\langle |\delta E_T|^2 \rangle$ and $\langle |\delta E_R|^2 \rangle$. In this section, we derive $\langle \delta E_{R1} \delta E^*_{R2} \rangle$, $\langle \delta E_{T1} \delta E^*_{T2} \rangle$ and $\langle \delta E_R \delta E^*_T \rangle$. These field-field correlation functions give access to the $C_1$ correlation in transmission, reflection or reflection/transmission.

### III.4.1 $C_1$ correlation in reflection/transmission

The purpose of this section is to derive the expression of the $C_1$ function correlation between reflection and transmission (R/T). We also derive in App. (.3) the expressions of the $C_1$ correlation functions in reflection/reflection (R/R) and transmission/transmission (T/T) in order to compare the three configurations. Let us remind first the definition of the $C_1$ correlation function between two points $\mathbf{r}_1$ and $\mathbf{r}_2$

$$C_1(\mathbf{r}_1, \mathbf{r}_2) = \frac{|\langle \delta E(\mathbf{r}_1) \delta E^*(\mathbf{r}_2)\rangle|^2}{\langle \widetilde{I}(\mathbf{r}_1)\rangle \langle \widetilde{I}(\mathbf{r}_2)\rangle}. \tag{III.34}$$

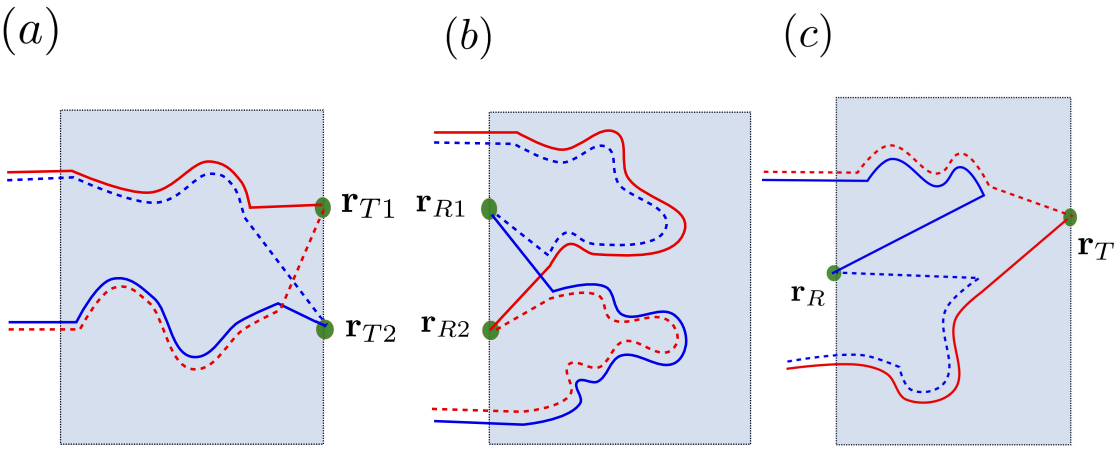


**Figure III.7** – Diagrammatic representation of the $C_1$ correlation in T/T [panel (a)], R/R [panel (b)] and R/T configurations [panel (c)]. We see that the pairs of fields start their propagation as average fields to enter the ladders (red with blue and vice versa). At the exit of the ladders they travel alone as average Green's functions to reach the two measurements points.

In Fig. III.7 we give the diagrammatic representation of $C_1$ in T/T [panel (a)], R/R [panel (b)] and R/T configurations [panel (c)]. To calculate $C_1$ in R/T we thus have to express the field-field correlation function between reflection and transmission. It reads

$$\begin{aligned}\langle \delta E_T \delta E_R^* \rangle &= \int |\langle E(\mathbf{r}_1)\rangle|^2 \, \mathrm{L}(\mathbf{r}_1,\mathbf{r}_2)\langle G(\mathbf{r}_T-\mathbf{r}_2)\rangle\langle G(\mathbf{r}_R-\mathbf{r}_2)\rangle^* \mathrm{d}\mathbf{r}_1\mathrm{d}\mathbf{r}_2 \\ &= I_0 \int \exp\left(-\frac{z_1}{\ell}\right) \mathrm{L}(z_1,z_2,\mathbf{q}) e^{i\mathbf{q}.(\mathbf{r}_{1,\perp}-\mathbf{r}_{2,\perp})} \langle G(\mathbf{k}_1)\rangle\langle G(\mathbf{k}_2)\rangle^* \\ &\times e^{i\mathbf{k_1}.(\mathbf{r}_T-\mathbf{r}_2)} e^{-i\mathbf{k_2}.(\mathbf{r}_R-\mathbf{r}_2)} \mathrm{d}\mathbf{r}_1\mathrm{d}\mathbf{r}_2 \frac{\mathrm{d}\mathbf{k}_1}{(2\pi)^d}\frac{\mathrm{d}\mathbf{k}_2}{(2\pi)^d}\frac{\mathrm{d}\mathbf{q}}{(2\pi)^{d-1}} \\ &= I_0 \int \exp\left(-\frac{z_1}{\ell}\right) \mathrm{L}(z_1,z_2,\mathbf{q}=0) \frac{e^{ik_{1z}(L-z_2)}}{k_{1z}^2+k_T^2-k_{eff}^2}\frac{e^{ik_{2z}z_2}}{k_{2z}^2+k_T^2-k_{eff}^{*2}} \\ &\times e^{i\mathbf{k}_T.\mathbf{\Delta R}} \mathrm{d}z_1\mathrm{d}z_2 \frac{\mathrm{d}k_{1z}}{(2\pi)}\frac{\mathrm{d}k_{2z}}{(2\pi)}\frac{\mathrm{d}\mathbf{k}_T}{(2\pi)^{d-1}}.\end{aligned} \tag{III.35}$$

To proceed further we disconnect the entry point of the ladder from the ballistic intensity considering that they vary on two different length scales, and we integrate over $k_{1z}$ and $k_{2z}$. This leads to

$$\langle \delta E_T \delta E_R^* \rangle \simeq \ell I_0 \int \mathrm{L}(0,z_2,\mathbf{q}=0) \frac{ie^{i\widetilde{k_1}(L-z_2)}}{2\widetilde{k_1}} \frac{ie^{i\widetilde{k_2}z_2}}{2\widetilde{k_2}} e^{i\mathbf{k}_T.\mathbf{\Delta R}} \mathrm{d}z_2 \frac{\mathrm{d}\mathbf{k}_T}{(2\pi)^{d-1}}. \tag{III.36}$$

In Eq. (III.39) $\widetilde{k_1}$ and $\widetilde{k_2}$ are

$$\widetilde{k_1} = \sqrt{k_0^2 - k_T^2 + i\frac{k_0}{\ell}} = K + iK' \tag{III.37}$$

$$\widetilde{k_2} = \sqrt{k_0^2 - k_T^2 - i\frac{k_0}{\ell}} = -K + iK' \tag{III.38}$$

with $K' \geq 0$. We can perform the integration over $z_2$, which gives

$$\begin{aligned}\langle \delta E_T \delta E_R^* \rangle &\simeq \ell I_0 \int \mathrm{L}(0, z_2, \mathbf{q}=0) \frac{e^{i(K+iK')(L-z_2)} e^{i(-K+iK')z_2}}{4(K^2+K'^2)} e^{i\mathbf{k}_T.\mathbf{\Delta R}} \mathrm{d}z_2 \frac{\mathrm{d}\mathbf{k}_T}{(2\pi)^{d-1}} \\ &\simeq \frac{d\gamma I_0 z_0}{\ell(L+2z_0)} \int (L+z_0-z_2) \frac{e^{i(K+iK')(L-z_2)} e^{i(-K+iK')z_2}}{4(K^2+K'^2)} e^{i\mathbf{k}_T.\mathbf{\Delta R}} \mathrm{d}z_2 \frac{\mathrm{d}\mathbf{k}_T}{(2\pi)^{d-1}} \\ &\simeq \frac{d\gamma I_0 z_0}{\ell(L+2z_0)} \int \mathrm{F}_{RT}(K,K') e^{i\mathbf{k}_T.\mathbf{\Delta R}} \frac{\mathrm{d}\mathbf{k}_T}{(2\pi)^{d-1}}.\end{aligned} \tag{III.39}$$

The expression involves the Fourier transform of the quantity $F_{RT}$ that reads

$$\mathrm{F}_{RT}(K,K') = \frac{e^{-(iK+K')L}\left(-1+2iKz_0+e^{2iKL}[1-2iK(L+z_0)]\right)}{4(K^2+K'^2)4K^2}. \tag{III.40}$$

In App. (.3) we present the same calculation for $C_1$ in transmission and in reflection. In these cases we end up with the same form of the field-field correlation as in Eq. (III.39), but with two different functions $F_{TT}$ and $F_{RR}$:

$$\begin{cases} \mathrm{F}_{TT}(K,K') \simeq \dfrac{1+2K'z_0}{4K'^2\,(4[K^2+K'^2])} \\ \mathrm{F}_{RR}(K,K') \simeq \dfrac{2K'L}{4K'^2\,(4[K^2+K'^2])}. \end{cases} \tag{III.41}$$

We can notice that:

$$\begin{cases} \langle |\delta E_T|^2 \rangle \simeq \dfrac{d\gamma I_0 z_0}{\ell(L+2z_0)} \displaystyle\int \mathrm{F}_{TT}(K,K') \frac{\mathrm{d}\mathbf{k}_T}{(2\pi)^{d-1}} \\ \langle |\delta E_R|^2 \rangle \simeq \dfrac{d\gamma I_0 z_0}{\ell(L+2z_0)} \displaystyle\int \mathrm{F}_{RR}(K,K') \frac{\mathrm{d}\mathbf{k}_T}{(2\pi)^{d-1}}. \end{cases} \tag{III.42}$$

We can now express the $C_1$ correlation in R/T normalizing Eq. (III.39) with Eq. (III.42):

$$C_1(\mathbf{r}_R, \mathbf{r}_T) = \frac{\left| \displaystyle\int \mathrm{F}_{RT}(K,K') e^{i\mathbf{k}_T.\mathbf{\Delta R}} \frac{\mathrm{d}\mathbf{k}_T}{(2\pi)^{d-1}} \right|^2}{\displaystyle\int \mathrm{F}_{RR}(K,K') \frac{\mathrm{d}\mathbf{k}_T}{(2\pi)^{d-1}} \int \mathrm{F}_{TT}(K,K') \frac{\mathrm{d}\mathbf{k}_T}{(2\pi)^{d-1}}} \tag{III.43}$$

while in R/R and T/T it reads

$$\begin{cases} C_1(\mathbf{r}_{R1}, \mathbf{r}_{R2}) = \dfrac{\left| \displaystyle\int \mathrm{F}_{RR}(K,K') e^{i\mathbf{k}_T.\mathbf{\Delta R}} \frac{\mathrm{d}\mathbf{k}_T}{(2\pi)^{d-1}} \right|^2}{\left( \displaystyle\int \mathrm{F}_{RR}(K,K') \frac{\mathrm{d}\mathbf{k}_T}{(2\pi)^{d-1}} \right)^2} \\ C_1(\mathbf{r}_{T1}, \mathbf{r}_{T2}) = \dfrac{\left| \displaystyle\int \mathrm{F}_{TT}(K,K') e^{i\mathbf{k}_T.\mathbf{\Delta R}} \frac{\mathrm{d}\mathbf{k}_T}{(2\pi)^{d-1}} \right|^2}{\left( \displaystyle\int \mathrm{F}_{TT}(K,K') \frac{\mathrm{d}\mathbf{k}_T}{(2\pi)^{d-1}} \right)^2}. \end{cases} \tag{III.44}$$

In Fig. III.8 we represent in panel (a) the numerically calculated $C_1$ correlation in R/T, versus the transverse distance between the points normalized by $\lambda$, and in panel (b) the analytical calculation Eq. (III.43) both for a dilute ($k_0\ell = 10$) and not too thick ($b = 2$) medium. It is hard to measure the

$C_1$ correlation in R/T for large $b$ because it decreases strongly with $b$ as can be understood in panel (c) in Fig. III.7. Indeed in this diagrammatic representation of $C_1(\mathbf{r}_R, \mathbf{r}_T)$, we see that the average Green functions connecting the ladder and the measurement points have to cross the entire medium. This part is really sensitive to the optical thickness of the sample and makes the $C_1$ correlation between reflection and transmission very weak when $b$ is large. Let us stress that the difference of amplitude between analytics and numerics in Fig. III.8 could be due to the diffusive ladder operator which should not be used for optical thicknesses close to unity, or to the use of bulk Green's functions instead of Green's functions of the slab. Nevertheless we see that we obtain a quite good estimate of $C_1$ even for an optical thickness $b = 2$.

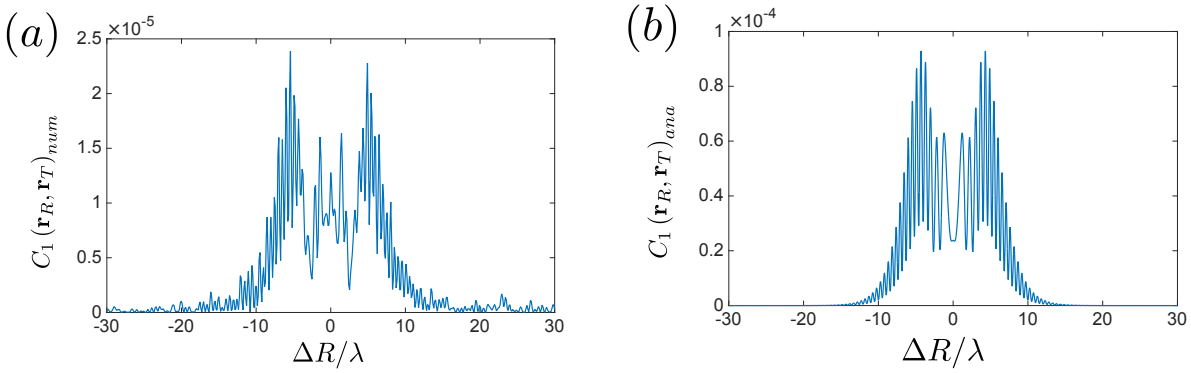


**Figure III.8** – Analytical and numerical calculation of $C_1(\mathbf{r}_R, \mathbf{r}_T)$ versus the transverse distance between the points normalized by $\lambda$ for a complex medium of optical thickness $b = 2$ and $k_0\ell = 10$.

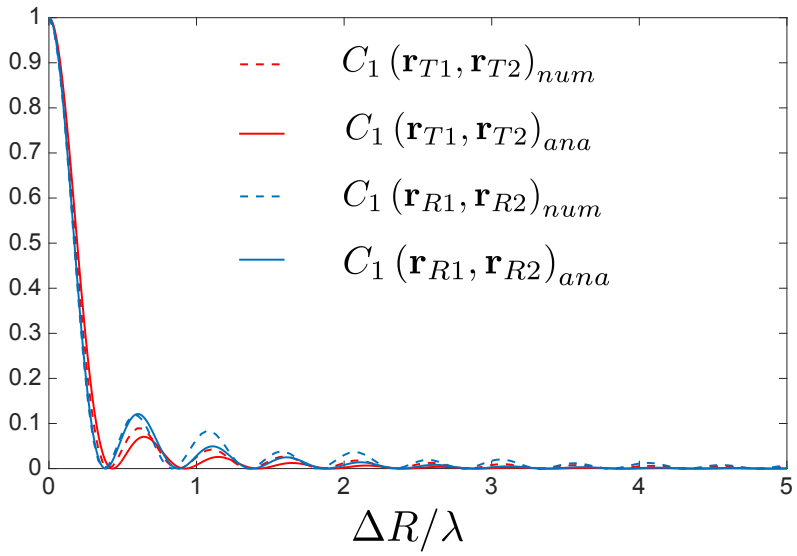


**Figure III.9** – Comparison between $C_1$ in R/R and in T/T (analytically and numerically) of a thick ($b = 10$) and dilute ($k_0\ell = 10$) complex medium.

In Fig. III.9 we plot the numerically and analytically calculated $C_1$ correlation in R/R and T/T for a thick ($b = 10$) and dilute ($k_0\ell = 10$) complex medium versus the transverse distance normalized by $\lambda$. We observe a good agreement between numerics and analytics for both R/R and T/T geometry. The $C_1$ correlation is in both cases an oscillating function whose value is unity at zero distance between the points, with a typical oscillating distance on the order of $\lambda/2$[7]. Appart from the small

[7]Let us notice that the need for a value of 1 at $\Delta R = 0$ for $C_1$ in R/R and T/T is what led us to choose the normalizations in Eq. (III.42)

deviations between numerics and analytics we see that there is a small difference between reflection and transmission due to the difference in exit point of the ladder operator (difference between $F_{RR}$ and $F_{TT}$). It is interesting to see that the analytical model captures this difference. Let us stress that if we make the crude approximation to completely disconnect the ladder from the exit vertex we obtain the same analytical function for $C_1$ in R/R and in T/T.

In summary, we have derived an expression for the gaussian correlation between intensities in R/R, T/T and R/T. We have seen that $C_1$ in R/R and T/T is one at $\Delta R = 0$ while it is not the case in the $R/T$ geometry. This is in good agreement with the discussion we had in the introductory section in Fig. II.12. In the next subsection we discuss the scaling of the value of $C_1(\mathbf{r}_R, \mathbf{r}_T)$ at $\Delta R = 0$ in the diffusive regime.

### Scaling at large optical thickness

In this section we derive a scaling expression for the value of $C_1$ at $\Delta R = 0$ in R/T in 2D and in 3D in the diffusive regime. To do so we start with the following expression of $C_1$:

$$C_1(\Delta R = 0) = \frac{1}{\langle \widetilde{I}_T \rangle \langle \widetilde{I}_R \rangle} \left| \frac{d\gamma I_0 z_0}{\ell(L+2z_0)} \int \mathrm{F}_{RT}(K, K') \frac{\mathrm{d}\mathbf{k}_T}{(2\pi)^{d-1}} \right|^2 . \tag{III.45}$$

Keeping in mind that $\langle \widetilde{I}_T \rangle \propto \ell/L$ and $\langle \widetilde{I}_R \rangle \propto 1$ we can write

$$C_1(\Delta R = 0) \propto \frac{L}{\ell} \left| \frac{d\gamma I_0 z_0}{\ell(L+2z_0)} \int \mathrm{F}_{RT}(K, K') \frac{\mathrm{d}\mathbf{k}_T}{(2\pi)^{d-1}} \right|^2 . \tag{III.46}$$

To find an equivalent of $C_1(\Delta R = 0)$ at large optical thickness we have to work on the expression of $F_{RT}$, $K$ and $K'$ for large $b$. The derivation is done in App. .3 and we obtain

$$C_1(\Delta R = 0) \propto \frac{1}{k_0 L} \frac{1}{k_0^2 \ell^2} \frac{L}{\ell} \exp\left(-\frac{L}{\ell}\right) \tag{III.47}$$

in the 2D case and

$$C_1(\Delta R = 0) \propto \frac{1}{k_0^2 L^2} \frac{1}{k_0^2 \ell^2} \frac{L}{\ell} \exp\left(-\frac{L}{\ell}\right) \tag{III.48}$$

in the 3D case. For large optical thickness, the important term in Eq. (III.47) and Eq. (III.48) is the negative exponential. This term prevents the field in reflection to be correlated with the field in transmission, and thus suppresses the $C_1$ correlation between reflection and transmission for large $b$. We can conclude this subsection by going back to Fig. II.12 and notice that we now have all the analytical expressions to discuss this figure. As we guessed in Chap. II, the field-field correlation function is strong in reflection and in transmission for points separated by distances smaller than $\lambda$, while it is small in R/T for thick samples.

## III.5 Non-gaussian correlation between reflected and transmitted intensities

The derivation of Eq. (III.47) and Eq. (III.48) in the previous section tells us that when the optical thickness becomes large, the $C_1$ contribution to the $\widetilde{I}$-$\widetilde{I}$ correlation between reflection and transmission decreases exponentially. Nonetheless in Fig. II.15 we have seen that the gaussian contribution is

not the only contribution to the $\widetilde{I}$-$\widetilde{I}$ correlation in transmission. In this section we derive the leading term of the non-gaussian correlation between reflected and transmitted intensities for a thick and dilute sample, and show that it dominates the $\widetilde{I}$-$\widetilde{I}$ correlation[8] between reflection and transmission.

### III.5.1 A diagrammatic guess

If there is such a non-gaussian correlation between reflected and transmitted intensities in the diffusive regime, what could be the leading term that describes it? In the introduction we discussed some of the important works on the subject of non-gaussian correlations in complex media. We have seen that depending on the observable we are interested in, different terms can dominate. Let us first remind that we illuminate the sample with a plane wave and measure intensities in a speckle spot on the sample surface. In transmission the result of this experiment is dominated by $C_1$. Nonetheless we have seen that in R/T configuration, $C_1$ is exponentially decreasing with the optical thickness of the sample, thus should be negligible in this case. We know that the first correction to the gaussian character of the field in T/T in the diffusive regime comes from one crossing of two trajectories inside the medium[9].

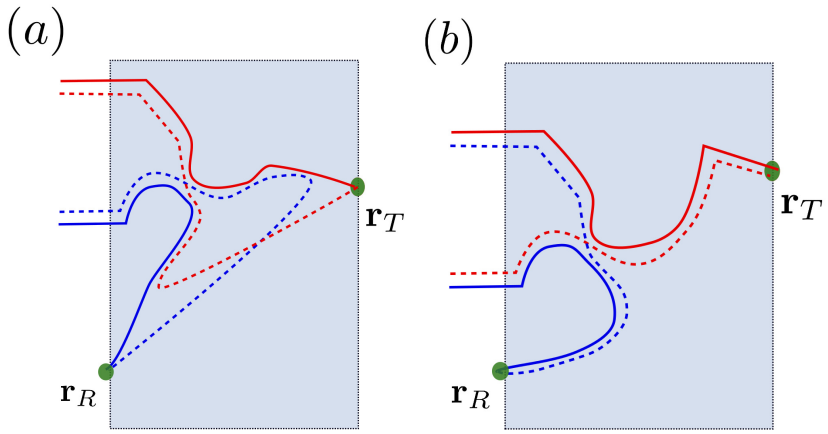


**Figure III.10** – Two typical diagrams contributing to the connected four-field correlations. In R/T the diagram depicted in panel (a) is negligible and we only have to consider the one represented in panel (b).

In Fig. III.10 we represent these two possibilities in the R/T geometry. Panel (a) corresponds to the case where the two pairs of fields propagates first together (red with red and blue with blue), then exchange inside the medium and at the end have to exchange again to eventually be measured in two different points. The last exchange looks like the exit vertex of the $C_1$ correlation in R/T. Panel (b) corresponds to the case where the fields exchange at the entrance (red with blue and blue with red), propagate and exchange inside the medium. After this exchange they can travel diffusively through long distances to eventually be measured at the observation points. Analyzing these two diagrams we already know how to calculate the diffusive propagations of the fields, but we have not yet described how to account for their crossing inside the medium. This crossing is described formally by an operator called a Hikami Box. At this point we would like to state it represents the exchange of the four fields in a volume small enough so that the phase acquired during their exchange does not suppress these terms on average. Let us now remind the conclusion from the last subsection where

[8] In the last subsection we show that in the diffusive regime the $\widetilde{I}$-$\widetilde{I}$ correlation between reflection and transmission is equal to the $I$-$I$ correlation between reflection and transmission which justifies the *a priori* reduction of the problem to the $\widetilde{I}$-$\widetilde{I}$ correlation.

[9] It is important to stress that when $b$ approaches unity this reasoning is not true anymore.

we calculated the $C_1$ correlation in R/T. We have seen that in this geometry the $C_1$ correlation is strongly suppressed because of the final part of this diagram (where the fields propagate through the whole medium as average Green's functions). Looking at panel (a) in Fig. III.10 we can see that the same exit vertex appears in this diagram. We believe that this will prevent this diagram from making a substantial contribution [compared to that in panel (b)]. Our first guess is that when $b \gg 1$, the scattering sequence dominating the $\widetilde{I}$-$\widetilde{I}$ correlation between reflection and transmission is the one depicted in panel (b) in Fig. III.10.

### III.5.2 Analytical calculation of $C_2$ between reflected and transmitted intensities in the diffusive regime

In this subsection we calculate the diagram represented in panel (b) in Fig. III.10 in the diffusive regime. Let us call $C_2$ the non gaussian contribution to the $\widetilde{I}$-$\widetilde{I}$ correlation coming from this diagram. Mathematically, this $C_2$ contribution comes from a connected four fields correlation which reads

$$\langle \delta E_R \delta E_R^* \delta E_T^* \delta E_T \rangle_{C_2} = \int |E(\mathbf{r}_1)|^2 |E(\mathbf{r}_2)|^2 \, \mathrm{L}(\mathbf{r}_2, \boldsymbol{\rho}_2) \, \mathrm{L}(\mathbf{r}_1, \boldsymbol{\rho}_1) \, \mathrm{H}(\boldsymbol{\rho}_1, \boldsymbol{\rho}_2, \boldsymbol{\rho}_3, \boldsymbol{\rho}_4) \\ \mathrm{L}(\mathbf{r}_3, \boldsymbol{\rho}_3) \, \mathrm{L}(\mathbf{r}_4, \boldsymbol{\rho}_4) |\langle \mathrm{G}(\mathbf{r}_R - \mathbf{r}_3) \rangle|^2 |\langle \mathrm{G}(\mathbf{r}_T - \mathbf{r}_4) \rangle|^2 \mathrm{d}\mathbf{r}_1 ... \mathrm{d}\mathbf{r}_4 \mathrm{d}\boldsymbol{\rho}_1 ... \mathrm{d}\boldsymbol{\rho}_4. \quad \text{(III.49)}$$

In this expression we recognize $\langle G(\mathbf{r}) \rangle$ the average Green function of the wave equation and the ladder operator $\mathrm{L}(\mathbf{r}, \mathbf{r}')$. The new operator $\mathrm{H}(\boldsymbol{\rho}_1, \boldsymbol{\rho}_2, \boldsymbol{\rho}_3, \boldsymbol{\rho}_4)$ is the Hikami box that stands for the diffusion partner exchange.

#### The Hikami vertex

The Hikami vertex (or Hikami box) represents the exchange of four fields in a small volume. It is a function of four positions. $\boldsymbol{\rho_1}$ and $\boldsymbol{\rho_2}$ are the points where the two ladders enter the exchange, $\boldsymbol{\rho_3}$ and $\boldsymbol{\rho_4}$ are the points where they leave the exchange. In the first Born approximation for this vertex, energy conservation imposes that there are three ways to exchange partners and we will call $\mathrm{H}_a$, $\mathrm{H}_b$ and $\mathrm{H}_c$ the contribution to the vertex coming from each part.

The first contribution $\mathrm{H}_a$ simply corresponds to the exchange with average Green's function:

$$\mathrm{H}_a(\boldsymbol{\rho}_1, \boldsymbol{\rho}_2, \boldsymbol{\rho}_3, \boldsymbol{\rho}_4) = \langle G(\boldsymbol{\rho}_3 - \boldsymbol{\rho}_1) \rangle \langle G^*(\boldsymbol{\rho}_4 - \boldsymbol{\rho}_1) \rangle \langle G^*(\boldsymbol{\rho}_3 - \boldsymbol{\rho}_2) \rangle \langle G(\boldsymbol{\rho}_4 - \boldsymbol{\rho}_2) \rangle. \quad \text{(III.50)}$$

$\mathrm{H}_b$ and $\mathrm{H}_c$ each contain one additional scattering event during the exchange:

$$\mathrm{H}_b(\boldsymbol{\rho}_1, \boldsymbol{\rho}_2, \boldsymbol{\rho}_3, \boldsymbol{\rho}_4) = \gamma \int \langle G^*(\boldsymbol{\rho}_4 - \boldsymbol{\rho}_1) \rangle \langle G^*(\boldsymbol{\rho}_3 - \boldsymbol{\rho}_2) \rangle \\ \times \langle G(\boldsymbol{\rho} - \boldsymbol{\rho}_1) \rangle \langle G(\boldsymbol{\rho} - \boldsymbol{\rho}_2) \rangle \langle G(\boldsymbol{\rho}_3 - \boldsymbol{\rho}) \rangle \langle G(\boldsymbol{\rho}_4 - \boldsymbol{\rho}) \rangle \mathrm{d}\boldsymbol{\rho}, \quad \text{(III.51)}$$

$$\mathrm{H}_c(\boldsymbol{\rho}_1, \boldsymbol{\rho}_2, \boldsymbol{\rho}_3, \boldsymbol{\rho}_4) = \gamma \int \langle G(\boldsymbol{\rho}_3 - \boldsymbol{\rho}_1) \rangle \langle G(\boldsymbol{\rho}_4 - \boldsymbol{\rho}_2) \rangle \\ \times \langle G^*(\boldsymbol{\rho} - \boldsymbol{\rho}_1) \rangle \langle G^*(\boldsymbol{\rho} - \boldsymbol{\rho}_2) \rangle \langle G^*(\boldsymbol{\rho}_3 - \boldsymbol{\rho}) \rangle \langle G^*(\boldsymbol{\rho}_4 - \boldsymbol{\rho}) \rangle \mathrm{d}\boldsymbol{\rho}. \quad \text{(III.52)}$$

After a cumbersome derivation, the sum of those three terms $\mathrm{H} = \mathrm{H}_a + \mathrm{H}_b + \mathrm{H}_c$ reads

$$\mathrm{H}(\boldsymbol{\rho}_1, \boldsymbol{\rho}_2, \boldsymbol{\rho}_3, \boldsymbol{\rho}_4) = \frac{h}{4} (\overbrace{\Delta_{\rho_1} + \Delta_{\rho_2} + \Delta_{\rho_3} + \Delta_{\rho_4}}^{1} + \overbrace{2\nabla\boldsymbol{\rho}_1 . \nabla\boldsymbol{\rho}_2}^{2} + \overbrace{2\nabla\boldsymbol{\rho}_3 . \nabla\boldsymbol{\rho}_4}^{3}) \delta(\boldsymbol{\rho}_1, \boldsymbol{\rho}_2, \boldsymbol{\rho}_3, \boldsymbol{\rho}_4), \quad \text{(III.53)}$$

where $\delta(\boldsymbol{\rho}_1,\boldsymbol{\rho}_2,\boldsymbol{\rho}_3,\boldsymbol{\rho}_4)=\int\delta(\boldsymbol{\rho}_1-\boldsymbol{\rho})\delta(\boldsymbol{\rho}_2-\boldsymbol{\rho})\delta(\boldsymbol{\rho}_3-\boldsymbol{\rho})\delta(\boldsymbol{\rho}_4-\boldsymbol{\rho})\mathrm{d}\boldsymbol{\rho}$ and $h$ is the weight of the vertex defined in ref. [37] and given by

$$h=\begin{cases}\dfrac{\ell^5}{16k_0^3} & \text{for 2D scalar waves,}\\[2ex] \dfrac{\ell^5}{24\pi k_0^2} & \text{for 3D scalar waves.}\end{cases} \tag{III.54}$$

The physical interpretation of the Dirac term in Eq. (III.53) is that the phases difference due to the exchange forces the exchange to happen in a small volume that can be considered point like. We have labelled three terms in Eq. (III.53). In the literature dedicated to mesoscopic physics it is often argued that term 1 is negligible (since it forces the crossing to occur at the sample surface, see ref. [26]), while the two others give rise to equal contributions, see ref. [84]. This was the approach we first adopted in ref. [85], where the Hikami vertex was replaced by twice the value of term 3. We call $C_2^{out}$ the analytical form of the correlation calculated this way. Similarly, we call $C_2^{in}$ the form obtained by keeping twice term 2. In fact, in the R/T configuration, there is no good reason to neglect term 1, nor to assume that terms 2 and 3 are of equal amplitude. We write the full correlator as

$$C_2(\mathbf{r}_R,\mathbf{r}_T)=C_2^{\Delta}(\mathbf{r}_R,\mathbf{r}_T)+\frac{C_2^{in}(\mathbf{r}_R,\mathbf{r}_T)+C_2^{out}(\mathbf{r}_R,\mathbf{r}_T)}{2}, \tag{III.55}$$

where the three contributions come from the three terms labelled in the vertex in Eq. (III.53).

### Derivation of $C_2^{out}$

In this subsection we derive the component coming from twice the value of term 3 in Eq. (III.53). The derivation of $C_2^{in}$ is almost identical and we will not detail it. Let us first deal with the entrance and exit part of Eq. (III.49), using the fact that

$$\int|E(\mathbf{r}_1)|^2\,\mathrm{L}(\mathbf{r}_1,\boldsymbol{\rho})\mathrm{d}\mathbf{r}_1=\gamma\langle I(\boldsymbol{\rho})\rangle \tag{III.56}$$

and that

$$\int|\langle\mathrm{G}(\mathbf{r}-\mathbf{r}_1)\rangle|^2\mathrm{d}\mathbf{r}_1=\frac{1}{\gamma}. \tag{III.57}$$

Using those two equalities (and the fact that the exit ladders vary slowly at the scale of $\ell$), we can rewrite Eq. (III.49) as

$$\langle\delta E_R\delta E_R^*\delta E_T^*\delta E_T\rangle_{C_2^{out}}=h\int\langle I(\boldsymbol{\rho})\rangle^2\boldsymbol{\nabla}\,\mathrm{L}(\boldsymbol{\rho},\boldsymbol{r}_R).\boldsymbol{\nabla}\,\mathrm{L}(\boldsymbol{\rho},\boldsymbol{r}_T)d\boldsymbol{\rho}. \tag{III.58}$$

The complicated part of the calculation is the dot product between the gradient of the ladders. To deal with it we can use Eq. (III.30). To do so let us rewrite Eq. (III.58) in the form

$$\begin{aligned}\langle\delta E_R\delta E_R^*\delta E_T^*\delta E_T\rangle_{C_2^{out}}&=h\int\langle I(z)\rangle^2\boldsymbol{\nabla}[\mathrm{L}(z,0,\mathbf{q}_1)\exp\left(i\mathbf{q}_1.[\mathbf{r}_{R,\perp}-\boldsymbol{\rho}_\perp]\right)].\boldsymbol{\nabla}[\mathrm{L}(z,L,\mathbf{q}_2)\exp\left(i\mathbf{q}_2.[\mathbf{r}_{T,\perp}-\boldsymbol{\rho}_\perp]\right)]\\&\quad\times\mathrm{d}\boldsymbol{\rho}_\perp\mathrm{d}z\frac{\mathrm{d}\boldsymbol{q_1}}{(2\pi)^{d-1}}\frac{\mathrm{d}\boldsymbol{q}_2}{(2\pi)^{d-1}}\\&=h\int\mathrm{d}\boldsymbol{\rho}_\perp\mathrm{d}z\frac{\mathrm{d}\boldsymbol{q_1}}{(2\pi)^{d-1}}\frac{\mathrm{d}\boldsymbol{q}_2}{(2\pi)^{d-1}}\langle I(z)\rangle^2\exp\left(i\mathbf{q}_1.[\mathbf{r}_{R,\perp}-\boldsymbol{\rho}_\perp]\right)\exp\left(i\mathbf{q}_2.[\mathbf{r}_{T,\perp}-\boldsymbol{\rho}_\perp]\right)\\&\quad\times[\partial_z\,\mathrm{L}(z,L,\mathbf{q}_2)\mathbf{e}_z-i\mathbf{q}_2\,\mathrm{L}(z,L,\mathbf{q}_2)].[\partial_z\,\mathrm{L}(z,0,\mathbf{q}_1)\mathbf{e}_z-i\mathbf{q}_1\,\mathrm{L}(z,0,\mathbf{q}_1)].\end{aligned}$$

We can integrate over the transverse component of $\boldsymbol{\rho}$

$$\int \exp\left(i[\mathbf{q}_1+\mathbf{q}_2].\boldsymbol{\rho}_\perp\right)\mathrm{d}\boldsymbol{\rho}_\perp = (2\pi)^{d-1}\delta(\mathbf{q}_1+\mathbf{q}_2) \tag{III.59}$$

and obtain

$$\begin{aligned}\langle \delta E_R \delta E_R^* \delta E_T \delta E_T^* \rangle_{C_2^{out}} &= h\int \mathrm{d}z \frac{\mathrm{d}\boldsymbol{q}}{(2\pi)^{d-1}} \langle I(z)\rangle^2 \exp\left(i\mathbf{q}.\boldsymbol{\Delta}\mathbf{R}\right) \\ &\quad\times \left[\partial_z \mathrm{L}(z,L,\mathbf{q})\partial_z \mathrm{L}(z,0,\mathbf{q}) + q^2\,\mathrm{L}(z,L,\mathbf{q})\,\mathrm{L}(z,0,\mathbf{q})\right] \\ &= h\int dz \frac{d\boldsymbol{q}}{(2\pi)^{d-1}} \langle I(z)\rangle^2 \exp\left(i\mathbf{q}.\boldsymbol{\Delta}\mathbf{R}\right)\left(\frac{d\gamma}{\ell^2}\right)^2 \\ &\quad\times \left(\frac{\mathrm{sh}\left(qz_0\right)}{\mathrm{sh}\left(q[L+2z_0]\right)}\right)^2 \mathrm{ch}\left(q[L-2z]\right).\end{aligned} \tag{III.60}$$

To go from the first to the second line in Eq. (III.60) we use Eq. (III.30) and hyperbolic trigonometric equalities. Now the integration over $z$ is straightforward using the approximate form of the diffuse intensity at large scale [compared to $\ell$ ,*i.e.* $\langle I(z)\rangle \simeq d(1+z_0/\ell)(L+z_0-z)/\left(L+2z_0\right)$]:

$$\int_0^L (L+z_0-z)^2\,\mathrm{ch}\left(q[L-2z]\right)\mathrm{d}z = \frac{-qL\,\mathrm{ch}(qL) + (1+q^2L^2(1+2z_0/L+2z_0^2/L^2))\,\mathrm{sh}(qL)}{2q^3}. \tag{III.61}$$

This allows us to rewrite Eq. (III.60) as

$$\begin{aligned}\langle \delta E_R \delta E_R^* \delta E_T^* \delta E_T \rangle_{C_2^{out}} &= h\left(\frac{d\gamma}{\ell^2}\right)^2\left(\frac{d(1+z_0/\ell)}{L+2z_0}\right)^2 \int \frac{\mathrm{d}\boldsymbol{q}}{(2\pi)^{d-1}} \exp\left(i\mathbf{q}.\boldsymbol{\Delta}\mathbf{R}\right)\left(\frac{\mathrm{sh}\left(qz_0\right)}{\mathrm{sh}\left(q[L+2z_0]\right)}\right)^2 \\ &\quad\times \frac{-qL\,\mathrm{ch}(qL) + (1+q^2L^2(1+2z_0/L+2z_0^2/L^2))\,\mathrm{sh}(qL)}{2q^3}.\end{aligned}$$

At this point we must take care of the dimension of the problem. Indeed in 3D we can use

$$\int_{-\pi}^{\pi} \exp\left(iq\Delta R\cos[\theta]\right)\mathrm{d}\theta = 2\pi\,\mathrm{J}_0(\Delta R) \tag{III.62}$$

while in 2D we have to use

$$\int_{-\infty}^{\infty} \exp\left(iq\Delta R\right) f(q)\mathrm{d}q = \int_0^{\infty} 2\cos\left(q\Delta R\right) f(q)\mathrm{d}q \tag{III.63}$$

valid if $f(q)$ is an even function of the variable $q$. Changing the variables $q' = qL$ and normalizing by

$$\langle|\delta E_R|^2\rangle\langle|\delta E_T|^2\rangle \simeq \frac{d^2(1+z_0/\ell)z_0^2/\ell}{L+2z_0} \tag{III.64}$$

we obtain the final expression of $C_2^{out}$ in 2D:

$$\begin{aligned}C_2^{out}(\mathbf{r}_R,\mathbf{r}_T) &= \frac{-32L}{\pi k_0\ell^2}\frac{(1+\frac{\pi}{4})}{\pi^2}\int \frac{\cos(\frac{q\Delta r}{L})\,\mathrm{sh}(q\frac{z_0}{L})^2}{q^3\,\mathrm{sh}[q\left(1+2\frac{z_0}{L}\right)]^2} \\ &\quad\times\left(-q\,\mathrm{ch}(q) + \left[1+q^2\left(1+\frac{2z_0}{L}+\frac{2z_0^2}{L^2}\right)\right]\mathrm{sh}(q)\right)\mathrm{d}q.\end{aligned} \tag{III.65}$$

In 3D the expression is

$$C_2^{out}(\mathbf{r}_R,\mathbf{r}_T) = \frac{-45}{8k^2\ell^2}\int \frac{\mathrm{J}_0(\frac{q\Delta r}{L})\,\mathrm{sh}(q\frac{z_0}{L})^2}{q^2\,\mathrm{sh}[q\left(1+2\frac{z_0}{L}\right)]^2} \times\left(-q\,\mathrm{ch}(q)+\left[1+q^2\left(1+\frac{2z_0}{L}+\frac{2z_0^2}{L^2}\right)\right]\mathrm{sh}(q)\right)\mathrm{d}q. \tag{III.66}$$

### Other terms in the expression of $C_2$

In App. we give the final expressions of all the terms entering Eq. (III.53). Let us here give the starting point of their derivation. For $C_2^{in}$ the calculation is really close to that done in the previous subsection. We simply have to change Eq. (III.58) into

$$\langle \delta E_R \delta E_R^* \delta E_T^* \delta E_T\rangle_{C_2^{in}} = h\int |\boldsymbol{\nabla}\langle I(\boldsymbol{\rho})\rangle|^2\,\mathrm{L}(\boldsymbol{\rho},\boldsymbol{r}_R)\,\mathrm{L}(\boldsymbol{\rho},\boldsymbol{r}_T)d\boldsymbol{\rho} \tag{III.67}$$

transform to the momentum space for the ladder and integrate over $z$. In ref. [84] it is stated that we can either calculate $C_2^{in}$ or $C_2^{out}$ to have the full expression of $C_2$ in the special case of T/T correlation. In the case of the R/T geometry we cannot do the same, because $C_2^{in}$ gives a positive contribution and $C_2^{out}$ gives a negative one.

To calculate the Laplacian terms we can use the diffusion equation for the ladder. For instance if we consider the Laplacian term acting on the exit ladder going back in reflection, we obtain

$$\begin{aligned}\langle \delta E_R \delta E_R^* \delta E_T^* \delta E_T\rangle_{C_2^{\Delta_3}} &= \frac{h}{4}\int \langle I(\boldsymbol{\rho})\rangle^2 \Delta\,\mathrm{L}(\boldsymbol{\rho},\boldsymbol{r}_R)\,\mathrm{L}(\boldsymbol{\rho},\boldsymbol{r}_T)d\boldsymbol{\rho}\\ &= \frac{-dh\gamma}{4\ell^2}\langle I(\mathbf{r}_R)\rangle^2\,\mathrm{L}(\mathbf{r}_R,\boldsymbol{r}_T).\end{aligned} \tag{III.68}$$

## III.5.3 Numerical validation

Taking all these terms into account one can calculate the $C_2$ correlation function as the sum of all terms. To validate the analytical model we numerically calculate the $\widetilde{I}$-$\widetilde{I}$ correlation function in R/T for three samples of same size ($k_0L = 120$) and of varying mean free path. The results are shown in Fig. III.11 versus the transverse distance normalized by $L$. The blue dashed line corresponds to $k_0\ell = 20$ and $b = 6$, the red dashed line corresponds to $k_0\ell = 15$ and $b = 8$ and the green dashed line corresponds to $k_0\ell = 10$ and $b = 12$. We also represent the analytical calculation of $C_2$ for parameters $k_0\ell = 15$ and $b = 8$.

Let us draw several conclusions from this figure:

- We see that $C(\mathbf{r}_R,\mathbf{r}_T)$ is a negative function of $\Delta R/L$ and has non zero values for $\Delta R/L \leq 1$.
- The maximum of the absolute value of this function is obtained for $\Delta R/L = 0$ (when points are in front of the other).
- When the optical thickness is large enough the amplitude of $C(\mathbf{r}_R,\mathbf{r}_T)$ appears not to depend anymore on the mean free path of the system and depends on a single parameter $k_0L$.
- The agreement with the analytical calculation is really good, we can thus conclude that in the deep diffusive regime, $C(\mathbf{r}_R,\mathbf{r}_T)$ is dominated by the $C_2$ correlation function [panel (b) in Fig. III.10].

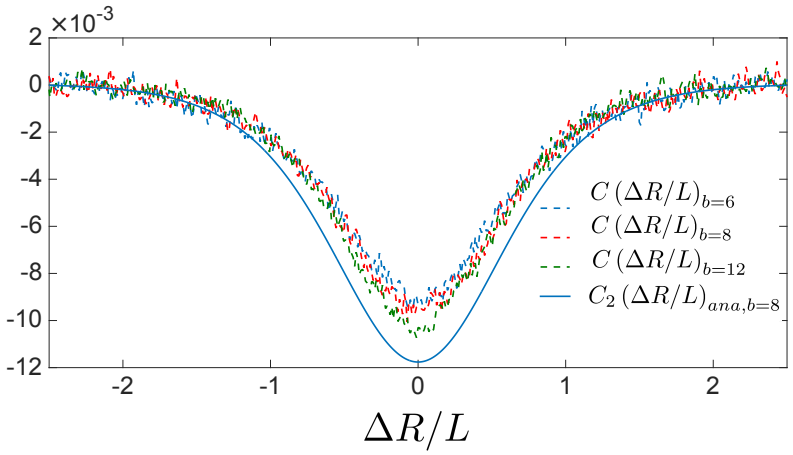


**Figure III.11** – Numerical calculation of the $\widetilde{I}$-$\widetilde{I}$ correlation between reflection and transmission for three different samples of same size ($k_0L = 120$). The blue dashed line corresponds to $k_0\ell = 20$ and $b = 6$, the red dashed line corresponds to $k_0\ell = 15$ and $b = 8$ and the green dashed line corresponds to $k_0\ell = 10$ and $b = 12$. We also represent the analytical calculation of $C_2$ for parameters $k_0\ell = 15$ and $b = 8$.

### Large optical thickness scaling

In this section we discuss the expression of $C_2$ in the limit of large optical depth $b \gg 1$, and find that $C_2(\mathbf{r}_R, \mathbf{r}_T) = -f(\Delta r/L)/(k_0L)^{d-1}$, where $f(x)$ is a positive decaying function of range unity given in 2D by

$$f(x) = \int_0^\infty \frac{q\cos(qx)}{\mathrm{sh}(q)} \left( \frac{(1+\pi/2)^2 + \pi(1+\pi/2)}{4\pi(1+\pi/4)} + \frac{1+\pi/4}{\pi} \frac{[-2q\,\mathrm{ch}(q) + \mathrm{sh}(q)(2+q^2)]}{q^2\,\mathrm{sh}(q)} \right) \mathrm{d}q \quad \text{(III.69)}$$

and in 3D by

$$f(x) = \int_0^\infty \frac{q^2\,\mathrm{J}_0(qx)}{\mathrm{sh}(q)} \left( \frac{21}{20} + \frac{5}{4} \frac{[-2q\,\mathrm{ch}(q) + \mathrm{sh}(q)(2+q^2)]}{q^2\,\mathrm{sh}(q)} \right) \mathrm{d}q. \quad \text{(III.70)}$$

In Fig. III.12, we represent the numerically calculated $\widetilde{I}$-$\widetilde{I}$ correlation between reflection and transmission normalized by $1/(k_0L)$ and the analytical calculation of $C_2$ normalized by $1/(k_0L)$ for various parameters. The $x$ axis is the transverse distance between the points normalized by the size of the sample. We observe a convergence of these curves towards $-f(\Delta R)$. We also observe that the analytical expressions becomes applicable only for very large optical thicknesses ($b \geq 60$). This could be due to the fact that the $C_2$ diagram is composed of many operators that all needs to be in the diffusive regime so that $C_2$ is exactly equal to its large optical thickness limit.

This also suggests that the R/T correlation function becomes independent on the disorder strength $k_0\ell$ in the deep diffusive regime, and depends only on one parameter $k_0L$.

### Comparison between $\widetilde{I}$-$\widetilde{I}$ and $I$-$I$ correlation functions in the diffusive regime

Let us conclude this section by showing that in the diffusive regime, the $\widetilde{I}$-$\widetilde{I}$ correlation function between reflected and transmitted speckle patterns is equal to the $I$-$I$ correlation function. The main reason is the exponential decrease of the ballistic field in transmission, and the fact that the reflected field is small in reflection. Let us call $C_{\mathcal{I}}$ the correlation between intensities.

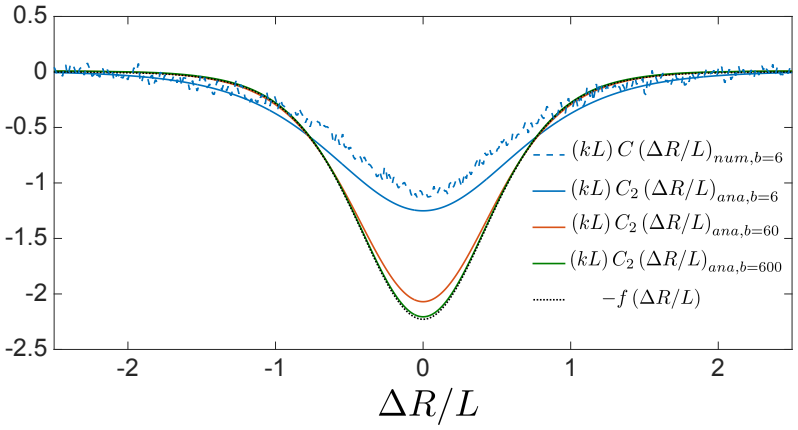


**Figure III.12** – Numerical calculation of the $\widetilde{I}$-$\widetilde{I}$ correlation normalized by $1/(k_0L)$, and analytical calculation of $(k_0L)C_2$ for optical thicknesses from 6 to 600 and analytical expression of the limit of those analytical expressions at large optical thickness. .

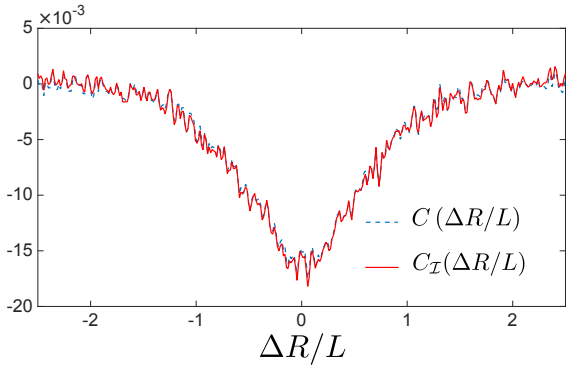


**Figure III.13** – Numerical calculation of the $\widetilde{I}$-$\widetilde{I}$ correlation (blue dashed line) and the $I$-$I$ correlation between (red solid line) reflection and transmission in the diffusive regime ($b = 7$ and $k_0\ell = 10$).

In Fig. III.13 we represent the numerically calculated $\widetilde{I}$-$\widetilde{I}$ correlation (blue dashed line) and the $I$-$I$ correlation between (red solid line) reflection and transmission in the diffusive regime ($b = 7$ and $k_0\ell = 10$). We observe no difference between the two curves. In the diffusive regime we thus conclude that

$$C(\mathbf{r}_R, \mathbf{r}_T) = C_{\mathcal{I}}(\mathbf{r}_R, \mathbf{r}_T) \tag{III.71}$$

and that all our conclusions drawn for $C$ are also valid for $C_{\mathcal{I}}$.

# Chapter IV

# Measurement of the reflection/transmission intensity correlation

## Table des matières

The heart of this chapter is the measurement of the intensity-intensity correlation function between reflection and transmission performed at the University of Exeter (UK) by I. Starshinov, A.M Paniagua-Diaz and J. Bertolotti in the framework of a collaboration with our group [86]. We first detail in a few words the experimental setup and the results obtained[1]. We then discuss the experimental observable, and show that it corresponds to the measurement of $C(\mathbf{r}_R, \mathbf{r}_T)$ for all optical thicknesses. Using Eq. (II.15) we estimate the relative weight of $C_1$ and of the non-gaussian correlation in the measurements. We conclude that even for optical thicknesses close to one, $C_1$ is always negligible compared to the non-gaussian contribution in the R/T geometry. Eventually we propose a scattering sequence that could explain some of the interesting features of the correlation function for optical thicknesses close to unity.

# IV.1 Description of the experiment

## IV.1.1 The experimental set up

The group in Exeter has performed the first measurement of the intensity-intensity correlation between transmitted and reflected speckle patterns, for scattering materials with thickness $L$ and scattering mean free path $\ell$ covering the entire range from quasi-ballistic to diffusive transport.

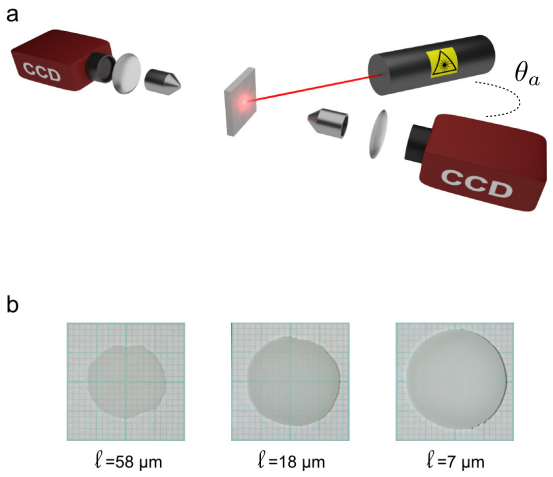


**Figure IV.1** – (a) Experimental setup: a scattering slab, formed by $TiO_2$ particles in glycerol between two microscope glass slides, is illuminated by a laser beam incident at an angle $\theta_a = 45°$, with an incident wavelength $\lambda = 632.8$ nm. (b) Examples of samples with thickness $L = 20\,\mu$m but different $TiO_2$ concentrations: from left to right 5 g/l, 10 g/l and 40 g/l. The corresponding scattering mean free path $\ell$ is indicated in the figure [86].

The experimental setup is shown in panel (a) in Fig. IV.1. A monochromatic wave is incident with an angle of incidence $\theta_a$ on a suspension of $TiO_2$ particles in glycerol, squeezed between two microscope

[1] The interested reader should read the thesis of I. Starshinov and A.M Paniagua-Diaz for more experimental details.

slides, forming a scattering slab with controlled thickness and mean free path. In ref [86] authors vary $L$ using stainless steel feeler gauges as spacers, and $\ell$ by modifying the $TiO_2$ concentration, allowing the sample to change from almost transparent to completely opaque (typical samples with different values of $\ell$ are shown in panel (b) in Fig. IV.1. For each thickness and concentration, the intensity pattern is measured on the surface of the sample, in both transmission and reflection with two identical imaging systems consisting of a microscope objective, a lens, and a CCD camera. The positions of the scatterers are continuously changing due to Brownian motion in glycerol, leading to a time-varying speckle pattern. The exposure time of the CCD cameras, and the time interval between two successive measurements are chosen such that the sample is effectively static during each measurement, but successive measurements refer to completely different realizations of disorder.

## IV.1.2 The experimental results

The correlation function $\langle C^{RT}(\Delta\mathbf{r})\rangle$ (analyzed in detail in the next section) for different values of the mean free path $\ell$ and the sample thickness $L$ is shown in Fig. IV.2. Both the shape and the sign of $\langle C^{RT}(\Delta\mathbf{r})\rangle$ substantially depend on $L$ and $\ell$. We observe that the evolution of the lineshape is subtle.

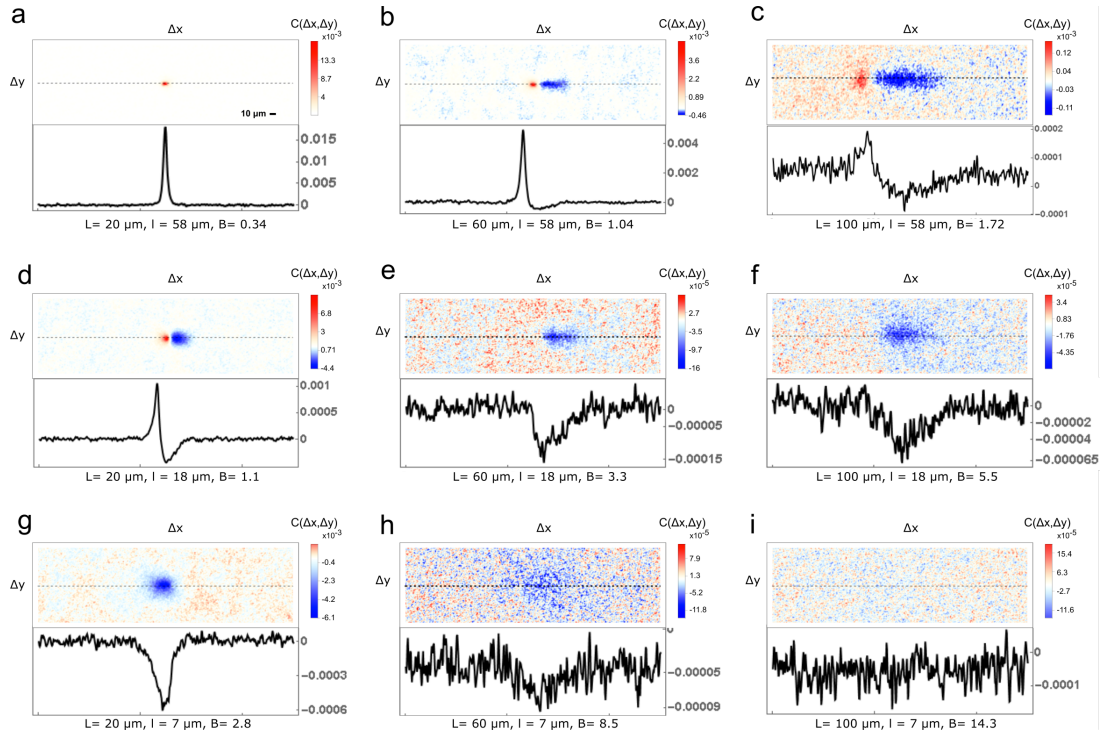


**Figure IV.2** – Average cross-correlation $\langle C^{RT}(\Delta\mathbf{r})\rangle$ between the transmitted and the reflected speckle patterns for different values of $L$ and $\ell$, and thus different values for the optical density $b = L/\ell$. In each panel the upper graph shows the 2D plot of $\langle C^{RT}(\Delta\mathbf{r})\rangle$ and the lower graph shows a cut through the dotted line.

- Let us first discuss the regime of large optical thickness $L \gg \ell$ [panels (e-i) in Fig. IV.2]. As predicted in the previous chapter we observe in this regime that $\langle C^{RT}(\Delta\mathbf{r})\rangle$ is negative and long-range.
- In the regime of moderate optical depth $\ell \sim L \gg \lambda$, the samples still show a cross-correlation with a range extending far beyond a speckle spot, but with a positive peak appearing in the

vicinity of the negative contribution discussed above [see panels (b-d) in Fig. IV.2]. The long-range character of this new contribution to the correlation function suggests that it originated from correlated scattering paths that become diffusive for $L \gtrsim \ell$.

- Panel (a) in Fig. IV.2 could be the limit between the regime of moderate optical thickness and the single quasi-ballistic regime ($\ell \gg L \gg \lambda$) we study in the next chapter. In this panel we see only a positive contribution with a range larger than a speckle spot.

## IV.2 Numerical study of $\langle C^{RT} \rangle$

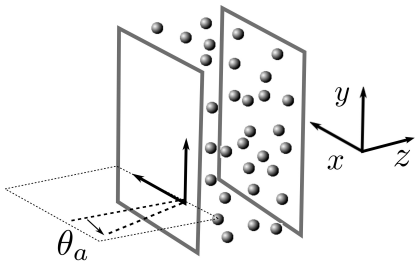


**Figure IV.3** – Scheme of the geometry used for the simulations. We illuminate a 3D disordered sample with a laser beam with an angle of incidence $\theta_a$. The $x$ direction is parallel to the transverse component of wave vector the laser beam and the $y$ direction is orthogonal to it.

The purpose of this section is to understand in detail the quantity measured in Fig. IV.2. The experiment done by our colleges from Exeter has several intriguing features. First, whatever the optical thickness of the sample, all features of the correlation function seem to be long-range (compared to the wavelength). Second, in the single scattering regime ($\ell \sim L$), the structure is asymmetric, with a positive and a negative contributions. To understand these unexpected features we first discuss the experimental observable.

### IV.2.1 Comparison between $\langle C^{RT} \rangle$ and $C$ for an off-axis experiment

The purpose of this section is to show that the expression of the correlation function measured experimentally, $\langle C^{RT}(\Delta\mathbf{r}) \rangle$, can be simplified into $C(\mathbf{r}_R, \mathbf{r}_T)$. The first point to understand is that the experiment is off-axis[2]. Thus the ballistic (specular) component of the reflected and the transmitted fields is not measured and the CCD is directly sensitive to $\widetilde{I}_T$ and $\widetilde{I}_R$. The experimental observable reads (before averaging over disorder configurations)

$$C^{RT}(\Delta\mathbf{r}) = \frac{\overline{\delta\widetilde{I}_R(\mathbf{r})\delta\widetilde{I}_T(\mathbf{r}+\Delta\mathbf{r})}}{\left[\delta\widetilde{I}_R(\mathbf{r}) - \overline{\delta\widetilde{I}_R(\mathbf{r})}\right]^{2^{1/2}} \left[\delta\widetilde{I}_T(\mathbf{r}+\Delta\mathbf{r}) - \overline{\delta\widetilde{I}_T(\mathbf{r}+\Delta\mathbf{r})}\right]^{2^{1/2}}}, \tag{IV.1}$$

where $\mathbf{r}$ and $\mathbf{r}+\Delta\mathbf{r}$ are transverse coordinates in the transmission plane and the reflection plane, respectively, and the overline represents the spatial average over the coordinate $\mathbf{r}$. Calculated from two speckle images obtained in a given configuration of disorder, the correlation function $C^{RT}$ appears random, with fluctuations on the scale of a speckle spot. By performing an ensemble average over a large number of configurations, the shape of the correlation function $\langle C^{RT} \rangle$ becomes apparent. Let

[2]When the scattering sample is removed, no intensity is measured neither in transmission nor in reflection.

us stress that the choice of this form of the correlation is driven by experimental constraints. It helps to be less sensitive to fluctuations of the laser during the averaging process. Assuming that averaging over the coordinates of the speckle image is equivalent to averaging over disorder, we first transform the ensemble average in Eq. (IV.1) into

$$\begin{aligned}\langle C^{RT}(\Delta\mathbf{r})\rangle &\simeq \frac{\langle \delta\widetilde{I}_R(\mathbf{r})\delta\widetilde{I}_T(\mathbf{r}+\Delta\mathbf{r})\rangle}{\left\langle\left[\delta\widetilde{I}_R(\mathbf{r})-\langle\delta\widetilde{I}_R(\mathbf{r})\rangle\right]^2\right\rangle^{1/2}\left\langle\left[\delta\widetilde{I}_T(\mathbf{r}+\Delta\mathbf{r})-\langle\delta\widetilde{I}_T(\mathbf{r}+\Delta\mathbf{r})\rangle\right]^2\right\rangle^{1/2}}\\ &= \frac{\langle \delta\widetilde{I}_R(\mathbf{r})\delta\widetilde{I}_T(\mathbf{r}+\Delta\mathbf{r})\rangle}{\langle\delta\widetilde{I}_R(\mathbf{r})^2\rangle^{1/2}\langle\delta\widetilde{I}_T(\mathbf{r}+\Delta\mathbf{r})^2\rangle^{1/2}}.\end{aligned} \tag{IV.2}$$

Second, we simplify the denominator in Eq. (IV.2) using the decomposition $\langle X(\mathbf{r})^2\rangle - \langle X(\mathbf{r})\rangle^2 = \langle X(\mathbf{r})\rangle^2 + \langle X(\mathbf{r})^2\rangle_c$ where $X$ stands for $\widetilde{I}_R$ or $\widetilde{I}_T$. The contribution $\langle X(\mathbf{r})^2\rangle_c$ would be zero if the reflected and transmitted fluctuating fields ($\delta E_R$ and $\delta E_T$) were Gaussian random variables. The correlation (IV.2) now takes the form

$$\langle C^{RT}(\Delta\mathbf{r})\rangle = \frac{\langle \delta\widetilde{I}_R(\mathbf{r})\delta\widetilde{I}_T(\mathbf{r}+\Delta\mathbf{r})\rangle}{\sqrt{\langle\widetilde{I}_R(\mathbf{r})\rangle^2+\langle\widetilde{I}_R(\mathbf{r})^2\rangle_c}\sqrt{\langle\widetilde{I}_T(\mathbf{r}+\Delta\mathbf{r})\rangle^2+\langle\widetilde{I}_T(\mathbf{r}+\Delta\mathbf{r})^2\rangle_c}}. \tag{IV.3}$$

Finally, we use the fact that our experiment is carried out in the weak scattering regime $k_0\ell \gg 1$, so that the non-Gaussian corrections, dubbed $C_2$ correlations, are negligible (*i.e.* $C_2^{XX} = \langle X(\mathbf{r})^2\rangle_c/\langle X(\mathbf{r})\rangle^2 \ll 1$). Finally the correlation function takes the simple form

$$\langle C^{RT}(\Delta\mathbf{r})\rangle \simeq \frac{\langle \delta\widetilde{I}_R(\mathbf{r})\delta\widetilde{I}_T(\mathbf{r}+\Delta\mathbf{r})\rangle}{\langle\widetilde{I}_R(\mathbf{r})\rangle\langle\widetilde{I}_T(\mathbf{r}+\Delta\mathbf{r})\rangle} = C(\mathbf{r}_R,\mathbf{r}_T). \tag{IV.4}$$

We illustrate the good agreement between Eq. (IV.3) and Eq. (IV.4) in Fig. IV.4, where both correlation functions have been calculated numerically (using the coupled dipole method presented in App. .3) for a 3D scattering medium with optical thickness $L/\ell = 1.5$ and scattering strength $k_0\ell = 10$. This result confirms that the experimentally measured correlation function is well described by Eq. (IV.4), which is the quantity studied in the previous chapter in the diffusive regime.

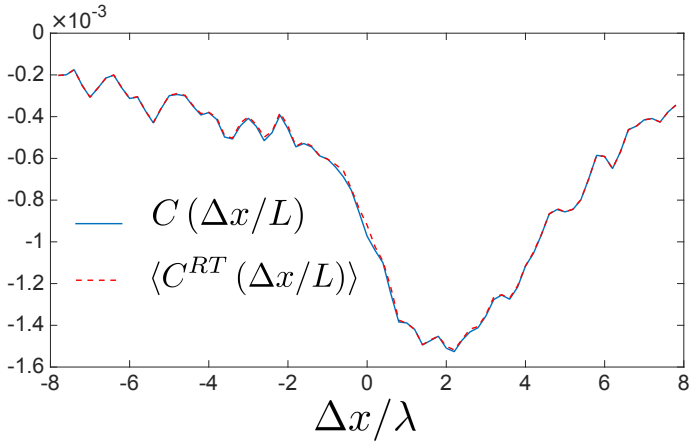


**Figure IV.4** – Comparison between two different definitions of the correlation function between reflection and transmission. The transverse distance $\Delta r = \Delta x$ is varied along the direction of the illumination plane. Parameters of the 3D numerical simulation: $L/\ell = 1.5$, $k_0\ell = 10$, $\theta_a \simeq 45°$.

To briefly summarize our reasoning, the design of the experiment geometry is such that the average field is not measured in this off axis experiment. Then using ergodicity and the mathematical expression for the moments of $\widetilde{I}_T$ and $\widetilde{I}_R$, we have shown that the experimental observable is equivalent to $C(\mathbf{r}_R,\mathbf{r}_T)$.

### IV.2.2 Numerical calculations of $C(\mathbf{r}_R, \mathbf{r}_T)$ in 3D

In Fig. IV.5 we present 3D numerical calculations of $C(\mathbf{r}_R, \mathbf{r}_T)$ obtained with the coupled dipole method. We have performed the calculation for a plane wave with shifted incidence $\theta_a = 45°$ illuminating three different 3D (see Fig. IV.3 for the definition of $x$ and $y$) samples of size $k_0 L = 20$ and various scattering mean free paths. Figure IV.5 should be compared with the first column in Fig. IV.2. Panel (a) corresponds to $b = 0.75$ and $k_0\ell = 20$, panel (b) corresponds to $b = 1$ and $k_0\ell = 15$, and panel (c) corresponds to $b = 1.5$ and $k_0\ell = 10$.

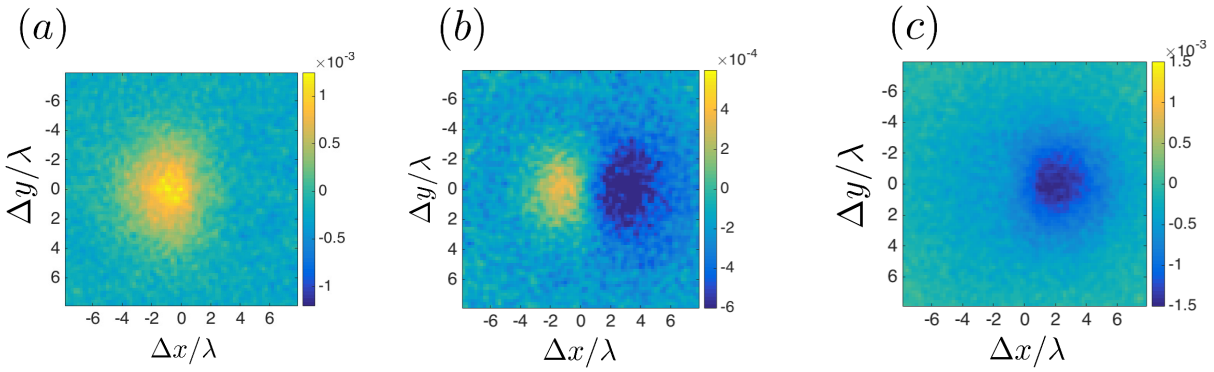


**Figure IV.5** – Numerical calculation of $C(\mathbf{r}_R, \mathbf{r}_T)$ for 3D scalar waves and three different samples of same length. Panel (a) corresponds to $b = 0.75$ and $k_0\ell = 20$, panel (b) corresponds to $b = 1$ and $k_0\ell = 15$ and panel (c) corresponds to $b = 1.5$ and $k_0\ell = 10$. The typical number of disorder realizations is $N_{conf} = 10^7$ and the number of dipoles for each configuration is $N_{dip} \simeq 1000$.

We see a clear change in the shape of the numerically calculated correlation function when $b$ varies.

- At small optical thickness ($b = 0.75$) we observe a positive contribution whose typical size is larger than the wavelength.
- At moderate optical thickness ($b = 1$), we observe an asymmetric correlation function with one positive and one negative contributions. If we draw a line between the center of both contributions, it is parallel to the transverse wave vector of the incident wave.
- Eventually for $b = 1.5$, only a negative contribution remains, the typical size of which is larger than the wavelength.

Let us now compare these three simulations with the experimental results in the first column in Fig. IV.2. The main difference between the numerical samples and the experimental ones is the value of $k_0 L$. For numerical samples $k_0 L = 20$ while in the first column in Fig. IV.2 $k_0 L \simeq 200$. For this reason we cannot expect a quantitative agreement between numerics and experiment. Nonetheless we see a qualitative agreement in the behavior of the correlation versus the optical thickness. Indeed in panel (a) in Fig. IV.2, we see a positive contribution the width of which is larger than a speckle spot, in panel (d) we see the asymmetric shape with both the positive and negative contributions and in panel (g) we observe only the negative contribution.

#### The diffusive regime

In the previous section we have seen that the experimental measurements give a direct access to $C(\mathbf{r}_R, \mathbf{r}_T)$ which follows Eq. (II.15). From the previous chapter, we know that this quantity should be dominated by its non-gaussian contribution $C_2$ in the diffusive regime, that is negative, and

has a typical width on the order of $L$. These two characteristics are recovered in the experimental results. Analytically, the amplitude is supposed to decrease as $1/(k_0L)^2$ in the diffusive regime. This behavior cannot be checked experimentally due to the difficulty to reach the diffusive regime in practice combined with the fact that the correlation is weak. Numerically, 3D simulations are really heavy, and we cannot reach optical thicknesses larger than $b = 1.5$. We cannot thus check the $1/(k_0L)^2$ law. Nonetheless we believe this law is applicable because it has been checked numerically in 2D for which a $1/(k_0L)$ law has been confirmed.

## IV.3 Study of the positive contribution in the regime of moderate optical thickness.

When the optical thickness decreases we are faced with two problems[3]:

- The experimental observable gives a direct access to $C(\mathbf{r}_R, \mathbf{r}_T)$ whatever the optical thickness. From Eq. (II.15), $C(\mathbf{r}_R, \mathbf{r}_T)$ is the sum of $C_1$ and of the non-gaussian contribution. The non-gaussian correlation is *a priori* not dominated by $C_2$ in this regime. Indeed when $b$ approaches unity, other scattering sequences connecting four fields can appear. In the previous chapter we showed analytically that $C_1$ is small in the diffusive regime compared to the non-gaussian correlation. We do not know *a priori* if this still holds when $b$ approaches unity.
- Quantities calculated analytically using the diffusion equation (for instance the ladder operator) are only approximate in this regime. We should rather use the radiative transfer equation to describe properly scattering by thin samples. Nonetheless it would complicate substantially the expressions.

In this section we discuss the regime $b \simeq 1$ (the regime $b \ll 1$ is studied in detail in the next chapter).

### IV.3.1 $C_1$ is negligible for optical thicknesses close to unity

In this section we discuss the relative weight of the $C_1$ correlation function and of the non-gaussian contribution for optical thicknesses close to unity. Indeed we have seen both numerically and experimentally that a positive contribution appears when $b$ approaches unity. *In this section we show that this contribution is not equal to* $C_1$. To proceed we use numerics that provide direct access to the field. It is thus easy to calculate the $C_1$ correlation function and the full $\widetilde{I}$-$\widetilde{I}$ correlation function and compare them.

In Fig. IV.6 we represent in panel (a) the full $\widetilde{I}$-$\widetilde{I}$ correlation, in panel (b) its connected part: $\langle \delta E_R \delta E_T \delta E_R^* \delta E_T^* \rangle_c / \left( \langle \delta E_R \delta E_R^* \rangle \langle \delta E_T \delta E_T^* \rangle \right)$, and in panel (c) the $C_1$ correlation function. The Parameters are $k_0\ell = 15$, $L/\ell = 1$, $\theta_a \simeq 45°$. We observe that even for thin samples, the $C_1$ correlation function is weak compared to the non gaussian correlation contribution. In addition, its shape is totally different from what is seen both numerically and experimentally.

This conclusion is really important. We claim here that the $\widetilde{I}$-$\widetilde{I}$ correlation function between reflection and transmission gives a direct access to the non-gaussian contribution to the intensity-intensity

[3]The mean transmitted field cannot be neglected anymore in this regime thus $C(\mathbf{r}_R, \mathbf{r}_T)$ differs from $C_{\mathcal{I}}(\mathbf{r}_R, \mathbf{r}_T)$. The reduction of the problem of the study of $C(\mathbf{r}_R, \mathbf{r}_T)$ is thus questionable. In App. .3 we discuss the aspect of $C_{\mathcal{I}}(\mathbf{r}_R, \mathbf{r}_T)$ and the difference between $C_{\mathcal{I}}(\mathbf{r}_R, \mathbf{r}_T)$ and $C(\mathbf{r}_R, \mathbf{r}_T)$ when the optical thickness is close to unity. We show that regarding $C_{\mathcal{I}}(\mathbf{r}_R, \mathbf{r}_T)$ this regime seems more complicated to describe than the diffusive regime. Nonetheless since the experiment directly measure $C(\mathbf{r}_R, \mathbf{r}_T)$ for all optical thicknesses, this point is not a problem.

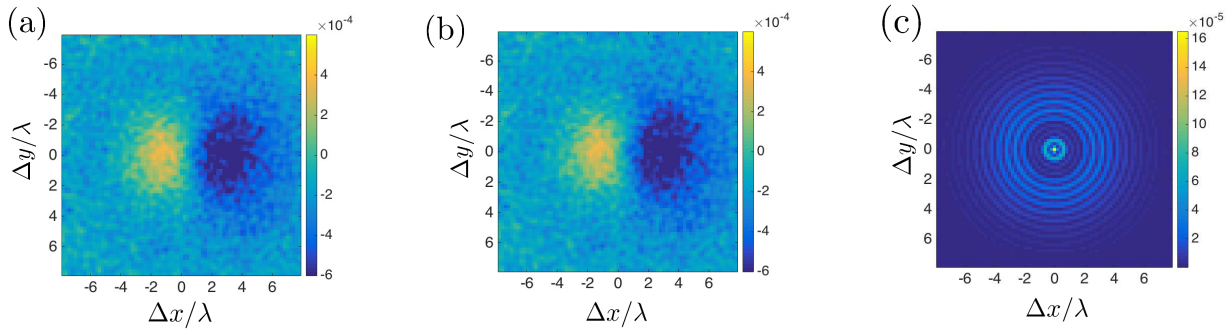


**Figure IV.6** – Correlation function $C$ obtained from numerical simulation of the wave equation in a 3D slab. (a) Full correlation; (b) Connected part of the correlation; (c) $C_1$ contribution tp the correlation. Parameters: $k_0\ell = 15$, $L/\ell = 1$, $\theta_a \simeq 45°$

correlation function whatever the optical thickness of the system[4]. We want to stress that the non gaussian correlation function is obtained experimentally without any field measurements (simply an off axis experiment). This is of fundamental interest for research in mesoscopic physics. For instance this quantity gives insight about some properties of the scattering medium (see refs. [87, 88, 89, 90]).

### IV.3.2 Variation with the angle of incidence

In the previous section we have made clear that the experiment is a direct measurement of the non-gaussian correlation for all optical thicknesses. Thus both the negative contribution (deep) and the positive contribution (peak) are non-gaussian correlations. To propose a connected four-field scattering sequence responsible for the positive contribution of $C$ we have investigated its behavior with the angle of incidence. In Fig. IV.7, we present the result of 3D numerical simulations of wave scattering in a disordered slab with optical thickness $b = 1$, disorder strength $k_0\ell = 15$, illuminated at a shifted incidence $\theta_a \simeq 75°$. We see that the correlation is positive for $|\Delta\mathbf{r}| \lesssim L$ and presents negative side lobes that are more pronounced along the illumination direction. We have analyzed the angular dependence of this shape along the direction $\Delta y = 0$. The results are presented in Fig. IV.8. For $\theta_a = 57°$, the correlation $C(\Delta x)$ is asymmetric. When the angle of incidence $\theta_a$ increases, both the positive central peak and the negative side lobes grow. In addition, the correlation function becomes more and more symmetric (with respect to the mirror symmetry along the direction $\Delta x = 0$). We interpret the shape of this correlation function as the result of the superposition of two contributions, $C_2$ and $C_0$[5]. The contribution $C_2$ is a negative deep with a minimum located at $\Delta x > 0$. As discussed in the previous sections, this contribution is almost independent on $\theta_a$ (apart from the shift that cannot be explained with diffusion theory). On the other hand, the contribution $C_0$ contains both a positive peak located at $\Delta x \simeq 0$ and symmetric negative side lobes. It is also strongly dependent on the illumination angle (see next section for details). Hence, the latter is responsible for the anisotropic shape observed in Fig. IV.7 and the evolution presented in Fig. IV.8. In particular, the correlation $C(\Delta x)$ shown in Fig. IV.8 becomes more and more symmetric when $\theta_a$ increases because the amplitude of the negative side lobes of $C_0$ gets larger than the $C_2$ deep. A microscopic interpretation of this phenomenon is proposed in the next section.

[4]At least for $k_0\ell \gg 1$ and in the range of $b$ going from 1 to $\infty$ for now. In the next chapter we discuss the regime $1 \gg b$.

[5]We discuss in detail the denomination $C_0$ in the next subsection.

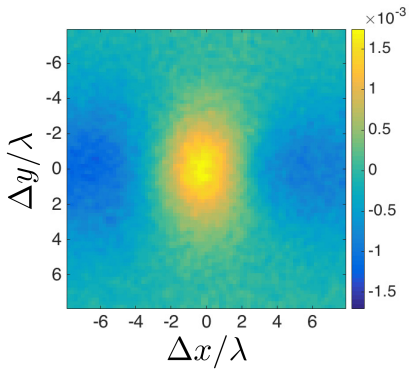


**Figure IV.7** – $C(\Delta\mathbf{r})$ calculated from 3D numerical simulations of the wave propagation in a disordered slab of moderate optical depth. The direction $\Delta y = 0$ is defined as the intersection of the incidence plane with the sample surface. Parameters: $b = 1$, $k_0\ell = 15$, $\theta_a \simeq 75°$.

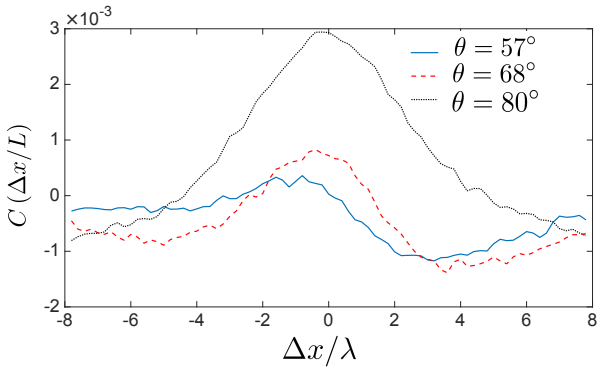


**Figure IV.8** – Dependence of $C(\Delta\mathbf{r})$ on the illumination angle $\theta_a$, along the illumination direction $\Delta y = 0$ (horizontal axis in Fig. IV.7). Parameters of the 3D simulation: $b = 1$, $k_0\ell = 15$.

### IV.3.3 A scattering sequence dependent on the angle of incidence

The angular dependence of the correlation function for optical thicknesses close to unity is an intriguing result that helped us in determining a diagram responsible for it.

#### $C_2$ does not depend on the angle of incidence

The first point to have in mind is that the $C_2$ diagram is not sensitive to a change in the angle of incidence. Let us write what happens to a shifted incident beam after propagation with the ladder operator:

$$\begin{aligned}
\int |\langle E(\mathbf{r})\rangle|^2_{\mathbf{q}_a} \,\mathrm{L}(\mathbf{r},\mathbf{r}_2)\mathrm{d}\mathbf{r} &= I_0 \int \exp\left(-z/\ell_a\right) \exp\left(i\mathbf{q}_a.\mathbf{r}_t\right) \exp\left(-i\mathbf{q}_a.\mathbf{r}_t\right) \mathrm{L}(z,z_2,\mathbf{r}_{2,t}-\mathbf{r}_t)\mathrm{d}z\mathrm{d}\mathbf{r}_t \qquad \text{(IV.5)}\\
&= I_0 \int \exp\left(-z/\ell_a\right) \mathrm{L}(z,z_2,\mathbf{q}) \exp\left(i\mathbf{q}.[\mathbf{r}_{2,t}-\mathbf{r}_t]\right) \mathrm{d}z\mathrm{d}\mathbf{r}_t d\mathbf{q}/(2\pi)^{d-1}\\
&= I_0 \int \exp\left(-z/\ell_a\right) \mathrm{L}(z,z_2,\mathbf{q}=\mathbf{0})\mathrm{d}z\\
&\simeq I_0 \ell_a \,\mathrm{L}(0,z_2,\mathbf{q}=\mathbf{0})
\end{aligned}$$

where we have used the expression of the mean field derived in Eq. (III.13).

The only memory of the angle of incidence appears in the coupling with the ladder operator. It can be represented by a corrected attenuation length that accounts for the angle of incidence and that reads as $\ell_a = \ell\mu_a$ with $\mu_a = \sqrt{1 - q_a^2/k_0^2} = \cos(\theta_a)$. This factor appears each time one connects a ladder with a shifted beam, squared in the numerator of the $C_2$ diagram and squared in the denominator (diffuse intensities). It is thus simplified by the normalization. This coupling effect cannot be the cause of the change of shape of the correlation function when the angle of incidence changes.[6]

### A diagrammatic guess

We thus look for a scattering sequence that contains the memory of the angle of incidence. This scattering sequence must also become negligible compared to $C_2$ when the optical thickness of the sample increases. To discuss the various scattering sequences appearing in the small optical thickness regime we follow refs. [39, 71]. In these theoretical works additional contributions are added to the intensity-intensity correlation in order to represent the R/R correlation correctly. The main idea is the following: for a thick medium in R/T, we showed that the dominant process to connect four fields is described by $C_2$. Two pairs of fields propagate diffusively, meet inside the scattering medium, exchange their partners, and leave diffusively towards the measurement points. Each time we used the word diffusively, mathematically we use the ladder operator to propagate the pairs of fields. This operator contains at least one scattering event. We can say that $C_2$ contains at least 5 scattering events (one in each ladder and one in the Hikami box). Going towards optical thicknesses of unity we should look at scattering sequences which contain fewer scattering events. In Fig. IV.9 we present two of such scattering sequences. We need to transform the $C_2$ diagram in order to avoid a diffusive propagation before the exchange of partners. One possibility is to use an extra scattering event (black dot in Fig. IV.9) that can connect the fields at the entrance of the scattering medium [panel (a)]. This contribution is long range because fields leave the exchange diffusively, and can *a priori* be sensitive to the angle of incidence thanks to the extra scattering event. We choose to call this diagram $C_0$ and we need to be clear about this notation. We are not looking at the same observable as the one leading to the *infinite range* correlation $C_0$ because we illuminate the system with a plane-wave and not with a point source. Nonetheless the diagrams represented in Fig. IV.9 have the exact same structure as the one used to calculate $C_0$ (but with a plane-wave and not a point source excitation). This is the reason why we choose to keep the denomination $C_0$ for this scattering sequence .

Let us notice that exactly as in the case of $C_2$, there is an analogous diagram for which the exchange appears after the diffusive propagation [panel (b) in Fig. IV.9]. Our guess is that this diagram should be sub-leading due to the propagation through the sample as average Green's functions (see App. .3.3 for a more detailed discussion of the diagrammatic construction of the $C_0$ scattering sequence).

In the next section we derive the analytical expression of the diagram represented in panel (a) in Fig. IV.9.

### Analytical calculation

The $C_0$ correlation has first been introduced in refs. [60, 91] in the case of a point source excitation. Here we consider the same class of scattering processes, but generated by a plane wave. As we show in this section, both the formal calculation and the qualitative consequences are different from

[6] This strong claim should be weakened by stressing that we are not in the diffusive regime when we observe the strong influence of the angle of incidence. Thus the expression in Eq. (IV.5) may be not exact in the regime of optical thickness reached experimentally.

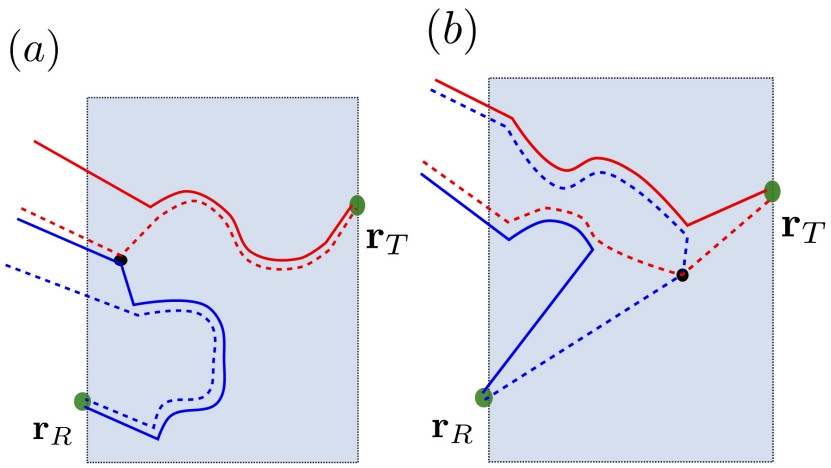


**Figure IV.9** – Panel (a): diagrammatic representation of the $C_0$ contribution in R/T: two ballistic intensities get mixed into two diffuse intensities using an extra scattering event. Panel (b): symmetric diagram where two diffuse intensities mix into four average Green's functions with the help of an extra scattering event.

the case of a point source excitation. The complete microscopic representation of the $C_0$ diagrams are represented in Fig. IV.10. Each diagram involves scattering paths that visit a common scatterer

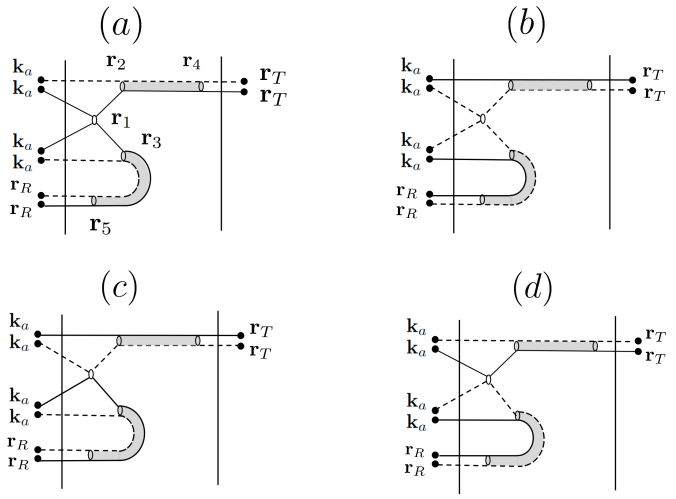


**Figure IV.10** – Leading diagrams contributing to $C_0$. Shaded tubes represent diffusive paths (ladders), single solid lines stand for averaged fields and single dashed lines for their complex conjugates. The extra scatterer located near the surface boundary can connect the ladders in four different ways.

located near the front side of the sample. The symmetric diagrams [panel (b) in Fig. IV.9] that involve a common scatterer at the outputs can be neglected for the same reason as the $C_1$ correlation. Using the same notations as in section V, the four-field correlator $\mathcal{C}_0(\Delta\mathbf{r}) = \langle \delta E_R \delta E_R^* \delta E_T \delta E_T^* \rangle_{C_0}$[7] takes, in 3D, the form

$$\mathcal{C}_0(\Delta\mathbf{r}) = \frac{4\pi}{\ell} \int V(\mathbf{r}_2, \mathbf{r}_3)\, \mathrm{L}(\mathbf{r}_2, \mathbf{r}_4)\, \mathrm{L}(\mathbf{r}_3, \mathbf{r}_5) |\langle \mathrm{G}(\mathbf{r}_T - \mathbf{r}_4) \rangle|^2 |\langle \mathrm{G}(\mathbf{r}_R - \mathbf{r}_5) \rangle|^2 \mathrm{d}\mathbf{r}_2 \mathrm{d}\mathbf{r}_3 \mathrm{d}\mathbf{r}_4 \mathrm{d}\mathbf{r}_5, \qquad \text{(IV.6)}$$

where $V(\mathbf{r}_2, \mathbf{r}_3)$ is the sum of the four possibilities for connecting the input plane wave to the ladder diagrams starting in $\mathbf{r}_2$ and $\mathbf{r}_3$, as represented in Fig. IV.10. For example the contribution in

[7] $\mathcal{C}_0$ is the non normalized version of $C_0$.

Fig. IV.10 (a) to the vertex $V$ is

$$V^{(a)}(\mathbf{r}_2,\mathbf{r}_3)=\int\langle E(\mathbf{r}_2)\rangle^*\langle E(\mathbf{r}_3)\rangle^*|\langle E(\mathbf{r}_1)\rangle|^2\langle \mathrm{G}(\mathbf{r}_2-\mathbf{r}_1)\rangle\langle \mathrm{G}(\mathbf{r}_3-\mathbf{r}_1)\rangle \mathrm{d}\mathbf{r}_1, \tag{IV.7}$$

where the average field $\langle E(\mathbf{r})\rangle$ depends on the incidence angle. By integrating over the transverse coordinates, we obtain

$$\mathcal{C}_0(\Delta\mathbf{r})=\frac{\ell}{16\pi^3}\int\Big([\tilde{V}^{(a)}_{\mathbf{q}_a,\mathbf{q}}(z_2,z_3)+\tilde{V}^{(c)}_{\mathbf{q}_a,\mathbf{q}}(z_2,z_3)]e^{i(\mathbf{q}_a-\mathbf{q}).\boldsymbol{\Delta r}}+[\tilde{V}^{(b)}_{\mathbf{q}_a,\mathbf{q}}(z_2,z_3)+\tilde{V}^{(d)}_{\mathbf{q}_a,\mathbf{q}}(z_2,z_3)]e^{i(\mathbf{q}-\mathbf{q}_a).\boldsymbol{\Delta r}}\Big)$$
$$\times\,\mathrm{L}_{\mathbf{q}-\mathbf{q}_a}(z_2,0)\,\mathrm{L}_{\mathbf{q}-\mathbf{q}_a}(z_3,L)\mathrm{d}\mathbf{q}\mathrm{d}z_2\mathrm{d}z_3, \tag{IV.8}$$

where $z$ labels are longitudinal coordinates, $\mathbf{q}_a$ is the transverse component of the incident wave vector $\mathbf{k}_a$, and $\mathrm{L}_{\mathbf{q}}(z,z')$ is the Fourier transform of $\mathrm{L}(\mathbf{r},\mathbf{r}')$ with respect to the transverse part of the coordinate $\mathbf{r}-\mathbf{r}'$. In addition, the components $\tilde{V}$ are given by

$$\tilde{V}^{(a)}_{\mathbf{q}_a,\mathbf{q}}(z_2,z_3)=(2ik_a)^4\,I_0^2\int\bar{G}_{\mathbf{q}_a}(0,z_1)^2\bar{G}_{2\mathbf{q}_a-\mathbf{q}}(z_1,z_3)\bar{G}_{\mathbf{q}}(z_1,z_2)\bar{G}_{\mathbf{q}_a}(0,z_2)^*\bar{G}_{\mathbf{q}_a}(0,z_3)^*\mathrm{d}z_1, \tag{IV.9}$$

$$\tilde{V}^{(c)}_{\mathbf{q}_a,\mathbf{q}}(z_2,z_3)=(2ik_a)^4\,I_0^2\int|\bar{G}_{\mathbf{q}_a}(0,z_1)|^2\bar{G}_{\mathbf{q}}(z_1,z_3)^*\bar{G}_{\mathbf{q}}(z_1,z_2)\bar{G}_{\mathbf{q}_a}(0,z_2)^*\bar{G}_{\mathbf{q}_a}(0,z_3),\mathrm{d}z_1, \tag{IV.10}$$

with $\tilde{V}^{(b)}=\tilde{V}^{(a)*}$, and $\tilde{V}^{(c)}=\tilde{V}^{(d)*}$. In these expressions, $\bar{G}_{\mathbf{q}}(z,z')=i/\left(2k_z\right)e^{ik_z(z'-z)}e^{-|z'-z|/2\mu\ell}$, with $k_z=\sqrt{k^2-q^2}\equiv k\mu$, is the transverse Fourier transform of the average Green function of the Helmholtz equation. We now make the approximations $\mathrm{L}(z_2,0,q-q_a)\simeq\mathrm{L}(0,0,q-q_a)$ and $\mathrm{L}(z_3,L,q-q_a)\simeq\mathrm{L}(0,L,q-q_a)$, and integrate Eq. (IV.8) over the longitudinal coordinates $z_1$, $z_2$ and $z_3$. The correlator becomes

$$\mathcal{C}_0(\Delta\mathbf{r})=\frac{\ell^4k_a^4I_0^2}{8\pi^3k^6}\int\cos\left[(\mathbf{q}_a-\mathbf{q}).\boldsymbol{\Delta r}\right]\mathrm{L}_{\mathbf{q}-\mathbf{q}_a}(0,0)\,\mathrm{L}_{\mathbf{q}-\mathbf{q}_a}(0,L)\,\mathrm{F}(\mu,\mu_a,k_0\ell)\mathrm{d}\mathbf{q}, \tag{IV.11}$$

with

$$\mathrm{F}(\mu,\mu_a,k_0\ell)=\frac{[\mu_a(2\mu_a-\mu)(\mu+\mu_a)]^{-1}2(\mu_a-\mu)\left[9\mu^3+18\mu^2\mu_a+11\mu\mu_a^2+2\mu_a^3+4\mu^3\mu_a^2(\mu-\mu_a)^2k^2\ell^2\right]}{\left[9\mu^2+\mu_a^2+6\mu\mu_a+4\mu^2\mu_a^2(\mu-\mu_a)^2k^2\ell^2\right]\left[(\mu+\mu_a)^2+4\mu^2\mu_a^2(\mu-\mu_a)^2k^2\ell^2\right]}, \tag{IV.12}$$

where $\mu_a=\sqrt{1-q_a^2/k^2}$ and $\mu=\sqrt{1-q^2/k^2}$. Normalizing the correlator by the intensity product $\langle|\delta E_R|^2\rangle\langle|\delta E_T|^2\rangle=\ell\left(2k_a\right)^4I_0^2/\left(6k^4\mu_a^2L\right)$ and the integration momentum variable by the sample thickness $L$, we finally obtain

$$C_0(\Delta\mathbf{r})=\frac{27\mu_a^2k_0L}{4\pi(k_0\ell)^3}\int\cos\left[(\mathbf{q}'_a-\mathbf{q}').\boldsymbol{\Delta r}/L\right]P(\mathbf{q}'_a,\mathbf{q}')\,\mathrm{F}(\mu,\mu_a,k_0\ell)\mathrm{d}\mathbf{q}', \tag{IV.13}$$

where $q'_a=q_aL=k_0L\sin\theta_a$. The ladder contribution $P(\mathbf{q}'_a,\mathbf{q}')$ is defined as

$$P(\mathbf{q}'_a,\mathbf{q}')=\frac{\mathrm{sh}\left[|\mathbf{q}'_a-\mathbf{q}'|z_0/L\right]^3\mathrm{sh}\left[|\mathbf{q}'_a-\mathbf{q}'|(1+z_0/L)\right]}{|\mathbf{q}'_a-\mathbf{q}'|^2\,\mathrm{sh}\left[|\mathbf{q}'_a-\mathbf{q}'|(1+2z_0/L)\right]^2}. \tag{IV.14}$$

In order to obtain Eq. (IV.13) we used various approximations that are justified in the diffusive regime $L>\ell$ only. Therefore, we must be cautious not to use this result in the quasi-ballistic regime $L\lesssim\ell$. We note also that in the deep diffusive regime $L\gg\ell$ and for small angle of incidence ($\mu_a\simeq1$), the $C_0$ correlation function with plane wave illumination takes the compact form

$$C_0(\Delta\mathbf{r})\simeq\frac{5}{16\pi k^4L^4}\int\cos\left[(\mathbf{q}'_a-\mathbf{q}').\boldsymbol{\Delta r}/L\right]\frac{q'^2|\mathbf{q}'_a-\mathbf{q}'|}{\mathrm{sh}[|\mathbf{q}'_a-\mathbf{q}'|]}\mathrm{d}\mathbf{q}', \tag{IV.15}$$

which scales as $C_0 \propto 1/(k_0 L)^4$. In this regime, it is therefore much smaller than $C_2 \propto 1/(k_0 L)^2$. This explains why it is not observed in the diffusive regime.

Before analyzing Eq. (IV.13) in more details, let us comment on the differences between this $C_0$ correlation function and that calculated with plane wave outputs, or point-source inputs. For plane-wave outputs, we find

$$C_0(\mathbf{k}_b, \mathbf{k}_{b'}) = \int \frac{\mathrm{d}\Delta\mathbf{r}}{\mathcal{A}} C_0(\Delta\mathbf{r}) = 0, \tag{IV.16}$$

for all observation directions $\mathbf{k}_b, \mathbf{k}_{b'}$. This striking result comes from the fact that $\mathrm{F}(\mu_a, \mu_a, k_0\ell) = 0$. This means that, for plane wave outputs, the diagram in panel (a) in Fig. IV.10 [resp. panel (b) in Fig. IV.10] is compensated by that in panel (c) in Fig. IV.10 [resp. in panel (d) in Fig. IV.10]. This result turns out to be completely different from that obtained in the configuration involving point-like sources and detectors, where the diagrams in Figs. IV.10 (a,b) do not contribute to the correlation function.

Let us now discuss the strong dependence of Eq. (IV.13) on the illumination angle $\theta_a$. At the origin of this dependence is the total momentum conservation during the interaction with the common scatterer in Fig. IV.10. The information carried by the illumination plane wave is transmitted to the ladder diagrams that conserve momentum over long distances, so that the input information finally reaches the sample boundaries. The same property holds in the well-known memory effect introduced in ref. [92]. We illustrate the dependence of the correlation given by Eq. (IV.13) on $\theta_a$ in Fig. IV.11. For $\theta_a = 0$, the rotational symmetry is preserved so that $C_0(\Delta\mathbf{r})$ depends on $\Delta r$ only. It presents a positive peak centered in $\Delta r = 0$, that extends over a distance $\Delta r \sim L$. Beyond this distance the correlation presents small negative side lobes, that are such that the sum rule given in Eq. (IV.16) is satisfied. When the rotational symmetry is broken ($\theta_a \neq 0$), the correlation becomes anisotropic. It now presents two mirror symmetries with respect to the intersection of the incidence plane with the sample surface. The direction of this intersection defines the horizontal axis in Fig. IV.11. We observe that the negative side lobes become more pronounced along this direction. In addition, the amplitude of both the central peak and the side lobes get larger for increasing $\theta_a$, in agreement with the sum rule given in Eq. (IV.16) as well as the experimental observations discussed in the previous section.

### IV.3.4 What could be improved?

The previous analysis shows that $C_0$ reproduces the features observed experimentally in the R/T correlation in the regime $L \sim \ell$. As observed numerically, $C_0$ is long-range, keeps a memory on the incidence angle, becomes anisotropic for $\theta_a \neq 0$, presents a central peak and negative side lobes, and both the peak and the side lobes becoming more pronounced when $\theta_a$ increases. That being said, it should be stressed that Eq. (IV.13) does not reproduce quantitatively the amplitude of the positive correlation function observed in the regime $L \sim \ell$. This is not much a surprise since, as we explained above, Eq. (IV.13) was obtained in the diffusive regime $L \gg \ell$. In addition, it is worth mentioning that the scattering processes described by $C_0$ and $C_2$ are not the only ones that could contribute in the quasi-ballistic regime $L \lesssim \ell$. Let us discuss three ways of improving this study

- For the range of approximation we consider (the Born approximation [39] for the four-field vertex[8] discussed in App. .3.3), we do not miss many diagrams to have the complete set. Adding the $C_0$ contribution, we considered contributions resulting from the mixing of two ballistic intensities (using an extra scatterer) into two diffuse intensities. We miss for instance the

[8]The fact that only two fields can scatter at the same impurity.

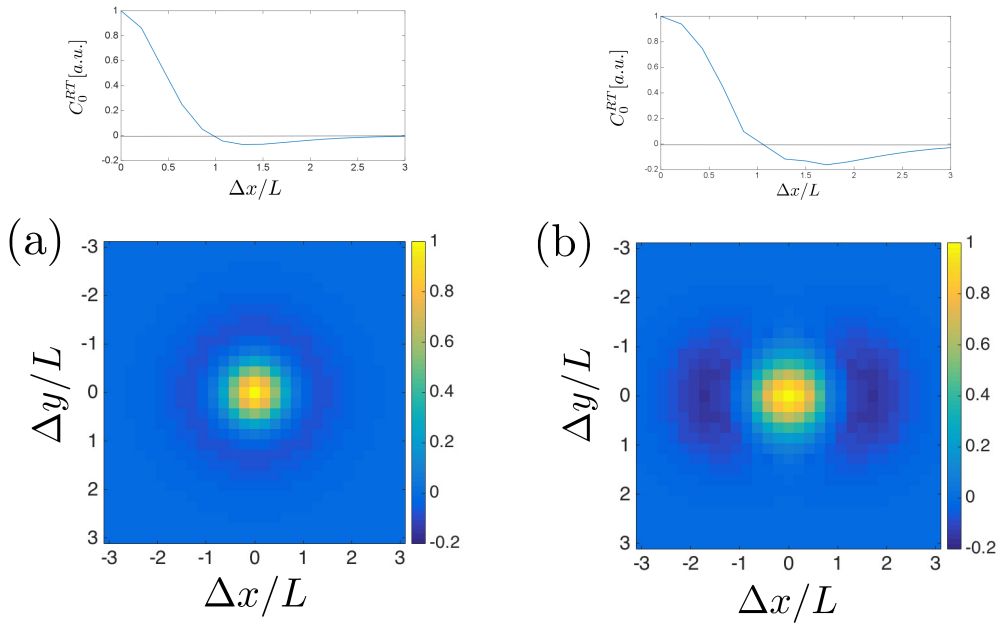


**Figure IV.11** – Analytical prediction for the $C_0$ correlation (normalized to unity) for two different illumination angles: (a) $\theta_a = 0$ and (b) $\theta_a = 45°$ and their cut (in caption) along the direction $\Delta y = 0$ which is defined as the intersection of the incidence plane with the sample surface. The caption corresponds to the cut along $\Delta y = 0$ . Parameters: $\lambda = 632$ nm, $L = 50\,\mu$m, $\ell = 15\,\mu$m. The diffusive approximation was used for the ladder diagrams.

family of diagrams depicted in Fig. IV.12. These diagrams correspond to one ballistic intensity and one diffuse intensity mixing to produce two diffuse intensities or all possibilities with one ballistic and three diffuse intensities. It would be useful to derive them and to investigate their behavior with the angle of incidence or the polarisation of the incident light[93, 94].

- To propose a scattering sequence which represents the $\widetilde{I}$-$\widetilde{I}$ correlation for optical thickness close to unity we thought in terms of number of scattering events. Let us remind that the quantity under study is $\langle \delta E_R \delta E_T \delta E_R^* \delta E_T^* \rangle_c$. The fact that we correlate fluctuating fields means that all sequences contain at least one interaction with the disorder. Thus we must look at all connected four-fields scattering sequences with at least one scattering event for each field. Decreasing the number of scattering events for all fields we eventually find the scattering sequence where the four fields interact with only one common scatterer. This scattering sequence should *a priori* play an important role in the quasi-ballistic regime ($L < \ell$). It is important to note that at the level of the Born approximation for the four-field vertex, only pairs of fields can interact with a common scatterer. Thus this scattering sequence does not exist at this order of approximation. It would be useful to study this class of diagram (usually forgotten in diagrammatic calculations). In order to look for those scattering sequences (beyond the usual model for the four-field vertex) we study in the next chapter the $\widetilde{I}$-$\widetilde{I}$ correlation in the regime $k_0\ell \gg k_0 L \gg 1$ (quasi-ballistic regime) where they give the dominant contribution to the non-gaussian correlation function.

- It would be useful to follow ref. [39] and use the radiative transfer equation to perform the calculation. We could thus have a quantitative agreement between analytics, numerics and experimental results for small optical thickness which is out of reach with diffusion theory.

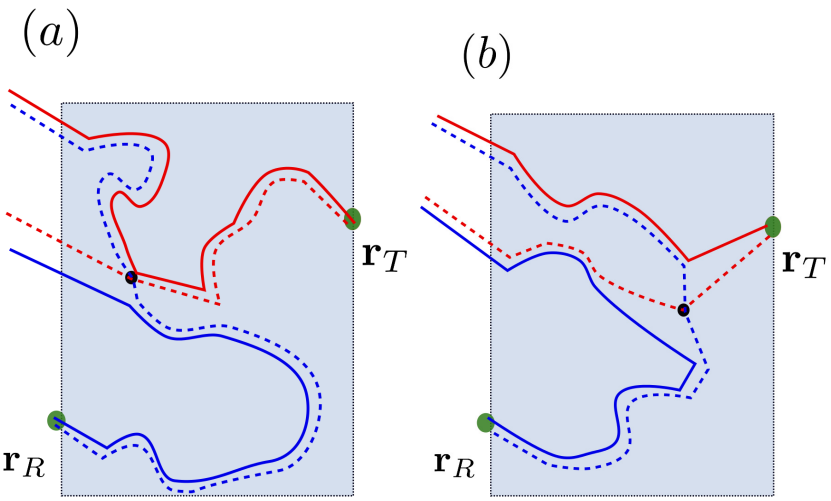


**Figure IV.12** – Representation of two diagrams belonging to a family we do not take into account. Panel (a): one ballistic intensity and one diffuse intensity mix into two diffuse intensities with the use of an extra scattering event. Panel (b) corresponds to the symmetric diagram for which two diffuse intensities mix into one diffuse intensity and two average Green's functions using an extra scattering event.

# Chapter V

# Intensity correlation in the quasi-ballistic regime with resonant scatterers

## Table des matières

In the previous chapter we discussed the measurements of the intensity-intensity correlation in R/T done at the University of Exeter (UK) by I. Starshinov, A. M. Paniagua-Diaz and J. Bertolotti in the framework of a collaboration with our group. The measurements embrace a large range of optical thicknesses. When the optical thickness approaches unity, we observe the appearance of a positive contribution. In the single scattering regime ($b \simeq 1$), this positive contribution is sensitive to the angle of incidence and we proposed a scattering sequence that could be responsible for this contribution. In this chapter we refine the previous discussion studying the regime $k_0\ell \gg k_0L \gg 1$ (quasi-ballistic regime). Let us stress that this regime should *a priori* be easier to study than the regime $b \simeq 1$. Indeed in the quasi-ballistic regime the three length scales of the problem are well separated which is not the case in the intermediate regime.

In this chapter we propose a diagrammatic representation of the quasi-ballistic regime $k_0\ell \gg k_0L \gg 1$. We compare our model to numerical calculations of the usual observables: average fields, average intensity etc. Our objective is to support the following claims:

- The non gaussian correlation in R/T dominates the gaussian correlation as soon as $k_0L \gg 1$.
- The non gaussian correlation is dominated by the common scattering of four fields on a single scatterer in the regime $k_0\ell \gg k_0L \gg 1$ (quasi-ballistic regime).

The quasi-ballistic regime can *a priori* be considered as not relevant for a diagrammatic expansion since ballistic terms are dominant in this regime (the system is almost transparent). Nonetheless, studying the fluctuating fields only, we can observe interesting phenomena that give insight about the multiple scattering process.

## V.1 Statistics of the fluctuating fields

Let us start by studying the scattered fields in the regime $k_0\ell \gg k_0L \gg 1$. We can even wonder whether there is a measurable non-zero scattered field to measure when the optical thickness is small.

### V.1.1 Average fields

The reasoning for the average fields we had in Chap. III remains valid in the regime $k_0\ell \gg k_0L \gg 1$. The average transmitted field should be close to $E_0$ because the attenuation is weak, and the average reflected field is on the order of $E_0/(4k_0\ell)$. The only difference is that the Fabry-Perot effects need to be taken into account for the average reflected field since there is almost no attenuation between two reflections by the boundaries.

In Fig. V.1 we represent the numerically and analytically calculated modulus of the average fields in transmission and reflection for a very thin ($b = 0.01$) and very dilute ($k_0\ell = 2000$) sample. We observe that the analytical expressions derived in Chap. III are in very good agreement with the numerical results. The modulus of the average field in transmission is close to $E_0$, and its decay is

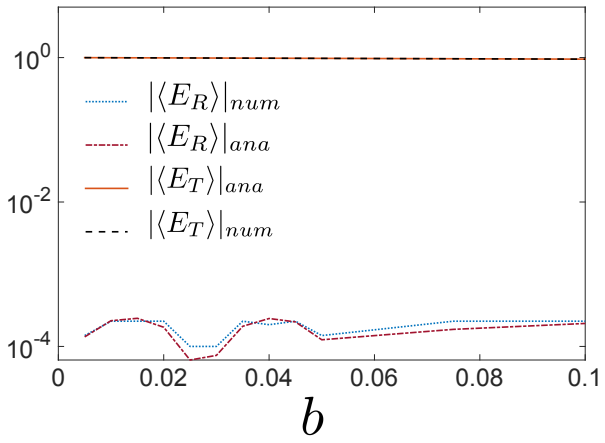


**Figure V.1** – Modulus of the average fields in transmission and reflection (numerically and analytically calculated) versus the optical thickness of a dilute $k_0\ell = 2000$ sample in log scale.

almost linear in this regime (first order expansion of the exponential decay). The modulus of the average field in reflection is on the order of $E_0/(4k_0\ell)$ and oscillates due to the Fabry-Perot effect. We conclude from Fig. V.1 that the vision we have of the average fields remains relevant even for very small optical thicknesses. Indeed the assumption we used in Chap. III to study the average fields is essentially the dilution of the system ($k_0\ell \gg 1$) which still holds in the regime $k_0\ell \gg k_0L \gg 1$.

## V.1.2 Fluctuating fields

Let us now briefly comment on the statistics of the fluctuating part of the transmitted and reflected fields. In panel (a) in Fig. V.2 we represent the fluctuating fields in transmission and reflection for a very thin ($b = 0.01$) and very dilute ($k_0\ell = 2000$) sample. In panel (b) in Fig. V.2 we represent the numerically calculated probability density function of the real part of the fluctuating transmitted field of a thin ($b = 0.01$) and very dilute ($k_0\ell = 2000$) sample and compare it with a gaussian fit. Strikingly, the fluctuating field seems to be gaussian even for a sample composed of a small number $N_{cyl} = 10$ of resonant scatterers[1].

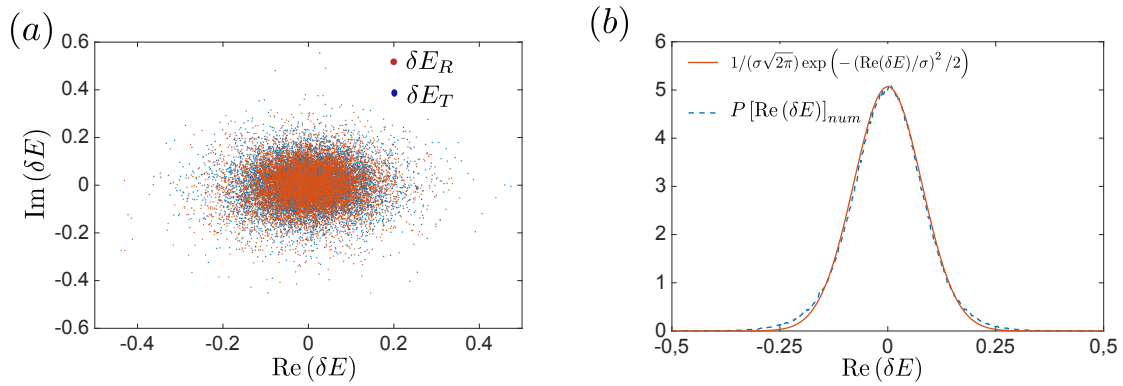


**Figure V.2** – Statistics of the fluctuating reflected an transmitted fields for a very thin ($b = 0.01$) and very dilute ($k_0\ell = 2000$) sample [Panel (a)]. In panel (b) we compare a cut along $\mathrm{Im}\,(\delta E) = 0$ of the statistics of the fluctuating field in transmission with a gaussian fit of zero mean and $\sigma \simeq 0.08$.

[1] In this regime the use of the central limit theorem is questionable.

## V.2 Intensity of the fluctuating field

The fact that the fluctuating fields look like gaussian random variables leads us to the conclusion that the intensity of the fluctuating fields should follow a Rayleigh law. In Chap 1 we showed that for a gaussian field, the only parameter entering the statistics of $\widetilde{I}$ is $\langle \widetilde{I} \rangle$. Let us thus study the average intensity of the fluctuating fields. This quantity is described in the diffusive regime by a ladder diagram as represented in panel (b) in Fig. II.7. In the quasi-ballistic regime, the ladder diagram is still the good operator to study $\langle \widetilde{I} \rangle$ [95], but its calculation cannot be performed using diffusion theory.

### V.2.1 Diagrammatic representation of $\langle \widetilde{I}_T \rangle$ and $\langle \widetilde{I}_R \rangle$ in the quasi-ballistic regime

We propose the scattering sequences depicted in Fig. V.3 to represent $\langle \widetilde{I}_T \rangle$ and $\langle \widetilde{I}_R \rangle$. The idea is to consider only the first term of the ladder diagram and to calculate it explicitly.

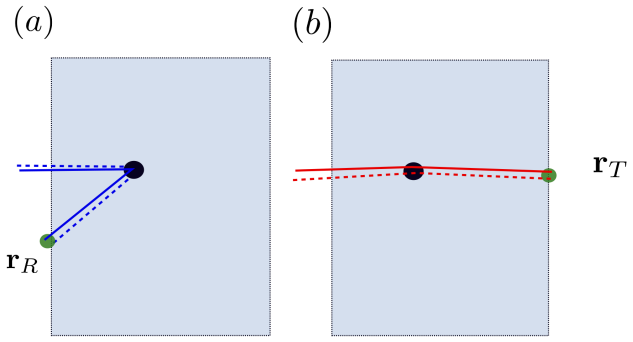


**Figure V.3** – Diagrammatic representation of $\langle \widetilde{I}_T \rangle$ and $\langle \widetilde{I}_R \rangle$ in the quasi-ballistic regime. The fields travel by pair and are scattered once by the same scatterer before propagating together towards their measurements points.

The diagrams read:

$$\begin{cases} \langle |\delta E_T|^2 \rangle = \gamma \int |\langle E(\mathbf{r}) \rangle|^2 |\langle G(\mathbf{r}_T - \mathbf{r}) \rangle|^2 \mathrm{d}\mathbf{r}, \\ \langle |\delta E_R|^2 \rangle = \gamma \int |\langle E(\mathbf{r}) \rangle|^2 |\langle G(\mathbf{r}_R - \mathbf{r}) \rangle|^2 \mathrm{d}\mathbf{r}. \end{cases} \tag{V.1}$$

The average field in the regime $k_0\ell \gg k_0 L \gg 1$ has a constant modulus inside the slab, and we can replace its expression by $E_0$ in the integrals[2]. We obtain

$$\begin{aligned} \langle |\delta E_T|^2 \rangle &= \gamma I_0 \int |\langle G(\mathbf{r}_T - \mathbf{r}) \rangle|^2 \mathrm{d}\mathbf{r} \\ &= \gamma I_0 \int \langle G(k) \rangle e^{i\mathbf{k}.(\mathbf{r}_T - \mathbf{r})} \langle G^*(k') \rangle e^{-i\mathbf{k}'.(\mathbf{r}_T - \mathbf{r})} \mathrm{d}\mathbf{r} \frac{\mathrm{d}\mathbf{k}}{(2\pi)^d} \frac{\mathrm{d}\mathbf{k}'}{(2\pi)^d}. \end{aligned} \tag{V.2}$$

[2]Once this assumption done, we can show mathematically that surprisingly $\langle \widetilde{I}_T \rangle = \langle \widetilde{I}_R \rangle$.

We can integrate over the transverse components of $\mathbf{r}$, leading to

$$\begin{aligned}\langle|\delta E_T|^2\rangle &= \gamma I_0 \int \frac{e^{i\widetilde{k_1}(L-z)}}{2\widetilde{k_1}} \frac{e^{-i\widetilde{k_2}(L-z)}}{2\widetilde{k_2}} \mathrm{d}z \frac{\mathrm{d}\mathbf{k}_T}{(2\pi)^{d-1}} \\ &= \gamma I_0 \int \frac{i\left(1-e^{i[\widetilde{k_1}-\widetilde{k_2}]L}\right)}{(\widetilde{k_1}-\widetilde{k_2})4|\widetilde{k_1}|^2} \frac{\mathrm{d}\mathbf{k}_T}{(2\pi)^{d-1}}\end{aligned} \tag{V.3}$$

with

$$\widetilde{k_1} = \sqrt{k_0^2 - k_T^2 + i\frac{k_0}{\ell}} = K + iK' = \widetilde{k_2}^*. \tag{V.4}$$

We finally obtain

$$\langle\widetilde{I_T}\rangle = \langle\widetilde{I_R}\rangle = \gamma I_0 \int \frac{\left(1-e^{-2K'L}\right)}{8K'(K^2+K'^2)} \frac{\mathrm{d}\mathbf{k}_T}{(2\pi)^{d-1}} = \gamma I_0 \int \mathcal{F}(K,K') \frac{\mathrm{d}\mathbf{k}_T}{(2\pi)^{d-1}} \tag{V.5}$$

with

$$\mathcal{F}(K,K') = \frac{\left(1-e^{-2K'L}\right)}{8K'(K^2+K'^2)}. \tag{V.6}$$

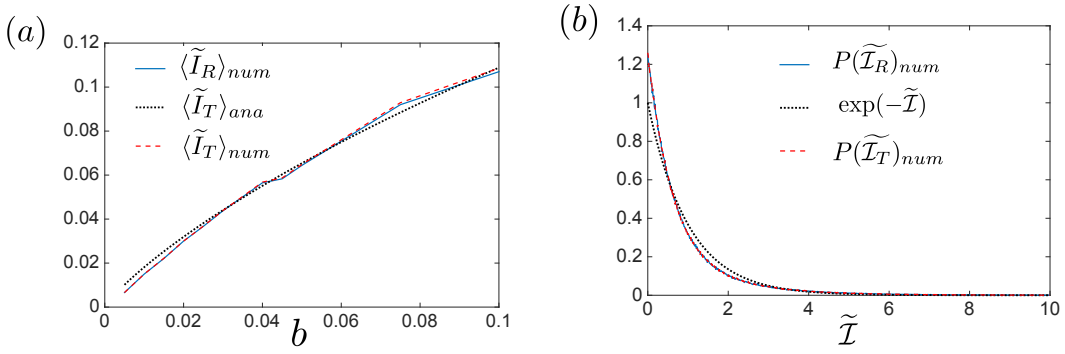


**Figure V.4** – Panel (a): numerical calculation of the average intensity of the fluctuating fields in transmission (red dashed line), reflection (blue solid line) and Eq. (V.5) (black dotted line) for a dilute ($k_0\ell = 2000$) sample of as a function of the optical thickness. Panel (b): statistics of $\widetilde{\mathcal{I}} = \widetilde{I}/\langle\widetilde{I}\rangle$ in reflection (blue solid line) and transmission (red dashed line) numerically calculated and the negative exponential law (black dotted line).

In panel (a) in Fig. V.4 we represent the numerically calculated average intensity of the fluctuating fields in reflection (blue solid line), transmission (red dashed line), and the result given by Eq. (V.5) (black dotted line) for a very dilute system ($k_0\ell = 2000$) as a function of the optical thickness. The condition $k_0\ell \gg k_0 L \gg 1$ is always satisfied. We observe a perfect agreement between numerics and analytics.

### V.2.2 Reflection and transmission statistics are identical

The previous analysis revealed that the average intensity of the fluctuating fields in reflection and in transmission are identical. Here we want to stress that this remains valid for all moments of $\delta E_R$ and $\delta E_T$. As we can see in Figs. V.2 (a) and V.4 (b), the whole statistics of the fluctuating fields and of their intensity are similar in reflection and transmission. In Fig. V.5 we give the diagrammatic

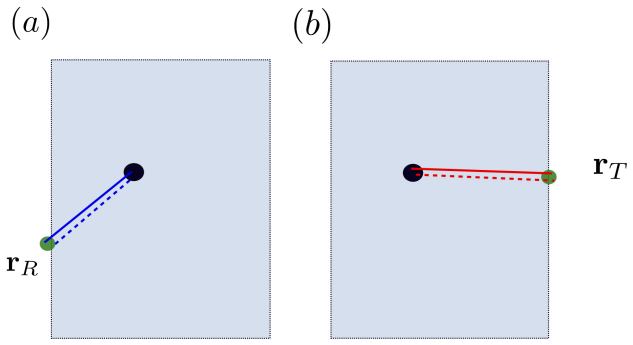


**Figure V.5** – Diagrammatic representation of the approximation of $\langle \widetilde{I}_T \rangle$ and $\langle \widetilde{I}_R \rangle$ in the quasi-ballistic regime considering that the modulus of the average field inside the slab is constant and equal to $E_0$. Changing the variables in the mathematical expressions of those two diagrams, we can show that they are equal.

explanation of this striking behavior. As discussed in the derivation of Eq. (V.5), in the regime $k_0\ell \gg k_0 L \gg 1$ the average field in the slab has a constant modulus $E_0$. We can thus transform Fig. V.3 into Fig. V.5 by removing the incident average field. This can be done for all moments of $\delta E_R$ and $\delta E_T$. After disconnection of these scattering sequences from the "outside world", there is no difference between reflection and transmission.

### V.2.3 An analogy between the diffusive and the quasi-ballistic regime

In panel (b) in Fig. V.4 we represent the statistics of $\widetilde{\mathcal{I}} = \widetilde{I}/\langle \widetilde{I} \rangle$ in reflection (blue solid line) and transmission (red dashed line) for a thin ($b = 0.01$) and dilute ($k_0\ell = 2000$) sample, and compare it with the negative exponential law. The agreement is good even in this very peculiar regime[3]. In Chap. II we discuss the Rayleigh law for the intensity in the diffusive regime. We observed that it was the consequence of two concomitant assumptions: the vanishing of the average field (always true when fluctuating fields are considered) and the gaussian character of the field. Diagrammatically, the gaussian character of the field can be reformulated by stating that the a moment of order $N$ of $\widetilde{I}$ can be built using the building block $\langle \widetilde{I} \rangle$ only. In the diffusive regime $\langle \widetilde{I} \rangle$ was governed by the ladder diagram, while in the present situation it is governed by the diagram represented in Fig. V.3. To push

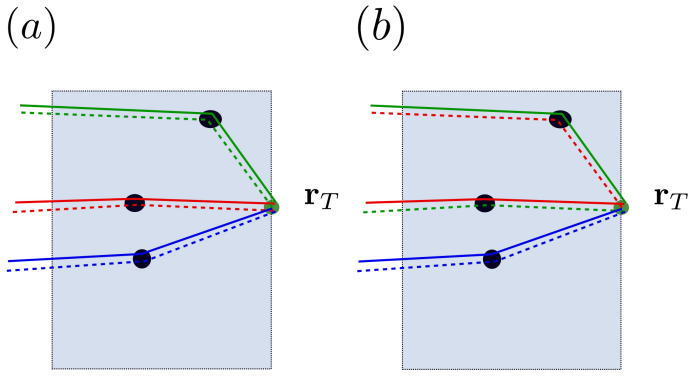


**Figure V.6** – Two different contributions of the moment of order 3 of the transmitted intensity of the fluctuating field in the quasi-ballistic regime. The various pairing give the $N!$ factor in the expression of the moments of the Rayleigh law.

[3]There are only $N_{cyl} = 10$ scatterers in each sample.

the comparison between the diffusive regime and the quasi-ballistic regime we represent in Fig. V.6 two over six contributions to the moment of order 3 of $\widetilde{I}_T$. This figure needs to be compared with Fig. II.8 in order to observe the strong analogy between the diffuse regime and the quasi-ballistic regime from a diagrammatic point of view[4].

## V.3 $C_1$ correlation

Let us discuss now the $C_1$ correlation in the quasi-ballistic regime. Let us remind that

$$C = \frac{\langle \delta\widetilde{I}_1 \delta\widetilde{I}_2 \rangle}{\langle \widetilde{I}_1 \rangle \langle \widetilde{I}_2 \rangle} = \underbrace{\frac{|\langle \delta E_1 \delta E_2^* \rangle|^2}{\langle \widetilde{I}_1 \rangle \langle \widetilde{I}_2 \rangle}}_{C_1} + \frac{\langle \delta E_1 \delta E_1^* \delta E_2 \delta E_2^* \rangle_c}{\langle \widetilde{I}_1 \rangle \langle \widetilde{I}_2 \rangle} \tag{V.7}$$

with $\widetilde{I}_1$ and $\widetilde{I}_2$ being either reflected or transmitted intensities of the fluctuating fields. In this section we deal with the first term of the right hand side in Eq. (V.7) in the regime $k_0\ell \gg k_0 L \gg 1$.

### V.3.1 Diagrammatic representation of the field-field correlation in the quasi-ballistic regime

In the quasi-ballistic regime, the field-field correlation function in R/T should be dominated by the scattering sequence represented in panel (a) in Fig. V.7. Since there is almost no attenuation due to scattering in the quasi-ballistic regime, panel (a) can be approximated by panel (b).

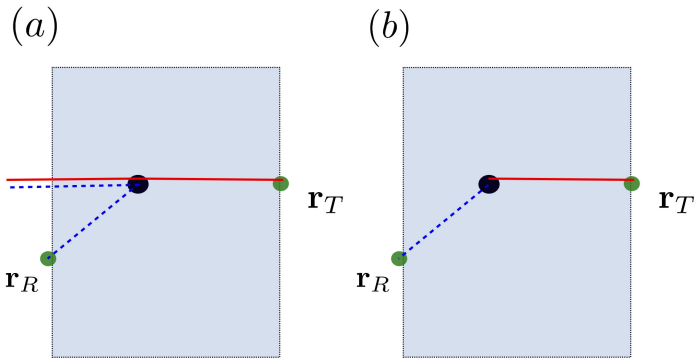


**Figure V.7** – Diagrammatic representation of $C_1(\mathbf{r}_R, \mathbf{r}_T)$ in the quasi-ballistic regime [panel (a)] and its approximation considering that the average field has a constant modulus equal to $E_0$ inside the slab [panel (b)]. The fields travel by pair and are scattered once by a common scatterer before traveling alone towards their different measurements points.

We have

$$\begin{aligned} \langle \delta E_T^* \delta E_R \rangle &= \gamma \int |\langle E(\mathbf{r}) \rangle|^2 \langle G^*(\mathbf{r}_T - \mathbf{r}) \rangle \langle G(\mathbf{r}_R - \mathbf{r}) \rangle \mathrm{d}\mathbf{r} \\ &= \gamma I_0 \int \langle G^*(\mathbf{r}_T - \mathbf{r}) \rangle \langle G(\mathbf{r}_R - \mathbf{r}) \rangle \mathrm{d}\mathbf{r} \\ &= \gamma I_0 \int \langle G^*(k') \rangle \langle G(k) \rangle e^{i\mathbf{k}.(\mathbf{r}_R - \mathbf{r})} e^{-i\mathbf{k}'.(\mathbf{r}_R - \mathbf{r})} \mathrm{d}\mathbf{r} \frac{\mathrm{d}\mathbf{k}}{(2\pi)^d} \frac{\mathrm{d}\mathbf{k}'}{(2\pi)^d}, \end{aligned} \tag{V.8}$$

[4]This analogy is simply due to the fact that both regimes are diluted ($k_0\ell \gg 1$).

and finally obtain:

$$\langle \delta E_T^* \delta E_R \rangle = \gamma I_0 \int e^{i\mathbf{k}_T.\mathbf{\Delta R}} \mathcal{F}_{RT}(K, K') \frac{\mathrm{d}\mathbf{k}_T}{(2\pi)^{d-1}} \tag{V.9}$$

with

$$\mathcal{F}_{RT}(K, K') = e^{-i(K-iK')L} \frac{e^{2iKL} - 1}{8K(K^2 + K'^2)}. \tag{V.10}$$

We can now express the $C_1$ correlation in R/T normalizing Eq. (V.9) with Eq. (V.5), which gives

$$C_1(\mathbf{r}_R, \mathbf{r}_T) = \frac{\left| \int \mathcal{F}_{RT}(K, K') e^{i\mathbf{k}_T.\mathbf{\Delta R}} \frac{\mathrm{d}\mathbf{k}_T}{(2\pi)^{d-1}} \right|^2}{\left( \int \mathcal{F}(K, K') \frac{\mathrm{d}\mathbf{k}_T}{(2\pi)^{d-1}} \right)^2}. \tag{V.11}$$

For the sake of comparison, in R/R and T/T it reads

$$C_1(\mathbf{r}_{R1}, \mathbf{r}_{R2}) = C_1(\mathbf{r}_{T1}, \mathbf{r}_{T2}) = \frac{\left| \int \mathcal{F}(K, K') e^{i\mathbf{k}_T.\mathbf{\Delta R}} \frac{\mathrm{d}\mathbf{k}_T}{(2\pi)^{d-1}} \right|^2}{\left( \int \mathcal{F}(K, K') \frac{\mathrm{d}\mathbf{k}_T}{(2\pi)^{d-1}} \right)^2}. \tag{V.12}$$

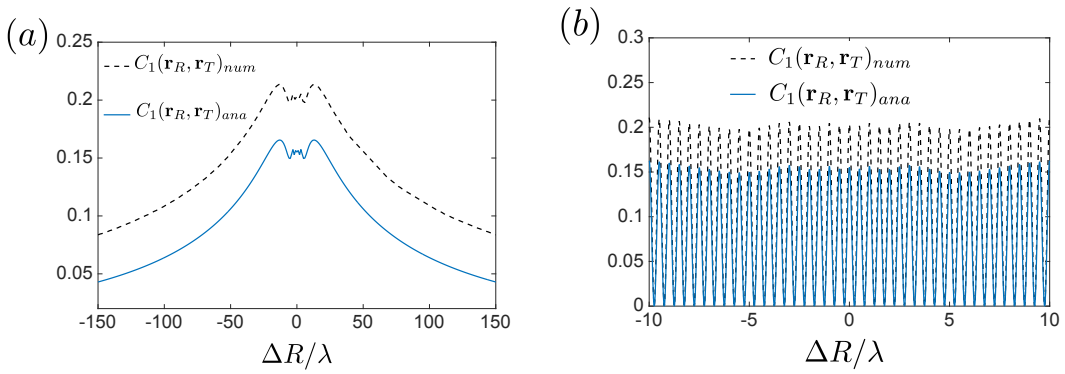


**Figure V.8** – Envelope of the $C_1$ correlation function in R/T for a thin ($b = 0.01$) and dilute ($k_0\ell = 2000$) sample calculated numerically and analytically [panel (a)]. In panel (b) we use a higher density of points in the vicinity of $\Delta R = 0$ in order to observe numerically and analytically the oscillating behavior of the $C_1$ correlation in R/T.

In panel (a) in Fig. V.8 and Fig. V.9 we represent the envelope of the gaussian correlation functions in R/T and T/T calculated numerically and analytically versus the transverse distance normalized by $\lambda$. In the quasi-ballistic regime the gaussian correlation has a long range envelope. In panel (b) in Fig. V.8 and Fig. V.9, we represent numerically and analytically the gaussian correlation functions in R/T and T/T calculated numerically and analytically versus the transverse distance with a higher density of points in the vicinity of $\Delta R = 0$ in order to see the oscillating behavior at $\lambda/2$. The agreement between analytics and numerics is strikingly good.

## V.4 Non gaussian correlation in the quasi-ballistic regime

In this section we deal with the second term of the right hand side in Eq. (V.7) in the regime $k_0\ell \gg k_0 L \gg 1$.

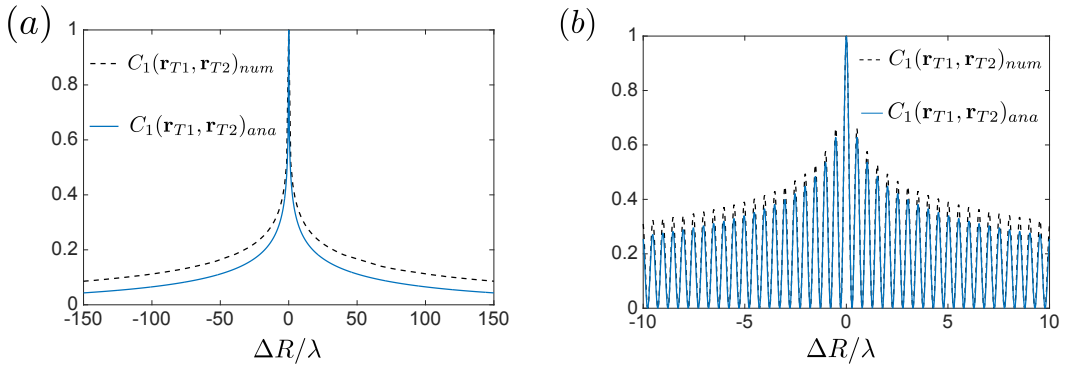


**Figure V.9** – Envelope of the $C_1$ correlation function in T/T for a thin ($b = 0.01$) and dilute ($k_0\ell = 2000$) sample calculated numerically and analytically [panel (a)]. In panel (b) we use a higher density of points in the vicinity of $\Delta R = 0$ in order to observe numerically and analytically the oscillating behavior of the $C_1$ correlation in T/T.

### V.4.1 Numerical evidence of the difference between $C$ and $C_1$

Let us compare $C$ and $C_1$ both in R/T and in T/T (or R/R since reflection and transmission are equivalent in this regime). In Fig. V.10 we represent the numerically calculated $\widetilde{I}$-$\widetilde{I}$ correlation in R/T [panel (a)] and T/T [panel (b)] for a thin ($b = 0.01$) and dilute ($k_0\ell = 2000$) sample. These two curves need to be compared with the curves represented in panel (a) in Fig. V.8 and Fig. V.9 where only the gaussian contribution to the $\widetilde{I}$-$\widetilde{I}$ correlation is calculated for the exact same parameters. We observe on these two curves a strong non gaussian additional contribution. Note the substantial non gaussian contribution to the $\widetilde{I}$-$\widetilde{I}$ correlation in T/T[5]. Let us enter into the calculation of the non

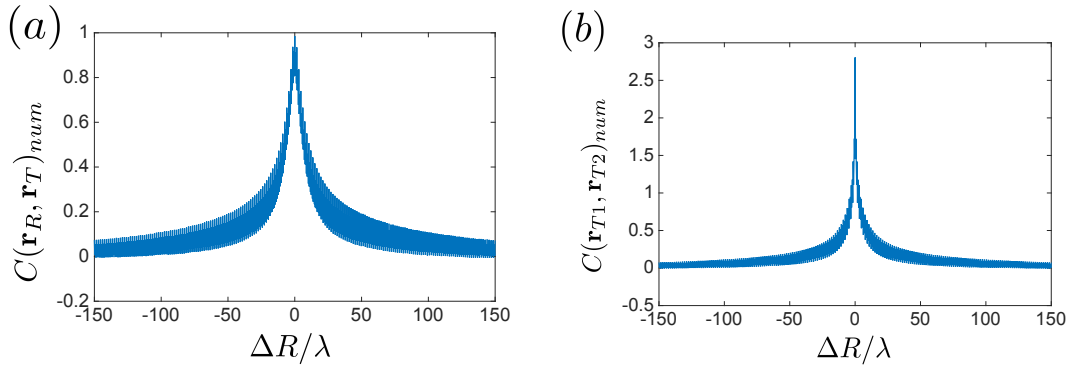


**Figure V.10** – Numerical calculation of the $\widetilde{I}$-$\widetilde{I}$ correlation versus the transverse distance normalized by $\lambda$ in R/T [panel (a)] and T/T [panel (b)] for a thin ($b = 0.01$) and dilute ($k_0\ell = 2000$) sample.

gaussian contribution in T/T, R/R and R/T in the quasi-ballistic regime.

[5]Let us stress that we use resonant scatterers. Thus the quasi-ballistic regime is equivalent for us to a regime of low number of scatterers. It would be useful to detune the excitation frequency from the resonance frequency of the scatterers (keeping $b$ constant) in order to increase the number of scatterers and observe the change in the $\widetilde{I}$-$\widetilde{I}$ correlation.

### V.4.2 Diagrammatic representation of the non gaussian correlation in the quasi-ballistic regime

Let us remind our guess that in the quasi-ballistic regime, scattering sequences beyond the usual approximation for the four-field vertex should be dominant. The idea is the following. In the $C_2$ diagram (dominant term of the non gaussian R/T correlation in the diffusive regime) the exchange of partners appears between two diffusive processes. In the quasi-ballistic regime, scattering events are scarce. We thus expect that the dominant term in this regime will be that for which the number of scattering event is the fewest. We represent this scattering sequence in panel (a) in Fig. V.11 in the R/T configuration. This diagram can be approximated by the one in panel (b) due to the absence of extinction in this regime.

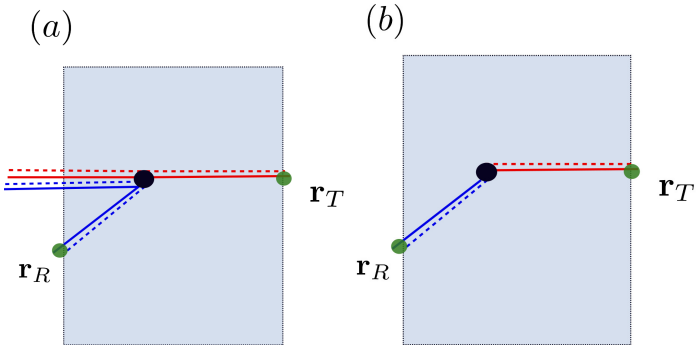


**Figure V.11** – Diagrammatic representation of the dominant term of the non gaussian correlation in the quasi-ballistic regime [panel (a)] and its approximation considering the fact that the average field has a constant modulus equal to $E_0$ in the quasi-ballistic regime [panel (b)]. The four fields are scattered once by a common scatterer.

The average weight for a common collision of two fields is $\gamma$. The average weight for the common collision between four fields is $\Gamma = \rho k_0^8 |\alpha|^4$ which in 2D is

$$\Gamma = \gamma^2/\rho = 16\gamma = 64 k_0/\ell. \tag{V.13}$$

Let us denote the contribution to the non gaussian correlation of the common scattering of four fields by $\langle \delta E_T^* \delta E_R \delta E_T \delta E_R^* \rangle_{ng}$. It reads

$$\begin{aligned} \langle \delta E_T^* \delta E_R \delta E_T \delta E_R^* \rangle_{ng} &= \Gamma \int |\langle E(\mathbf{r}) \rangle|^4 |\langle G(\mathbf{r}_T - \mathbf{r}) \rangle|^2 |\langle G(\mathbf{r}_R - \mathbf{r}) \rangle|^2 \mathrm{d}\mathbf{r} \\ &= \Gamma I_0^2 \int |\langle G^*(\mathbf{r}_T - \mathbf{r}) \rangle|^2 |\langle G(\mathbf{r}_R - \mathbf{r}) \rangle|^2 \mathrm{d}\mathbf{r}. \end{aligned} \tag{V.14}$$

Normalizing Eq. (V.14) by Eq. (V.3) we obtain

$$C_{ng}(\mathbf{r}_1, \mathbf{r}_2) = \frac{\Gamma \int |\langle G^*(\mathbf{r}_1 - \mathbf{r}) \rangle|^2 |\langle G(\mathbf{r}_2 - \mathbf{r}) \rangle|^2 \mathrm{d}\mathbf{r}}{\left( \gamma \int \mathcal{F}(K, K') \dfrac{\mathrm{d}\mathbf{k}_T}{(2\pi)^{d-1}} \right)^2} \tag{V.15}$$

where $\mathbf{r}_1$ and $\mathbf{r}_2$ are the measurements points (either in transmission or in reflection).

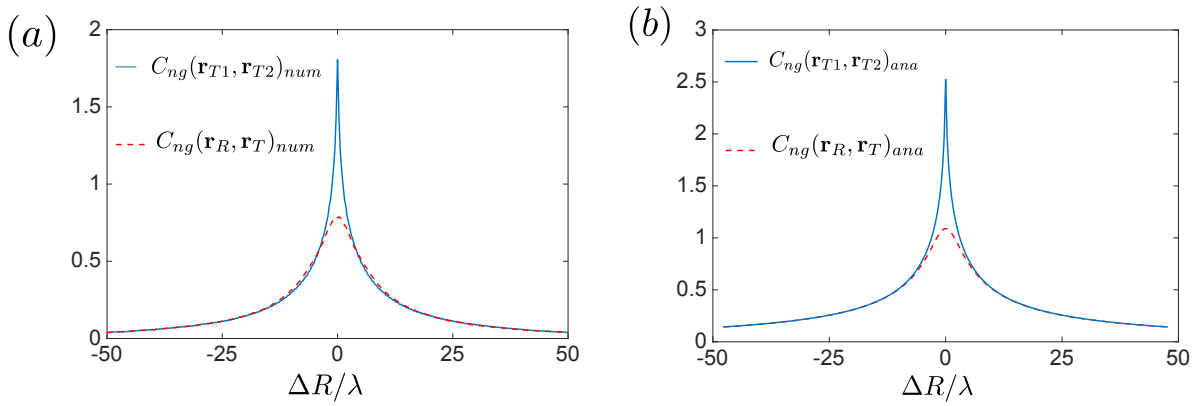


**Figure V.12** – Numerical calculation [Panel (a)] and analytical calculation using Eq. (V.15) [panel (b)] of the non gaussian correlation in T/T (blue solid line) and R/T (red dashed line) for a thin ($b = 0.01$) and dilute ($k_0\ell = 2000$) sample.

### V.4.3 Numerical calculation of the non gaussian correlation function

In Fig. V.12 we represent in panel (a) the numerically calculated non gaussian correlation function in R/T (red dashed line) and in T/T (blue solid line) for a thin ($b = 0.01$) and dilute ($k_0\ell = 2000$) sample. In panel (b) we represent the analytical calculation based on Eq. (V.15) in T/T (blue solid line) and in R/T (red dashed line) for the same parameters. We observe a very good qualitative agreement between numerics and analytics. If we compare in detail the analytical and numerical calculations of $C_{ng}$, we observe a difference in the tail of the functions. This difference also appears when we calculate the $C_1$ correlation. There are at least two explanations for this discrepancy. One possibility could be that the average Green functions that are used are not valid. Indeed we use bulk Green's functions while we should use the average Green functions of a thin slab. The other possibility could be that in this regime the correlation functions are really sensitive to the transverse size of the medium.

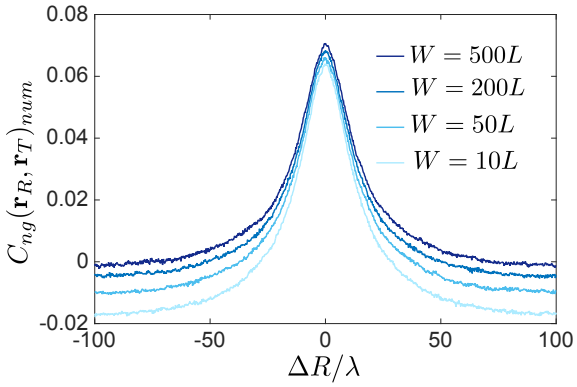


**Figure V.13** – Numerical calculation of the non gaussian correlation in R/T versus the transverse distance normalized by $\lambda$ of a thin ($b = 0.1$) and dilute ($k_0\ell = 500$) sample of varying transverse dimension $W$.

In Fig. V.13 we represent the non gaussian correlation function in R/T for different transverse size of a slab with parameters $b = 0.1$ and $k_0\ell = 500$. We observe that the tail of the correlation function is very sensitive to the transverse size of the scattering medium. We can also note that the value at zero transverse distance is less sensitive to it.

### V.4.4 Dependence on the angle of incidence

In the quasi-ballistic regime we used several times the fact that the modulus of the average field is constant and equal to $E_0$. This result remains valid whatever the angle of incidence $\theta_a$. Analytically, we thus predict that none of the quantities studied in this chapter depends on the angle of incidence. In Fig. V.14 we numerically prove this prediction comparing the non gaussian correlation at zero incidence (blue solid line) and at a large angle of incidence (red dashed line) in R/T [panel (a)] and in T/T [panel (b)] for a thin ($b = 0.01$) and dilute ($k_0\ell = 2000$) sample. We observe no difference

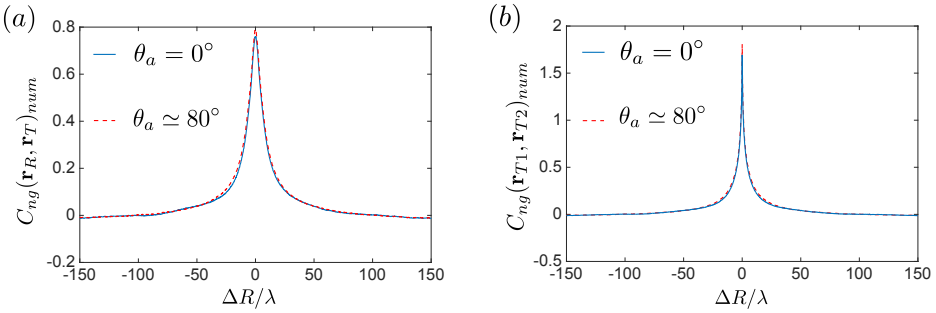


**Figure V.14** – Numerical calculation of the non gaussian correlation in R/T [panel (a)] and in T/T [panel (b)] at normal incidence (blue solid line) and at shifted incidence (red dashed line) of a thin ($b = 0.01$) and dilute ($k_0\ell = 2000$) sample.

between non gaussian correlations for a normal incidence and for a shifted incidence. From this subsection we conclude that there is no angular dependence in the quasi-ballistic regime.

### V.4.5 Amplitude of the non gaussian correlation function

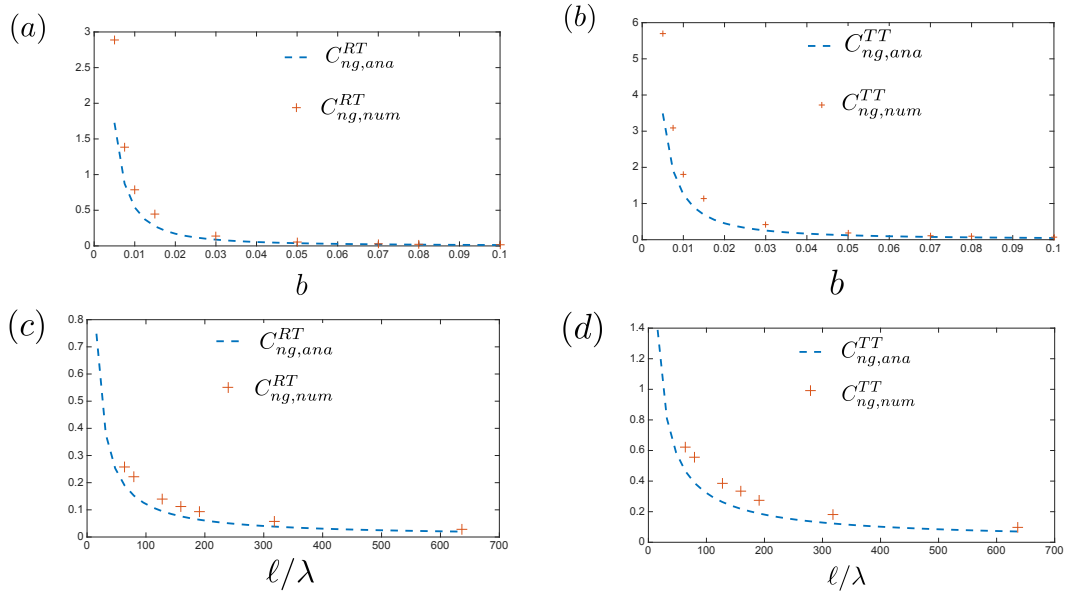


**Figure V.15** – Numerical and analytical calculations of the amplitude of the non gaussian correlation versus the optical thickness in R/T [panel (a)] and in T/T [panel (b)] for a dilute sample ($k_0\ell = 2000$). In panels (c) (R/T configuration) and (d) (T/T configuration), we vary the normalized scattering mean free path $\ell/\lambda$ numerically and analytically keeping the optical thickness constant to a value $b = 0.1$.

In subsection V.4.3 we derived analytical expressions of $C_{ng}$ in T/T and R/T in good agreement with numerical results. In this section we propose a slightly more quantitative approach by analyzing the value at $\Delta R = 0$ of the non gaussian correlation versus the parameters of the system both analytically and numerically. We call $C_{ng}^{RT}$ this quantity in R/T and $C_{ng}^{TT}$ in T/T. In panels (a) and (c) in Fig. V.15 we represent the numerically calculated (red crosses) and analytically calculated (blue dashed line) value of $C_{ng}^{RT}$ versus the optical thickness and versus the mean free path of the medium. In panels (b) and (d) of the same figure we present the same results for $C_{ng}^{TT}$. The very good agreement between numerics and analytics in Fig. V.15 is a proof of the validity of the diagrammatic model of the quasi-ballistic regime that we presented in this chapter.

## V.5 Relative weight of $C_{ng}$ and $C_1$ in R/T in the quasi-ballistic regime

In this section we support our guess that for all optical thicknesses, as long as $k_0 L \gg 1$, $C_1$ is negligible compared to the non gaussian correlation $C_{ng}$ in R/T. In Fig. V.10 $C_1$ was small but not completely negligible. Nonetheless in this sample $k_0 L = 20$ which is not so large. In Fig. V.16 we present numerical calculation of $C_1$ in R/T for a constant optical thickness of $b = 0.05$ but various sample sizes $L$ and mean free paths $\ell$. In Fig. V.17 we show the non gaussian correlation for the same parameters. We observe on these figures that $C_1$ decreases faster than $C_{ng}$ in R/T when $\ell$ and $L$ increase (keeping $b$ constant). This brute-force approach supports our guess that even in the quasi-ballistic regime, as long as $k_0 L \gg 1$, $C_1$ is negligible compared to the non gaussian correlation in R/T. This makes the R/T configuration a perfect configuration to study non gaussian correlations.

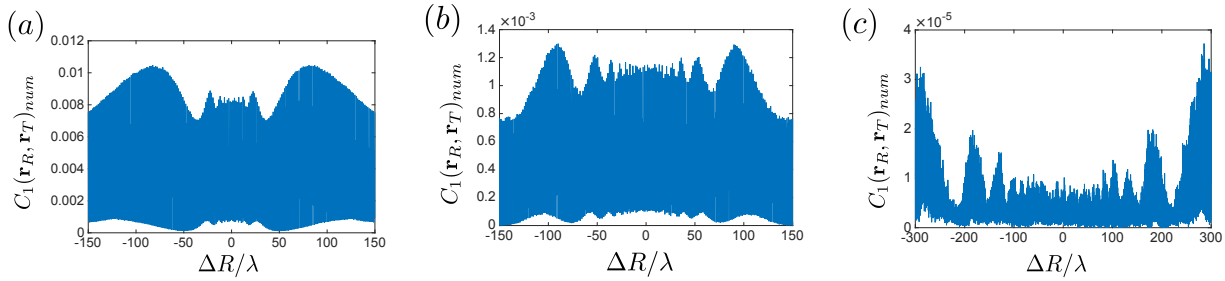


**Figure V.16** – Numerical calculations of $C_1$ in R/T versus the transverse distance normalized by $\lambda$ for three different samples of constant optical thickness $b = 0.05$. Parameters are $k_0\ell = 1000$ for panel (a), $k_0\ell = 2000$ for panel (b) and $k_0\ell = 4000$ for panel (c).

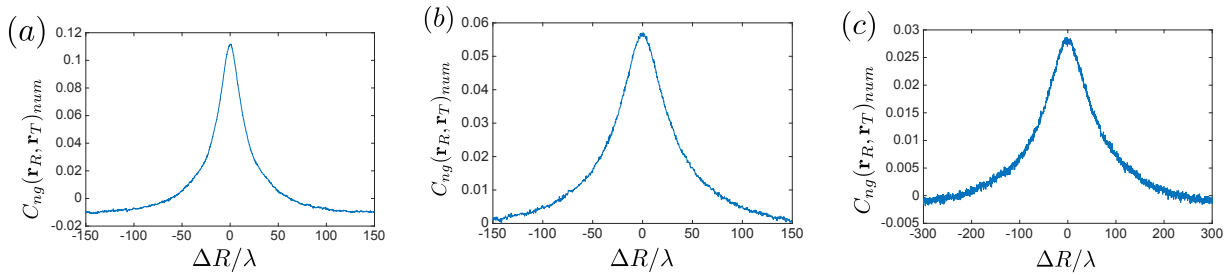


**Figure V.17** – Numerical calculations of $C_{ng}$ in R/T versus the transverse distance normalized by $\lambda$ for three different samples of constant optical thickness $b = 0.05$. Parameters are $k_0\ell = 1000$ for panel (a), $k_0\ell = 2000$ for panel (b) and $k_0\ell = 4000$ for panel (c).

## V.6 Conclusion

Let us summarize conclusions reached in this chapter.

- We believe that this study is convincing enough to claim that the diagrammatic model we propose is relevant in the quasi-ballistic regime. The most interesting observation is the dominant term of the non gaussian correlation. As discussed in the previous chapter, it was claimed in ref. [39] that additional contributions to the long range correlation exist beyond the usual vertex. The contribution we consider in Fig. V.11 belongs to this class but was never observed. This study is to our knowledge the first numerical observation of such un-usual contributions to non gaussian correlations.
- Our result suggest that the contribution described in this chapter has a non negligible weight in the experimental result shown in panel (a) in Fig. IV.2. It would be useful to follow ref. [39] in order to obtain a general expression of the correlation function valid for any parameters of the system to study the regime $\ell \simeq L \gg \lambda$ that is complicated from a diagrammatic point of view.
- We believe that the R/T geometry is perfectly suited to study mesoscopic effects since non gaussian correlation are dominant in the $\widetilde{I}$-$\widetilde{I}$ correlation *whatever the optical thickness*[6] of the system (as soon as $L \gg \lambda$). This allows one to track and study the evolution of the connected four-field correlation in all scattering regimes.

[6]This is a guess supported by Fig. V.16 and Fig. V.17.

# Chapter VI

# An application: Blind Ghost Imaging

## Table des matières

In this chapter we propose a new imaging modality based on the existence of an intensity correlation between reflection and transmission, that we call *Blind Ghost Imaging* (BGI). This chapter is a numerical proof of concept of the feasibility of Blind Ghost Imaging performed in the framework of a collaboration with our colleagues from the University of Exeter (UK): I. Starshinov, A.M Paniagua Diaz and J. Bertolotti.

# VI.1 Introduction

In this section we introduce the imaging modality know as *Ghost Imaging*. The BGI idea that we propose is an extension of this technique.

## VI.1.1 Standard Ghost Imaging

Ghost imaging (GI) is a modality based on the intensity cross correlation between two beams. In its original form (represented in Fig. VI.1) a classical (or quantum) fluctuating source generates two identical paraxial optical fields [96, 97]. These two fields propagate through the system to eventually be measured in two different detection planes. At one detection plane the field illuminates a thin object (modeled as a thin transmission mask denoted by $\mathcal{O}$) and the intensity transmitted through the object is directly integrated by a mono pixel detector (usually called a bucket detector) that does not provide a direct image of the thin mask. At the second detection plane, the intensity which did not interact with the object is measured by a CCD camera placed at the same distance from the source than the object. The two measurements are correlated and the process is repeated a large number of times in order to perform an average (over the fluctuations of the source). The correlation reveals the squared modulus of the transmission mask convolved with the intensity-intensity correlation function of the beam. More formally, the signal reads:

$$\begin{aligned} \mathrm{S}(\mathbf{r}_{2,\perp}) &= \frac{\langle \int_{\text{detector}} |\mathcal{O}(\mathbf{r}_{1,\perp})|^2 I(\mathbf{r}_{1,\perp}) I(\mathbf{r}_{2,\perp}) \mathrm{d}\mathbf{r}_{1,\perp} \rangle - \langle \int_{\text{detector}} |\mathcal{O}(\mathbf{r}_{1,\perp})|^2 I(\mathbf{r}_{1,\perp}) \mathrm{d}\mathbf{r}_{1,\perp} \rangle \langle I(\mathbf{r}_{2,\perp}) \rangle}{\langle \int_{\text{detector}} |\mathcal{O}(\mathbf{r}_{1,\perp})|^2 I(\mathbf{r}_{1,\perp}) \mathrm{d}\mathbf{r}_{1,\perp} \rangle \langle I(\mathbf{r}_{2,\perp}) \rangle} \\ &= \frac{\int_{\text{detector}} |\mathcal{O}(\mathbf{r}_{1,\perp})|^2 \langle \delta I(\mathbf{r}_{1,\perp}) \delta I(\mathbf{r}_{2,\perp}) \rangle \mathrm{d}\mathbf{r}_{1,\perp}}{\int_{\text{detector}} |\mathcal{O}(\mathbf{r}_{1,\perp})|^2 \langle I(\mathbf{r}_{1,\perp}) \rangle \mathrm{d}\mathbf{r}_{1,\perp} \langle I(\mathbf{r}_{2,\perp}) \rangle}. \end{aligned} \tag{VI.1}$$

In Eq. (VI.1), $\mathbf{r}_{1,\perp}$ is the transverse position on the mono pixel detector, $\mathbf{r}_{2,\perp}$ is the transverse position on the CCD camera and $\mathcal{O}$ is the field transmittance of the thin mask. In Eq. (VI.1), $\langle \delta I(\mathbf{r}_{1,\perp}) \delta I(\mathbf{r}_{2,\perp}) \rangle \propto C(\mathbf{r}_{2,\perp} - \mathbf{r}_{1,\perp})$, with $C(\mathbf{r}_{2,\perp} - \mathbf{r}_{1,\perp})$ the intensity correlation function of the incoming beam which allows us to recognize into Eq. (VI.1) a convolution product between the squared modulus of the transmittance of the object and the intensity-intensity correlation function

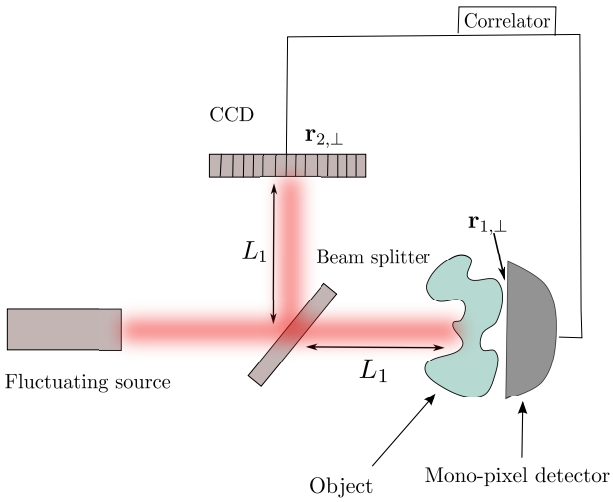


**Figure VI.1** – Scheme of the conventional GI set-up. A fluctuating source generates a field separated in two beams by a beam splitter. In one arm a CCD camera measures the intensity with a high resolution. In the other arm, the intensity illuminates a thin object. A mono pixel detector integrates all the light coming through the object providing no spatial resolution. The distance from the beam splitter to the camera equals the distance from the beam splitter to the object. The signal from the mono pixel detector is correlated with the signal measured in each pixel of the CCD camera and the process is repeated many times.

between the intensity at the CCD plane. The narrower the intensity correlation function is, the better resolved will be the GI image.

## VI.1.2 Variants of Ghost Imaging

### Computationnal Ghost Imaging

Soon it has been realized that for free space propagation the second arm of the set-up could be removed provided the incident field is known. This scheme is called computational Ghost Imaging [98, 99]. Practically, a plane wave is used and encounters a spatial light modulator (SLM) shaping the field. Since the distance from the SLM to the object is known, one can numerically propagate the field from the SLM position to the position where the CCD should be. Additionally the intensity correlation can be controlled using the SLM. This is represented in Fig. VI.2.

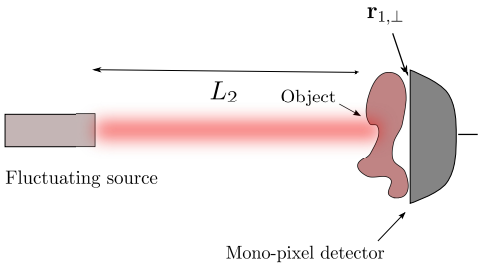


**Figure VI.2** – Scheme of the computational GI set-up. A fluctuating source producing a known field illuminates an object whose distance from the source is known. A mono pixel detector integrates all the light coming through the object. This signal is correlated with the intensity numerically propagated at the position of the object. The process is repeated many times.

### Reflection Ghost Imaging

It is also possible to use reflected photons for GI in free space [100] as represented in Fig. VI.3. This allows in principle to place the CCD camera far away from the object. Note also that introducing scattering in the reflected GI set-up has been done considering atmospheric turbulence between the object and the CCD [101], or considering an object immersed inside a scattering medium (at a depth small compared to the mean free path of the sample) [102].

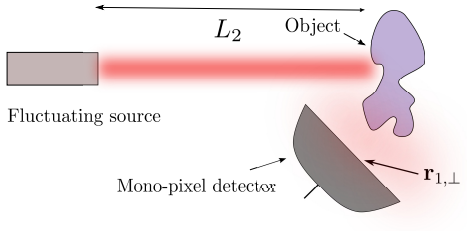


**Figure VI.3** – Scheme of the computational GI in reflection. A fluctuating source producing a known field illuminates an object whose distance from the source is known. A mono pixel detector integrates all the light reflected from the object. This signal is correlated with the intensity numerically propagated at the position of the object. The process is repeated many times.

### Ghost Imaging in transmission though a scattering medium

It is also possible to use a scattering medium to produce a sharp intensity correlation in transmission [103]. This scheme of GI is represented in Fig. VI.4. In comparison with the usual GI set-up, the fluctuating source is replaced by the combination of a non fluctuating source and a scattering medium. We call GI($\mathbf{r}$) the signal given by Eq. (VI.1) obtained with this set-up. The GI signal is thus

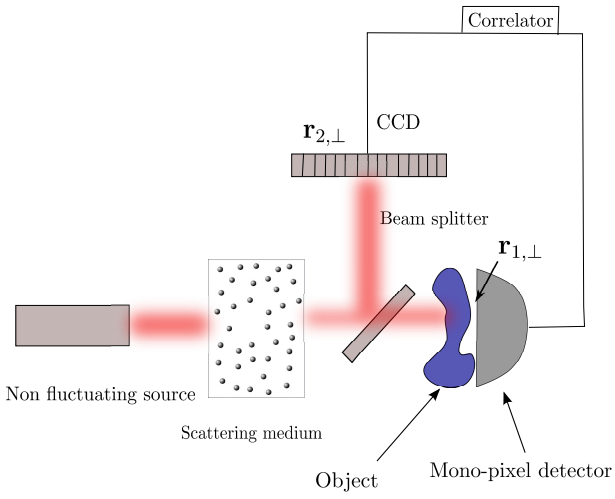


**Figure VI.4** – Scheme of the GI in transmission though a scattering medium. A plane wave illuminates a scattering medium. The transmitted intensity is split in two by a beam splitter. In one arm a CCD camera measures the intensity, while in the other arm the transmitted intensity illuminates a thin object. A mono pixel detector integrates all the light coming through the object providing no spatial resolution. The signal from the mono pixel detector is correlated with the signal in each pixel of the CCD camera. The process is repeated for many realizations of disorder.

proportional to the convolution product of the T/T intensity correlation with the squared modulus

of the transmittance of the object. The interesting property of GI in transmission though a thick scattering medium is that the intensity correlation has a typical size $\lambda$ (as represented in panel (a) in Fig. VI.6) permitting a good resolution of the object. Also, the amplitude of the correlation is close to one, and thus provides a good SNR to this imaging modality. Eventually the correlation function does not change too much with the parameters of the system in the diffusive regime ($b \gg 1$ and $k_0\ell \gg 1$). In this regime, the image does not depend on the parameters of the scattering medium.

### VI.1.3 Blind Ghost Imaging

In this chapter we propose a new approach to GI that we call Blind Ghost Imaging (BGI) (see Fig. VI.5) after a suggestion by J. Bertolotti from the University of Exeter (UK). In the BGI set-up, a non fluctuating monochromatic source illuminates a scattering medium[1]. The reflected intensity is measured using a CCD camera. On the transmission side of the sample an object with transmittance $\mathcal{O}$ is illuminated by the transmitted intensity. Behind the object, a mono pixel detector integrates all the light coming though the object with no spatial resolution. The two signals are correlated and the process is repeated many times. We call BGI($\mathbf{r}$) the signal given by Eq. (VI.1) obtained in the

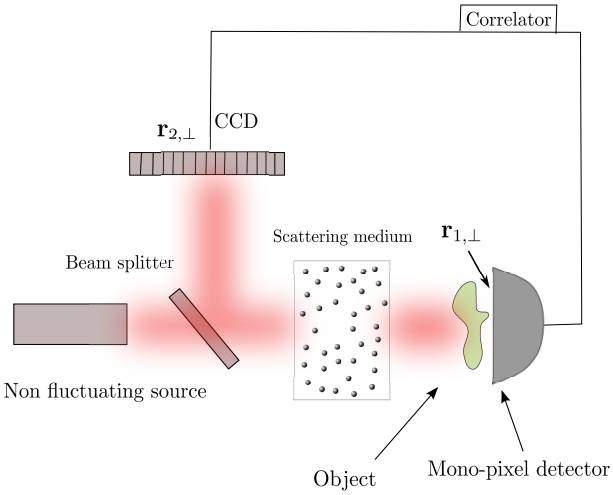


**Figure VI.5** – Scheme of the BGI set-up. A plane wave illuminates a scattering medium. The reflected intensity is measured by a CCD camera while the transmitted intensity illuminates a thin object. A mono pixel detector integrates all the light coming through the object providing no spatial resolution. The signal from the mono pixel detector is correlated with the one in each pixel of the CCD camera. The process is repeated for many disorder realizations.

BGI configuration. The BGI signal is proportional to the convolution product of the R/T intensity correlation with the squared modulus of the transmittance of the object. In panel (b) in Fig. VI.6 we represent the intensity-intensity correlation in R/T convolving[2] the transmittance of the object to build the BGI signal. We observe that the amplitude of the R/T correlation is much lower than the T/T intensity correlation [and decreases with $1/(k_0L)$]. The typical width of the correlation function is $L$ in R/T. Thus the SNR and the resolution of the BGI image decrease when $L$ increases.

[1]The optical thickness can be *a priori* arbitrary large provided the number of statistical configurations is large enough.

[2]Note that in Eq. (VI.1) we obtain the convolution of the squared modulus of the transmittance of the object with the intensity-intensity correlation times a factor depending on the area of the object and on the surface of the mono pixel detector. We leave the exact study of the amplitude of the signal obtained for future work. Here we focus on the proof of concept of BGI and its scaling with the thickness of the medium $L$.

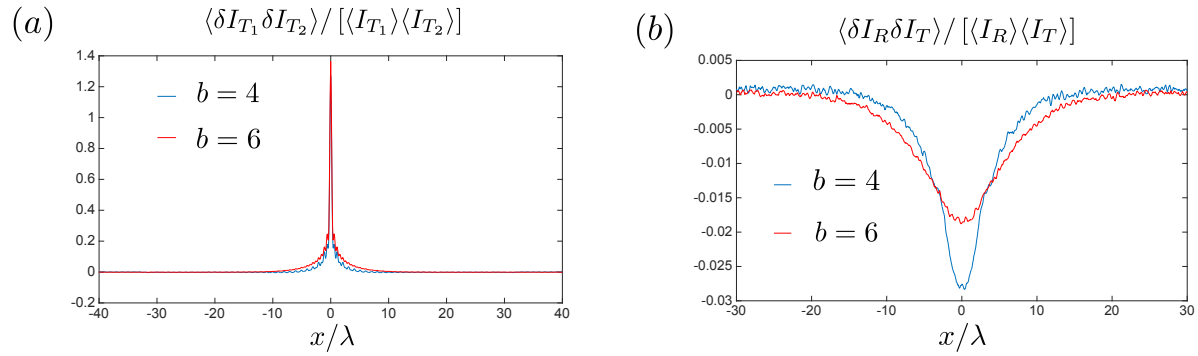


**Figure VI.6** – Numerical calculation of intensity-intensity correlation functions in T/T [panel (a)] and in R/T [panel (b)] for two different optical thicknesses ($b = 4$ and $b = 6$). We have set $k_0\ell = 10$ in the simulations.

## VI.2 Numerical results

In order to demonstrate the feasibility of the BGI we present some numerical simulations of BGI and compare them with numerical simulations of GI in transmission of a scattering medium. We consider a scattering sample with varying optical thickness. The transmitted and reflected intensities are measured on the surface of the sample. To keep the numerical experiment as simple as possible, we mimic the object using a perfect numerical mask of transmittance $\mathcal{O}$ (instead of a real object with a given permittivity). The transmittance reads

$$\mathcal{O}(\mathbf{r'}_{T,\perp}) = \begin{cases} 0 & \text{if } |\mathbf{r'}_{T,\perp}| \leq L_{obj}/2, \\ 1 & \text{if } |\mathbf{r'}_{T,\perp}| > L_{obj}/2. \end{cases} \tag{VI.2}$$

In Eq. (VI.2) $L_{obj}$ is the size of the numerical object. This allows us to define the field after the object as the field before the object multiplied by $\mathcal{O}(\mathbf{r'}_{T,\perp})$. In Fig. VI.7 we show numerical simulations of GI and BGI for two different optical thicknesses ($b = 4$ and $b = 6$), and for four different sizes $L_{obj}$ of the object hidden behind the thick scattering medium. The number of disorder realizations used for the averaging process is $N = 10^6$. As predicted GI produces a well resolved image of the object with a rather good SNR, while BGI gives a less resolved image of the object with a lower SNR. The variation of the GI and the BGI images with the parameter $L$ is in perfect agreement with the evolution of the intensity-intensity correlation functions in T/T and R/T. Indeed the GI image seems independent of $L$ while both the SNR and the resolution of the BGI image diminish when $L$ increases.

The BGI scheme could represent a real advance both conceptually and practically. Indeed, the intensity exciting the object is unknown, in contrast to usual GI modalities. Here we correlate a completely different intensity with the signal measured by the mono pixel detector, and we do not assume knowledge about the intensity illuminating the object (we only use a statistical information about it). BGI relies solely on the intensity-intensity correlation between two totally different beams. Practically, with this modality we may image an object in transmission though a thick scattering medium having only one information in the transmission side of the sample: the total integrated intensity. The price to pay is the decrease of the SNR and of the resolution with the thickness $L$ of the medium.

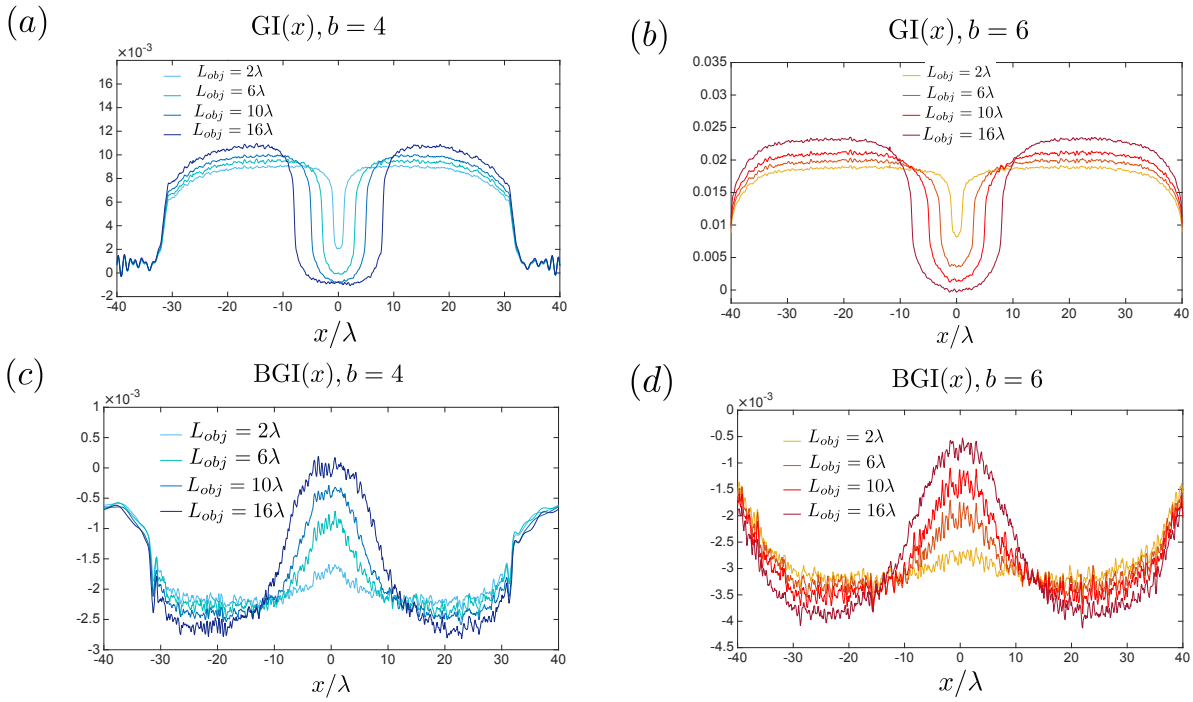


**Figure VI.7** – GI images of four different objects of increasing size hidden behind two diluted ($k_0\ell = 10$) scattering media of optical thicknesses $b = 4$ [panel (a)] and $b = 6$ [panel (b)]. BGI images of four different objects of increasing size hidden behind two two diluted ($k_0\ell = 10$) scattering media of optical thicknesses $b = 4$ [panel (c)] and $b = 6$ [panel (d)]. The number of disorder realizations used is $N = 10^6$.

## VI.3 What could be improved?

Finally let us discuss a few points which could motivate further studies.

- The use of a numerical object allowed us to simplify the proof of concept of BGI, but it hides numerous complex questions on conceptual and numerical aspects. A full study of BGI versus the parameters of a real object (its distance from the slab, its thickness, its permittivity) is needed.
- It would probably be interesting to adapt the clever algorithm given in [104] to the special case of BGI in order to increase the SNR. We should keep in mind that in 3D, the intensity correlation in R/T is lower than in 2D, thus the SNR will be lower.
- 3D numerical simulations are required in order to have an order of magnitude of the number of disorder realizations needed to experimentally observe an object with sufficient contrast using the BGI modality.
- Note that in this section we did not remove the average fields in the intensity for practical purpose. Removing them would allow us to reduce the optical thicknesses without producing some oscillating terms in the correlation function in R/T.

With this short chapter, we end the first part of this thesis devoted to the study of the intensity correlation function in R/T. The use of this novel correlation in this very practical application of imaging an object behind a scattering medium is encouraging and justifies by itself the need for a better understanding of this phenomenon.

# Part II

# Joint-statistics and mutual information

# Chapter VII

# Introduction

## Table des matières

In the first part of this thesis we have studied in detail the existence and the shape of the correlation function between reflection and transmission when the parameters of the physical system change. In the diffusive regime, we have shown that a negative and long range correlation survives. Its amplitude scales as $1/(k_0 L)$ in 2D and $1/(k_0 L)^2$ in 3D. Based on the existence of this correlation imaging methods could be developed, such as ghost imaging with the CCD camera collecting a signal in reflection from the scattering medium.

## VII.1 Need for a more detailed analysis of the joint-statistics in R/T

The amplitude of the correlation function is weak in the diffusive regime, and we may conclude from this statement that this correlation cannot be used in practice. Nonetheless it may be possible, due to complexity of scattering medium, to increase "information" between R/T simply by considering more than one speckle spot on each side of the sample. Indeed we know that the information between two sets of random variables is linked to statistical dependence between them. Let $X$ and $Y$ be two random variables. The definition of statistical dependence between $X$ and $Y$ is that $P(X,Y) \neq P(X)\,P(Y)$. In Fig. VII.1 we represent two joint distributions $P_1(X,Y)$ and $P_2(X,Y)$. In the case of $P_1$, $X$ and $Y$ are independent random variables and $P_1(X,Y) = P_1(X)P_1(Y)$. This can easily be observed in panel (c) in Fig. VII.1 where we compare the distribution of $X$ knowing that $Y$ equals 0.1, 1 and 2 and observe no difference between the three curves. This is in contrast with $P_2$ for which $X$ and $Y$ are two dependent random variables. This is easily observed in panel (d) in Fig. VII.1 in which we compare the distribution of $X$ knowing that $Y$ equals 0.1, 1 and 2 and observe a substantial difference between the three curves.

This statistical dependence can result from the correlation between the two random variables (second order moment), but it can also result from higher joint moments of $X$ and $Y$. In our case, the existence of a non zero correlation between reflection and transmission proves the existence of a statistical dependence between reflection and transmission, but it is not a direct measure of this dependence. The quantity we need to calculate in order to be able to fully describe the statistical dependency is the joint distribution between the random variables. In our case it would be useful to derive $P(\mathcal{R},\mathcal{T})$ with $\mathcal{R} = (\widetilde{\mathcal{I}}_{R_1},...,\widetilde{\mathcal{I}}_{R_m})$ and $\mathcal{T} = (\widetilde{\mathcal{I}}_{T_1}...,\widetilde{\mathcal{I}}_{T_n})$. This is the purpose of chap. VIII in which we obtain the joint distribution $P(\mathcal{R},\mathcal{T})$ using diagrammatic techniques.

## VII.2 Mutual information

In order to quantitatively study the statistical dependence between $\mathcal{R} = (\widetilde{\mathcal{I}}_{R_1},...,\widetilde{\mathcal{I}}_{R_m})$ and $\mathcal{T} = (\widetilde{\mathcal{I}}_{T_1}...,\widetilde{\mathcal{I}}_{T_n})$ we introduce a quantity referred as mutual information (MI) [105]. The MI is built from another function of the probability density function called *entropy*. The entropy of a continuous

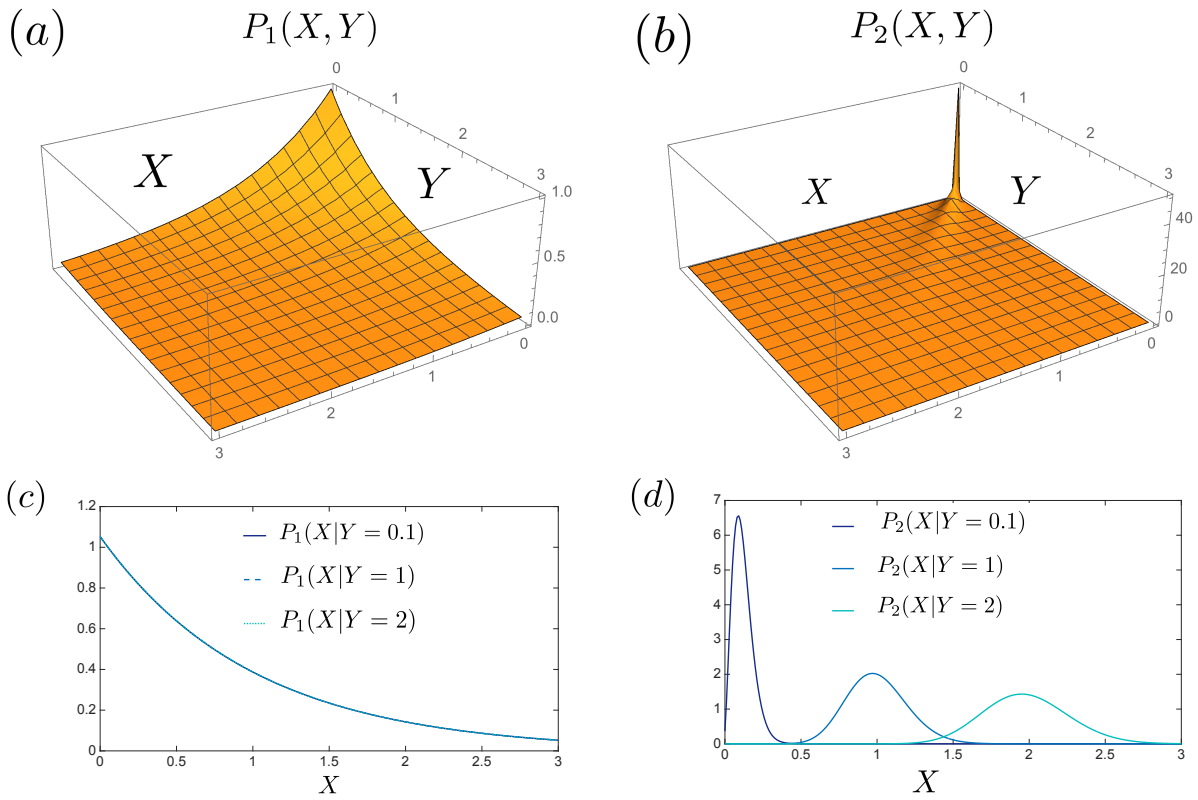


**Figure VII.1** – Representation of the joint probability $P_1$ (respectively $P_2$) between two independent (respectively dependent) random variables $X$ and $Y$ in panel (a) [respectively in panel (b)]. In panels (c,d) we plot the conditional statistics of $X$ knowing that $Y$ equals 0.1, 1 and 2.

random variable $X$, denoted $\mathcal{H}(X)$, is defined by

$$\mathcal{H}(X) = \frac{-1}{\log(2)} \int P(X) \log\left[P(X)\right] \mathrm{d}X. \tag{VII.1}$$

It is always positive and is commonly accepted as a measure of the diversity of the possible results of a random variable. For instance, if a random variable is defined on a finite range $[a, b]$, then the probability density function maximizing the entropy is $P(X) = 1/(b-a)$. Indeed, in this case the probability is uniformly distributed and the diversity of the results is maximum. As soon as we confine the probability of $X$ in certain region of $[a, b]$ we decrease the entropy because we increase the *a priori* knowledge of the result of $X$.

The MI between $\mathcal{R}$ and $\mathcal{T}$ is defined the following way:

$$\mathrm{MI}(\mathcal{R}, \mathcal{T}) = \frac{1}{\log(2)} \int P(\mathcal{R}, \mathcal{T}) \log\left[\frac{P(\mathcal{R}, \mathcal{T})}{P(\mathcal{R})\, P(\mathcal{T})}\right] \mathrm{d}\mathcal{R}\mathrm{d}\mathcal{T}. \tag{VII.2}$$

Let us here give two complementary interpretations of the MI:

- $\mathrm{MI}(\mathcal{R}, \mathcal{T}) = \mathcal{H}(\mathcal{R}) + \mathcal{H}(\mathcal{T}) - \mathcal{H}(\mathcal{R}, \mathcal{T}) = \mathcal{H}(\mathcal{T}) - \mathcal{H}(\mathcal{T}|\mathcal{R})$ measures the reduction in the uncertainty of $\mathcal{T}$ (respectively $\mathcal{R}$) due to the knowledge of $\mathcal{R}$ (respectively $\mathcal{T}$) [105].
- $\mathrm{MI}(\mathcal{R}, \mathcal{T})$ is the Kullback Leibler distance between $P(\mathcal{R}, \mathcal{T})$ and $P(\mathcal{R})\, P(\mathcal{T})$. It can be understood as a distance between the joint distribution and the product of the marginal probability density functions, thus as a distance from independence [105].

We can also discuss some mathematical properties of MI that will be useful in the following:

- $\mathrm{MI}(\mathcal{R},\mathcal{T}) \geq 0$ and is zero if and only if $\mathcal{R}$ and $\mathcal{T}$ are independent. This is a consequence of the intuitive inequality $\mathcal{H}(\mathcal{T}) \geq \mathcal{H}(\mathcal{T}|\mathcal{R})$ stating that the knowledge of a random variable can only reduce the uncertainty about another random variable.
- $\mathrm{MI}(\mathcal{R},\mathcal{T}) = \mathrm{MI}(f[\mathcal{R}], g[\mathcal{T}])$ with $f$ and $g$ two homeomorphisms. We will use this property to transform the numerical data in order to simplify the numerical estimation of MI.

In Chap. IX we study numerically and analytically $\mathrm{MI}(\mathcal{R},\mathcal{T})$ versus the number of points considered in reflection and transmission, their transverse distances, and the parameters of the system.

## VII.3 Conditional statistics

Another property, related to the statistical dependence between $X$ and $Y$, is the difference between the conditional statistics $P(X|Y \in \mathcal{V})$ ($\mathcal{V}$ is a sub-ensemble of the ensemble of definition of $Y$) and the marginal statistics $P(X)$ [106]. This is illustrated in panel (d) in Fig. VII.1 where we can observe changes in the conditional statistics when the knowledge of the second random variable changes. In Chap. X, we pay special interest to the first moment of the conditional statistics of the transmitted intensity (conditional average value of $\widetilde{\mathcal{I}}_{\mathcal{T}}$) that could be a good observable to describe wavefront shaping experiments as that in ref. [107]. In this work, the authors focused the light in a well defined area in transmission of the sample, and observed a simultaneous decrease of the light in front of this area in reflection. In chap. X we study in detail the conditional average value of the transmitted intensity and show that whatever the parameters of the system, one can modify quantitatively the transmitted intensity at one given position only using reflected information.

# Chapter VIII

# Joint-statistics between reflected and transmitted speckle patterns

## Table des matières

In previous chapter we have discussed information theory and its building block: probability density functions. We observed that to use all the tools defined in information theory, we need to obtain first the analytical expressions of the probability density functions. We thus intent to derive the joint statistics between an arbitrary number of intensities measured in reflection and transmission. From the previous chapter we know that a correlation in R/T appears due to crossing of trajectories between reflected and transmitted diffuse light. Here we study the effects of the non gaussian correlation on the joint-statistics of an arbitrary number of speckle spots for diluted samples ($k_0\ell \gg 1$). We build the joint statistics taking into account one possibility of crossing between intensities. This crossing can occur between transmitted intensities, reflected intensities, or between one reflected intensity and one transmitted intensity creating correlations between pairs of intensities.

The main steps are the following:

- First we derive analytical expression of the probability density function of one intensity taking into account connected four-field correlations.
- Then we derive the joint-statistics between one reflected intensity and one transmitted intensity in the diffusive regime taking into account connected four-field correlations.
- Eventually we derive the joint-statistics between an arbitrary number of intensities in reflection and in transmission taking into account connected four-field correlations. The derivation is performed assuming that the $C_1$ correlation is negligible between all pairs of intensities[1]. This corresponds to $d^{TT}_{i,i+1} \gg \lambda$ and $d^{RR}_{i,i+1} \gg \lambda$ in Fig. VIII.1.

Even if the results presented here may be more general, we focus on the diffusive regime with $b \gg 1$ and $k_0\ell \gg 1$. Assuming the optical thickness to be larger than one allows us to restrict the non gaussian correlation to its $C_2$ component.

To derive the various statistics we follow the ideas developed in previous studies published in the 90's. It was shown at the time that the statistics of the intensity scattered by the medium is strongly dependent on the gaussian character of the field [28] and carries information about long range correlations in the sample [108, 109]. These works were inspired by ref. [110] in which the approach relied on path integral techniques. In this chapter we follow the reasoning in ref. [111] in which a clear diagrammatic expansion of the statistics in terms of various connected moments of the intensity is given. Since it is a perturbative approach, the higher the order of the connected moment, the more complex the analytical expression of the statistics. Using RMT we can obtain a more complete expression of the statistics [112, 113], nonetheless it looses its physical interpretation in terms of number of crossings of trajectories inside the medium. The interested reader can find details about the first measurements of the statistics of the intensity, and its dependance on the non gaussian character of the field in refs. [35, 114, 115]. Note that all these works deal with statistics of the intensity at one given position, or with the statistics of the integrated transmitted intensity, while we are interested in joint statistics between intensities.

[1] In other words we study the joint statistics between different speckle spots.

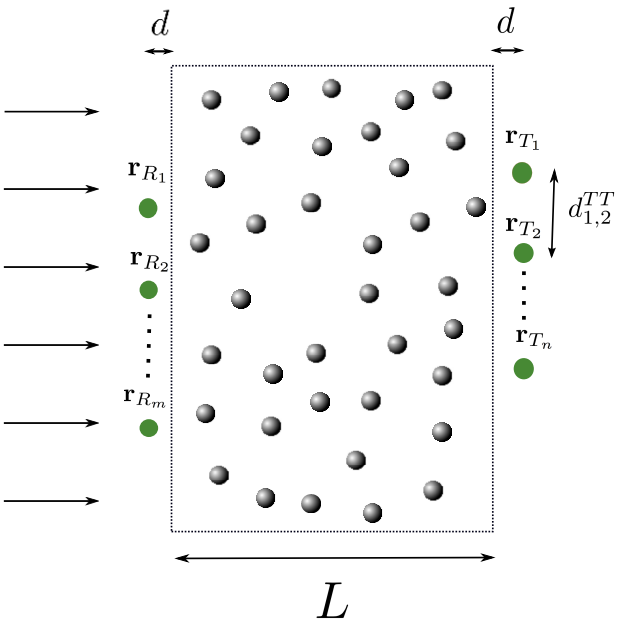


**Figure VIII.1** – Scheme of the system studied. A plane wave at normal incidence illuminates a 2D disordered sample of depth $L$. The field is measured in transmission and reflection at various positions $\mathbf{r}_{T_i}$ and $\mathbf{r}_{R_j}$. The planes of measurement are at a distance $d$ from the sample surfaces. The transverse distance between $\mathbf{r}_{T_i}$ and $\mathbf{r}_{T_j}$ is denoted by $d_{i,j}^{TT}$, between $\mathbf{r}_{R_i}$ and $\mathbf{r}_{R_j}$ it is denoted by $d_{i,j}^{RR}$, and between $\mathbf{r}_{T_i}$ and $\mathbf{r}_{R_j}$ it is denoted by $d_{i,j}^{RT}$.

## VIII.1 Statistics of the intensity

The aim of this section is to derive the statistics of the transmitted or reflected intensity of the fluctuating fields ($\delta E = E - \langle E \rangle$). To do so we need to derive the expression of all the moments of $\widetilde{I}$. Indeed, we can access the full statistics of $\widetilde{I}$ using

$$P(\widetilde{I}) = \frac{1}{2\pi} \int \sum_{N=0}^{\infty} \frac{(ik)^N}{N!} \langle \widetilde{I}^N \rangle \exp(-ik\widetilde{I}) \mathrm{d}k. \tag{VIII.1}$$

We can thus observe the impact of non gaussian correlations in the model on the statistics of the intensity at one given position.

### VIII.1.1 Rayleigh law

Let us start by deriving the Rayleigh law (statistics of the intensity of the fluctuating field in the gaussian approximation). The reasoning leading to the expression of the moments of the Rayleigh law is the following:

- The average value of the field is zero, thus the only non zero moments of the fields are moments of the intensity.
- The moment of order $N$ of the intensity is equal to $\langle \widetilde{I}^N \rangle = N! \langle \widetilde{I} \rangle^N$. The full statistics is thus built with $\langle \widetilde{I} \rangle$ as a single parameter.

The $N!$ term is a combinatory factor coming from the fact that each field in the ensemble $\{\delta E_1, ...., \delta E_N\}$ can be paired with a complex conjugate in the ensemble $\{\delta E_1^*, ...., \delta E_N^*\}$ (see ref. [28]). The first field

has $N$ possibilities for his pairing, the second $N-1$, etc. Two different pairing possibilities are represented in Fig. II.8.

Inserting $\langle \widetilde{I}^N \rangle = N! \langle \widetilde{I} \rangle^N$ into Eq. (VIII.1) we obtain the Rayleigh law

$$P_{Ray}(\widetilde{I}) = \frac{1}{2\pi} \int \sum_N (ik \langle \widetilde{I} \rangle)^N \exp(-ik\widetilde{I}) \mathrm{d}k = \frac{1}{2\pi} \int \frac{\exp(-ik\widetilde{I})}{1 - ik\langle \widetilde{I} \rangle} \mathrm{d}k \qquad \text{(VIII.2)}$$
$$= \frac{1}{\langle \widetilde{I} \rangle} \exp(-\widetilde{I}/\langle \widetilde{I} \rangle).$$

Normalizing the intensity by its average value we obtain the normalized version of the Rayleigh law:

$$P_{Ray}(\widetilde{\mathcal{I}}) = \exp(-\widetilde{\mathcal{I}}). \qquad \text{(VIII.3)}$$

### VIII.1.2 Statistics of the intensity beyond the Rayleigh law

In this subsection we intend to derive the statistics of the intensity (either in reflection or in reflection) taking into account the connected fourth-order moment of the field.

#### Second-order moment of $\widetilde{I}$

We know that the first correction to the gaussian character of the field arise in the $\widetilde{I}$-$\widetilde{I}$ correlation (fourth-order moment of the field):

$$\langle \widetilde{I}^2 \rangle = 2\langle \widetilde{I} \rangle^2 + \langle \delta E \delta E^* \delta E \delta E^* \rangle_c. \qquad \text{(VIII.4)}$$

We represent the decomposition in Eq. (VIII.4) in Fig. VIII.2. Panels (a) and (b) together give the $2\langle \widetilde{I} \rangle^2$ contribution to the second order moment of $\widetilde{I}$. Note that panel (b) is in reality the square of the field-field correlation evaluated at one given position. It is thus non distinguishable from the square of the average intensity. In the diffusive regime in T/T we know that the non gaussian correlation has two dominant contributions represented in panels (c) and (d) in Fig. VIII.2. Evaluated at one given position, these two contributions are non distinguishable. We thus merge them into one single quantity called $\langle \widetilde{I}^2 \rangle_{C_2} = \langle \delta E \delta E^* \delta E \delta E^* \rangle_{C_2}$. We define this new notation because we need a more compact form in this chapter to discuss the non gaussian intensity correlation.

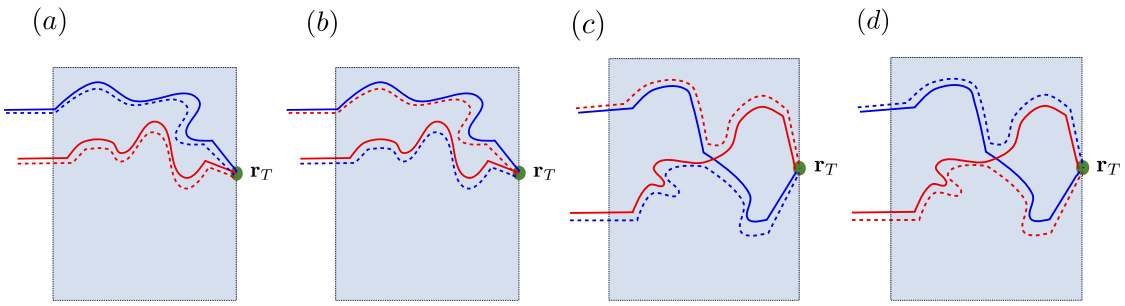


**Figure VIII.2** – Diagrammatic representation of Eq. (VIII.4). Panels (a) and (b) give a contribution of $2\langle \widetilde{I} \rangle^2$ to the second order moment of the intensity while panels (c) and (d) give the contribution $\langle \widetilde{I}^2 \rangle_{C_2}$.

Equation (VIII.4) can be rewritten in the diffusive regime the following way:

$$\langle \widetilde{I}^2 \rangle = 2\langle \widetilde{I} \rangle^2 + \langle \widetilde{I}^2 \rangle_{C_2} \qquad \text{(VIII.5)}$$

keeping in mind that $\langle \widetilde{I}^2 \rangle_{C_2}$ contains two different diagrams.

### Arbitrary moment of $\widetilde{I}$. The example of the transmission geometry

We intend here to build the moment of order $N$ of $\widetilde{I}$ taking into account the first correction due to the non gaussian character of the field, exactly as we did for the second order moment of $\widetilde{I}$. The idea is to correct the moment of order $N$ with one (and only one) crossing of two trajectories. We derive here the various moments of $\widetilde{I}_T$ keeping in mind that the discussion is also valid for $\widetilde{I}_R$ .

We already know the dominant term in the moment of order $N$. It results from the disconnected propagation of $N$ ladder diagrams with a combinatory factor of $N!$. This term reads

$$\langle \widetilde{I_T}^N \rangle_{Ray} = N! \langle \widetilde{I_T} \rangle^N. \tag{VIII.6}$$

The first correction is the disconnected propagation of $N-2$ ladder diagrams together with the connected propagation of two intensities. The disconnected part of the correction is multiplied by a $(N-2)!$ factor and its connected part is weighted by a $\binom{N}{2}^2$. This results from the choice of two fields in the ensemble $\{\delta E_{T_1}, ...., \delta E_{T_N}\}$ to be paired with two complex conjugate in the ensemble $\left\{\delta E^*_{T_1}, ...., \delta E^*_{T_N}\right\}$. This term reads

$$\langle \widetilde{I_T}^N \rangle_{TT} = (N-2)! \binom{N}{2}^2 \langle \widetilde{I_T}^2 \rangle_{C_2} \langle \widetilde{I_T} \rangle^{N-2} = N! \frac{N(N-1)}{4} \langle \widetilde{I_T}^2 \rangle_{C_2} \langle \widetilde{I_T} \rangle^{N-2}. \tag{VIII.7}$$

The subscript $(...)_{TT}$ specifies that the moment contains one crossing between two transmitted intensities.

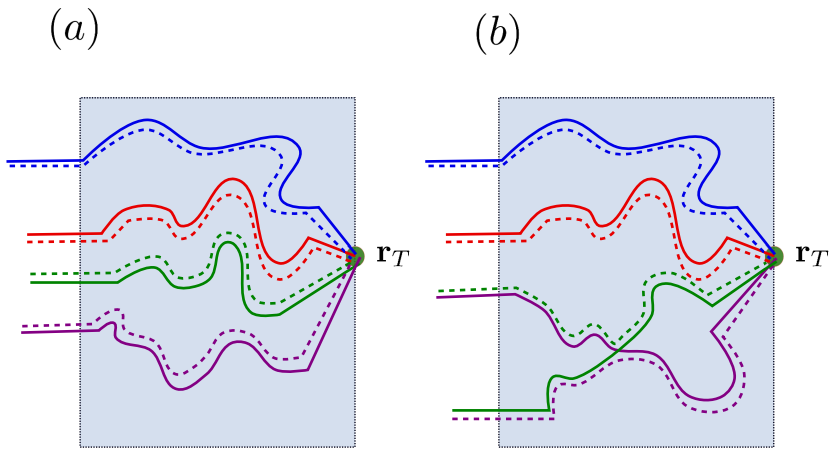


**Figure VIII.3** – Two typical diagrams for the two components of the 4th order moment of the transmitted intensity. Panel (a) corresponds to the disconnected propagation of 4 ladder diagrams. Panel (b) corresponds to the disconnected propagation of two ladder diagrams and the connected propagation of two intensities.

Diagrammatically, we represent these two terms in Fig. VIII.3. Panel (a) corresponds to one of the $N!$ disconnected scattering sequences while panel (b) corresponds to one of the $N!N(N-1)/4$ connected scattering sequences. The expression of the $N$th order moment of the intensity can be

written as the sum of the two contributions:

$$\begin{aligned}\langle \widetilde{I_T}^N \rangle &= \langle \widetilde{I_T}^N \rangle_{Ray} + \langle \widetilde{I_T}^N \rangle_{TT} \\ &= N! \langle \widetilde{I_T} \rangle^N \left( 1 + \frac{N(N-1)}{4} C_2^{TT} \right)\end{aligned} \tag{VIII.8}$$

with $C_2^{TT} = \langle \widetilde{I_T}^2 \rangle_{C_2} / \langle \widetilde{I_T} \rangle^2$.

### Derivation of $P(\widetilde{\mathcal{I}})$. The case of transmission geometry

Knowing the different moments of $\widetilde{I}$, we can access the statistics of $P(\widetilde{I})$ inserting Eq. (VIII.8) into Eq. (VIII.1). Let us derive the expression of $P(\widetilde{I}_T)$:

$$P(\widetilde{I}_T) = \frac{1}{2\pi} \int \sum_N (ik \langle \widetilde{I}_T \rangle)^N \left( 1 + \frac{N(N-1)}{4} C_2^{TT} \right) \exp(-ik\widetilde{I}_T) \mathrm{d}k = P_{Ray}(\widetilde{I}_T) + P_{TT}(\widetilde{I}_T) \tag{VIII.9}$$

Let us calculate $P_{TT}(\widetilde{I}_T)$. To proceed, let us first deal with the expression of the sum over $N$

$$\begin{aligned}\sum_N (ik \langle \widetilde{I}_T \rangle)^N \left( \frac{N(N-1)}{4} C_2^{TT} \right) &= (ik \langle \widetilde{I}_T \rangle)^2 \frac{C_2^{TT}}{4} \sum_N (ik \langle \widetilde{I}_T \rangle)^N (N+2)(N+1) \\ &= (ik \langle \widetilde{I}_T \rangle)^2 \frac{C_2^{TT}}{4} \frac{\partial^2}{\partial^2 [ik \langle \widetilde{I}_T \rangle]} \frac{1}{1 - ik \langle \widetilde{I}_T \rangle} \\ &= \frac{C_2^{TT}}{4} \frac{-2(ik \langle \widetilde{I}_T \rangle)^2}{\left(1 - ik \langle \widetilde{I}_T \rangle\right)^3}\end{aligned} \tag{VIII.10}$$

and use the residue theorem:

$$\begin{aligned}P_{TT}(\widetilde{I}_T) &= \frac{C_2^{TT}}{4(2\pi)} \int \frac{-2(ik \langle \widetilde{I}_T \rangle)^2}{\left(1 - ik \langle \widetilde{I}_T \rangle\right)^3} \exp(-ik\widetilde{I}_T) \mathrm{d}k \\ &= \frac{C_2^{TT}}{4(2\pi) i \langle \widetilde{I}_T \rangle} \int \frac{2k^2}{\left(k + i/\langle \widetilde{I}_T \rangle\right)^3} \exp(-ik\widetilde{I}_T) \mathrm{d}k \\ &= \frac{C_2^{TT}}{8 \langle \widetilde{I}_T \rangle} \lim_{k \to i/\langle \widetilde{I}_T \rangle} \frac{\partial^2}{\partial^2 k} \left( 2k^2 \exp(-ik\widetilde{I}_T) \right) \\ &= \frac{C_2^{TT}}{4 \langle \widetilde{I}_T \rangle} \exp\left( -\frac{\widetilde{I}_T}{\langle \widetilde{I}_T \rangle} \right) \left( \frac{\widetilde{I}_T^2}{\langle \widetilde{I}_T \rangle^2} - 4 \frac{\widetilde{I}_T}{\langle \widetilde{I}_T \rangle} + 2 \right).\end{aligned} \tag{VIII.11}$$

The complete probability density function thus reads

$$P(\widetilde{I}_T) = P_{Ray}(\widetilde{I}_T) \left( 1 + \frac{C_2^{TT}}{4} \left[ \frac{\widetilde{I}_T^2}{\langle \widetilde{I}_T \rangle^2} - 4 \frac{\widetilde{I}_T}{\langle \widetilde{I}_T \rangle} + 2 \right] \right) \tag{VIII.12}$$

which gives after normalization

$$P(\widetilde{\mathcal{I}_T}) = \exp\left( -\widetilde{\mathcal{I}_T} \right) \left( 1 + \frac{C_2^{TT}}{4} \left[ \widetilde{\mathcal{I}_T}^2 - 4\widetilde{\mathcal{I}_T} + 2 \right] \right). \tag{VIII.13}$$

We recognize in Eq. (VIII.12) the expression given in ref. [109]. Taking into account the first correction to the gaussian character of the field modifies the Rayleigh law by a polynomial function weighted by the non gaussian correlation function. It is important to stress that Eq. (VIII.13) is also valid in reflection in the diffusive regime. It reads:

$$P(\widetilde{\mathcal{I}_R}) = \exp\left(-\widetilde{\mathcal{I}_R}\right)\left(1 + \frac{C_2^{RR}}{4}\left[\widetilde{\mathcal{I}_R}^2 - 4\widetilde{\mathcal{I}_R} + 2\right]\right). \tag{VIII.14}$$

## Analysis of $P(\widetilde{\mathcal{I}})$

In this subsection we give the basic properties of Eq. (VIII.13). As every probability density function, $P(\widetilde{\mathcal{I}})$ is normalized:

$$\int P(\widetilde{\mathcal{I}})\mathrm{d}\widetilde{\mathcal{I}} = 1. \tag{VIII.15}$$

Let us also note that

$$P(\widetilde{\mathcal{I}} = 0) = 1 + \frac{C_2}{2}, \tag{VIII.16}$$

a property observed numerically.

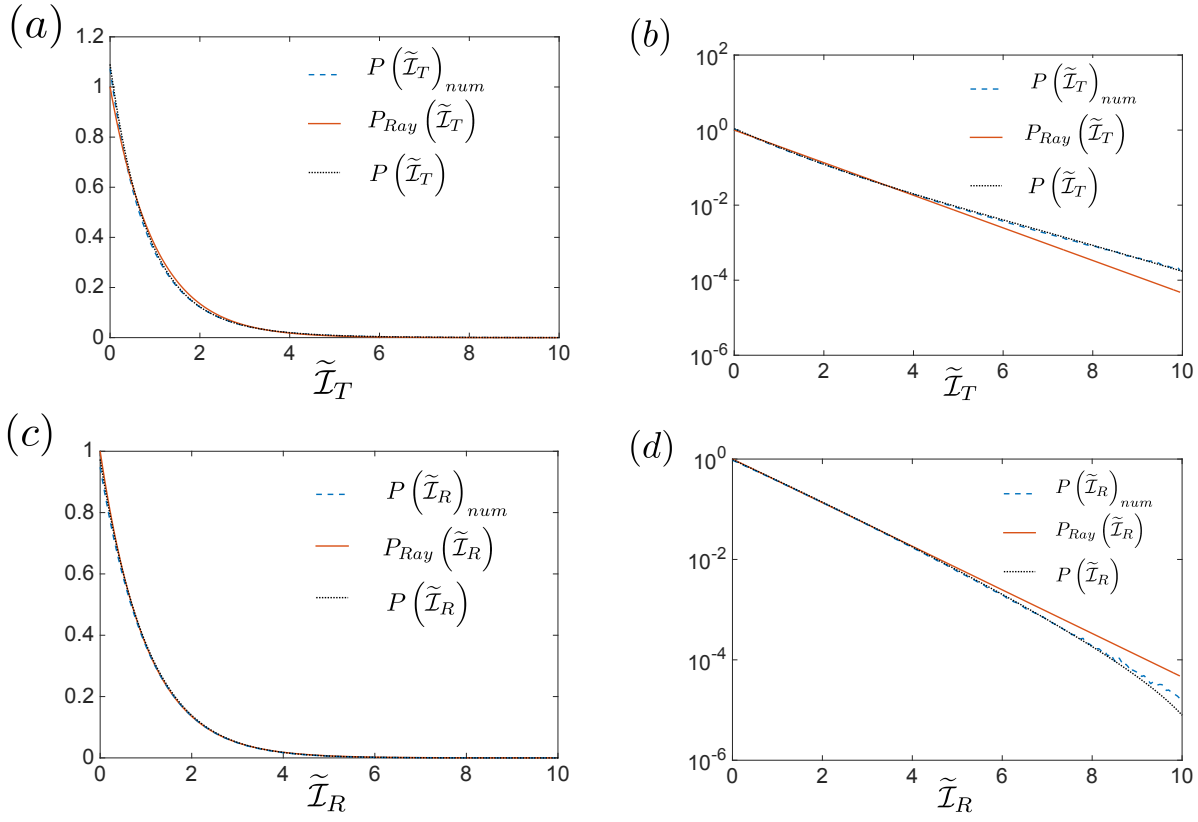


**Figure VIII.4** – Numerical calculation of the statistics of $\widetilde{\mathcal{I}_T}$ in linear [panel (a)] and log scale [panel (b)] and of $\widetilde{\mathcal{I}_R}$ in linear [panel (c)] and log scale [panel (d)] for a thick ($b = 8$) and dilute ($k_0\ell = 10$) sample. Each curve is compared to Eq. (VIII.3) (red solid line) and Eq. (VIII.13) (black dotted line). The points where intensities are calculated are at a distance $d = 2\lambda$ of the scattering sample (see Fig. VIII.1).

In Fig. VIII.4 we plot the numerically calculated statistics of $\widetilde{\mathcal{I}_T}$ and the statistics of $\widetilde{\mathcal{I}_R}$ in for a thick ($b = 8$) and dilute ($k_0\ell = 10$) sample. Each curve is compared to Eq. (VIII.3) and Eq. (VIII.13).

We observe an almost perfect agreement between numerics and Eq. (VIII.13) in both reflection and transmission.

To conclude this subsection, non gaussian correlations can be taken into account into the statistics of the intensity. It modifies the Rayleigh law with a polynomial function weighted by the non gaussian correlation. Eq. (VIII.13) has been used in transmission to study the strength of the disorder ($k_0\ell$) in various samples [115]. Indeed, in transmission of a 2D scattering sample the strength of the correction scales as $C_2 \propto 1/(k_0\ell)$ which is small in the diffusive regime, and increases when $k_0\ell$ decreases.

## VIII.2 Joint-statistics of one-point transmitted and reflected intensities

In this section we study the joint-statistics between $\widetilde{\mathcal{I}}_R$ and $\widetilde{\mathcal{I}}_T$. We follow the reasoning in the previous section for the statistics of one intensity. We derive the moments of the joint distribution between $\widetilde{\mathcal{I}}_R$ and $\widetilde{\mathcal{I}}_T$ with well defined assumptions, and insert them into

$$P(\widetilde{I}_R, \widetilde{I}_T) = \frac{1}{(2\pi)^2} \int \sum_{N,M=0}^{\infty} \frac{(ik_T)^N}{N!} \frac{(ik_R)^M}{M!} \langle \widetilde{I}_T^N \widetilde{I}_R^M \rangle \exp(-ik_T \widetilde{I}_T) \exp(-ik_R \widetilde{I}_R) \mathrm{d}k_T \mathrm{d}k_R. \tag{VIII.17}$$

We start by considering only disconnected ladder diagrams to build the moments of the joint distribution between $\widetilde{\mathcal{I}}_R$ and $\widetilde{\mathcal{I}}_T$. We observe that this model leads to statistical independence between one reflected intensity and on transmitted intensity. Eventually we build the joint-statistics using the first correction to the gaussian character to its moments. We observe that under this assumption the reflected and the transmitted intensity are statistically dependent, due to non gaussian correlations in R/T.

### VIII.2.1 The joint Rayleigh law in R/T

In this section we quickly derive the joint statistics $P(\widetilde{\mathcal{I}}_R, \widetilde{\mathcal{I}}_T)$ in the gaussian approximation in the diffusive regime. The gaussian correlation between reflection and transmission is exponentially small in this regime as observed in Chap. III, and we will neglect it. Thus the joint moment arises from the disconnected propagation of $N$ transmitted ladder diagrams with a combinatory factor $N!$ and $M$ reflected ladder diagrams with a combinatory factor of $M!$. It reads

$$\langle \widetilde{I}_T^N \widetilde{I}_R^M \rangle_{Ray} = N! M! \langle \widetilde{I}_R \rangle^M \langle \widetilde{I}_T \rangle^N. \tag{VIII.18}$$

Inserting this expression into Eq. (VIII.17), we obtain the joint distribution between $\widetilde{I}_R$ and $\widetilde{I}_T$ in the gaussian approximation:

$$P_{Ray}(\widetilde{I}_R, \widetilde{I}_T) = \frac{1}{\langle \widetilde{I}_R \rangle} \exp\left(-\frac{\widetilde{I}_R}{\langle \widetilde{I}_R \rangle}\right) \frac{1}{\langle \widetilde{I}_T \rangle} \exp\left(-\frac{\widetilde{I}_T}{\langle \widetilde{I}_T \rangle}\right) = P_{Ray}(\widetilde{I}_R) P_{Ray}(\widetilde{I}_T). \tag{VIII.19}$$

In the gaussian approximation, $\widetilde{I}_T$ and $\widetilde{I}_R$ are independent random variables. Measuring one of them gives no information about the other.

### VIII.2.2 Joint statistics between $\widetilde{I}_T$ and $\widetilde{I}_R$ taking into account non gaussian correlations

In this subsection we intend to derive the joint statistics between $\widetilde{I}_T$ and $\widetilde{I}_R$ taking into account the first correction due to non gaussian correlations. We already know the dominant term in the moment of order $(N, M)$. It is given in Eq. (VIII.18) and comes from the disconnected propagation of the intensities. One of these diagrams for the moment $(2, 2)$ is represented in panel (a) in Fig. VIII.5.

The first correction in terms of number of crossing of trajectories comes from three different contributions:

- One crossing between two transmitted intensities together with $(N-2)$ transmitted ladder diagrams and $M$ reflected ladder diagrams. This term gives a contribution $\langle \widetilde{I}_T^N \widetilde{I}_R^M \rangle_{TT} = N!M!N(N-1)/4 \langle \widetilde{I}_R \rangle^M \langle \widetilde{I}_T \rangle^{N-2} \langle \widetilde{I}_T^2 \rangle_{C_2}$ to the $(N, M)$ moment. One of these diagrams for the moment $(2, 2)$ is represented in panel (b) in Fig. VIII.5.

- One crossing between two reflected intensities together with $N$ transmitted ladder diagrams and $(M-2)$ reflected ladder diagrams. This term gives a contribution $\langle \widetilde{I}_T^N \widetilde{I}_R^M \rangle_{RR} = M!N!M(M-1)/4 \langle \widetilde{I}_R \rangle^{M-2} \langle \widetilde{I}_T \rangle^N \langle \widetilde{I}_R^2 \rangle_{C_2}$ to the $(N, M)$ moment. One of these diagrams for the moment $(2, 2)$is represented in panel (c) in Fig. VIII.5.

- One crossing between one reflected and one transmitted intensities together with $(N-1)$ transmitted ladder diagrams and $(M-1)$ reflected ladder diagrams. This term gives a contribution $\langle \widetilde{I}_T^N \widetilde{I}_R^M \rangle_{RT} = N!M!NM \langle \widetilde{I}_R \rangle^{M-1} \langle \widetilde{I}_T \rangle^{N-1} \langle \widetilde{I}_T \widetilde{I}_R \rangle_{C_2}$ to the $(N, M)$ moment. One of these diagrams for the moment $(2, 2)$ is represented in panel (d) in Fig. VIII.5.

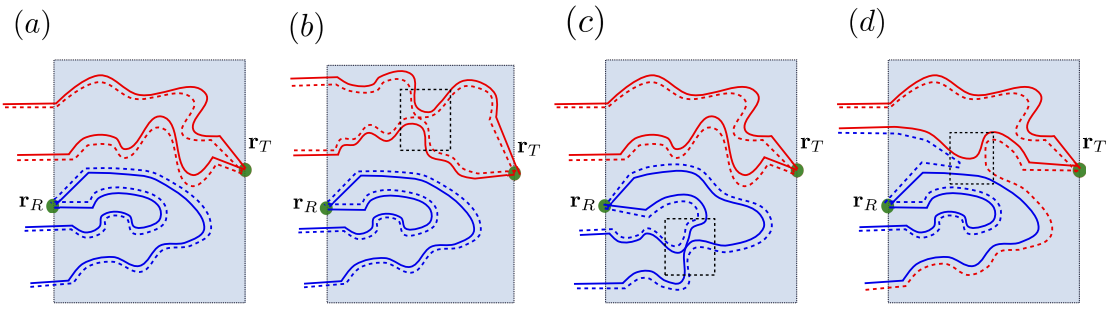


**Figure VIII.5** – Four typical diagrams for the four components of the $(2, 2)$ joint moment of the transmitted and the reflected intensity. Panel (a) corresponds to the disconnected propagation of 2 ladder diagrams in reflection and 2 ladder diagrams in transmission. Panel (b) corresponds to the disconnected propagation of two ladder diagrams in reflection and the connected propagation of two intensities in transmission. Panel (c) corresponds to the disconnected propagation of two ladder diagrams in transmission and the connected propagation of two intensities in reflection. Panel (d) corresponds to the disconnected propagation of one ladder diagram in reflection, one ladder diagram in transmission and the connected propagation of one reflected and one transmitted intensities. The crossings of trajectories are highlighted with black boxes in panels (b,c,d).

Taking into account these four contributions we obtain the following expression for the $(N, M)$

moment:

$$\begin{aligned}\langle \widetilde{I}_T^N \widetilde{I}_R^M \rangle &= \overbrace{\langle \widetilde{I}_T^N \widetilde{I}_R^M \rangle_{Ray} + \langle \widetilde{I}_T^N \widetilde{I}_R^M \rangle_{TT} + \langle \widetilde{I}_T^N \widetilde{I}_R^M \rangle_{RR}}^{\langle \widetilde{I}_T^N \widetilde{I}_R^M \rangle_S} + \langle \widetilde{I}_T^N \widetilde{I}_R^M \rangle_{RT} \\ &= N!M!\langle \widetilde{I}_R \rangle^M \langle \widetilde{I}_T \rangle^N \left(1 + \frac{N(N-1)C_2^{TT}}{4} + \frac{M(M-1)C_2^{RR}}{4} + NMC_2^{RT}\right)\end{aligned} \tag{VIII.20}$$

with

$$\begin{cases} C_2^{TT} = \dfrac{\langle \widetilde{I}_T^2 \rangle_{C_2}}{\langle \widetilde{I}_T \rangle^2}, \\ C_2^{RR} = \dfrac{\langle \widetilde{I}_R^2 \rangle_{C_2}}{\langle \widetilde{I}_R \rangle^2}, \\ C_2^{RT} = \dfrac{\langle \widetilde{I}_R \widetilde{I}_T \rangle_{C_2}}{\langle \widetilde{I}_R \rangle \langle \widetilde{I}_T \rangle}. \end{cases} \tag{VIII.21}$$

Note that we introduce the notation $\langle \widetilde{I}_T^N \widetilde{I}_R^M \rangle_S$ for the joint moment built with non gaussian correlation in T/T and R/R (the subscript $(...)_S$ means that we consider non gaussian correlation between points on the same surface). Each term in Eq. (VIII.20) gives a contribution to $P(\widetilde{I}_R, \widetilde{I}_T)$, that can be written in the form

$$P(\widetilde{I}_R, \widetilde{I}_T) = P_{Ray}(\widetilde{I}_R, \widetilde{I}_T) + P_{TT}(\widetilde{I}_R, \widetilde{I}_T) + P_{RR}(\widetilde{I}_R, \widetilde{I}_T) + P_{RT}(\widetilde{I}_R, \widetilde{I}_T). \tag{VIII.22}$$

The only contribution not derived so far is $P_{RT}(\widetilde{I}_R, \widetilde{I}_T)$. To perform the calculation we use

$$\begin{aligned}\sum_{N=0}^{\infty} (ik\langle \widetilde{I} \rangle)^N (N) &= (ik\langle \widetilde{I} \rangle) \sum_{N=0}^{\infty} (ik\langle \widetilde{I} \rangle)^N (N+1) \\ &= (ik\langle \widetilde{I} \rangle) \frac{\partial}{\partial ik\langle \widetilde{I} \rangle} \frac{1}{1 - ik\langle \widetilde{I} \rangle} \\ &= \frac{ik\langle \widetilde{I} \rangle}{\left(1 - ik\langle \widetilde{I} \rangle\right)^2}\end{aligned} \tag{VIII.23}$$

combined with the residue theorem

$$\begin{aligned}\frac{1}{(2\pi)} \int \frac{ik\langle \widetilde{I} \rangle}{\left(1 - ik\langle \widetilde{I} \rangle\right)^2} \exp(-ik\widetilde{I}) \mathrm{d}k &= \frac{1}{(2\pi) i \langle \widetilde{I} \rangle} \int \frac{k}{\left(k + i/\langle \widetilde{I} \rangle\right)^2} \exp(-ik\widetilde{I}) \mathrm{d}k \\ &= \frac{1}{\langle \widetilde{I} \rangle} \lim_{k \to i/\langle \widetilde{I} \rangle} \frac{\partial}{\partial k} \left(k \exp(-ik\widetilde{I})\right) \\ &= \frac{1}{\langle \widetilde{I} \rangle} \exp\left(-\frac{\widetilde{I}}{\langle \widetilde{I} \rangle}\right) \left(\widetilde{I} - \langle \widetilde{I} \rangle\right).\end{aligned} \tag{VIII.24}$$

This leads to the following joint probability density function of the reflected and transmitted intensities of the fluctuating fields:

$$\begin{aligned}&P(\widetilde{I}_R, \widetilde{I}_T) = P_{Ray}(\widetilde{I}_R) P_{Ray}(\widetilde{I}_T) \\ &\times \left(1 + \frac{C_2^{TT}}{4} \left[\frac{\widetilde{I}_T^2}{\langle \widetilde{I}_T \rangle^2} - 4\frac{\widetilde{I}_T}{\langle \widetilde{I}_T \rangle} + 2\right] + \frac{C_2^{RR}}{4} \left[\frac{\widetilde{I}_R^2}{\langle \widetilde{I}_R \rangle^2} - 4\frac{\widetilde{I}_R}{\langle \widetilde{I}_R \rangle} + 2\right] + C_2^{RT} \left[\left(\frac{\widetilde{I}_T}{\langle \widetilde{I}_T \rangle} - 1\right)\left(\frac{\widetilde{I}_R}{\langle \widetilde{I}_R \rangle} - 1\right)\right]\right).\end{aligned} \tag{VIII.25}$$

The normalized version of Eq. (VIII.25) is

$$P(\widetilde{\mathcal{I}}_R,\widetilde{\mathcal{I}}_T) = \exp\left(-\widetilde{\mathcal{I}}_R\right)\exp\left(-\widetilde{\mathcal{I}}_T\right) \times\left(1+\frac{C_2^{TT}}{4}\left[\widetilde{\mathcal{I}}_T^2-4\widetilde{\mathcal{I}}_T+2\right]+\frac{C_2^{RR}}{4}\left[\widetilde{\mathcal{I}}_R^2-4\widetilde{\mathcal{I}}_R+2\right]+C_2^{RT}\left[(\widetilde{\mathcal{I}}_T-1)(\widetilde{\mathcal{I}}_R-1)\right]\right). \quad \text{(VIII.26)}$$

## Analysis of $P(\widetilde{I}_R,\widetilde{I}_T)$

The key feature of Eq. (VIII.25) is that $P(\widetilde{I}_R,\widetilde{I}_T)\neq P(\widetilde{I}_R)P(\widetilde{I}_T)$ showing that $\widetilde{I}_T$ and $\widetilde{I}_R$ are two statistically dependent random variables. The statistical dependence directly results from the non gaussian correlation in R/T. In Chap. IX we study in detail the implication of Eq. (VIII.25) in terms of Mutual Information between one reflected and one transmitted intensities, while in Chap. X we discuss its implication in terms of conditional statistics of the transmitted intensity forcing the reflected intensity to be dark or bright. In this section we support Eq. (VIII.25) using 2D numerical simulations. An easy way to compare the numerical distribution with the analytical result is to compare their moments. In Fig. VIII.6 we plot the logarithm of the ratio between the $(N,M)$ moment calculated numerically and the one resulting from three different analytical calculations versus the order of the $(N,M)$ moment.

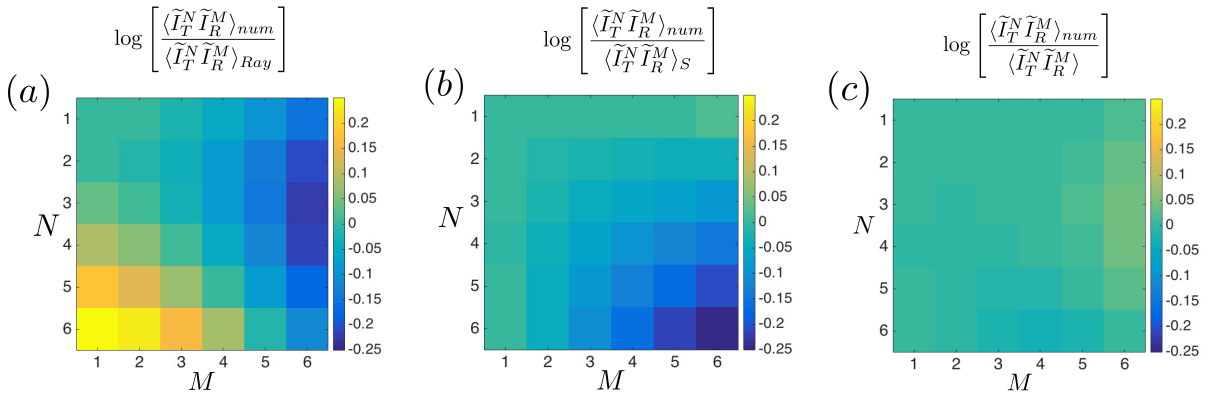


**Figure VIII.6** – Logarithm of the ratio between $\langle\widetilde{I}_T^N\widetilde{I}_R^M\rangle_{num}$ and $\langle\widetilde{I}_T^N\widetilde{I}_R^M\rangle_{Ray}$ [panel (a)], between $\langle\widetilde{I}_T^N\widetilde{I}_R^M\rangle_{num}$ and $\langle\widetilde{I}_T^N\widetilde{I}_R^M\rangle_S$ [panel (b)], and between $\langle\widetilde{I}_T^N\widetilde{I}_R^M\rangle_{num}$ and $\langle\widetilde{I}_T^N\widetilde{I}_R^M\rangle$. The calculation is done for a thick ($b=6$) and dilute ($k_0\ell=10$) sample.The points are in front one of another ($d^{RT}=0\lambda$) and are at a distance $d=2\lambda$ of the scattering sample (see Fig. VIII.1).

We observe in panel (a) in Fig. VIII.6 that $\langle\widetilde{I}_T^N\widetilde{I}_R^M\rangle_{num}$ is higher for large $N$ and lower for larger $M$ than $\langle\widetilde{I}_T^N\widetilde{I}_R^M\rangle_{Ray}$. This is due to the non gaussian correlation in T/T and R/R which are positive in transmission and negative in reflection in this regime. In panel (b) we correct the analytical model with non gaussian correlations in T/T and R/R. We see that the precision of the calculation of the moments for large $N$ or large $M$ is improved. Nonetheless, for both large $N$ and large $M$ the moment calculated numerically is lower than the moment resulting from the analytical result. In panel (c) we correct this taking into account non gaussian correlation in R/T. We believe Fig. VIII.6 is a proof of the validity of the analytical model leading to Eq. (VIII.25).

## VIII.3 Joint-statistics between $n$ transmitted speckle spots and $m$ reflected speckle spots

In this section we derive the joint statistics between $n$ speckle spots in transmission and $m$ speckle spots in reflection taking into account the first order correction to the gaussian approximation.

### VIII.3.1 Joint-statistics between two different transmitted (respectively reflected) speckle spots

In the previous section we derived the joint statistics between one reflected intensity and one transmitted intensity. To derive the joint statistics between an arbitrary number of reflected and transmitted different speckle spots, we also need to derive the joint statistics between two different speckle spots in transmission or in reflection.

First, it is important to note that considering the $C_1$ correlation in the joint statistics between many intensities is cumbersome in the diagrammatic approach. We have performed the calculation for two transmitted intensities, and obtained the same result as the known result given in Eq. (II.13). Nonetheless, we did not manage to extend this result to a useful analytical expression for the joint statistics of $N$ transmitted intensity correlated with $C_1$. In a nutshell, the issue is that we use a perturbative expansion of the moments to build the distribution taking into account non gaussian contribution. The $C_1$ correlation in T/T or R/R can be close to unity, as shown in Fig. III.9, and cannot be treated perturbatively. We handle this problem by considering points separated by distances larger than $\lambda$ (different speckle spots). Doing so, the $C_1$ correlations are small and the intensities are mainly correlated due to non gaussian correlations. In this regime, the $(N, M)$ joint moment of $P(\widetilde{I}_{T_1}, \widetilde{I}_{T_2})$ has the exact same expression as that in the R/T configuration. It reads

$$\langle \widetilde{I}_{T_1}^N \widetilde{I}_{T_2}^M \rangle = N!M! \langle \widetilde{I}_{T_1} \rangle^M \langle \widetilde{I}_{T_2} \rangle^N \left( 1 + \frac{N(N-1)C_2^{T_1T_1}}{4} + \frac{M(M-1)C_2^{T_2T_2}}{4} + NMC_2^{T_1T_2} \right) \quad \text{(VIII.27)}$$

with $C_2^{T_i,T_j}$ being the non gaussian correlations between $\widetilde{I}_{T_i}$ and $\widetilde{I}_{T_j}$. This leads to the following joint probability density function for two transmitted intensities:

$$\begin{aligned} P(\widetilde{I}_{T_1}, \widetilde{I}_{T_2}) = P_{Ray}(\widetilde{I}_{T_1}) P_{Ray}(\widetilde{I}_{T_2}) \Bigg( 1 + \frac{C_2^{T_1T_1}}{4} \left[ \frac{\widetilde{I}_{T_1}^2}{\langle \widetilde{I}_{T_1} \rangle^2} - 4 \frac{\widetilde{I}_{T_1}}{\langle \widetilde{I}_{T_1} \rangle} + 2 \right] \\ + \frac{C_2^{T_2T_2}}{4} \left[ \frac{\widetilde{I}_{T_2}^2}{\langle \widetilde{I}_{T_2} \rangle^2} - 4 \frac{\widetilde{I}_{T_2}}{\langle \widetilde{I}_{T_2} \rangle} + 2 \right] + C_2^{T_1T_2} \left[ \left( \frac{\widetilde{I}_{T_1}}{\langle \widetilde{I}_{T_1} \rangle} - 1 \right) \left( \frac{\widetilde{I}_{T_2}}{\langle \widetilde{I}_{T_2} \rangle} - 1 \right) \right] \Bigg). \end{aligned} \quad \text{(VIII.28)}$$

Its normalized version is

$$\begin{aligned} P(\widetilde{\mathcal{I}}_{T_1}, \widetilde{\mathcal{I}}_{T_2}) = \exp\left(-\widetilde{\mathcal{I}}_{T_1}\right) \exp\left(-\widetilde{\mathcal{I}}_{T_2}\right) \\ \times \left( 1 + \frac{C_2^{T_1T_1}}{4} \left[ \widetilde{\mathcal{I}}_{T_1}^2 - 4\widetilde{\mathcal{I}}_{T_1} + 2 \right] + \frac{C_2^{T_2T_2}}{4} \left[ \widetilde{\mathcal{I}}_{T_2}^2 - 4\widetilde{\mathcal{I}}_{T_2} + 2 \right] + C_2^{T_1T_2} \left[ (\widetilde{\mathcal{I}}_{T_1} - 1)(\widetilde{\mathcal{I}}_{T_2} - 1) \right] \right). \end{aligned} \quad \text{(VIII.29)}$$

Note that the same discussion remains valid in the reflection geometry. We can note that Eq. (VIII.29) has the exact same shape as Eq. (VIII.26).

### Analysis of $P(\widetilde{I}_{T_1}, \widetilde{I}_{T_2})$

Let us check the validity of Eq. (VIII.29) using numerics. In panels (a,d) in Fig. VIII.7 we plot the logarithm of the ratio between $\langle \widetilde{I}^N_{T_1} \widetilde{I}^M_{T_2} \rangle_{num}$ and $\langle \widetilde{I}^N_{T_1} \widetilde{I}^M_{T_2} \rangle_{Ray}$. In panel (b,e), we plot the logarithm of the ratio between $\langle \widetilde{I}^N_{T_1} \widetilde{I}^M_{T_2} \rangle_{num}$ and $\langle \widetilde{I}^N_{T_1} \widetilde{I}^M_{T_2} \rangle_{S}$. In panel (c,f), we plot the logarithm of the ratio between $\langle \widetilde{I}^N_{T_1} \widetilde{I}^M_{T_2} \rangle_{num}$ and $\langle \widetilde{I}^N_{T_1} \widetilde{I}^M_{T_2} \rangle$. In panels (a,b,c) in Fig. VIII.7 the two transmitted points are separated by a transverse distance of $d^{TT}_{1,2} = 18.6\lambda$. Over this distance $C_1$ is very small, and the model should be valid. We observe indeed that the moments are closer to the numerical result when corrected with all the non gaussian correlations. In panels (d,e,f) in Fig. VIII.7 the two transmitted points are separated by a transverse distance of $d^{TT}_{1,2} = 0.31\lambda$. Over this distance $C_1$ is not negligible. This explains why the discrepancy between the numerical simulations and the analytical model considering only non gaussian correlations is so large. Note that correcting the moments with non gaussian correlations has little effect when $d^{TT}_{1,2} = 0.31\lambda$ because the dominant contribution is the gaussian correlation.

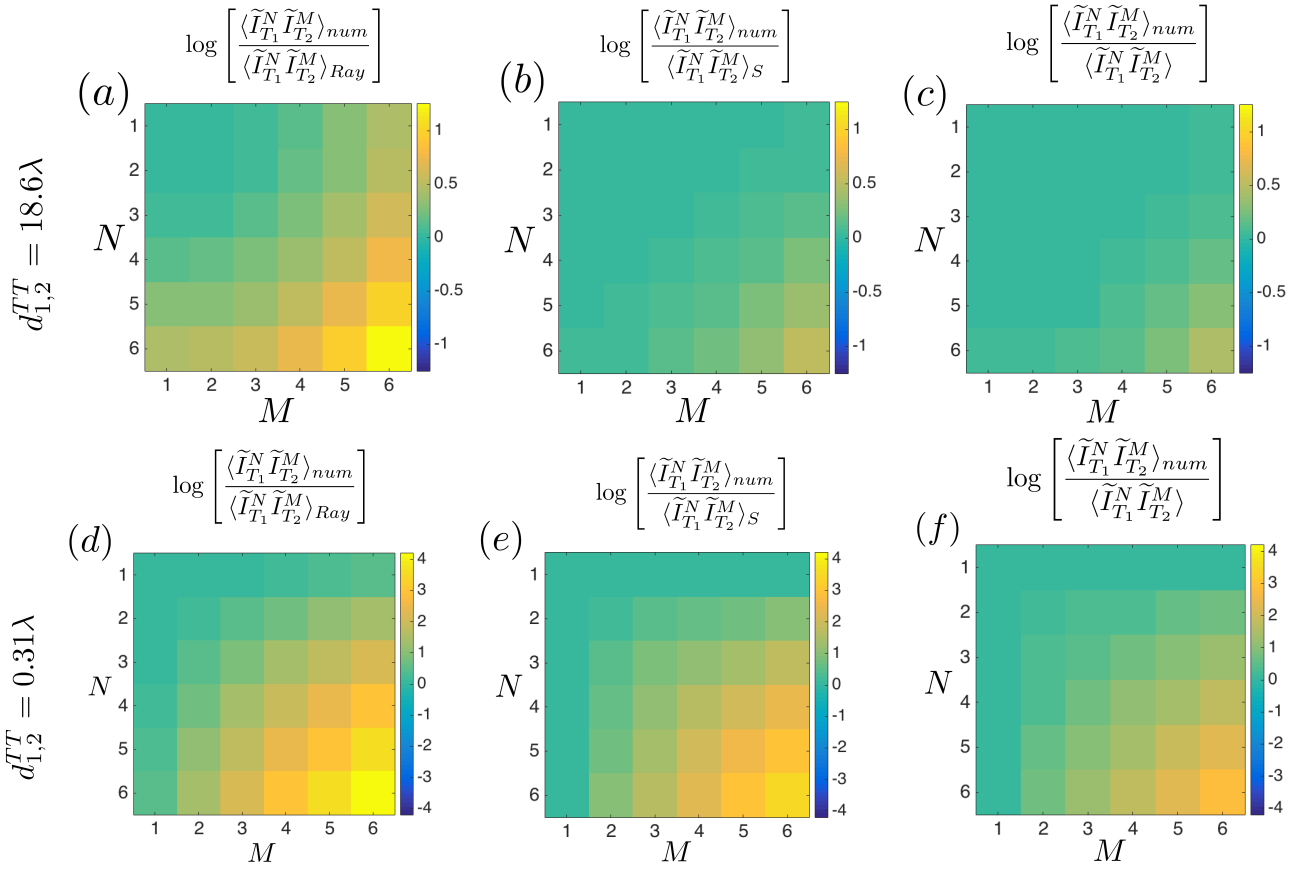


**Figure VIII.7** – Logarithm of the ratio between $\langle \widetilde{I}^N_{T_1} \widetilde{I}^M_{T_2} \rangle_{num}$ and $\langle \widetilde{I}^N_{T_1} \widetilde{I}^M_{T_2} \rangle_{Ray}$ [panels (a,d)], between $\langle \widetilde{I}^N_{T_1} \widetilde{I}^M_{T_2} \rangle_{num}$ and $\langle \widetilde{I}^N_{T_1} \widetilde{I}^M_{T_2} \rangle_{S}$[panels (b,e)], and between $\langle \widetilde{I}^N_{T_1} \widetilde{I}^M_{T_2} \rangle_{num}$ and $\langle \widetilde{I}^N_{T_1} \widetilde{I}^M_{T_2} \rangle$ [panels (c,f)]. This is done for a thick ($b = 8$) and dilute ($k_0\ell = 10$) sample and for two transmitted points separated by a transverse distance of $d^{TT}_{1,2} = 18.6\lambda$ [panels (a,b,c)] and of $d^{TT}_{1,2} = 0.31\lambda$ [panels (d,e,f)]. The distance from the slab is $d = 2\lambda$.

We can also note that the difference between numerics and analytics is larger for $P(\widetilde{I}_{T_1}, \widetilde{I}_{T_2})$ in Fig. VIII.7 than for $P(\widetilde{I}_T, \widetilde{I}_R)$ in Fig. VIII.6. The main reason is that $C_2^{TT}$ is larger than $C_2^{RR}$. It is clear that the parameter that drives the validity of the model is the strength of the non gaussian correlations (because we use a perturbative approach). The lower it is, the better the validity of the model will be.

### VIII.3.2 Extension to an arbitrary number of speckle spots

We intend now to build $P(\widetilde{I}_{R_1},...,\widetilde{I}_{R_m},\widetilde{I}_{T_1},...,\widetilde{I}_{T_n})$, taking into account one crossing of trajectories in T/T, R/R or R/T. We remain in the regime where $C_1$ is negligible between all pairs of points. In the diffusive regime this is always true in R/T, but in T/T and R/R it implies that points need to be separated by many $\lambda$ (points belong to different speckle spots). The joint moment is built considering the dominant term (disconnected propagation of ladder diagrams) and its first correction in which two intensities are connected. The connection of two intensities can occur between all pairs of intensities considered in the problem. This leads to

$$\begin{aligned}\langle \widetilde{I}_{T_1}^{N_1}...\widetilde{I}_{T_n}^{N_n}\widetilde{I}_{R_1}^{M_1}...\widetilde{I}_{R_m}^{M_m}\rangle &= N_1!...N_n!M_1!...M_m!\langle\widetilde{I}_{T_1}\rangle^{N_1}...\langle\widetilde{I}_{T_n}\rangle^{N_n}\langle\widetilde{I}_{R_1}\rangle^{M_1}...\langle\widetilde{I}_{R_m}\rangle^{M_m} \\ &\times\left(1+\sum_{i=1}^{n}\frac{N_i(N_i-1)C_2^{T_iT_i}}{4}+\sum_{j=1}^{m}\frac{M_j(M_j-1)C_2^{R_jR_j}}{4}\right. \\ &\left.+\sum_{i,j}^{n,m}N_iM_jC_2^{T_iR_j}+\sum_{i<j}^{n,n}N_iN_jC_2^{T_iT_j}+\sum_{i<j}^{m,m}M_iM_jC_2^{R_iR_j}\right)\end{aligned} \tag{VIII.30}$$

which gives for the normalized joint distribution function:

$$\begin{aligned}P(\widetilde{\mathcal{I}}_{R_1},...,\widetilde{\mathcal{I}}_{R_m},\widetilde{\mathcal{I}}_{T_1}...,\widetilde{\mathcal{I}}_{T_n}) &= P_{Ray}\left(\widetilde{\mathcal{I}}_{R_1}\right)...P_{Ray}\left(\widetilde{\mathcal{I}}_{R_m}\right)P_{Ray}\left(\widetilde{\mathcal{I}}_{T_1}\right)...P_{Ray}\left(\widetilde{\mathcal{I}}_{T_n}\right) \\ &\times\left(1+\sum_{i}^{n}\frac{C_2^{T_iT_i}}{4}\left[\widetilde{\mathcal{I}}_{T_i}^2-4\widetilde{\mathcal{I}}_{T_i}+2\right]+\sum_{j}^{m}\frac{C_2^{R_jR_j}}{4}\left[\widetilde{\mathcal{I}}_{R_j}^2-4\widetilde{\mathcal{I}}_{R_j}+2\right]\right. \\ &\left.+\sum_{i,j}^{n,m}C_2^{R_iT_j}\left[(\widetilde{\mathcal{I}}_{T_i}-1)(\widetilde{\mathcal{I}}_{R_j}-1)\right]+\sum_{i<j}^{n,n}C_2^{T_iT_j}\left[(\widetilde{\mathcal{I}}_{T_i}-1)(\widetilde{\mathcal{I}}_{T_j}-1)\right]+\sum_{i<j}^{m,m}C_2^{R_iR_j}\left[(\widetilde{\mathcal{I}}_{R_i}-1)(\widetilde{\mathcal{I}}_{R_j}-1)\right]\right).\end{aligned} \tag{VIII.31}$$

Equation (VIII.31) expresses the joint distribution between $m$ reflected and $n$ transmitted speckle spots as the joint Rayleigh law corrected with all possible non gaussian correlations. It is valid in the diffusive regime as long as the $\widetilde{I}$-$\widetilde{I}$ correlation between all pairs of points is dominated by its non gaussian contribution.

### VIII.3.3 An alternative derivation of the joint statistics

In this section we give a slightly different derivation of the joint statistics. The result obtained is of course equivalent to that obtained in the previous sections in the diffusive regime. Nonetheless, it needs fewer assumptions about the statistics of the transmitted and the reflected intensities. It is thus more general. The idea is to perform a perturbative expansion only on the correlation between the reflected intensities and the transmitted intensities. In other words, we do not specify the statistics in reflection or in transmission, we simply argue that the two sides of the sample are correlated with small non gaussian R/T correlations.

These assumptions have two implications:

- The dominant term of the joint moment is the disconnected moment between reflection and transmission. This term gives a contribution $\langle \widetilde{I}_{T_1}^{N_1}...\widetilde{I}_{T_n}^{N_n}\widetilde{I}_{R_1}^{M_1}...\widetilde{I}_{R_m}^{M_m}\rangle = \langle \widetilde{I}_{R_1}^{M_1}...\widetilde{I}_{R_m}^{M_m}\rangle\langle \widetilde{I}_{T_1}^{N_1}...\widetilde{I}_{T_n}^{N_n}\rangle$ to the joint moment.

- The first correction results from one and only one correlation in R/T. This term gives a contribution $\langle \widetilde{I}_{T_1}^{N_1} ... \widetilde{I}_{T_n}^{N_n} \widetilde{I}_{R_1}^{M_1} ... \widetilde{I}_{R_m}^{M_m} \rangle = \sum_{i,j}^{m,n} \langle \widetilde{I}_{R_1}^{M_1} ... \widetilde{I}_{R_i}^{M_i - 1} ... \widetilde{I}_{R_m}^{M_m} \rangle \langle \widetilde{I}_{T_1}^{N_1} ... \widetilde{I}_{T_j}^{N_j - 1} ... \widetilde{I}_{T_n}^{N_n} \rangle NM \langle \widetilde{I}_{R_i} \widetilde{I}_{T_j} \rangle_{C_2}$ to the joint moment.

This leads to the following expression of the joint moment:

$$\begin{aligned} \langle \widetilde{I}_{T_1}^{N_1} ... \widetilde{I}_{T_n}^{N_n} \widetilde{I}_{R_1}^{M_1} ... \widetilde{I}_{R_m}^{M_m} \rangle &= \langle \widetilde{I}_{R_1}^{M_1} ... \widetilde{I}_{R_m}^{M_m} \rangle \langle \widetilde{I}_{T_1}^{N_1} ... \widetilde{I}_{T_n}^{N_n} \rangle \\ &+ \sum_{i,j}^{m,n} \langle \widetilde{I}_{R_1}^{M_1} ... \widetilde{I}_{R_i}^{M_i - 1} ... \widetilde{I}_{R_m}^{M_m} \rangle \langle \widetilde{I}_{T_1}^{N_1} ... \widetilde{I}_{T_j}^{N_j - 1} ... \widetilde{I}_{T_n}^{N_n} \rangle NM \langle \widetilde{I}_{R_i} \widetilde{I}_{T_j} \rangle_{C_2}. \end{aligned} \tag{VIII.32}$$

Inserting Eq. (VIII.32) into Eq. (VIII.17), we directly obtain for the normalized quantities:

$$\begin{aligned} P(\widetilde{\mathcal{I}}_{R_1}, ..., \widetilde{\mathcal{I}}_{R_m}, \widetilde{\mathcal{I}}_{T_1} ..., \widetilde{\mathcal{I}}_{T_n}) &= P(\widetilde{\mathcal{I}}_{R_1}, ..., \widetilde{\mathcal{I}}_{R_m}) P(\widetilde{\mathcal{I}}_{T_1}, ..., \widetilde{\mathcal{I}}_{T_n}) \\ &\times \left( 1 + \sum_{i,j}^{m,n} C_2^{R_i T_j} v_i(\widetilde{\mathcal{I}}_{R_1}, ..., \widetilde{\mathcal{I}}_{R_m}) v_j(\widetilde{\mathcal{I}}_{T_1}, ..., \widetilde{\mathcal{I}}_{T_n}) \right) \end{aligned} \tag{VIII.33}$$

with

$$v_i(X_1, ...X_N) = \frac{\frac{\partial}{\partial X_i} \left[ X_i \frac{\partial}{\partial X_i} P(X_1, ...X_N) \right]}{P(X_1, ...X_N)} \tag{VIII.34}$$

and $X$ being $\widetilde{\mathcal{I}}_R$ or $\widetilde{\mathcal{I}}_T$.

Equation (VIII.33) is a milestone because it directly expresses the joint distribution between reflected and transmitted intensities $(\widetilde{\mathcal{I}}_{R_1}, ..., \widetilde{\mathcal{I}}_{R_m}, \widetilde{\mathcal{I}}_{T_1} ..., \widetilde{\mathcal{I}}_{T_n})$ as the independent product of the reflected and the transmitted joint distributions multiplied by a correction. When this correction differs from unity, we know that the reflected and the transmitted intensities are statistically dependent. Note that the correction is simply defined by the derivatives of the distribution in transmission and in reflection, and by all the non gaussian correlations in R/T. Let us stress that if we insert the joint distribution in transmission or in reflection built taking into account the non gaussian correlation into Eq. (VIII.33), we recover to first order in terms of non gaussian correlations the result given in Eq. (VIII.31).

Since we have derived the joint-distribution between an arbitrary number of speckle spots in reflection and an arbitrary number of speckle spots in transmission we can enter information theory. This is the topic of the next chapter.

# Chapter IX

# Mutual information between reflected and transmitted speckle patterns

## Table des matières

In this chapter we study the mutual information (MI) between an arbitrary number of reflected and transmitted distant speckle spots both numerically and analytically. The geometry of interest is represented in Fig. IX.1. Between the writing of the thesis and the defense of the thesis, we submitted an article summarizing the work discussed in this chapter [116]

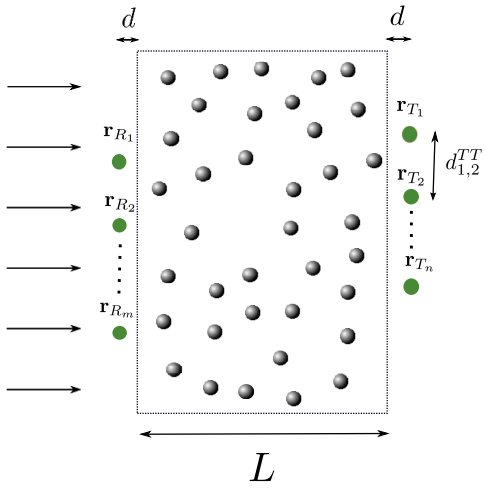


**Figure IX.1** – Scheme of the system: a plane wave at normal incidence illuminates a 2D disordered sample of depth $L$. The field is measured in transmission and reflection at various positions $\mathbf{r}_{T_i}$ and $\mathbf{r}_{R_j}$. The planes of measurement are at a distance $d$ from the sample surfaces. The transverse distance between $\mathbf{r}_{T_i}$ and $\mathbf{r}_{T_j}$ is denoted by $d_{i,j}^{TT}$, between $\mathbf{r}_{R_i}$ and $\mathbf{r}_{R_j}$ it is denoted by $d_{i,j}^{RR}$ and between $\mathbf{r}_{T_i}$ and $\mathbf{r}_{R_j}$ it is denoted by $d_{i,j}^{RT}$.

We first derive a perturbative expression of the MI in terms of non gaussian correlation functions in R/R, T/T and R/T. Then we discuss the shape of the non gaussian correlation functions in T/T and R/R to get insight about their contribution to MI. Based on this, we analytically discuss the main features of the MI and its dependence on the parameters of the physical problem. Eventually we study numerically the MI between a large number of reflected and transmitted intensities. We observe a rich and subtle behavior of this quantity versus the parameters of the system.

## IX.1 Mutual information in terms of $C_2^{TT}$, $C_2^{RR}$ and $C_2^{RT}$

Let us recall the expression of the MI between two ensembles of random variables $\mathcal{R} = (\widetilde{\mathcal{I}}_{R_1}, ..., \widetilde{\mathcal{I}}_{R_m})$ and $\mathcal{T} = (\widetilde{\mathcal{I}}_{T_1} ..., \widetilde{\mathcal{I}}_{T_n})$ [105]:

$$\mathrm{MI}\left(\mathcal{R},\mathcal{T}\right) = \frac{1}{\log(2)} \int P\left(\mathcal{R},\mathcal{T}\right) \log\left[\frac{P\left(\mathcal{R},\mathcal{T}\right)}{P\left(\mathcal{R}\right) P\left(\mathcal{T}\right)}\right] \mathrm{d}\mathcal{R}\mathrm{d}\mathcal{T}. \tag{IX.1}$$

The MI between two random variables is often considered as a "distance" between the joint distribution and the product of the marginal distributions[1]. Indeed, it vanishes if and only if the two random variables are independent and is positive otherwise. In Chap. VIII we derived the expression of the joint distribution $P(\mathcal{R},\mathcal{T})$ in terms of the product of the marginal probability densities:

$$\begin{aligned} P(\widetilde{\mathcal{I}}_{R_1},...,\widetilde{\mathcal{I}}_{R_m},\widetilde{\mathcal{I}}_{T_1}...,\widetilde{\mathcal{I}}_{T_n}) &= P(\widetilde{\mathcal{I}}_{R_1},...,\widetilde{\mathcal{I}}_{R_m})P(\widetilde{\mathcal{I}}_{T_1},...,\widetilde{\mathcal{I}}_{T_n}) \\ &\times \left(1+\underbrace{\sum_{i,j}^{m,n} C_2^{R_iT_j} v_i(\widetilde{\mathcal{I}}_{R_1},...,\widetilde{\mathcal{I}}_{R_m}) v_j(\widetilde{\mathcal{I}}_{T_1},...,\widetilde{\mathcal{I}}_{T_n})}_{u(\mathcal{R},\mathcal{T})}\right). \end{aligned} \tag{IX.2}$$

The importance of the form of Eq. (IX.2) is revealed when inserted into the expression of the MI between $\mathcal{R}$ and $\mathcal{T}$:

$$\begin{aligned} \mathrm{MI}(\mathcal{R},\mathcal{T}) &= \frac{1}{\log(2)}\int P(\mathcal{R})\,P(\mathcal{T})\,[1+u(\mathcal{R},\mathcal{T})]\log[1+u(\mathcal{R},\mathcal{T})]\,\mathrm{d}\mathcal{R}\mathrm{d}\mathcal{T} \\ &\simeq \frac{1}{\log(2)}\int P(\mathcal{R})\,P(\mathcal{T})\left[u(\mathcal{R},\mathcal{T})+\frac{u^2(\mathcal{R},\mathcal{T})}{2}\right]\mathrm{d}\mathcal{R}\mathrm{d}\mathcal{T} \end{aligned} \tag{IX.3}$$

where we assumed that $u(\mathcal{R},\mathcal{T}) \ll 1$. This assumption is ensured by the scaling of $C_2^{RT}$ as $1/(k_0 L) \ll 1$ in 2D. We can show that the average value of $u(\mathcal{R},\mathcal{T})$ has a zero contribution using

$$\begin{aligned} \int P(\widetilde{\mathcal{I}}_{R_1},...,\widetilde{\mathcal{I}}_{R_m}) v_i(\widetilde{\mathcal{I}}_{R_1},...,\widetilde{\mathcal{I}}_{R_m})\mathrm{d}\widetilde{\mathcal{I}}_{R_1}...\mathrm{d}\widetilde{\mathcal{I}}_{R_m} &= \int \partial_{\widetilde{\mathcal{I}}_{R_i}}\left[\widetilde{\mathcal{I}}_{R_i}\partial_{\widetilde{\mathcal{I}}_{R_1}} P(\widetilde{\mathcal{I}}_{R_1},...,\widetilde{\mathcal{I}}_{R_m})\right]\mathrm{d}\widetilde{\mathcal{I}}_{R_1}...\mathrm{d}\widetilde{\mathcal{I}}_{R_m} \\ &= \int \left[\widetilde{\mathcal{I}}_{R_i}\partial_{\widetilde{\mathcal{I}}_{R_1}} P(\widetilde{\mathcal{I}}_{R_1},...,\widetilde{\mathcal{I}}_{R_m})\right]_0^{\infty} \mathrm{d}\widetilde{\mathcal{I}}_{R_1}...d\widetilde{\mathcal{I}}_{R_{i-1}}d\widetilde{\mathcal{I}}_{R_{i+1}}...\mathrm{d}\widetilde{\mathcal{I}}_{R_m} \\ &= 0. \end{aligned} \tag{IX.4}$$

This leads to a simple form of the MI between $\mathcal{R}$ and $\mathcal{T}$:

$$\mathrm{MI}(\mathcal{R},\mathcal{T}) = \frac{1}{\log(2)}\int P(\mathcal{R})\,P(\mathcal{T})\,\frac{u^2(\mathcal{R},\mathcal{T})}{2}\mathrm{d}\mathcal{R}\mathrm{d}\mathcal{T}. \tag{IX.5}$$

To calculate the MI explicitly, let us recall the expression of $u$

$$u(\mathcal{R},\mathcal{T}) = \sum_{i,j}^{m,n} C_2^{R_iT_j} v_i(\mathcal{R}) v_j(\mathcal{T}) \tag{IX.6}$$

and of $u^2$

$$u^2(\mathcal{R},\mathcal{T}) = \sum_{i,j,i',j'}^{m,n,m,n} C_2^{R_iT_j} v_i(\mathcal{R}) v_j(\mathcal{T}) C_2^{R_{i'}T_{j'}} v_{i'}(\mathcal{R}) v_{j'}(\mathcal{T}). \tag{IX.7}$$

We can show that the MI reads

$$\mathrm{MI}(\mathcal{R},\mathcal{T}) = \frac{1}{2\log(2)}\sum_{i,j,i',j'}^{m,n,m,n} C_2^{R_iT_j} C_2^{R_{i'}T_{j'}} \langle v_i(\mathcal{R})\,v_{i'}(\mathcal{R})\rangle\langle v_j(\mathcal{T})\,v_{j'}(\mathcal{T})\rangle \tag{IX.8}$$

with

$$\begin{cases} \langle v_i(\mathcal{R})\,v_{i'}(\mathcal{R})\rangle = \int P(\mathcal{R}) v_i(\mathcal{R})\,v_{i'}(\mathcal{R})\,\mathrm{d}\mathcal{R}, \\ \langle v_i(\mathcal{T})\,v_{i'}(\mathcal{T})\rangle = \int P(\mathcal{T}) v_i(\mathcal{T})\,v_{i'}(\mathcal{T})\,\mathrm{d}\mathcal{T}. \end{cases} \tag{IX.9}$$

[1]Thus it is commonly accepted as a distance to independence.

To proceed further, we need to specify the joint distribution on each surface $[P(\widetilde{\mathcal{I}}_{R_1},...,\widetilde{\mathcal{I}}_{R_m})$ and $P(\widetilde{\mathcal{I}}_{T_1},...,\widetilde{\mathcal{I}}_{T_n})]$. We consider points separated by transverse distances larger than $\lambda$ so that the $C_1$ correlation is negligible. We have shown in Eq. (VIII.29) that the joint distribution in transmission reads

$$P(\mathcal{T}) = P(\widetilde{\mathcal{I}}_{T_1},...,\widetilde{\mathcal{I}}_{T_n}) = \exp\left(-\widetilde{\mathcal{I}}_{T_1}\right)...\exp\left(-\widetilde{\mathcal{I}}_{T_n}\right) \times \left(1+\sum_i^n \frac{C_2^{T_iT_i}}{4}\left[\widetilde{\mathcal{I}}_{T_i}^2 - 4\widetilde{\mathcal{I}}_{T_i}+2\right] + \sum_{i<j}^{n,n} C_2^{T_iT_j}\left[(\widetilde{\mathcal{I}}_{T_i}-1)(\widetilde{\mathcal{I}}_{T_j}-1)\right]\right). \tag{IX.10}$$

Inserting Eq. (IX.10) (and its analog in reflection) into Eq. (IX.8), we obtain

$$\mathrm{MI}\left(\mathcal{R},\mathcal{T}\right) = \frac{1}{2\log(2)}\,\mathrm{Tr}\left[\boldsymbol{C}^{RR}\boldsymbol{C}^{RT}\boldsymbol{C}^{TT}\boldsymbol{C}^{TR}\right] \tag{IX.11}$$

where

$$\begin{cases} \boldsymbol{C}^{RR}(i,j) = \delta(i,j) - C^{RR}(i,j), \\ \boldsymbol{C}^{TT}(i,j) = \delta(i,j) - C^{TT}(i,j), \\ \boldsymbol{C}^{RT}(i,j) = C_2^{RT}(i,j). \end{cases} \tag{IX.12}$$

In Eq. (IX.12) we have not specified the matrices $C^{RR}$ and $C^{TT}$ on purpose. In the following (in order to give insight and to improve the agreement between analytics and numerics) we vary the accuracy of the derivation of these matrices in terms of non gaussian correlations in T/T and R/R. In Eq. (IX.13) we give the expression to three different orders of the non diagonal terms of the $C^{XX}$ matrices used in this chapter ($XX$ refers to $TT$ or $RR$). In Eq. (IX.14), we give the same result for the diagonal terms:

$$\begin{cases} C^{XX_0}(i,j) = 0, \\ C^{XX_1}(i,j) = 0 + C_2^{XX}(i,j), \\ C^{XX_2}(i,j) = 0 + C_2^{XX}(i,j)\left(1 - C_2^{XX}(i,i) - C_2^{XX}(j,j)\right), \end{cases} \tag{IX.13}$$

and

$$\begin{cases} C^{XX_0}(i,i) = 0, \\ C^{XX_1}(i,i) = 0 + C_2^{XX}(i,i), \\ C^{XX_2}(i,i) = 0 + C_2^{XX}(i,i) - 5\left(C_2^{XX}(i,i)\right)^2. \end{cases} \tag{IX.14}$$

In Eq. (IX.13) and Eq. (IX.14) we have labeled three different terms which correspond to different order in the development of $C^{XX}$ in terms of non gaussian correlation (we use the superscript $(...)^{XX_2}$ for instance to refer to $C^{XX}$ to second order in terms of non gaussian correlations). The first term ($C^{XX_0}$) corresponds to the the Rayleigh law in both reflection and transmission. The second term ($C^{XX_1}$) corresponds to a statistics in both reflection and transmission following Eq. (IX.10). It is a development to first order in term of non gaussian correlations in T/T and R/R. To obtain the third term ($C^{XX_2}$) we add to the model the possibility of having two pairs of transmitted (or reflected) intensities crossing at the same time[2]. Whatever the order in the development of the matrices $C^{RR}$ and $C^{TT}$, we can develop Eq. (IX.11) using Eq. (IX.12) in order to obtain the MI as a sum of three terms :

$$\mathrm{MI}\left(\mathcal{R},\mathcal{T}\right) = \frac{1}{2\log(2)}\left(\mathrm{Tr}\left[\left(C^{RT}\right)^2\right] - \mathrm{Tr}\left[\left(C^{RR}+C^{TT}\right)\left(C^{RT}\right)^2\right] + \mathrm{Tr}\left[C^{RR}C^{RT}C^{TT}C^{TR}\right]\right). \tag{IX.15}$$

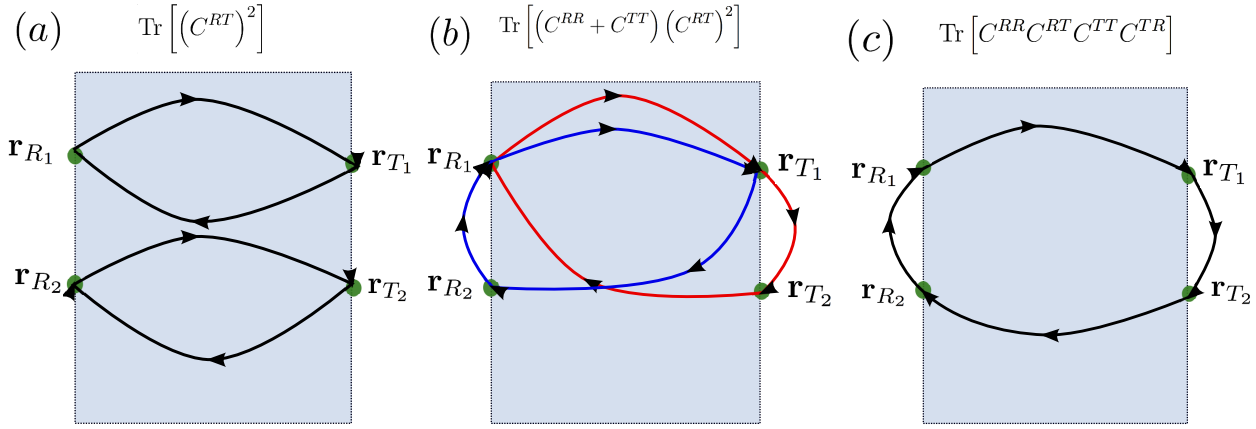


**Figure IX.2** – Scheme of the decomposition of the MI between $\mathcal{R}$ and $\mathcal{T}$ performed in Eq. (IX.15). Panel (a) represent the term resulting from $\mathrm{Tr}\left[(C^{RT})^2\right]$. Panel (b) represents the term resulting from $\mathrm{Tr}\left[\left(C^{RR}+C^{TT}\right)(C^{RT})^2\right]$ and panel (c) the term resulting from $\mathrm{Tr}\left[C^{RR}C^{RT}C^{TT}C^{TR}\right]$.

In Fig. IX.2 we represent schematically the meaning of Eq. (IX.15). Its interpretation is the following: the MI between $\mathcal{R}$ and $\mathcal{T}$ is carried by loops of correlation. The first possibility is to correlate back and forth reflection and transmission via a 2 points loop [panel (a)]. When non gaussian correlations in T/T or R/R are added to the model we can also consider a three points loop with a correlation between reflection and transmission, a correlation on the surface (with $C^{RR}$ or $C^{TT}$) and a R/T correlation going back to the first point [panel (b)]. The last possibility is a four points loop with two R/T correlations, one T/T correlation and one R/R correlation [panel (c)].

Let us define three analytical expressions deduced from Eq. (IX.15) that will be of interest in this study:

$$\mathrm{MI}_1\left(\mathcal{R},\mathcal{T}\right)=\frac{1}{2\log(2)}\,\mathrm{Tr}\left[\left(C^{RT}\right)^2\right], \tag{IX.16}$$

$$\mathrm{MI}_2\left(\mathcal{R},\mathcal{T}\right)=\frac{1}{2\log(2)}\left(\mathrm{Tr}\left[\left(C^{RT}\right)^2\right]-\mathrm{Tr}\left[\left(C^{RR_1}+C^{TT_1}\right)\left(C^{RT}\right)^2\right]\right), \tag{IX.17}$$

and

$$\mathrm{MI}_3\left(\mathcal{R},\mathcal{T}\right)=\frac{1}{2\log(2)}\left(\mathrm{Tr}\left[\left(\mathbf{I}-C^{RR_2}-C^{TT_2}\right)\left(C^{RT}\right)^2\right]+\mathrm{Tr}\left[C^{RR_1}C^{RT}C^{TT_1}C^{TR}\right]\right). \tag{IX.18}$$

In Eq. (IX.17), $\mathbf{I}$ is the identity matrix of dimension $n$. To build $\mathrm{MI}_1$ we inserted $C^{XX_0}$ into Eq. (IX.15). This analytical expression is represented schematically in panel (a) in Fig. IX.2. To build $\mathrm{MI}_2$ we inserted $C^{XX_1}$ into Eq. (IX.15) and dropped the third term in Eq. (IX.15) . $\mathrm{MI}_2$ only takes into account the first correction of order $1/(k_0\ell)$ in Eq. (IX.15) (due to non gaussian correlations in T/T and R/R). In $\mathrm{MI}_3$ we incorporated higher order contributions due to non gaussian correlations in T/T and R/R. Note that $\mathrm{MI}_2$ does not contain four points loops as represented in panel (c) in Fig. IX.2.

Let us stress that when the dimension of the vectors $\mathcal{R}$ and $\mathcal{T}$ are larger than 1, the three terms are not a simple development in $1/(k_0\ell)$. Indeed in this case the transverse distance $d^{TT}_{i,j}$ and $d^{RR}_{i,j}$ enter

[2]Mathematically we add the possibility to take into account $\left(\langle\widetilde{I_{T_i}}^2\rangle_{C_2}\right)^2$,$\langle\widetilde{I_{T_i}}\widetilde{I_{T_j}}\rangle_{C_2}\langle\widetilde{I_{T_i}}^2\rangle_{C_2}$, $\left(\langle\widetilde{I_{R_i}}^2\rangle_{C_2}\right)^2$ and $\langle\widetilde{I_{R_i}}\widetilde{I_{R_j}}\rangle_{C_2}\langle\widetilde{I_{R_i}}^2\rangle_{C_2}$ in the (N,M) joint moment.

into account and play an important role. Nonetheless when the dimension of both $\mathcal{R}$ and $\mathcal{T}$ is equal to 1, then $\mathrm{MI}_1$ is the first order expansion of MI in terms of the small parameter $1/(k_0\ell)$.

## IX.2 Study of reflection and transmission non gaussian correlation functions

In the previous section we derived an expression of MI $(\mathcal{R}, \mathcal{T})$ and observed that it depends not only on the R/T non gaussian correlation but also on the T/T and the R/R non gaussian correlations. As a consequence, in this section we study the non gaussian correlations in reflection and in transmission. The complexity of the diagrammatic approach in the R/R configuration leads us to look for simple fitting functions for the T/T and the R/R non gaussian correlations. These fitting functions are expected to give us insight about the dependence of the non gaussian correlations on the parameters of the system.

### IX.2.1 Diagrammatic approach

In this section, we give a very short presentation of the diagrammatic calculations of $C_2^{TT}$ and $C_2^{RR}$. The purpose is mainly to warn the reader about difficulties encountered with diffusion theory in the R/R geometry.

#### Non gaussian correlation function in transmission

In App. we give the analytical expression of the non gaussian correlation in R/R and T/T in 2D and 3D. To derive these expressions we took into account the two diagrams represented in the R/T geometry in Fig. III.10[3]. The T/T non gaussian correlation function calculated this way is a positive and peaked function of the transverse distance between the points. It takes non zero values in a range of transverse distances larger than $\lambda$. In Fig. IX.3 we compare the analytical calculation given in App. with numerical simulations for a thick ($b = 10$) and dilute ($k_0\ell = 10$) medium. We observe a good agreement between the two curves.

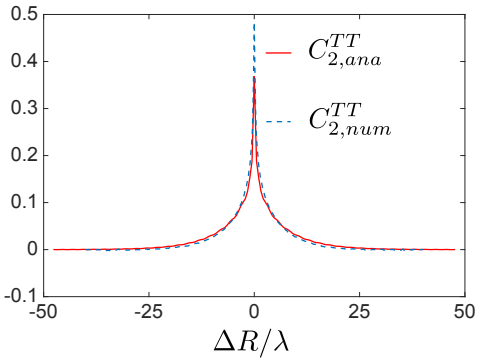


**Figure IX.3** – Numerical calculations (blue dashed curve) of the non gaussian correlation function and analytical calculation of the $C_2^{TT}$ (red solid curve) in transmission for a thick ($b = 10$) and dilute ($k_0\ell$) sample versus the transverse distance normalized by $\lambda$.

[3]Since we do not use the analytical formulas of $C_2^{TT}$ and $C_2^{RR}$ to study MI we only give them in App. .

### Non gaussian correlation function in reflection

In Fig. IX.4 we represent the R/R non gaussian correlation for two media with same size ($k_0L = 200$) and various optical thicknesses ($b = 10$ for the red curve and $b = 20$ for the blue curve) both numerically [panel (a)] and analytically [panel (b)]. The R/R non gaussian correlation function is a very peculiar function of the transverse distance. It is negative for transverse distances larger than a few wavelengths and is positive otherwise. We can also note that it is a long range function. The comparison between numerics and analytics is not perfect in R/R. This discrepancy is due to the use of ladder diagrams calculated with diffusion theory which cannot represent well the short paths that exist in reflection. Nonetheless, we can observe that the amplitude, the peculiar form of the function and their variations with the parameters of the system are qualitatively reproduced with the analytical calculation. To improve the accuracy in the R/R configuration, we should use radiative transfer theory to have a better representation of short paths in the calculation of the diagrams. This is not our purpose, and we propose instead to find simple functions that represents well the numerical data.

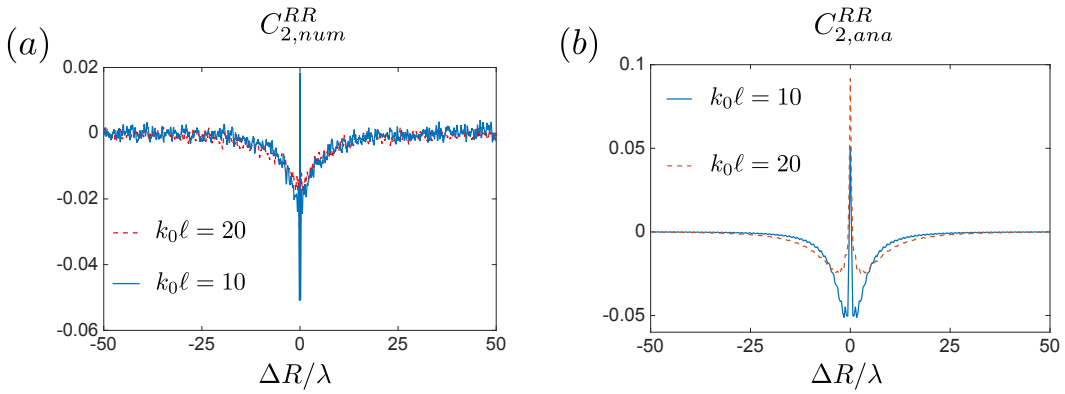


**Figure IX.4** – Numerical calculations of the non gaussian correlation in reflection [panel (a)] and analytical calculation of the $C_2^{RR}$ correlation [panel (b)] for two different samples of same length ($k_0L = 200$) and varying mean free path versus the transverse distance normalized by $\lambda$.

## IX.2.2 Fitting non gaussian correlations in T/T, R/R and R/T

In this subsection we intend to find fitting functions for the non gaussian correlations in T/T, R/R and R/T in terms of the parameters of the system. We first vary these parameters to understand the scaling laws followed by the T/T and the R/R non gaussian correlations.

### Dependence of the T/T non gaussian correlation one the parameters of the system

In Fig. IX.5 we study the numerically calculated non gaussian correlation in transmission considered as a function of the transverse distance $\Delta R$. In panel (a) we vary the mean free path for a given length of the system ($k_0L = 120$). In panel (b) we fix the mean free path ($k_0\ell = 10$) and vary the optical thickness. In panels (c,d) we plot the non gaussian correlation normalized by its maximum value in order to observe the change in the shape of the function with the parameters. From Fig. IX.5 we can conclude that $C_2^{TT}$ varies in amplitude with the mean free path and in shape with the depth $L$ of the medium.

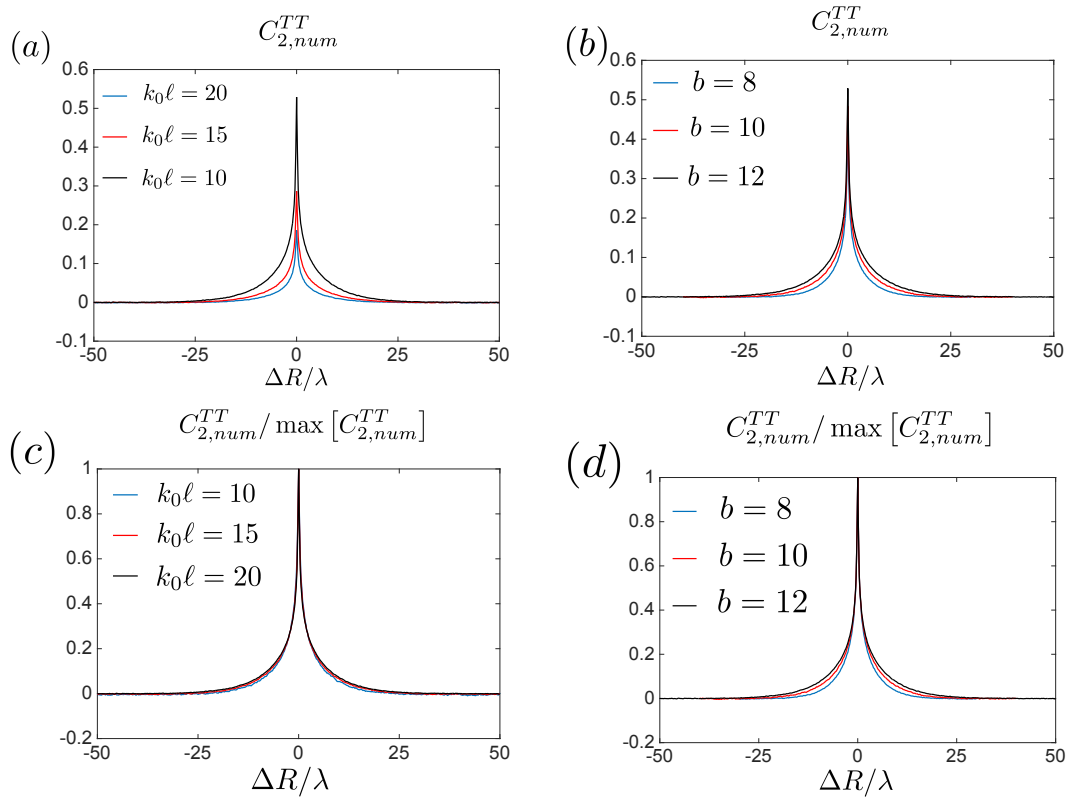


**Figure IX.5** – Panel (a): numerical calculation of $C_2^{TT}$ versus $\Delta R/\lambda$ for three different samples of same size $k_0 L = 120$ and various mean free paths. Panel (b): numerical calculation of $C_2^{TT}$ versus $\Delta R/\lambda$ for three different samples of same mean free path $k_0\ell = 10$ and various optical thicknesses. In panels (c) and (d) we plot the same two curves normalized by their maximum.

## Dependence of the R/R non gaussian correlation on the parameters of the system

In Fig. IX.6 we study the numerically calculated non gaussian correlation in reflection. In panel (a) we vary the mean free path for a given length of the system ($k_0 L = 120.$) In panel (b) we fix the mean free path ($k_0\ell = 10$) and vary the optical thickness of the system. From Fig. IX.6 we can conclude that $C_2^{RR}$ vary both in amplitude and in shape with the mean free path. Note that $C_2^{RR}$ seems to become independent on $L$ in the deep diffusive regime.

## Fitting functions for $C_2^{RR}$, $C_2^{TT}$ and $C_2^{RT}$

We can propose fitting functions for $C_2^{RR}$, $C_2^{TT}$ and also $C_2^{RT}$ based on the previous numerical study. We observed that $C_2^{RR}$ and $C_2^{TT}$ vary in amplitude with the mean free path, while $C_2^{RT}$ vary with the size of the medium. We also observed that the typical length scale of $C_2^{RR}$ is $\ell$, while both $C_2^{TT}$ and $C_2^{RT}$ vary on a typical distance of $L$. We can thus propose the following form for the correlation

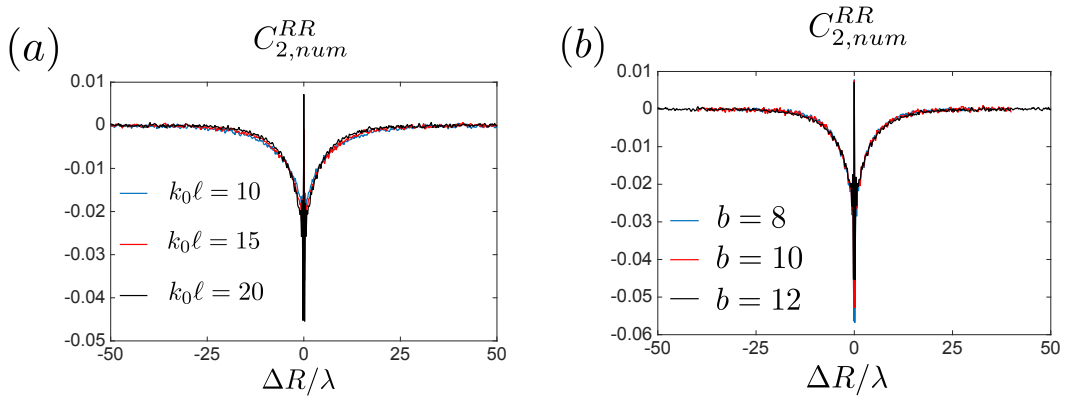


**Figure IX.6** – Panel (a): numerical calculation of $C_2^R R$ versus $\Delta R/\lambda$ for three different samples of same size ($k_0 L = 120$) and various mean free paths. Panel (b): numerical calculation of $C_2^R R$ versus $\Delta R/\lambda$ for three different samples of same mean free path ($k_0\ell = 10$) and various optical thicknesses.

functions[4]:

$$\begin{cases} C_2^{TT}(\Delta R) = \dfrac{1}{k_0\ell} f_{TT}\left(\dfrac{\Delta R}{L}\right), \\ C_2^{RR}(\Delta R) = \dfrac{1}{k_0\ell} f_{RR}\left(\dfrac{\Delta R}{\ell}\right), \\ C_2^{RT}(\Delta R) = \dfrac{1}{k_0 L} f_{RT}\left(\dfrac{\Delta R}{L}\right). \end{cases} \tag{IX.19}$$

with

$$\begin{cases} f_{TT}\left(\dfrac{\Delta R}{L}\right) = \alpha_{TT} \exp\left(-\beta_{TT}\dfrac{\Delta R}{L}\right), \\ f_{RR}\left(\dfrac{\Delta R}{\ell}\right) = \alpha_{RR} \exp\left(-\beta_{RR}\dfrac{\Delta R}{\ell}\right), \\ f_{RT}\left(\dfrac{\Delta R}{L}\right) = \alpha_{RT} \exp\left(-\beta_{RT}\left[\dfrac{\Delta R}{L}\right]^2\right). \end{cases} \tag{IX.20}$$

where $\alpha$ and $\beta$ are dependent on the optical thickness of the sample. We know from Chap. III that $\alpha_{RT}$ and $\beta_{RT}$ have a well defined asymptotic value in the deep diffusive regime, but we do not know if this is also true in the T/T and the R/R configurations. Indeed mathematically in the diffusive approach we cannot put the T/T and R/R correlation in a simple form like the one given in Eq. (IX.20). In the literature, this aspect is handled by specifying the form of the correlation function in different domains (for instance for $0 \leq \Delta R \leq \ell$). Here we accept to loose accuracy in the region $|\Delta R| \leq \ell$ and gain simplicity in the expression of the correlation function. In the following study the values of the fitting parameters will be of little interest. Nonetheless, we give in the table below the parameters of the fitting functions for a moderate optical thickness ($b = 3$ and $k_0\ell = 10$) and for a large optical thickness ($b = 8$ and $k_0\ell = 10$) in order to give insight about the correlation functions:

| | T/T | R/R | R/T |
|---|---|---|---|
| $b = 3$ | $\alpha_{TT} = 1.3$ , $\beta_{TT} = 5.2$ | $\alpha_{RR} = -0.25$ , $\beta_{RR} = 0.5$ | $\alpha_{RT} = -0.8$ , $\beta_{RT} = 1.2$ |
| $b = 8$ | $\alpha_{TT} = 2.2$ , $\beta_{TT} = 3.8$ | $\alpha_{RR} = -0.3$ , $\beta_{RR} = 0.45$ | $\alpha_{RT} = -1.1$ , $\beta_{RT} = 1.4$ |
| $b \gg 1$ | $\alpha_{TT} =?$ , $\beta_{TT} =?$ | $\alpha_{RR} =?$ , $\beta_{RR} =?$ | $\alpha_{RT} = -2.2$ , $\beta_{RT} = 2.0$ |

[4]We look for a gaussian fitting function for $C_2^{RT}$ and for exponential fitting functions for $C_2^{TT}$ and $C_2^{RR}$ due to their sharp appearance.

The last line in the table means that we have no clear analytical expressions for the fitting functions in T/T and in R/R in the diffusive regime.

### Dependence of non gaussian correlations on the distance from the scattering sample

Here we discuss a numerical simulation demonstrating that the non gaussian correlation functions are strongly dependent on the distance between the observation points and the scattering sample, denoted by $d$ in Fig. IX.1. In Fig. IX.7 we represent $C_2^{TT}$,$C_2^{RR}$ and $C_2^{RT}$ for two different distances from the slab $d = 0$ and $d = 2\lambda$ and observe a substantial change between the two curves.

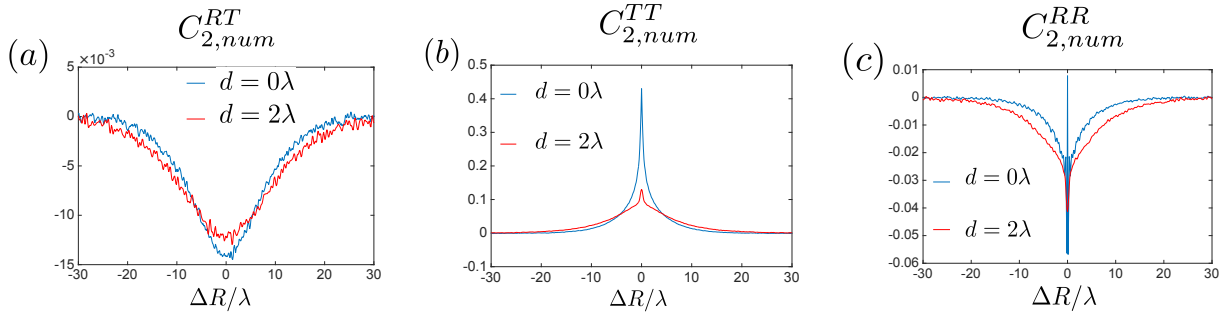


**Figure IX.7** – Numerical calculation of non gaussian correlation in R/T [panel (a)], T/T [panel (b)] and R/R [panel (c)] for points at two different distances from the slab. The parameters of the simulation are $b = 8$ and $k_0\ell = 10$.

The reader should keep in mind that the results presented in this chapter are strongly dependent on the parameter $d$.

## IX.3 Analytical expression of the mutual information between reflection and transmission

In this section we use our knowledge about non gaussian correlations to discuss Eq. (IX.15). We consider first the geometry represented in Fig. IX.8, *i.e.* the MI between $\widetilde{I}_R$ and $\widetilde{I}_T$ versus the transverse distance between the points and versus the parameters of the system in the diffusive regime. The second geometry we consider corresponds to $n$ reflected intensities "aligned" ($d_{i,i}^{RT} = 0$) with $n$ transmitted intensities, as represented in Fig. IX.10. The distance between each neighbor points in transmission or reflection is $d_{i,i+1}^{TT} = d_{i,i+1}^{RR} = a$. In this case, we study the MI between the ensemble of reflected intensities and the ensemble of transmitted intensities versus $k_0 a$, and the parameters of the system in the diffusive regime.

### IX.3.1 Analytical expression of the mutual information between one reflected intensity and one transmitted intensity

Let us start with the easiest configuration: the MI between $\widetilde{I}_R$ and $\widetilde{I}_T$ versus the transverse distance between the observation points, as represented in Fig. IX.8.

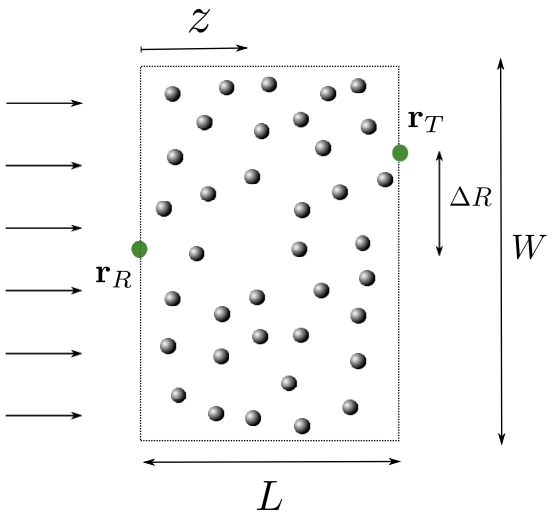


**Figure IX.8** – Scheme of the system studied in this section. A 2D disordered sample with depth $L$ and transverse size $W \gg L$ is illuminated from the left by a plane wave at normal incidence.

In this specific configuration the dominant term in Eq. (IX.15) in the diffusive regime reduces to $\mathrm{MI}_1$ when $k_0\ell \gg 1$. It reads

$$\mathrm{MI}_1\left(\widetilde{I}_R, \widetilde{I}_T\right) = \frac{1}{2\log(2)}\left[C_2^{RT}\left(\widetilde{I}_R, \widetilde{I}_T\right)\right]^2. \tag{IX.21}$$

In Eq. (III.69) we give the exact analytical expression of $C_2^{RT}$ in the diffusive regime. We can insert this expression into Eq. (IX.21) to obtain the exact expression of the MI between $\widetilde{I}_R$ and $\widetilde{I}_T$ in the diffusive regime. Nonetheless, in this chapter we do not put forward the microscopic derivation of the non gaussian correlations. We rather use the fitting functions obtained in the previous subsection. Equation (IX.21) becomes

$$\mathrm{MI}_1\left(\widetilde{I}_R, \widetilde{I}_T\right) = \frac{1}{2\log(2)(k_0L)^2} f_{RT}\left(\Delta R/L\right)^2. \tag{IX.22}$$

From Eq. (IX.22) we can discuss the basic properties of the MI between $\widetilde{I}_R$ and $\widetilde{I}_T$ in 2D. As represented in Fig. IX.9, it scales as $1/(k_0L)^2$, is maximum when points are in front of each other and has a non zero value for transverse distances $\Delta R \leq L$. Note that to first order in $1/(k_0\ell)$, MI between $\widetilde{I}_R$ and $\widetilde{I}_T$ is independent on the mean free path of the medium. In 3D the MI scales as $1/(k_0L)^4$ and has non zero value on an area of typical surface $L^2$.

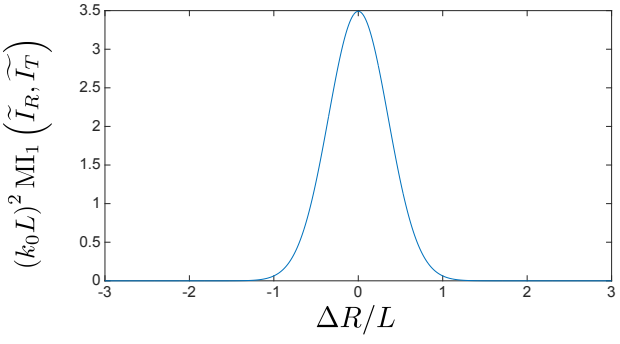


**Figure IX.9** – Large optical thickness expression of Eq. (IX.22) normalized by $1/\left(k_0L\right)^2$ versus the transverse distance normalized by $L$.

The scaling of the MI between $\widetilde{I}_R$ and $\widetilde{I}_T$ as $1/(k_0L)^2$ in 2D and $1/(k_0L)^4$ in 3D could lead us to the conclusion that the MI between reflection and transmission is too small to be useful. This statement is wrong. Indeed since $W \gg L$ (and all other length scales) it is possible to consider an arbitrary number $n$ of pairs of reflected and transmitted intensities far from each other ($d^{TT}_{i,i+1} \gg L$ and $d^{RT}_{i,i} = 0$). In that case the information should be proportional to $n$. It is even possible to consider $n$ pairs of reflected intensities whose transverse distance is comparable to $L$, $\ell$ or $\lambda$. There may be a regime of transverse distance between the points where the information is even larger than $n$ times the MI for one reflected intensity aligned with one transmitted intensity. In the next subsection we study analytically this possibility.

### IX.3.2 Analytical expression of the mutual information between $n$ reflected intensities facing $n$ transmitted intensities

Following the conclusion of the last subsection we now address the analytical study of the mutual information between $n$ reflected intensities facing $n$ transmitted intensities versus the transverse distance between the points, as represented in Fig. IX.10.

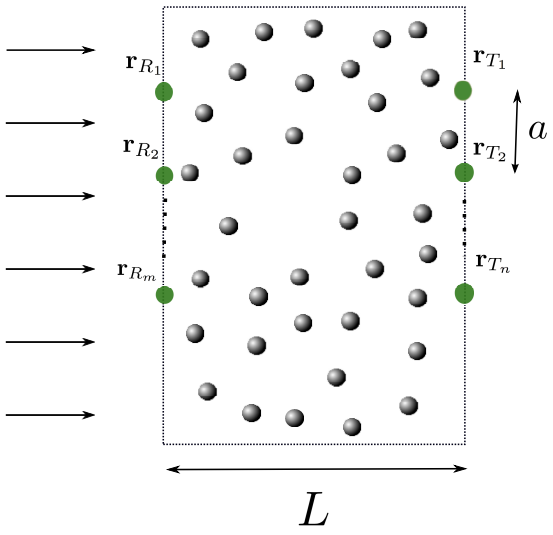


**Figure IX.10** – Scheme of the geometry considered to study MI between an arbitrary number of speckle spots in reflection and in transmission ($n = m$). Each reflected speckle spot has the same transverse coordinates as a transmitted speckle spot. The transverse distance between intensities in a given speckle pattern is denoted by $a$.

#### Large number of speckle spots ($n \gg 1$) with intermediate spacing between them ($\ell \gg a \gg \lambda$)

When the dimension of $\mathcal{R}$ and $\mathcal{T}$ is larger than 1, a new parameter enters the problem: the spacing between the observation points in a given speckle, denoted by $a$ in Fig. IX.10. To understand the role of this parameter, we first extract the main ingredients of the MI using Eq. (IX.15). To do so we transform the trace formula in a spatial integration. For this continuous limit to be valid, we need to consider $n \gg 1$ and $\ell \gg a \gg \lambda$. The distance between intensities $a$ needs to be kept larger than $\lambda$ to avoid the presence of the $C_1$ correlation. This continuous limit allows us to compare the relative

weight of two, three and four points loop processes[5] in the MI as represented in Fig. IX.2.

The dominant term in the two points loop process in Eq. (IX.15) reads

$$\begin{aligned}\mathrm{Tr}\left[\left(C^{RT}\right)^2\right] &\simeq n\int C_2^{RT}(\Delta R)^2\frac{\mathrm{d}\Delta R}{a} \\ &= \frac{n}{(k_0L)^2}\int f_{RT}(\Delta R/L)^2\frac{\mathrm{d}\Delta R}{a} \\ &= \frac{n}{(k_0Lk_0a)}\int f_{RT}(\Delta R')^2\mathrm{d}\Delta R' \\ &\sim \frac{n}{(k_0Lk_0a)}.\end{aligned} \tag{IX.23}$$

The dominant term in the three points loop process in Eq. (IX.15) reads

$$\begin{aligned}\mathrm{Tr}\left[\left(C^{RR_1}+C^{TT_1}\right)\left(C^{RT}\right)^2\right] &\simeq n\int C_2^{RT}(\Delta R)C_2^{TT}(\Delta R')C_2^{RT}(|\mathbf{\Delta R}+\mathbf{\Delta R'}|)\frac{\mathrm{d}\Delta R}{a}\frac{\mathrm{d}\Delta R'}{a} \\ &= \frac{n}{(k_0L)^2k_0\ell}\int f_{RT}(\Delta R/L)f_{TT}(\Delta R'/L)f_{RT}(|\mathbf{\Delta R}+\mathbf{\Delta R'}|/L)\frac{\mathrm{d}\Delta R}{a}\frac{\mathrm{d}\Delta R'}{a} \\ &= \frac{n}{(k_0a)^2k_0\ell}\int f_{RT}(X)f_{TT}(Y)f_{RT}(X+Y)\mathrm{d}X\mathrm{d}Y \\ &\sim \frac{n}{(k_0a)^2k_0\ell}.\end{aligned} \tag{IX.24}$$

The dominant term in the four points loop process in Eq. (IX.15) reads

$$\begin{aligned}\mathrm{Tr}\left[C^{RR_1}C^{RT}C^{TT_1}C^{TR}\right] &\simeq n\int C_2^{RT}(\Delta R)C_2^{TT}(\Delta R')C_2^{RT}(\Delta R'')C_2^{RR}(|\mathbf{\Delta R}+\mathbf{\Delta R'}+\mathbf{\Delta R''}|)\frac{\mathrm{d}\Delta R...\mathrm{d}\Delta R''}{a^3} \\ &= \frac{n}{(k_0a)^3k_0\ell}\int f_{RT}(X)f_{RR}(Y)f_{RT}(Z)f_{TT}(X+\frac{Y}{b}+Z)\mathrm{d}X\mathrm{d}Y\mathrm{d}Z \\ &\sim \frac{n}{(k_0a)^3k_0\ell},\end{aligned} \tag{IX.25}$$

when $b\gg 1$. Let us notice that the three points loop process dominates the two points process when $1/\left(k_0^2a^2k_0\ell\right)\gg 1/(k_0Lk_0a)$ or equivalently

$$k_0a\ll b. \tag{IX.26}$$

Note that this regime is captured by the model since for $b\gg 1$, we can have $1\ll k_0a\ll b\ll k_0\ell$. Let us also find the condition for the four points loop process to dominate over the three points process. This occurs when $1/\left[(k_0a)^3k_0\ell\right]\gg 1/\left[(k_0a)^2k_0\ell\right]$, or

$$k_0a\ll 1 \tag{IX.27}$$

which is not possible in the regime $a\gg\lambda$.

The conclusion from this section is that when we consider many speckle spots, we have to take into account the first correction in the MI due to $C_2^{TT}$ and $C_2^{RR}$. Indeed they are responsible for three points loop processes that cannot be neglected in the regime $1\ll k_0a\ll b$. The competing effects between two points loop processes in Eq. (IX.23) and three points loop processes in Eq. (IX.24) should lead to an interesting behavior of the MI versus $k_0a$ and the physical parameters of the system.

[5]Note that we do not need to take into corrections of second order in terms of $C_2^{XX}(i,i)$ because they are only corrections in terms of $k_0\ell\gg 1$ of these processes.

### Arbitrary spacing $a \gg \lambda$ between the points in the limit $n \gg 1$

Let us derive the expression of $\mathrm{MI}(\mathcal{R},\mathcal{T})$ for an arbitrary spacing between the points (still larger than $\lambda$). To start the derivation, we restrict Eq. (IX.15) to $\mathrm{MI}_2$ and use the Szegö theorem for the trace of a product of Toeplitz matrixes detailed in ref. [117]:

$$\mathrm{MI}_2(\mathcal{R},\mathcal{T}) = \frac{n}{2\log(2)}\int_0^{2\pi}\left(1-\left[C_2^{RR}(\mu)+C_2^{TT}(\mu)\right]\right)\left[C_2^{RT}(\mu)\right]^2\frac{\mathrm{d}\mu}{2\pi} \tag{IX.28}$$

with

$$C_2^{XX}(\mu) = \sum_{k=-\infty}^{\infty} C_2^{XX}(|k|a)\exp(ik\mu)\,. \tag{IX.29}$$

Equation (IX.28) is valid for Toeplitz matrixes of large dimension. Integrating over $\mu$ we obtain

$$\mathrm{MI}_2(\mathcal{R},\mathcal{T}) = \frac{n}{2\log(2)}\sum_{p,l=-\infty}^{\infty} C_2^{RT}(|p|a)C_2^{RT}(|p+l|a)\left(\delta(l)-\left[C_2^{RR}(|p|a)+C_2^{TT}(|p|a)\right]\right). \tag{IX.30}$$

Inserting the expression of the fitting functions for the non gaussian correlations, we obtain

$$\mathrm{MI}_2(\mathcal{R},\mathcal{T}) = \frac{n\alpha_{RT}^2}{2\log(2)(k_0L)^2}\left(\Theta_3\left(0,e^{-2\beta_{RT}a^2/L^2}\right)\right.$$
$$\left.-\sum_{p=-\infty}^{\infty}\mathcal{C}(\beta_{RT},p,a,L)\left[\frac{\alpha_{RR}}{k_0\ell}e^{-|p|a\beta_{RR}/\ell}+\frac{\alpha_{TT}}{k_0\ell}e^{-|p|a\beta_{TT}/L}\right]\right), \tag{IX.31}$$

with

$$\mathcal{C}(\beta_{RT},p,a,L) = e^{-\beta_{RT}pa^2/(2L)^2}\frac{\sqrt{\pi/2}L}{|a|\sqrt{\beta_{RT}}}\Theta_3\left(p\pi/2,e^{-L^2\pi^2/(2\beta_{RT}a^2)}\right). \tag{IX.32}$$

$\Theta_3$ is the elliptic function of order 3. In Fig. IX.11 we computed $\mathrm{MI}_2(\mathcal{R},\mathcal{T})/n$ using Eq. (IX.31) for three different cases. In panel (a) we use the parameters of the fit derived in this chapter for the non gaussian correlations for $b=3$ and $b=8$. In panel (b) we use Eq. (IX.31) to observe the behavior of the MI in the deep diffusive regime when $b$ changes and $k_0\ell = 10$. The parameters of the fit have been extracted from numerical simulations at large $b$, and are supposed not to change in the deep diffusive regime. In panel (c) we vary $k_0\ell$ with $k_0L = 200$.

From Fig. IX.11 we can discuss the general shape of $\mathrm{MI}(\mathcal{R},\mathcal{T})$ in the diffusive regime in the configuration depicted in Fig. IX.10 ($k_0a$ is always larger than 1). $\mathrm{MI}_2(\mathcal{R},\mathcal{T})/n$ is a function of $b$ and $k_0L$.

- It is a function of $k_0L$ via the non gaussian correlation in R/T which drives the amplitude of the MI for $k_0a \gg k_0L$ as observed in panel (c) in Fig. IX.11. This part of the curves scales as $1/(k_0L)^2$ in 2D and $1/(k_0L)^4$ in 3D.
- The MI is a function of $b$ via the competing effects between the cross talks between pairs of points due to $C_2^{RT}$ and the correlation between the points on the same surface $C_2^{TT}$ and $C_2^{RR}$. For a fixed value of $k_0L$, increasing $b$ is equivalent to decreasing $k_0\ell$, thus to increasing the strength of $C_2^{TT}$ and $C_2^{RR}$. The position of the maximum thus shifts towards the large $k_0a$ and the value of the maximum is reduced.

Note that the MI scales linearly with $n$ in the two regimes $k_0a \gg k_0L$ and and $k_0L \sim k_0a \gg 1$.

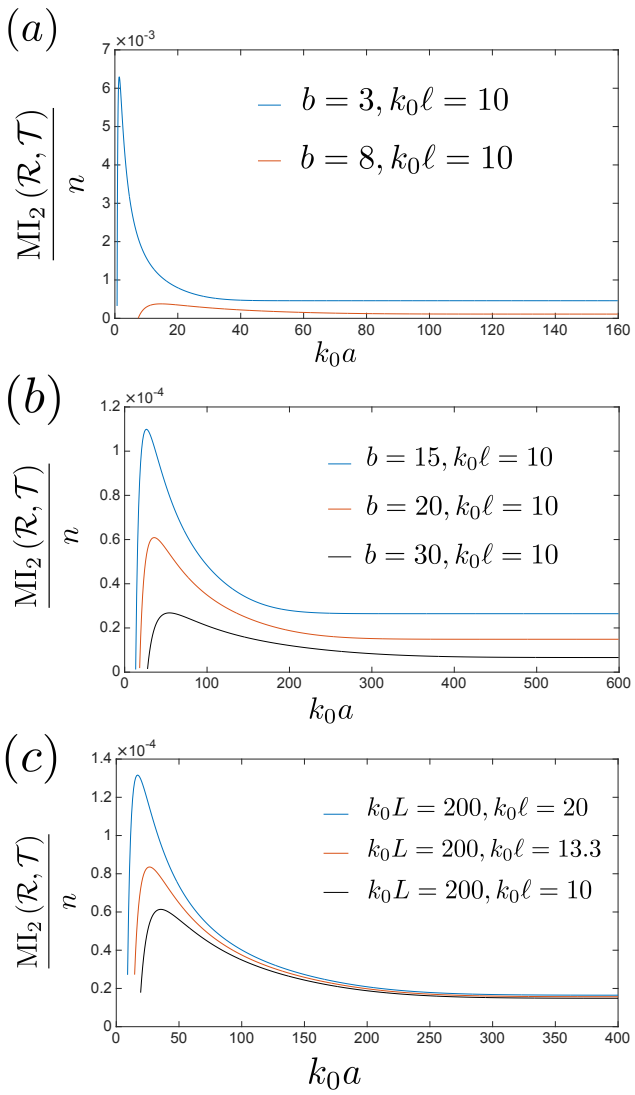


**Figure IX.11** – Panel (a): analytical calculation of $\mathrm{MI}_2(\mathcal{R},\mathcal{T})/n$ using Eq. (IX.31) and the fitting parameters of the non gaussian correlations for $b = 3$ and $b = 8$. Panel (b): analytical calculation of $\mathrm{MI}_2(\mathcal{R},\mathcal{T})/n$ using Eq. (IX.31) in the diffusive regime with $k_0\ell = 10$ and varying $b$. Panel (c): analytical calculation of $\mathrm{MI}_2(\mathcal{R},\mathcal{T})/n$ using Eq. (IX.31) in the diffusive regime with $k_0L = 200$ and varying $b$. The fitting parameters used in panels (b) and (c) have been extracted from numerical simulations at large $b$ and are supposed not to change in the diffusive regime.

## IX.4 Numerical estimation of the mutual information

In order to support the analytical study in the previous sections, we enter a complex topic: the numerical estimation of $\mathrm{MI}(X,Y)$. This domain is far to vast for us to resume it. Nonetheless, we can simply say that the MI is difficult to estimate, and that it is a work in progress for scientists to find a "good" estimator for it. There exists a large number of estimators with different capabilities. We can note that for all of them the estimation gets more difficult when the dimension of $X$ and $Y$ increases. *This technical part is not fundamental to understand the results (nonetheless it is to reproduce them). The reader can go directly to Sec. IX.5 where numerical results are discussed.*

### Bias and standard deviation of an estimator

Here we shaded light on the two difficulties we have to face in the estimation of the MI: the standard deviation and the bias of its estimators. To be schematic, let us assume that we try to estimate a quantity $X$ with a biased and deviated estimator. Let us assume that we estimate the quantity $X$ using a data set with $N_{tot}$ data, and that we can split these data into $N_{paq}$ ensembles each containing $N_p$ data, and perform $N_{paq}$ times the estimation of $X$ on $N_p$ data (of course $N_{tot} = N_{paq}N_p$). Thanks to the splitting of the data in $N_{paq}$ ensembles, we can estimate the standard deviation of the estimator. The bias by definition means that the average value of the estimation of $X$ with $N_p$ differs from the real value, and changes with $N_p$. For asymptotically unbiased estimator, the bias tends to zero when $N_p$ tends to infinity. Technically we can never be sure to have converged towards the real value. One way to convince ourselves that the bias is "defeated" is to increase the number of data $N_p$ on which the estimation is made and observe that the average value of the estimator does not change quantitatively. Nonetheless, since we have less ensembles $N_{paq}$ to estimate the results, the process is more sensitive to the standard deviation of the estimator. This discussion reveals how difficult it is to fight both bias and standard deviation simultaneously.

## IX.4.1 The histogram based estimator of the mutual information

The easiest method we could think of to estimate the MI is the histogram based estimator. Let us assume that we study two random variables $X$ and $Y$ with a joint distribution $f(X,Y)$. Following ref. [118] we can define a grid of $(k_X \times k_Y)$ equally spaced cells of size $(\Delta_X \times \Delta_Y)$ in a part of the $X$-$Y$ space. The grid has a finite size $k_X\Delta_X = n_X\sigma_X$ and $k_Y\Delta_Y = n_Y\sigma_Y$, with $(n_X, n_Y) > 0$, $\sigma_X$ and $\sigma_Y$ being the standard deviation of the probability density functions of $X$ and $Y$.

### The naive estimator

Let us call $N_{tot}$ the number of pairs $(X,Y)$ falling into the grid, and $k_{i,j}$ the number of points falling into the cell $(i,j)$. We have: $\sum_{i,j} k_{i,j} = N_{tot}$, and $\sum_i k_{i,j} = k_j$. If the probability density function is almost constant on one cell, and if the summation over the grid can be approximated by the summation over the whole space then we can use the following estimator for the MI:

$$\mathrm{MI}_{\mathrm{his}}(X,Y) = \sum_{i,j} \frac{k_{i,j}}{N_{tot}} \log\left[\frac{k_{i,j}N_{tot}}{k_i k_j}\right]. \tag{IX.33}$$

If we try to use this estimator without taking care of the size of the bins of the histograms, we obtain a strongly biased estimation of MI. Nonetheless, because of its simple form, it is possible (as in ref. [118] for gaussian variables) to give an analytical expression of the bias of the estimator in terms of the parameters of the histogram and of the joint density function:

$$\mathrm{MI}_{\mathrm{his}}(X,Y) = \mathrm{MI}(X,Y) + \frac{(k_X-1)(k_Y-1)}{2N_{tot}} - \frac{\rho^2}{24(1-\rho^2)}\left[\left(\frac{n_X}{k_X}\right)^2 + \left(\frac{n_Y}{k_Y}\right)^2\right]. \tag{IX.34}$$

Here $\rho$ denotes the correlation between $X$ and $Y$. Note that for fixed $(n_X, n_Y)$ and $(k_X, k_Y)$, this estimator is asymptotically negatively biased.

### Adaptable bin size

Equation (IX.34) is interesting because it expresses the bias as the sum of two terms with opposite sign, one depending only on $N_{tot}$ and on the binning, the other one depending only on the correlation $\rho$ between the variables $(X, Y)$ and on the parameters of the histogram $(n_X, n_Y)$ and $(k_X, k_Y)$. It is thus possible to find the right binning of the histogram which cancels these two terms. We can assume that $k_X = k_Y = k_b$, and observe that the equality of the two terms force $k_b$ to follow the equation:

$$k_b^2 - k_b = n_x|\rho|\sqrt{\frac{N_{tot}}{6(1-\rho^2)}}. \tag{IX.35}$$

Searching the closest integer of the positive solution of Eq. (IX.35) we find:

$$k_b = \text{round}\left[\frac{1}{2} + \frac{1}{2}\sqrt{1 + 4n_x|\rho|\sqrt{N_{tot}/(6(1-\rho^2))}}\right]. \tag{IX.36}$$

The variance of the estimator is given in ref. [118] and reads:

$$\text{Var}\left[\text{MI}_{\text{his}}(X, Y)\right] = \frac{\rho^2}{N_{tot}}. \tag{IX.37}$$

Thus the typical error due to the standard deviation of this estimator is on the order of

$$\delta_{\text{his}} \sim \frac{\rho}{\sqrt{N_{tot}}}. \tag{IX.38}$$

Note that the time needed to estimate the MI with a large set of data using this estimator is reasonable (a few minutes for $10^8$ realizations of $(X,Y)$ using Matlab).

## IX.4.2 The nearest neighbor method

The analytical expression of the bias in terms of the parameters of the histogram allowed us to find an adaptive binning in order to cancel the bias. Unfortunately such expressions do not exist when $X$ and $Y$ are of higher dimensions and we are left with a highly biased (even probably asymptotically biased) estimator. We thus turn to other types of estimator of the MI that are claimed to have a minimal bias, and to be asymptotically unbiased even for large dimensions of $X$ and $Y$. The estimator we decided to use is based on entropy estimates from $k$-nearest neighbor distances [119]. The important point about this estimator is that it is claimed to work well even when both $x$ and $y$ are random variables of dimensions larger than 1.

### An asymptotically unbiased estimator of the mutual information

The principle is the following: we choose two norms ($\|X\|$ and $\|Y\|$) on the subspaces of $X$ and $Y$ ($X$ and $Y$ lie in space of dimensions $n$ and $m$). These two norms allow us to define for the complete space $Z = (X, Y)$ the maximal norm:

$$\|z\| = \max\left(\|X\|, \|Y\|\right). \tag{IX.39}$$

Let us assume that we have measured $N_{tot}$ realizations of the pair $(X, Y)$. To estimate the MI we first have to choose an integer $k$ which is now a parameter of the estimator, and find for each realization

$Z_i = (X_i, Y_i)$ the distance (in term of the maximal norm) $\epsilon_i$ from $Z_i$ to its kth neighbor. Note that $\epsilon_i = \max(\epsilon_{X,i}, \epsilon_{Y,i})$ with $\epsilon_{X,i}$ the distance (in term of the norm over $X$) from $X_i$ to its kth neighbor and $\epsilon_{Y,i}$ the distance (in term of the norm over $Y$) from $Y_i$ to its kth neighbor. We can call $n_X$ (respectively $n_Y$) the number of points in the $X$ subspace (respectively in the $Y$ subspace) whose distance from $X_i$ (respectively $Y_i$) is less than $\epsilon_i$. Alternatively, we can call $n_{X,2}$ (respectively $n_{Y,2}$) the number of points in the $X$ subspace (respectively in the $Y$ subspace) whose distance from $X_i$ (respectively $Y_i$) is less than $\epsilon_{X,i}$ (respectively $\epsilon_{Y,i}$).

In ref. [119] the authors define two different estimators:

$$\mathrm{MI}_{k,1}(X,Y) = \psi(k) - \overline{\psi(n_X+1) + \psi(n_Y+1)} + \psi(N_{tot}) \tag{IX.40}$$

and

$$\mathrm{MI}_{k,2}(X,Y) = \psi(k) - 1/k - \overline{\psi(n_{X,2}) + \psi(n_{Y,2})} + \psi(N_{tot}) \tag{IX.41}$$

$\psi$ being the digamma function and $\overline{(...)} = 1/N_{tot}\sum_i(...)$. $\mathrm{MI}_{k,1}$ and $\mathrm{MI}_{k,2}$ have approximatively the same properties that depend both on $k$ and $N_{tot}$. In ref. [119] it is argued that these estimators are minimally biased and are asymptotically unbiased.

### Transformation of our data

The estimator is expected to work better when the distributions are "flatten" due to a transformation [119]. Keeping in mind that the MI is invariant under the application of homeomorphisms on $X$ and $Y$, we can transform the data in order to have flatter density probability functions. We work with intensities that almost follow a Rayleigh law, thus the transformation we use is the following:

$$J = \exp\left(-\widetilde{\mathcal{I}}\right). \tag{IX.42}$$

This transformation applied to a Rayleigh law should give a flat density probability function. Since there are non gaussian correlations in T/T and in R/R, the density probability functions of the transformed data are note exactly flat as represented in Fig. IX.12.

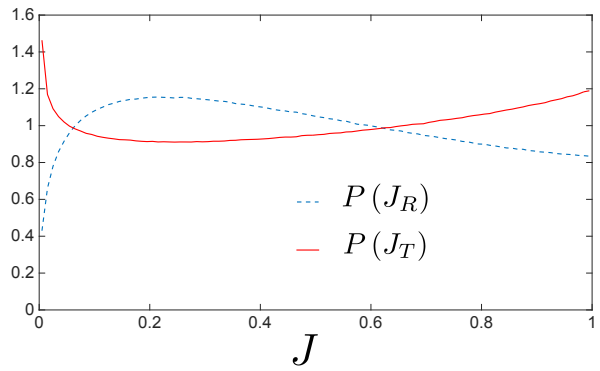


**Figure IX.12** – Statistics of the intensities in reflection and in transmission after the transformation given by Eq. (IX.42). The parameters of the scattering sample are: $b = 8$ and $k_0\ell = 10$.

### Definition of an estimator of the mutual information

The nearest neighbor method is costly in terms of computer time. Using first a ranking process on $X$ and $Y$ allows us to go from a complexity of the algorithm scaling as $N^2$ to a complexity scaling as $N\sqrt{kN}$ [119]. This quantity remains costly and we cannot perform the estimation of the MI with typically $10^8$ data. Moreover since we have no idea *a priori* of the standard deviation of the estimator, we decides to separate the $N_{tot}$ data into $N_{paq}N_p$ data, and perform $N_{paq}$ times the estimation of the MI using $N_p$ data. Doing so, we can numerically estimate the standard deviation of the estimator. Indeed, over $N_{paq}$ estimations, we can observe how the estimators fluctuates around its average value. Nonetheless, since we perform the estimation on a lower number of data $N_p$, each estimation will be more biased.

We propose the following estimator

$$\mathrm{MI}_{\mathrm{num}}(X,Y) = 1/(N_{paq}) \sum_{N_{paq}} \mathrm{MI}_{k,1}(X,Y) \tag{IX.43}$$

for which each $\mathrm{MI}_{k,1}$ is estimated over $N_p$ data. We can write that

$$\mathrm{MI}_{\mathrm{num}}(X,Y) = \mathrm{MI}(X,Y) + \delta_{\mathrm{MI}} + \mathcal{B} \tag{IX.44}$$

with $\mathrm{MI}(X,Y)$ the true value of the mutual information, $\delta_{\mathrm{MI}}$ the fluctuations due to the standard deviation of the estimator, and $\mathcal{B}$ its bias. Because Eq. (IX.43) is actually the unbiased estimation of the average value of the estimator $\mathrm{MI}_{k,1}$, we can express the order of magnitude of $\delta_{\mathrm{MI}}$ in terms of the standard deviation of $\mathrm{MI}_{k,1}$:

$$\delta_{\mathrm{MI}} \sim \frac{\sigma_{\mathrm{MI}_{k,1}}}{\sqrt{N_{paq}}}. \tag{IX.45}$$

Note that the bias $\mathcal{B}$ is exactly equal to the bias of the estimator $\mathrm{MI}_{k,1}$.

## IX.4.3 Accuracy of the estimator

In this section we study numerically the bias and the standard deviation of the estimator given by Eq. (IX.43) in order to find the best strategy to estimate $\mathrm{MI}(\mathcal{R},\mathcal{T})$.

### Study of the fluctuations $\delta_{\mathrm{MI}}$

The first interesting property is the standard deviation of the estimator. *A priori* the standard deviation depends on $N_p$, $k$, $n$ (dimension of $\mathcal{R}$ and $\mathcal{T}$) and $a$. In panel (a) in Fig. IX.13 we represent the numerical estimation of the standard deviation of the estimator $\mathrm{MI}_{k,1}$ given by Eq. (IX.40) versus $n = m$ for points separated by $a \simeq 4L$, for a scattering medium with optical thickness $b = 3$ and $k_0\ell = 10$. We observe no dependence of the standard deviation on the dimension of $\mathcal{R} = (\widetilde{\mathcal{I}}_{R_1}, ..., \widetilde{\mathcal{I}}_{R_m})$ and $\mathcal{T} = (\widetilde{\mathcal{I}}_{T_1} ..., \widetilde{\mathcal{I}}_{T_n})$.

In panel (b) in Fig. IX.13 we represent the estimation of the standard deviation of the estimator $\mathrm{MI}_{k,1}$ for $n = m = 1$ (geometry represented in Fig. IX.8) versus $\Delta R/L$ for a scattering medium with optical thickness $b = 3$ and $k_0\ell = 10$. We observe no dependence of the standard deviation on $\Delta R/L$, therefore on the value of the MI (which is changing substantially in the case $n = m = 1$ versus this parameter as seen in Fig. IX.15). In panel (c) in Fig. IX.13 we represent the estimation of the standard deviation of the estimator $\mathrm{MI}_{k,1}$ versus the parameter $k$ together with a $1/\sqrt{k}$ law for a

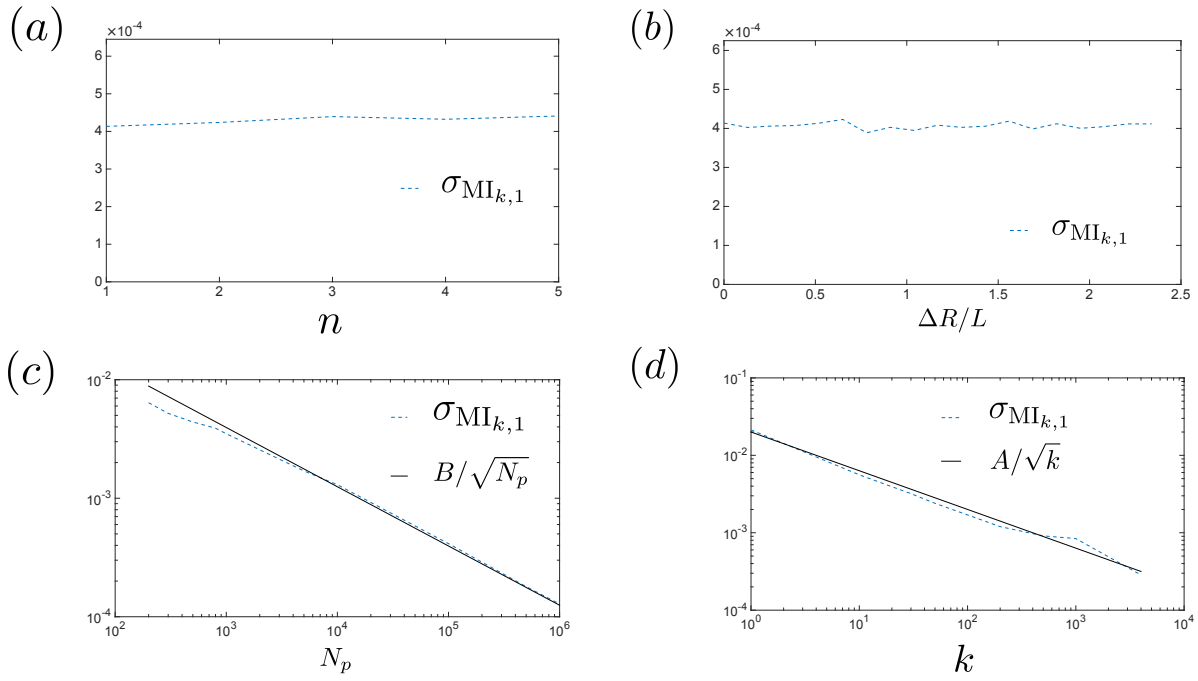


**Figure IX.13** – Panel (a): numerical estimation of the standard deviation of $\mathrm{MI}_{k,1}$ versus the dimensions of the vectors $\mathcal{R}$ and $\mathcal{T}$ for $k = 100$ and $N_p = 10^5$. Panel (b): Numerical estimation of the standard deviation of $\mathrm{MI}_{k,1}$ versus the transverse distance between the transmitted intensity and the reflected intensity for $n = m = 1$, $k = 100$ and $N_p = 10^5$. Panel (c): numerical estimation of the standard deviation of $\mathrm{MI}_{k,1}$ versus $N_p$ for $k = 100$ and panel (d): numerical estimation of the standard deviation of $\mathrm{MI}_{k,1}$ versus $k$ for $N_p = 10^5$. The parameters of the scattering sample are $b = 3$ and $k_0\ell = 10$, $A$ and $B$ are numerical constants.

scattering medium of optical thickness $b = 3$ and $k_0\ell = 10$. We can see that the standard deviation of the estimator $\mathrm{MI}_{k,1}$ scales as $1/\sqrt{k}$. In panel (d) in Fig. IX.13 we represent the estimation of the standard deviation of the estimator $\mathrm{MI}_{k,1}$ versus the parameter $N_p$ together with a $1/\sqrt{N_p}$ law for a scattering medium of optical thickness $b = 3$ and $k_0\ell = 10$. We can see that the standard deviation of the estimator $\mathrm{MI}_{k,1}$ scales as $1/\sqrt{N_p}$.

In conclusion $\delta_{\mathrm{MI}}$ has the following properties:

- $\delta_{\mathrm{MI}}$ decreases as $1/\sqrt{k}$,
- $\delta_{\mathrm{MI}}$ is independent of $n = m$ and of the value of the MI,
- $\delta_{\mathrm{MI}}$ depends on $N_{tot}$ as $1/\sqrt{N_{tot}}$ and does not depend on the splitting of the data into $N_{paq}$ ensembles of $N_p$ data.

### Study of the bias $\mathcal{B}$

The second important quantity is the bias $\mathcal{B}$ of the estimator. To illustrate the difficulty to handle a bias, we represent in panel (a) in Fig. IX.14 the estimation of the MI between one transmitted intensity and one reflected intensity versus the transverse distance normalized by $L$ using various parameters for the estimator. We consider a finite set of data with $N_{tot} \sim 10^8$, we vary $N_p$ and $N_{paq}$ and compare the estimation of the MI using the estimator given by Eq. (IX.43) with the estimation using the non biased histogram based estimator. We observe that the bias decreases when $N_p$ increases. We also observe that the bias depends on the value of the MI: it vanishes when the MI = 0

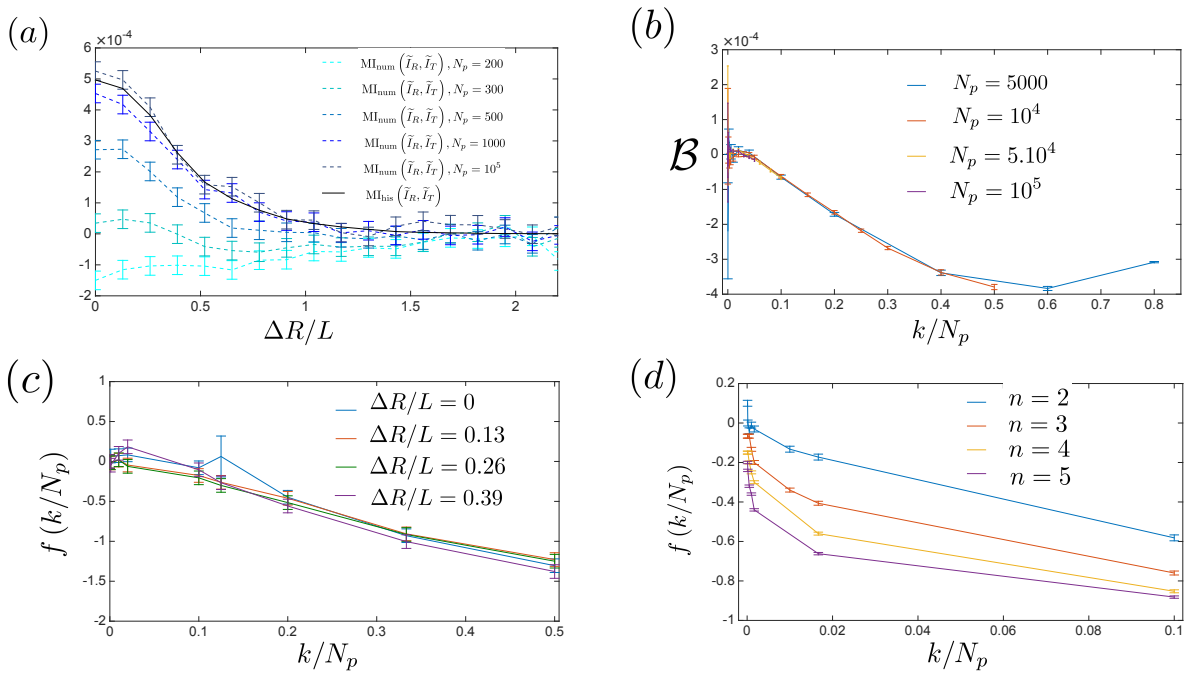


**Figure IX.14** – Panel (a): numerical estimation of $\mathrm{MI}_{\mathrm{num}}$ for $n = m = 1$ for various $N_p$ compared with $\mathrm{MI}_{\mathrm{his}}$ versus the transverse distance between the points normalized by $L$. Panel (b): numerical estimation of $\mathcal{B}$ for $n = m = 1$ for various $N_p$ versus $k/N_p$. Panel (c): numerical estimation of $f\left(k/N_p\right)$ for $n = m = 1$ for various $\Delta R$ between the points versus $k/N_p$. Panel (d): numerical estimation of $f\left(k/N_p\right)$ for various $n = m$ with $a \simeq 4L$ between the points versus $k/N_p$.

and seems to increase with the value of the MI. In panel (b) in Fig. IX.14 we follow ref. [119] and plot the bias $\mathcal{B}$ versus $k/N_p$ using various $N_p$ and observe that all the curves fall into a function of $k/N_p$.

In ref. [119] it is stated that if one considers a family of joint probabilities $\mu(x, y, r)$ depending smoothly on a single parameter $r$, then the bias is linear with the true value of the MI for each $r$. More precisely it reads

$$\mathcal{B}/\,\mathrm{MI} = f\left(k/N_p\right). \tag{IX.46}$$

In panel (c) in Fig. IX.14 we estimate numerically $\mathcal{B}/\,\mathrm{MI}$ versus $k/N_p$ for various transverse distance between the transmitted and the reflected intensities (thus for various MI) and observe that all the curves fall into the same function of $k/N_p$. In panel (d) we plot $\mathcal{B}/\,\mathrm{MI}$ versus $k/N_p$ for various $n = m$ and observe that the curves do not fall into the same function of $k/N_p$ meaning that in this case the guess of ref. [119] is not valid. We can see in panel (d) that the bias normalized by MI seems more important when $n = m$ increases. From this subsection we can conclude that:

- for fixed $n = m$ the bias is linear with the MI,
- the bias normalized by the true MI is a function of $f(k/N_p)$ with $f(0) = 0$, thus to decrease the bias we can whether increase $N_p$ or decrease $k$,
- this function $f(k/N_p)$ changes when $n = m$ changes.

## IX.5 Numerical results

In this section we use the estimator given by Eq. (IX.43), that has been characterized, to study the MI between reflection and transmission.

### IX.5.1 Mutual information between $\widetilde{I}_T$ and $\widetilde{I}_R$

In this subsection we start with the simplest configuration depicted in Fig. IX.8. We study the MI between one reflected intensity and one transmitted intensity versus the transverse distance between them. This low dimension case ($n = m = 1$) allows us to compare the results using the estimator given in Eq. (IX.43) with the non biased estimator using adaptable bin sized histogram.

#### MI $\left(\widetilde{I}_T, \widetilde{I}_R\right)$ to zeroth order in terms of $C_2^{TT}$ and $C_2^{RR}$

From the analytical study we know that the dominant term of the MI should be on the order of $\left(C_2^{RT}\right)^2/(2\log[2])$ [term denoted by $\mathrm{MI}_1$ in Eq. (IX.16)]. Because this value is small, we need a large value of the parameter $k$ of the estimator given in Eq. (IX.43) not to be blurred by the standard deviation of the estimator. Since this is a one dimensional problem ($n = m = 1$) we can use a strong value of $k$ without getting a strong bias.

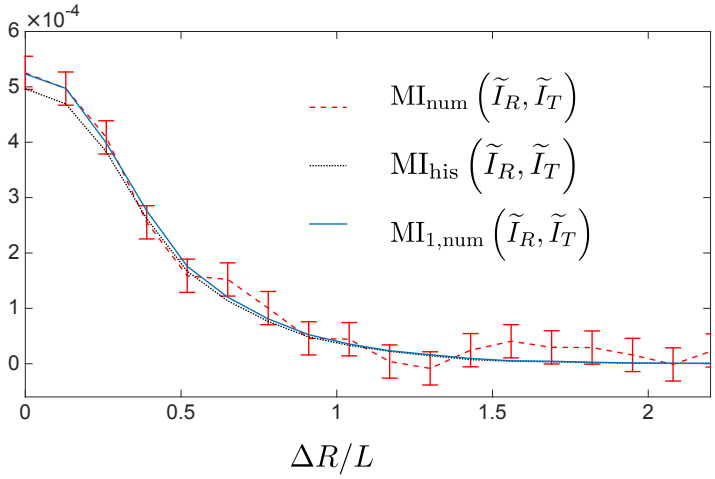


**Figure IX.15** – Numerical estimation of MI $\left(\widetilde{I}_T, \widetilde{I}_R\right)$ using using the estimator given in Eq. (IX.43) with the parameters $k = 100$, $N_p = 10^5$ and $N_{paq} = 1200$ (red dashed line) together with the numerical estimation using the adaptable histogram based estimator applied on the $N = 1.2 \times 10^8$ data (black dotted line). We compare those two curves with the semi-analytical calculation of Eq. (IX.47) (blue solid line). The parameters of the scattering sample are $b = 3$ and $k_0\ell = 10$.

In Fig. IX.15 we plot the numerically estimated MI using Eq. (IX.43) together with the MI estimated using the histogram based estimator. We compare these estimations with the trace formula $\mathrm{MI}_1$:

$$\mathrm{MI}(\widetilde{I}_R, \widetilde{I_T}) \simeq \mathrm{MI}_1(\widetilde{I}_R, \widetilde{I_T}) = \frac{1}{2\log(2)}\left[C_2^{RT}(\Delta R)\right]^2. \tag{IX.47}$$

We call $\mathrm{MI}_{1,\mathrm{num}}(\widetilde{I}_R, \widetilde{I_T})$ the semi-analytical function given by Eq. (IX.47) with $C_2^{RT}$ estimated numerically. The parameters of the scattering medium are $b = 3$ and $k_0\ell = 10$ (we prefer to estimate $C_2^{RT}$

numerically since the expression in the diffusive regime is not valid for moderate optical thickness). We observe that the MI between $\widetilde{I}_T$ and $\widetilde{I}_R$ is very well represented by the trace formula to first order in $1/(k_0\ell)$.

This result confirms the conclusion drawn from the analytical study of $\mathrm{MI}_1(\widetilde{I}_R, \widetilde{I_T})$ in Eq. (IX.22). In 2D $\mathrm{MI}(\widetilde{I}_R, \widetilde{I_T})$ scales as $1/(k_0L)^2$ while in 3D it scales as $1/(k_0L)^4$. It takes non zero value on a typical transverse distance $L$.

### MI $\left(\widetilde{I}_T, \widetilde{I}_R\right)$ with first order corrections in terms of $C_2^{TT}$ and $C_2^{RR}$

The trace formula given by Eq. (IX.47) is the first term of a development in $1/(k_0\ell)$ (both $C_2^{RR}$ and $C_2^{TT}$ scale with this quantity). Nonetheless, for $b = 3$ and $k_0\ell = 10$, the non gaussian correlation $C_2^{TT}(\Delta R = 0) \simeq 0.15$ which is not negligible. The trace formula taking into account the first order correction in terms of $1/(k_0\ell)$ [term denoted by $\mathrm{MI}_2$ in Eq. (IX.17)] reads in the $n = m = 1$ case

$$\mathrm{MI}_2(\widetilde{I}_R, \widetilde{I}_T) = \frac{1}{2\log(2)} C_2^{RT}(\Delta R)^2 \left(1 - C_2^{TT}(0) - C_2^{RR}(0)\right). \tag{IX.48}$$

We call $\mathrm{MI}_{2,\mathrm{num}}(\widetilde{I}_R, \widetilde{I}_T)$ its semi-analytical calculation using numerical calculation for the non gaussian correlations. In Fig. IX.16 we represent $\mathrm{MI}_{2,\mathrm{num}}(\widetilde{I}_R, \widetilde{I}_T)$ and compare it with the numerically estimated MI using Eq. (IX.43) together with the MI estimated using the histogram based estimator. We observe that, because of the strong amplitude of $C_2^{TT}$, $\mathrm{MI}_{2,\mathrm{num}}(\widetilde{I}_R, \widetilde{I}_T)$ does not represent better the numerical MI than $\mathrm{MI}_{1,\mathrm{num}}(\widetilde{I}_R, \widetilde{I}_T)$. This reveals that we work at the limit of the regime $C_2^{TT} \ll 1$ and $C_2^{RR} \ll 1$.

### MI $\left(\widetilde{I}_T, \widetilde{I}_R\right)$ taking into second order corrections in terms of $C_2^{TT}$ and $C_2^{RR}$

We thus go to higher orders in terms of $C_2^{TT}$ and $C_2^{RR}$ [term denoted by $\mathrm{MI}_3$ in Eq. (IX.18)]. It reads

$$\begin{aligned}\mathrm{MI}_3(\widetilde{I}_R, \widetilde{I}_T) = &\frac{1}{2\log(2)} C_2^{RT}(\Delta R)^2 \\ &\times \left(1 - C_2^{RR}(0) + 5C_2^{RR}(0)^2 - C_2^{TT}(0) + 5C_2^{TT}(0)^2 + C_2^{TT}(0)C_2^{RR}(0)\right). \end{aligned}\tag{IX.49}$$

We call $\mathrm{MI}_{3,\mathrm{num}}(\widetilde{I}_R, \widetilde{I}_T)$ the trace formula where the non gaussian correlations are evaluated numerically. In Fig. IX.16 we observe that $\mathrm{MI}_{3,\mathrm{num}}(\widetilde{I}_R, \widetilde{I}_T)$ is in good agreement with the numerical results. Note that both $\mathrm{MI}_3(\widetilde{I}_R, \widetilde{I}_T)$ and $\mathrm{MI}_2(\widetilde{I}_R, \widetilde{I}_T)$ tend towards $\mathrm{MI}_1(\widetilde{I}_R, \widetilde{I}_T)$ when $k_0\ell \gg 1$ (because $n = m = 1$).

## IX.5.2 Mutual information between $\mathcal{R} = (\widetilde{\mathcal{I}}_{R_1}, ..., \widetilde{\mathcal{I}}_{R_m})$ and $\mathcal{T} = (\widetilde{\mathcal{I}}_{T_1} ..., \widetilde{\mathcal{I}}_{T_n})$

The conclusion from the previous subsection is that MI $\left(\widetilde{I}_T, \widetilde{I}_R\right)$ scales with $1/(k_0L)^2$ in 2D while in 3D it scales with $1/(k_0L)^4$. These are small quantities, and we could argue now that the information contained in reflection on the transmission is small. This is not always accurate, indeed there are many speckle spots available in reflection possessing information on the transmission.

Let us enter the numerical estimation of the MI between $n$ reflected intensities "aligned" ($d_{i,i}^{RT} = 0$) with $n$ transmitted intensities as represented in Fig. IX.10. The distance between each neighbor in

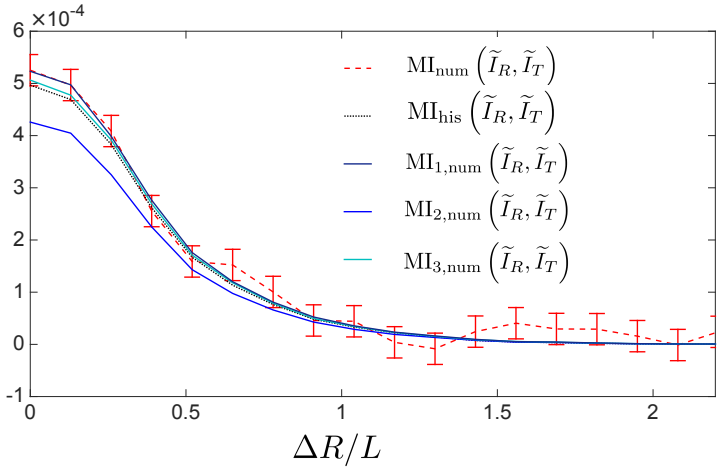


**Figure IX.16** – Numerical estimation of MI $\left(\widetilde{I}_T,\widetilde{I}_R\right)$ using the estimator given in Eq. (IX.43) with the parameters $k=100$, $N_p=10^5$ and $N_{paq}=1200$ (red dashed line) together with the numerical estimation using the adaptable histogram estimator applied on the $N=1.2\times10^8$ data (black dotted line). We compare those two curves with the semi-analytical calculation of Eq. (IX.47), Eq. (IX.48) and Eq. (IX.49) (solid lines). The parameters of the scattering sample are: $b=3$ and $k_0\ell=10$

transmission or reflection is $d^{TT}_{i,i+1}=d^{RR}_{i,i+1}=a$. The analytical study of this configuration summarized in Fig. IX.11 showed that for all the regimes captured by the analytical model, increasing the number of points increases the MI between $\mathcal{R}$ and $\mathcal{T}$. We also observed analytically that the competing effects between non gaussian correlations in R/T, and in T/T and R/R ,is the cause of the existence of a maximum of the curves MI($k_0a$). Here we intend to confirm numerically these results, and discuss the regime $k_0a\leq1$ that is out of reach analytically.

### Numerical results without compensation for the bias

In this section we study numerically the MI between $\mathcal{R}=(\widetilde{\mathcal{I}}_{R_1},...,\widetilde{\mathcal{I}}_{R_m})$ and $\mathcal{T}=(\widetilde{\mathcal{I}}_{T_1}...,\widetilde{\mathcal{I}}_{T_n})$ versus $k_0a$, and versus the number of points $n=m$ (we consider the same number of points in reflection and in transmission). We consider two optical thicknesses $b=3$ and $b=8$ and expect to see the shift of the maximum of the MI versus $k_0a$ when the optical thickness increases. The numerical estimation of the MI [done with the estimator given in Eq. (IX.43)] for $b=3$ is easier than for $b=8$ since the value to estimate is larger. The result is that we are less sensitive to the standard deviation of the estimator and can choose a value of $k=10$, $N_{paq}=600$ and $N_p=10^5$. For $b=8$ it is harder because $(C_2^{RT})^2$ (which gives the overall amplitude of the MI) is much smaller. We thus choose a value of $k=100$ in order not to be sensitive to the standard deviation of the estimator, but the result in this case is really sensitive to the bias thus we increase the value of $N_p=10^6$ decreasing $N_{paq}=60$. In Fig. IX.17 we represent the results obtained for $n=m$ going from 2 to 5, both in linear scale, and in log scale for the $x$ axis in order to separate better the different regimes. In these curves we observe three different regimes:

- In the regime $k_0a\gg k_0L$, the problem reduces to $n$ times the $n=m=1$ problem. Indeed the various pairs of points are so separated that there are no cross talk between them. We thus have an information that should scale linearly with $n$. More precisely, it is equal to $n$ times the value at $\Delta R=0$ of the $n=m=1$ information.
- The regime $k_0L\sim k_0a\gg1$ is the most difficult to analyze. In this regime, there exists cross talks between the different pairs of points that increase the information compared to the regime

$k_0 a \gg k_0 L$. In this regime the information seems also to scale with $n = m$.

- The regime $k_0 a \leq 1$ is quite easy to understand based on numerical calculations. In this regime all the $n = m$ pairs of points are in the same speckle spot. Thus increasing $n = m$ has no effect on the information which is equal to the $n = m = 1$ information. Because this regime is out of our reach analytically (the $C_1$ correlation in T/T and R/R is important in this regime), this conclusion could not be obtained from the analytical study.

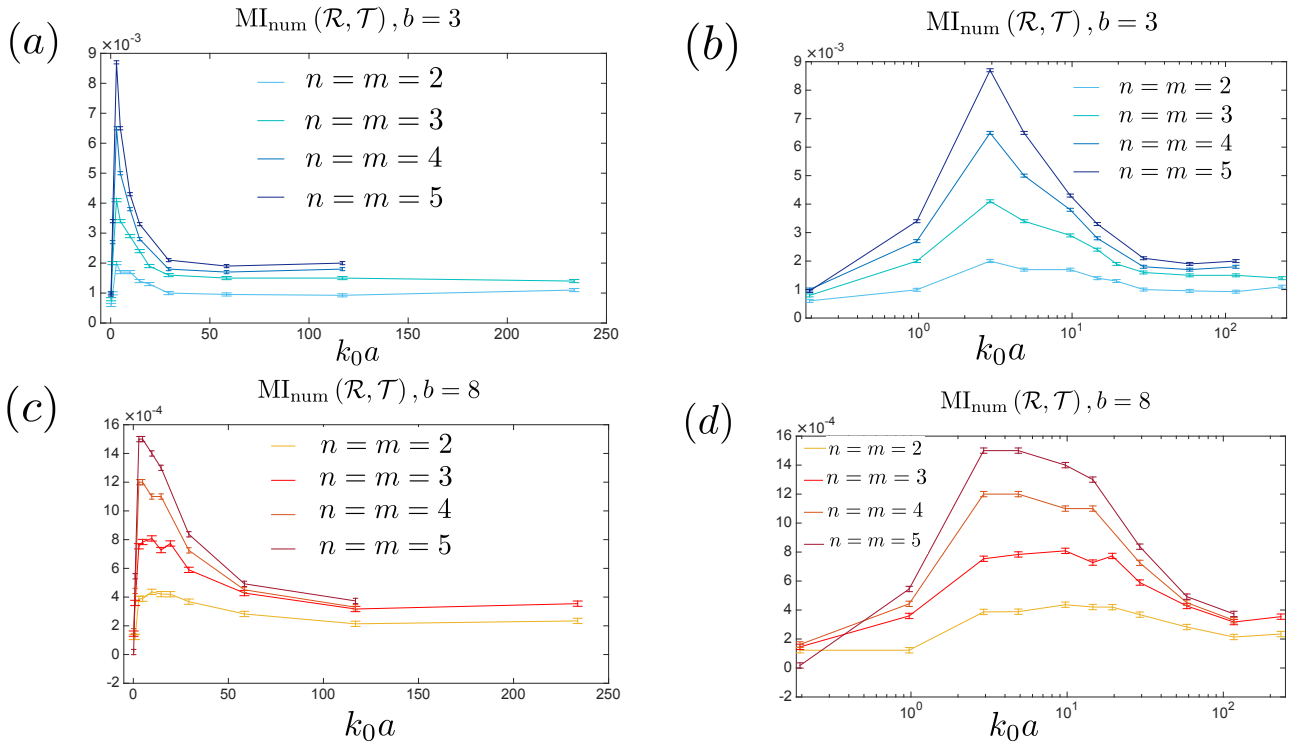


**Figure IX.17** – Panel (a) [respectively panel (c)]: numerical estimation of MI using the estimator given in Eq. (IX.43) versus $k_0 a$ for $n = m$ going to 2 to 5 for $b = 3$ (respectively $b = 8$) and $k_0 \ell = 10$. Panel [respectively panel (d)]: numerical estimation of MI using the estimator given in Eq. (IX.43) versus $k_0 a$ in log scale for the $x$ coordinates for $n = m$ going to 2 to 5 for $b = 3$ (respectively $b = 8$) and $k_0 \ell = 10$. The parameters chosen for the estimator given in Eq. (IX.43) are $k = 10$, $N_p = 10^5$ and $N_{paq} = 600$ for $b = 3$ and $k = 100$, $N_p = 10^6$ and $N_{paq} = 60$ for $b = 8$.

## Comparison with the trace formulas

In Fig. IX.18 we compare the various trace formulas with the estimation of the MI for $n = m = 5$ with $b = 3$ and $b = 8$. To compare the numerical data with semi analytical calculations, we first have to discuss the bias.

Our method is the following: we use the fact (observed numerically) that the bias normalized by the real value of MI seems to be a function of $n = m$ only, combined with the knowledge that the MI for $k_0 a \gg k_0 L$ is $n = m$ times the MI for $n = m = 1$ at $\Delta R = 0$. For $b = 3$ we know precisely this value thanks to the precise study summarized in Fig. IX.15. For $b = 8$ we did not perform the same study, we rather used the analytical expression of $\mathrm{MI}_{3,\mathrm{num}}(\mathcal{R},\mathcal{T})$ for $k_0 a \gg k_0 L$ as a reference value.

Once we have this value, we multiply all the curves by this reference value divided by the value of the estimation with bias. This operation should remove the bias for all points. We call $\widetilde{\mathrm{MI}}$ the value of the MI corrected for bias using this procedure.

In panels (a) and (c) in Fig. IX.18 we represent $\widetilde{\mathrm{MI}}$ versus the various trace formulas. For $b = 3$ the amplitude of the functions changes less than for $b = 8$ due to the difference of amplitude of $C_2^{TT}$ in the two cases ($C_2^{TT}(0) \simeq 0.45$ for $b = 8$ and $C_2^{TT}(0) \simeq 0.15$ for $b = 3$). To appreciate the difference of shape of the trace formula functions, we represent in panels (b) and (d) all the curves normalized to the value of $\mathrm{MI}_{3,\mathrm{num}}(\mathcal{R},\mathcal{T})$ for $k_0a \gg k_0L$ ( the superscript $\widetilde{(...)}$ over the trace formulas[6] means normalized to the value of $\mathrm{MI}_{3,\mathrm{num}}(\mathcal{R},\mathcal{T})$ for $k_0a \gg k_0L$). We observe that $\mathrm{MI}_{1,\mathrm{num}}(\mathcal{R},\mathcal{T})$ represent the data quite well for large $k_0a$, but does not reproduce the decrease of the function for small $k_0a$. $\mathrm{MI}_{2,\mathrm{num}}(\mathcal{R},\mathcal{T})$ and $\mathrm{MI}_{3,\mathrm{num}}(\mathcal{R},\mathcal{T})$ both capture the decrease of the function for small $k_0a$ but have different shape especially for $b = 8$. Basically, going to second order in terms of $C_2^{TT}$ and $C_2^{RR}$ with $\mathrm{MI}_3(\mathcal{R},\mathcal{T})$ weakens the corrective terms responsible for the decrease of the function for small $k_0a$, and thus shifts the position of the maximum towards small $k_0a$ [in comparison with $\mathrm{MI}_2(\mathcal{R},\mathcal{T})$]. This explains why the shape of the functions are different.

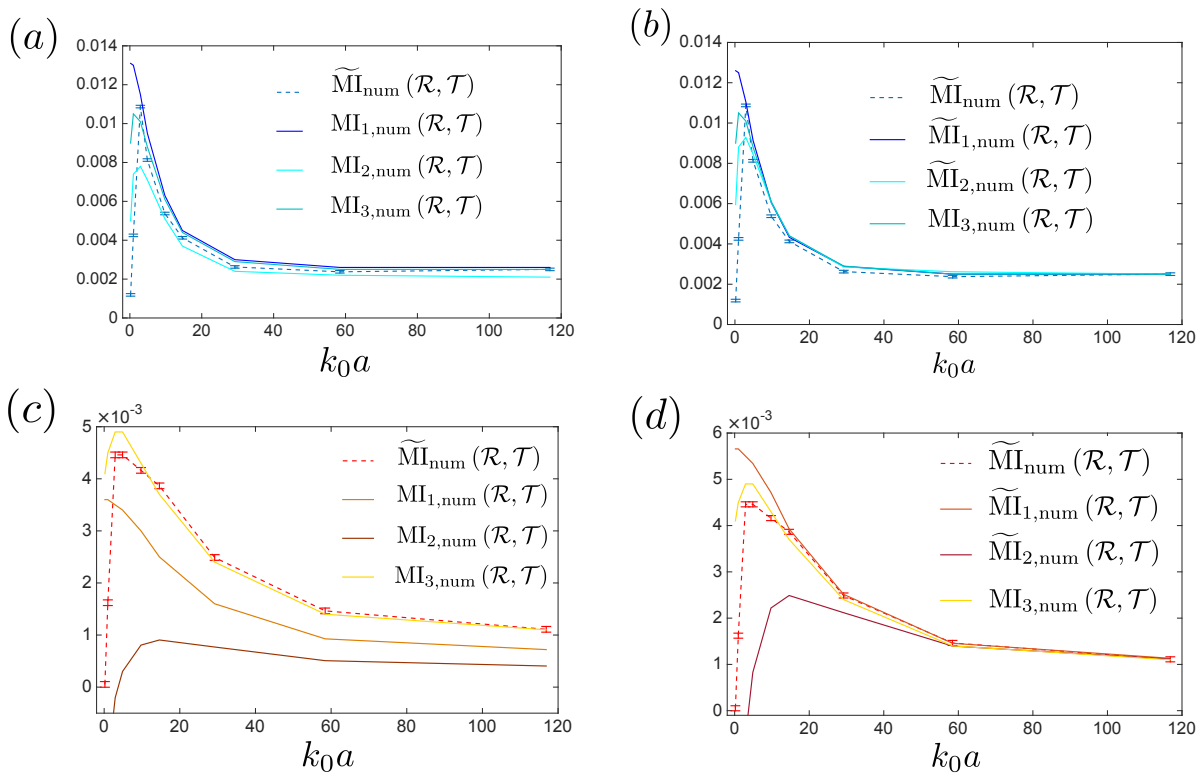


**Figure IX.18** – Panel (a) (respectively panel (c)) comparison of the numerically estimated $\widetilde{\mathrm{MI}}$ with three different trace formulas versus $k_0a$ for $b = 3$ (respectively $b = 8$) and $k_0\ell = 10$ for $n = m = 5$. In panels (b) and (d) we normalize all the trace formulas by the value for $k_0a \gg k_0L$ in order to compare only the form of the functions. The parameters chosen for the estimator given in Eq. (IX.43) are $k = 10$ $N_p = 10^5$ and $N_{paq} = 600$ for $b = 3$ and $k = 100$ $N_p = 10^6$ and $N_{paq} = 60$ for $b = 8$.

This study allows us to give the main conclusion of this subsection. The shape and the amplitude of the MI changes with the optical thickness. When the optical thickness increases (keeping $k_0\ell$ constant) the amplitude of the MI decreases due to the decrease of the R/T non gaussian correlation with $k_0L$. An important and subtle result is that the position of the maximum of the function $\mathrm{MI}(k_0a)$ increases with the optical thickness, as observed in panels (c,d) in Fig. IX.17.

[6]For instance $\widetilde{\mathrm{MI}}_{2,\mathrm{num}} = \mathrm{MI}_{2,\mathrm{num}}\,[\mathrm{MI}_{3,\mathrm{num}}(k_0a \gg k_0L)/\,\mathrm{MI}_{2,\mathrm{num}}(k_0a \gg k_0L)]$.

# IX.6 Conclusion and future work

## IX.6.1 Conclusion

Let us here summarize the results of this chapter, and discuss some possible future work. We have studied analytically and numerically the MI between an arbitrary number of speckle spots in reflection and in transmission.

The MI between one transmitted and one reflected speckle spot is proportional to the square of the non gaussian intensity correlation function between the two intensities. It thus takes a non zero value for points separated by transverse distances less or equal than $L$, and scales as $1/(k_0L)^2$ in 2D and $1/(k_0L)^4$ in 3D.

When the number of points in transmission and in reflection increases, many degrees of freedom add to the problem. In this study we consider the same number of reflected and transmitted speckle spots. Moreover, we chose to align them ($d_{i,i}^{RT} = 0$). Doing so we reduced the parameters of the problem to $k_0a$, $n = m$, $k_0L$ and $k_0\ell$. We have studied numerically the MI versus $k_0a$ for $n = m$ ranging from to 2 to 5, and for two different optical thicknesses ($b = 3$ and $b = 8$) for dilute ($k_0\ell = 10$) scattering sample. We observed a rich behavior of the curves with three different regimes of $k_0a$:

- When $k_0a \gg k_0L$ the problem reduces to $n = m$ times the $n = m = 1$ problem (due to the absence of cross talks between pairs of reflected and transmitted intensities). The MI thus scales as $n/(k_0L)^2$ in 2D and $n/(k_0L)^4$ in 3D.
- When $k_0a \sim k_0L$, the MI increases strongly due to the increasing weight of $C_2^{RT}$ between different pairs of points. When $k_0a$ decreases, these curves have a maximum. We explained the presence of this maximum with the increasing weight of long range correlations in T/T and R/R when $k_0a$ decreases. The position of the maximum is predicted to scale with $k_0a = b$. The MI at the position of the maximum scales with $n/(k_0L)^2$ in 2D and $n/(k_0L)^4$ in 3D (and should depend on $b$ as observed analytically in panel (c) of Fig. IX.11).
- When $k_0a \leq 1$, the MI tends toward the MI for $n = m = 1$ because all intensities lie in the same speckle spot. Thus the MI in this regime scales $1/(k_0L)^2$ in 2D and $1/(k_0L)^4$ in 3D.

## IX.6.2 Future work

Let us discuss a few possible extensions. The part of the curves for which we lack knowledge here is the value of the MI at the maximum of the curves. A precise study of this would be useful[7]. We believe the easiest way to study this part of the curve precisely is to follow the panel (c) in Fig. IX.11 fixing $k_0L \gg 1$ and varying the optical thickness (but keeping it large compared to one). It would also be nice to capture the $C_1$ correlation in the model so that we could describe analytically the entire function MI($k_0a$). Eventually, it is necessary to learn how to use the MI between reflection and transmission in real applications. For instance, in the context of imaging though a scattering medium. The MI could also help focusing light in transmission measuring only reflected intensities. In the next chapter we make one step in this direction studying how we can use the information contained on a large number of reflected speckles to change the average value of one transmitted intensity.

[7]Note that this study has been done in [116]

# Chapter X

# Conditional statistics of the transmitted intensity

## Table des matières

The purpose of this chapter is to study a property equivalent to the statistical dependence between $\mathcal{R} = (\tilde{\mathcal{I}}_{R_1}, ..., \tilde{\mathcal{I}}_{R_m})$ and $\mathcal{T} = (\tilde{\mathcal{I}}_{T_1} ..., \tilde{\mathcal{I}}_{T_n})$: the difference between the conditional statistics of $\mathcal{T}$ with some knowledge of $\mathcal{R}$, and the statistics of $\mathcal{T}$ without knowledge of $\mathcal{R}$. The negative correlation means that on average a bright reflected intensity coincides with a dark transmitted intensity and vice versa. Nonetheless we cannot predict how the variation of the average value of $\mathcal{T}$ depends on the measurement done on $\mathcal{R}$ only with the knowledge of the correlation. In ref. [85] we numerically observed the change in the average transmitted intensity when the reflected intensity was known to be bright or dark, but since we did not (at this time) know the analytical expression Eq. (VIII.33) of the joint probability in R/T we could not describe this phenomena in detail. The study of $C_2^{RT}$ combined with the analysis of MI$(\mathcal{R}, \mathcal{T})$ lead us to interest ourselves to the impact of a constraint (for instance the restriction to disorder realizations where all the reflected intensities are bright) applied on many reflected speckle spots on the statistics of the transmitted intensity at one point as represented in Fig. X.1. We believe that this study is relevant due to its relationship to wavefront shaping experiment.

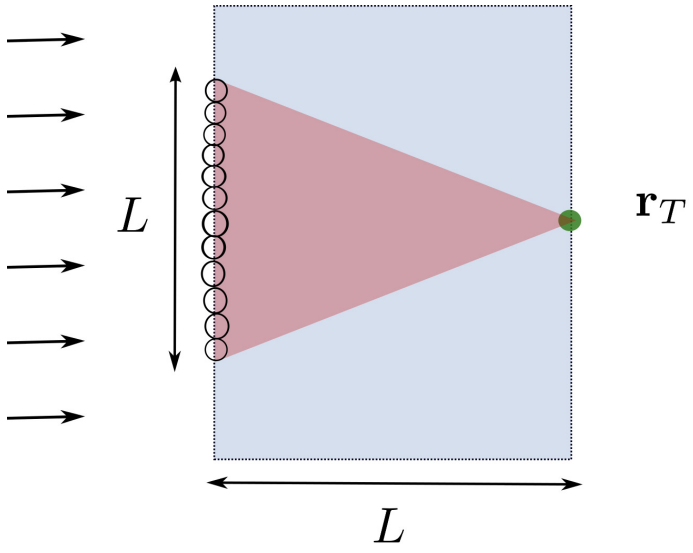


**Figure X.1** – Schema of the geometry studied in this chapter. A wave illuminates a scattering medium with depth $L$ and scattering mean free path $\ell \ll L$. Due to multiple scattering process, one transmitted intensity is correlated with many independent reflected speckle spots (dark circles separated by a transverse distance on the order of $\lambda$) on a transverse size that remains smaller than $L$.

In this chapter we use our knowledge about the joint statistics between $\mathcal{R}$ and $\mathcal{T}$ detailed in Chap. VIII to study the conditional statistics of one transmitted speckle spot given some information on the reflected intensity. We first derive analytically the conditional statistics of the transmitted intensity for two different types of constraints[1] in reflection (bright or dark). Then we study the average value of the conditional statistics of the transmitted intensity versus the strength of the constraint, the parameters of the physical problem and the number of reflected intensities considered.

[1]We call constraint the information that the reflected intensities belongs to a sub-ensemble of $\mathbb{R}_+$.

Then we numerically estimate these quantities and compare them to the analytical model, before concluding by discussing the possible applications of this study to wavefront shaping techniques.

# X.1 Analytical study

## X.1.1 Conditional statistics

In Chap. VIII we have shown that the analytical expression of the joint distribution between one transmitted intensity (normalized by its average value) and $N_R$ reflected normalized intensities separated by transverse distances larger than $\lambda$ can be cast in the form

$$P(\tilde{\mathcal{I}}_{R_1},...,\tilde{\mathcal{I}}_{R_{N_R}},\tilde{\mathcal{I}}_T) = P(\tilde{\mathcal{I}}_{R_1},...,\tilde{\mathcal{I}}_{R_{N_R}})P(\tilde{\mathcal{I}}_T)\left(1+\sum_i^{N_R} C_2^{R_iT} v_i(\tilde{\mathcal{I}}_{R_1},...,\tilde{\mathcal{I}}_{R_{N_R}})v(\tilde{\mathcal{I}}_T)\right) \tag{X.1}$$

with

$$v_i(X_1,...X_N) = \frac{1}{P(X_1,...X_N)}\frac{\partial}{\partial X_i}\left[X_i\frac{\partial}{\partial X_i}P(X_1,...X_N)\right] \tag{X.2}$$

$X$ being either $\tilde{\mathcal{I}}_R$ or $\tilde{\mathcal{I}}_T$. In this chapter we are interested in the conditional statistics of the transmitted intensity knowing that $(\tilde{\mathcal{I}}_{R_1},...,\tilde{\mathcal{I}}_{R_{N_R}}) \in \mathcal{V}$, with $\mathcal{V}$ an ensemble of $\mathbb{R}_+^{N_R}$. We consider two different ensembles $\mathcal{V}_+$ and $\mathcal{V}_-$ defined the following way:

$$\begin{cases} \mathcal{V}_- = [0,v]^{N_R}, \\ \mathcal{V}_+ = [v,\infty]^{N_R}. \end{cases} \tag{X.3}$$

The parameter $v$ defines the strength of the constraint. In $\mathcal{V}_-$, we consider only reflected intensities smaller than $v$ times their average values, while in $\mathcal{V}_+$ we consider only transmitted intensities larger than $v$ times their average value. Although we assume a uniform constraint applied on all the $N_R$ reflected points, it is clear that this study can be generalized to arbitrary $\mathcal{V}$.

Let us define $P_\mathcal{V}(\tilde{\mathcal{I}}_T)$ as

$$P_\mathcal{V}(\tilde{\mathcal{I}}_T) = \frac{\int_\mathcal{V} P(\tilde{\mathcal{I}}_{R_1},...,\tilde{\mathcal{I}}_{R_{N_R}},\tilde{\mathcal{I}}_T)\mathrm{d}\tilde{\mathcal{I}}_{R_1}...\mathrm{d}\tilde{\mathcal{I}}_{R_{N_R}}}{\int_\mathcal{V} P(\tilde{\mathcal{I}}_{R_1},...,\tilde{\mathcal{I}}_{R_{N_R}})\mathrm{d}\tilde{\mathcal{I}}_{R_1}...\mathrm{d}\tilde{\mathcal{I}}_{R_{N_R}}}. \tag{X.4}$$

$P_\mathcal{V}(\tilde{\mathcal{I}}_T)$ is the conditional probability density function of $\tilde{\mathcal{I}}_T$ knowing that $(\tilde{\mathcal{I}}_{R_1},...,\tilde{\mathcal{I}}_{R_{N_R}}) \in \mathcal{V}$. Inserting Eq. (X.1) into Eq. (X.4) and performing the integral we obtain

$$P_\mathcal{V}(\tilde{\mathcal{I}}_T) = P(\tilde{\mathcal{I}}_T) + \sum_i^{N_R} C_2^{R_iT} \frac{\partial_{\tilde{\mathcal{I}}_T}\left[\tilde{\mathcal{I}}_T\partial_{\tilde{\mathcal{I}}_T}P\left(\tilde{\mathcal{I}}_T\right)\right]\left[\tilde{\mathcal{I}}_{R_i}\partial_{\tilde{\mathcal{I}}_{R_i}}P\left(\tilde{\mathcal{I}}_{R_1},...,\tilde{\mathcal{I}}_{R_{N_R}}\right)\right]_{\mathcal{V}_{i,\inf}}^{\mathcal{V}_{i,\sup}}}{\int_\mathcal{V} P(\tilde{\mathcal{I}}_{R_1},...,\tilde{\mathcal{I}}_{R_{N_R}})\mathrm{d}\tilde{\mathcal{I}}_{R_1}...\mathrm{d}\tilde{\mathcal{I}}_{R_{N_R}}}. \tag{X.5}$$

Equation (X.5) is valid for every $\mathcal{V}$, $\mathcal{V}_{i,\sup}$ is the upper limit of the constrained $\tilde{\mathcal{I}}_{R_i}$ and $\mathcal{V}_{i,\inf}$ its lower limit (for instance $\mathcal{V}_{+,i,\sup} = \infty$ and $\mathcal{V}_{+,i,\inf} = v$). Using the analytical expression of the probability density function of the normalized transmitted intensity, given in Eq. (VIII.13), in Eq. (X.5) we

obtain

$$P_{\mathcal{V}}(\tilde{\mathcal{I}}_T) = \exp\left(-\tilde{\mathcal{I}}_T\right)\left[1 + C_2^{TT}\left(\tilde{\mathcal{I}}_T^2 - 4\tilde{\mathcal{I}}_T + 2\right) + (\tilde{\mathcal{I}}_T - 1)\sum_i^{N_R} C_2^{R_iT}\frac{\left[\tilde{\mathcal{I}}_{R_i}\partial_{\tilde{\mathcal{I}}_{R_i}}\left(P(\tilde{\mathcal{I}}_{R_1},...,\tilde{\mathcal{I}}_{R_{N_R}})\right)\right]_{\mathcal{V}_{i,\inf}}^{\mathcal{V}_{i,\sup}}}{\int_{\mathcal{V}} P(\tilde{\mathcal{I}}_{R_1},...,\tilde{\mathcal{I}}_{R_{N_R}})\mathrm{d}\tilde{\mathcal{I}}_{R_1}...\mathrm{d}\tilde{\mathcal{I}}_{R_{N_R}}}\right]. \quad \text{(X.6)}$$

In Eq. (X.6), the transmitted intensity has been retained up to first order in $1/(k_0\ell)$.

### X.1.2 Conditional average value of the transmitted intensity

The conditional average value of the transmitted intensity is an interesting quantity for two main reasons: the simplicity of its study and the possibility that it may be the good observable to describe a wavefront shaping experiment in transmission using a reflected feedback. Let us define

$$\begin{cases} \langle\tilde{\mathcal{I}}_T\rangle_+ = \int \tilde{\mathcal{I}}_T P_{\mathcal{V}_+}(\tilde{\mathcal{I}}_T)\mathrm{d}\tilde{\mathcal{I}}_T, \\ \langle\tilde{\mathcal{I}}_T\rangle_- = \int \tilde{\mathcal{I}}_T P_{\mathcal{V}_-}(\tilde{\mathcal{I}}_T)\mathrm{d}\tilde{\mathcal{I}}_T. \end{cases} \quad \text{(X.7)}$$

$\langle\tilde{\mathcal{I}}_T\rangle_+$ is the conditional average value of the transmitted intensity knowing that $(\tilde{\mathcal{I}}_{R_1},...,\tilde{\mathcal{I}}_{R_{N_R}}) \in \mathcal{V}_+$ (*i.e.*, reflected intensities are bright). $\langle\tilde{\mathcal{I}}_T\rangle_-$ is the conditional average value of the transmitted intensity knowing that $(\tilde{\mathcal{I}}_{R_1},...,\tilde{\mathcal{I}}_{R_{N_R}}) \in \mathcal{V}_-$ (dark reflected intensities). Inserting Eq. (X.6) into Eq. (X.7) we can show that

$$\langle\tilde{\mathcal{I}}_T\rangle_+ = 1 + \sum_i^{N_R} C_2^{R_iT}\frac{\left[\tilde{\mathcal{I}}_{R_i}\partial_{\tilde{\mathcal{I}}_{R_i}}\left(P(\tilde{\mathcal{I}}_{R_1},...,\tilde{\mathcal{I}}_{R_{N_R}})\right)\right]_v^\infty}{\int_{\mathcal{V}_+} P(\tilde{\mathcal{I}}_{R_1},...,\tilde{\mathcal{I}}_{R_{N_R}})\mathrm{d}\tilde{\mathcal{I}}_{R_1}...\mathrm{d}\tilde{\mathcal{I}}_{R_{N_R}}} \quad \text{(X.8)}$$

and

$$\langle\tilde{\mathcal{I}}_T\rangle_- = 1 + \sum_i^{N_R} C_2^{R_iT}\frac{\left[\tilde{\mathcal{I}}_{R_i}\partial_{\tilde{\mathcal{I}}_{R_i}}\left(P(\tilde{\mathcal{I}}_{R_1},...,\tilde{\mathcal{I}}_{R_{N_R}})\right)\right]_0^v}{\int_{\mathcal{V}_-} P(\tilde{\mathcal{I}}_{R_1},...,\tilde{\mathcal{I}}_{R_{N_R}})\mathrm{d}\tilde{\mathcal{I}}_{R_1}...\mathrm{d}\tilde{\mathcal{I}}_{R_{N_R}}}. \quad \text{(X.9)}$$

To zeroth order in terms of non gaussian correlations in R/R, we have

$$\begin{cases} \int_{\mathcal{V}_+} P(\tilde{\mathcal{I}}_{R_1},...,\tilde{\mathcal{I}}_{R_{N_R}})\mathrm{d}\tilde{\mathcal{I}}_{R_1}...\mathrm{d}\tilde{\mathcal{I}}_{R_{N_R}} = [\exp(-N_R v)], \\ \left[\tilde{\mathcal{I}}_{R_i}\partial_{\tilde{\mathcal{I}}_{R_i}}\left(P(\tilde{\mathcal{I}}_{R_1},...,\tilde{\mathcal{I}}_{R_{N_R}})\right)\right]_v^\infty = -v\,[\exp(-N_R v)], \end{cases} \quad \text{(X.10)}$$

and

$$\begin{cases} \int_{\mathcal{V}_-} P(\tilde{\mathcal{I}}_{R_1},...,\tilde{\mathcal{I}}_{R_{N_R}})\mathrm{d}\tilde{\mathcal{I}}_{R_1}...\mathrm{d}\tilde{\mathcal{I}}_{R_{N_R}} = [1-\exp(-v)]^{N_R}, \\ \left[\tilde{\mathcal{I}}_{R_i}\partial_{\tilde{\mathcal{I}}_{R_i}}\left(P(\tilde{\mathcal{I}}_{R_1},...,\tilde{\mathcal{I}}_{R_{N_R}})\right)\right]_0^v = -v\exp(-v)\,[1-\exp(-v)]^{N_R-1}. \end{cases} \quad \text{(X.11)}$$

Using the previous results we obtain the main results of this section:

$$\langle\tilde{\mathcal{I}}_T\rangle_+ = 1 + v\sum_i^{N_R} C_2^{R_iT} \quad \text{(X.12)}$$

and

$$\langle \widetilde{\mathcal{I}}_T \rangle_- = 1 - v \frac{\exp(-v)}{1-\exp(-v)} \sum_i^{N_R} C_2^{R_i T}. \tag{X.13}$$

The results given in Eq. (X.12) and Eq. (X.13) have interesting properties:

- First the correction to the average value of the intensity scales with $C_2^{RT}$ thus as $1/(k_0 L)$ in two dimension and as $1/(k_0 L)^2$ in three dimension.
- Second, to this order in the calculation the effect seems to scale linearly with the number of reflected intensities, thus increasing $N_R$ increases the correction to the average value of the transmitted intensity.
- Third, the sign of the correction depends on the applied constraint. A bright (respectively dark) constraint leads to a negative (respectively positive) correction to the average value of the transmitted intensity.
- Fourth, the very simple form of Eq. (X.12) and Eq. (X.13) makes them potentially useful in practice.

Those properties are really encouraging. Indeed we know that the R/T correlation survives for transverse distances between the reflected and the transmitted intensities smaller than $L$ as represented in Fig. X.1 in a 2D geometry. This area contains many speckle spots that are correlated with the transmitted intensity we consider. We also know from the study of MI$(\mathcal{R}, \mathcal{T})$ that it is useless to consider many points in one speckle spot since this does not add information on the transmission. If we neglect non gaussian correlation in R/R, we find that the number of independent speckle spots correlated with the transmitted intensity in $\mathbf{r}_T$ is on the order of $k_0 L$ in 2D and of $(k_0 L)^2$ in 3D. Thus the naive product of the maximum number of correlated speckle spots times the amplitude of the correlation gives unity whatever the parameters of the system (in the diffusive regime) meaning that the change in the conditional average intensity in transmission given in Eq. (X.12) and Eq. (X.13) could be substantial.

### X.1.3 How to observe this phenomenon with the fewest realizations of disorder?

The results given by Eq. (X.12) and Eq. (X.13) are interesting in their linear scaling with the number of reflected points. Let us discuss here a practical issue. In Fig. X.2 we schematically represent the topic of the following discussion. We denote by $\Omega$ the ensemble of all possible realizations of disorder. We know that the average value of $\widetilde{\mathcal{I}}_T$ in this ensemble is the average value $\langle \widetilde{\mathcal{I}}_T \rangle$ without constraint. Now let us consider a constraint on a given reflected intensity. The realizations of disorder corresponding to this case corresponds to an ensemble denoted by $A$. This ensemble is included in $\Omega$ and gets smaller in volume when the strength of the constraint increases. When the constraint is applied independently on two others reflected points we obtain different realizations of the disorder building the ensembles $B$ and $C$, as represented in Fig. X.2. Now if we consider the ensemble corresponding to the constraint applied on the three points *at the same time* we obtain the ensemble $A \cap B \cap C$ which is smaller than $A$ or $B$ or $C$. Analytically, there is no issue since these ensembles can always be discussed. Conversely, numerically or experimentally we have to observe enough configurations of disorder to estimate the statistics on these small ensembles. In this subsection we discuss this issue and try to give insight about the best constraint to apply to observe the change of the average value of the transmitted intensity using the fewest number of realizations of disorder.

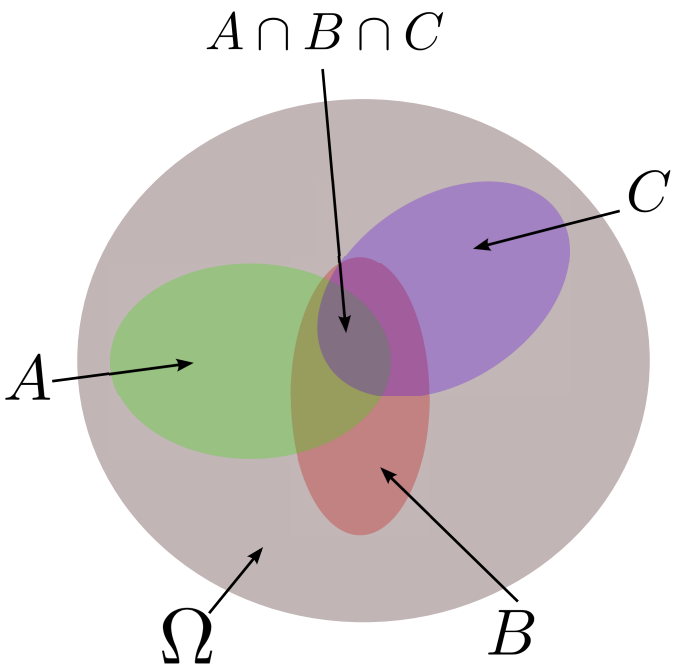


**Figure X.2** – Scheme of the total space of probability $\Omega$ encompassing three different sub-ensembles $A$, $B$ and $C$. The three ensembles correspond to the subspace in which one given reflected intensity follows a restrictive rule. The sub-ensemble for which the three reflected intensities follow this restrictive rule is given by $A \cap B \cap C$.

### Required number of realizations of the disorder

Let us assume that we study $N_{tot}$ realizations of a given disorder, and that we consider a constraint applied on $N_R$ points. Here we are interested in the number of realizations needed to observe the difference between the conditional average value of the transmitted intensity and the average value without constraint. Let us denote $N_{\mathcal{V}_+}$ and $N_{\mathcal{V}_-}$ the number of realizations falling into the constrained ensembles. They are given by

$$\begin{cases} N_{\mathcal{V}_+} = N_{tot}[\exp(-v)]^{N_R}, \\ N_{\mathcal{V}_-} = N_{tot}[1-\exp(-v)]^{N_R}. \end{cases} \tag{X.14}$$

In Eq. (X.14), $[\exp(-v)]^{N_R}$ and $[1-\exp(-v)]^{N_R}$ are the probability for one realization to fall into the constrained ensembles. The typical error on the estimation of the conditional average values due to the finite number of realizations are

$$\begin{cases} \delta_{\mathcal{V}_+} = \dfrac{\sigma}{\sqrt{N_{\mathcal{V}_+}}}, \\ \delta_{\mathcal{V}_-} = \dfrac{\sigma}{\sqrt{N_{\mathcal{V}_-}}}. \end{cases} \tag{X.15}$$

In these expressions $\sigma$ is the standard deviation of the conditional normalized Rayleigh law in transmission equal to one to first order. Let us consider the limiting case where the desired signal ($\langle\widetilde{\mathcal{I}}_T\rangle_- - \langle\widetilde{\mathcal{I}}_T\rangle$ or $\langle\widetilde{\mathcal{I}}_T\rangle_+ - \langle\widetilde{\mathcal{I}}_T\rangle$) is equal to $S$ times the typical error (we can observe the signal if $S > 1$). This leads to the equations for $N_{tot,+}$ and $N_{tot,-}$ (the limiting number of realizations to

observe the effect of the two different constraints):

$$\begin{cases} N_{tot,+} = \dfrac{S^2\sigma^2 \exp(v)^{N_R}}{\left(N_R C_2^{RT}\right)^2 v^2}, \\ N_{tot,-} = \dfrac{S^2\sigma^2 \left[1-\exp(-v)\right]^{2-N_R} \exp(v)^2}{\left(N_R C_2^{RT}\right)^2 v^2}. \end{cases} \tag{X.16}$$

These limiting numbers of realizations are a function of $k_0 L$ (via the $C_2^{RT}$ correlation), of $v$ and of $N_R$. In Fig. X.3 we represent these limiting numbers versus $v$ for a value of $k_0 L = 80$ and $N_R$ going from 1 to 4, $\sigma = 1$ and $S = 5$. Figure X.3 is interesting in many ways:

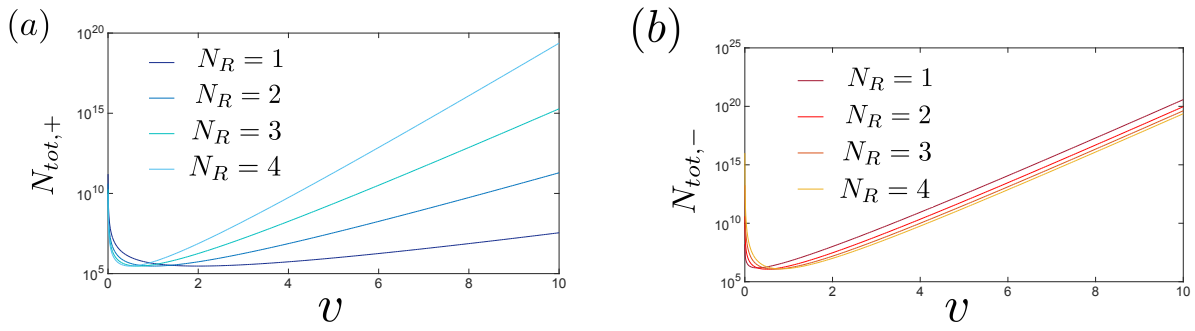


**Figure X.3** – Panel (a) (respectively [panel (b)]) analytical calculation of $N_{tot,+}$ (respectiveley $N_{tot,-}$) given in Eq. (X.16) for a value of $k_0 L = 80$ and $N_R$ going from 1 to 4, $\sigma = 1$ and $S = 5$.

- First we see that changing $N_R$ changes the form of the curves.
- Second all the curves possess a minimum. Thus there exists a constraint for which the number of realizations of the disorder needed to observe the change in the conditional average value of the transmitted intensity is minimal. This minimum results from the competition between two processes. For a weak constraint the change of average value of the transmitted intensity is very small thus is hard to observe (low signal with low noise), while for a strong constraint the number of realizations falling into the constrained ensembles is very small thus the effect is hard to see (strong signal with strong noise).
- Eventually the number of realizations of the disorder needed to observe the effect (at the minimum of the curves) seems to be independent of $N_R$.

### The most discernible constraint

Let us track now the position of the minimum of these curves (that we call $v_+$ and $v_-$). Unfortunately, the position of the minimum is hard to find analytically in the case $N_{tot,-}$, but it is easy to follow for $N_{tot,+}$ (thus this subsection is only valid for the study of panel (a) in Fig. X.3). For a positive constraint, the most discernible constraint is

$$v_+ = \frac{2}{N_R}, \tag{X.17}$$

and the minimum number of realizations needed to observe the effect of the optimal constraint is

$$N_{opt,+} = \frac{S^2\sigma^2}{\left(2C_2^{RT}\right)^2}. \tag{X.18}$$

In Eq. (X.18) we remind that $S$ is the numerical factor that defines a SNR (it is on the order of unity) and $\sigma$ is the standard deviation of the normalized transmitted intensity (it is on the order of unity). This result is important since it is independent on $N_R$, and because it shows that the minimum number of realizations to observe properly the effect discussed in this chapter is $(k_0L)^2$ in 2D and $(k_0L)^4$ in 3D. Note that the derivation assumes that $C_2^{RT}$ is constant for all the reflected points considered. Thus it is strictly valid when the transverse distance between the $N_R$ reflected points is small compared to $L$ .

## X.2 Numerical results

In this section we present numerical simulations of the conditional average value of the transmitted intensity for a scattering slab with two different optical thicknesses. We first consider the easiest situation of a constraint applied on a single point in reflection. Eventually we increase the number $N_R$ of constrained reflected points in order to observe the scaling of the change in the conditional average value of the transmitted intensity with $N_R$.

### X.2.1 Constraint applied on a single reflected speckle spot

In order to check the validity of Eq. (X.12) and Eq. (X.13) numerically we use the couple dipole method. We calculate a large number of disorder realizations and record all pairs of intensity $(\widetilde{\mathcal{I}}_R, \widetilde{\mathcal{I}}_T)$. In this global ensemble, we can define sub-ensembles by the constraint we apply on $\widetilde{\mathcal{I}}_R$, for instance $\widetilde{\mathcal{I}}_R < v$ or $\widetilde{\mathcal{I}}_R > v$. In these sub-ensembles we can estimate the average value of $\widetilde{\mathcal{I}}_T$.

In Fig. X.4 we represent $\langle\widetilde{\mathcal{I}}_T\rangle_+$ and $\langle\widetilde{\mathcal{I}}_T\rangle_-$ calculated both numerically and semi-analytically (using Eq. (X.12) and Eq. (X.13) with $C_2^{RT}$ calculated numerically) for two optical thicknesses ($b = 3$ and $b = 6$) versus the strength of the constraint $v$. The agreement between the numerical simulations and the semi-analytical approach is almost perfect.

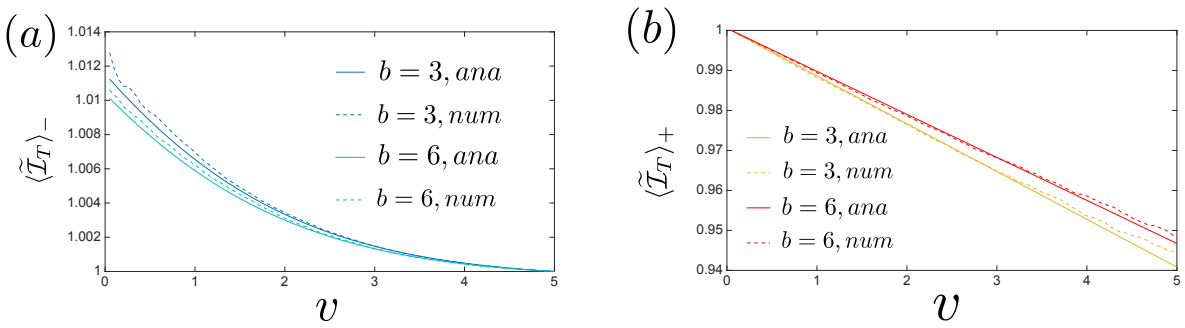


**Figure X.4** – Panel (a): numerical and analytical calculations of $\langle\widetilde{\mathcal{I}}_T\rangle_-$ versus the strength of the constraint applied on a given speckle spot for two dilute ($k_0\ell = 10$) samples of different optical thicknesses $b = 3$ and $b = 6$. Panel (b): numerical and analytical calculations of $\langle\widetilde{\mathcal{I}}_T\rangle_+$ versus the strength of the constraint applied on a given speckle spot for two dilute ($k_0\ell = 10$) samples of different optical thicknesses $b = 3$ and $b = 6$.

We can observe in Fig. X.4 that the two constraints have a different impact on the average value in transmission, as predicted by the analytical formulas Eq. (X.12) and Eq. (X.13). When one considers a bright reflected spot, the average value of the average transmitted intensity varies linearly with the constraint and the slope of the curve is exactly $C_2^{RT}$. When one considers a dark spot in reflection,

the value of the average transmitted intensity is a slightly more complicated function of the strength of the constraint given in Eq. (X.12). Increasing the optical thickness decreases the strength of $C_2^{RT}$ which scales as $1/(k_0 L)$. This explains why we observe that the curves for $b = 6$ are closer to the average value without a constraint than the curves for $b = 3$. We can note that the limit of $\langle \widetilde{\mathcal{I}}_T \rangle_-$ for $v = 0$ is $1 - C_2^{RT}$. When the transverse distance between the transmitted and the reflected points increases, the strength of the correlation decreases, and the changes in the average value of the transmitted intensity tends to zero.

### X.2.2 Constraint applied on a large number of reflected speckle spots

Let us now enter the study of a constraint applied simultaneously on many reflected speckle spots. This situation is more complex both from the numerical and the analytical point of view. Numerically it is more complicated because the ensemble of configurations in which we estimate the average value of the transmitted intensity reduces in size when the number of points on which the constraint is applied increases. As a consequence it becomes harder and harder to estimate the conditional average value of the transmitted intensity when $N_R$ increases. Analytically it is harder because our model neglects both $C_1$ and $C_2$ between pairs of reflected intensities. From our study of $\mathrm{MI}(\mathcal{R}, \mathcal{T})$ in Chap. IX we know that it is useless to consider more than one reflected intensity within one speckle spot. This leads us to choose $N_R$ reflected intensities in the zero of the $C_1$ function of the central reflected speckle. This ensures the use of independent speckle spots (in the sense of $C_1$) all correlated with the transmitted intensity.

#### An encouraging numerical observation

In Fig. X.5 we represent $\langle \widetilde{\mathcal{I}}_T \rangle_+$ and $\langle \widetilde{\mathcal{I}}_T \rangle_-$ calculated numerically for $N_R$ varying from 1 to 10 versus the strength of the constraint $v$ for a scattering medium with optical thickness $b = 3$ and $k_0 \ell = 10$. The first observation in this figure is that as the number of points increases the impact of the constraint increases as predicted by Eq. (X.12) and Eq. (X.13). We also see the numerical difficulties encountered when we approach strong constraints with a large number of reflected points. In this case the number of points in the constrained ensemble is too small to properly estimate the average value of the transmitted intensity (this is reflected in the noisy character of the numerical estimation of $\langle \widetilde{\mathcal{I}}_T \rangle_+$ and $\langle \widetilde{\mathcal{I}}_T \rangle_-$).

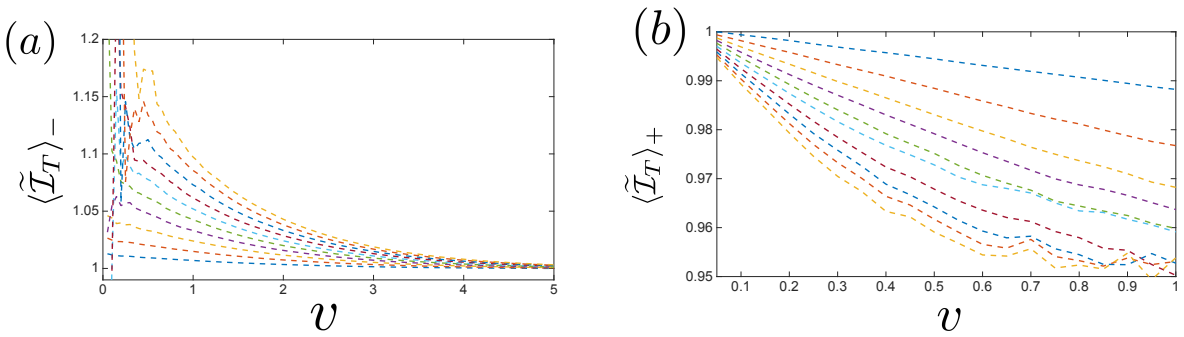


**Figure X.5** – Panel (a) [respectively panel (b)] numerical calculation of $\langle \widetilde{\mathcal{I}}_T \rangle_-$ [respectively $\langle \widetilde{\mathcal{I}}_T \rangle_+$] versus the strength of the constraint applied on a varying number of reflected speckle spots $1 \leq N_R \leq 10$ ($N_R = 1$ corresponds to the blue curve and $N_R = 10$ corresponds to the yellow curve). The parameters of the scattering sample are $b = 3$ and $k_0 \ell = 10$.

### Discrepancy from the model

In Fig. X.6 we represent $\langle\widetilde{\mathcal{I}}_T\rangle_+$ and $\langle\widetilde{\mathcal{I}}_T\rangle_-$ calculated both numerically and analytically for $N_R$ varying from 1 to 4, versus the strength of the constraint $v$ for a scattering medium with optical thickness $b = 3$ and $k_0\ell = 10$. We observe that the numerical and the semi-analytical calculations of Eq. (X.12) and Eq. (X.13) are in good agreement when the constraint is small but tends to separate when the constraint increases. In addition, when $N_R$ increases, the deviation increases and is surprisingly of opposite sign regarding the constraint applied on the reflected spots. For $\langle\widetilde{\mathcal{I}}_T\rangle_-$ it seems that the discrepancy increases the effect of the constraint while for $\langle\widetilde{\mathcal{I}}_T\rangle_+$ it decreases the effect of the constraint.

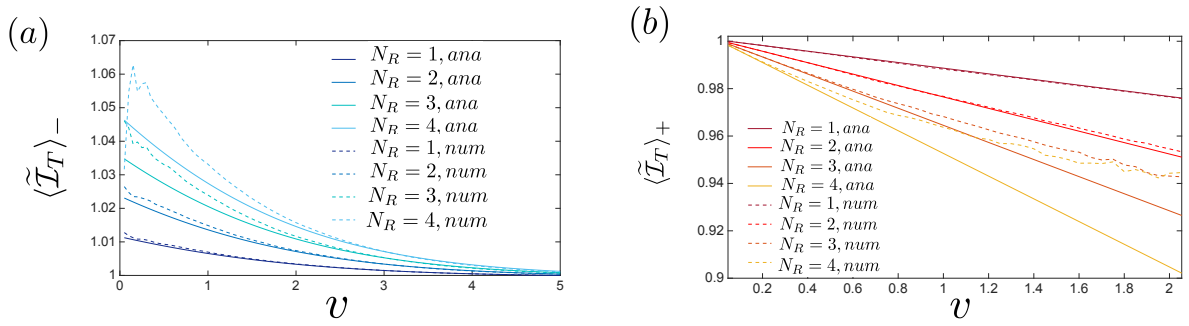


**Figure X.6** – Panel (a) [respectively panel (b)] numerical and analytical calculation of $\langle\widetilde{\mathcal{I}}_T\rangle_-$ [respectively $\langle\widetilde{\mathcal{I}}_T\rangle_+$] versus the strength of the constraint applied on various number of reflected speckle spots ($N_R$ is varied from 1 to 4). The parameters of the scattering sample are $b = 3$ and $k_0\ell = 10$.

We propose the following explanation for this deviation from the model. Let us define $C_{2,+}^{RT}$ and $C_{2,-}^{RT}$ as the non gaussian correlation of one pair of reflected and transmitted intensities under the constraint applied on an other reflected intensity. In Fig. X.7 we numerically calculate $C_{2,+}^{RT}/|C_2^{RT}|$ and $C_{2,-}^{RT}/|C_2^{RT}|$ versus the strength of the constraint applied on a nearby reflected intensity (a reflected intensity considered the first zero of the $C_1$ function of the central reflected intensity). Even if this figure is really noisy due to the small value of the calculated quantity, we can clearly see a trend (the black dotted line corresponds to the independent case). The important point for

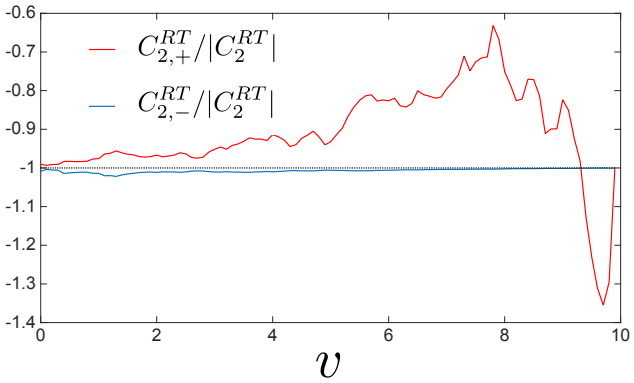


**Figure X.7** – Numerical calculation of the $C_{2,+}^{RT}/|C_2^{RT}|$ and $C_{2,-}^{RT}/|C_2^{RT}|$ versus the strength of the constraint. The parameters of the scattering sample are: $b = 3$ and $k_0\ell = 10$.

this discussion is that $C_{2,+}^{RT}$ is reduced in absolute value ,and $C_{2,-}^{RT}$ is increased, when the constraint increases. Both the sign and the amplitude of the change in the normalized correlation are consistent with the numerical observation in Fig. X.6. There may be a microscopic scattering sequence (or many

of them) responsible for the change of the conditional non gaussian correlation in R/T, nonetheless we do not want to enter this question in deeper details at this stage. We believe this observation is sufficient to motivate a further work on this topic.

## X.3 Conclusion

### A universal effect?

This chapter aimed at shading light on the use of the long range character of the $C_2^{RT}$ correlation. Indeed, as discussed in the introduction of this chapter, we consider a phenomenon (variation of the average value of the transmitted intensity) proportional to $C_2^{RT}$ and scaling linearly with the number of independent speckle considered [Eq. (X.12) and Eq. (X.13)]. When the maximum number of reflected speckle spots correlated with the transmitted one is used, the change of the normalized average intensity should be independent on the parameters of the system *in the diffusive regime*. Moreover the change in the average transmitted value should be on the order 100% for both 2D and 3D geometries. This study is encouraging, indeed in Fig. X.5 the scaling with $N_R$ is observable and the change observed in the average value of the transmitted intensity is around 15%. If we extrapolate to zero the curve at $N_R = 10$ in panel (a) in Fig. X.5 we obtain a change of approximatively 30%. Now let us remind that we used $N_R = 10$ points in this study while the maximum number of points available for this scattering medium ($k_0L = 30$) is $N_R = 30$ leading to a potential 90% increase of the average transmitted intensity. This agrees with the prediction.

Note that the observation of a positive discrepancy between the numerical and the analytical calculations for $\langle \widetilde{\mathcal{I}}_T \rangle_-$ is a welcome news. Indeed, this configuration is the most interesting for applications and could lead to an enhancement of the transmitted intensity higher than that predicted by the model. Note that in that case the extra factor will probably not be universal and would deserve a proper study.

### Is the conditional statistics approach equivalent to a wavefront shaping experiment?

The universal behavior of the maximum change of average transmitted intensity predicted may be difficult to observe due to a practical difficulty that increases when $k_0L$ increases. Indeed, the correlation function decreases in amplitude with $1/(k_0L)$ but the number of correlated points increases inversely with $k_0L$. Nonetheless, the scheme proposed in this chapter is sensitive to the spreading of the "information" on various speckle spots, and it is harder to observe the same amount of variation of the average transmitted intensity when $k_0L$ increases. Indeed, as represented in Fig. X.2, when one increases the number of points under a constraint, the corresponding ensemble becomes smaller and smaller thus harder and harder to observe. One could argue that it is thus impossible to experimentally observe realizations of these ensembles without observing for a very long time a dynamic scattering sample.

Nonetheless, it is possible that wavefront shaping could be the solution to observe such rare events. Let us start by stressing that in the numerical experiment presented in this chapter we do not shape the incident light (we send a plane wave at normal incidence), but we let the medium change randomly and create some lucky realizations for which the plane wave is shaped for our purpose. It would be interesting to study the opposite case for which the disorder is set, and the wave is shaped to increase or reduce the scattered light in some chosen reflected speckle spots, and observe the change of the transmitted intensity. Doing this in an area of typical size $L$ in reflection may allow

one to observe the change in the transmitted intensity described in this chapter without looking for a long time for rare events. This result could thus have direct applications for wavefront-shaping experiments [107, 120].

# Chapter XI

# Conclusion

In this thesis we have studied statistical links between the scattered light in reflection and in transmission of a complex medium.

The first part of this thesis was devoted to the study of the intensity-intensity correlation function between reflection and transmission when the medium is illuminated with a plane wave at normal incidence.

- In Chap. III we have studied this correlation in the diffusive regime numerically (in 2D) and analytically in both 2D and 3D configurations. We have shown that the correlation function is negative, has a typical size of $L$ (thickness of the scattering sample), and has an amplitude scaling as $1/(k_0 L)$ in 2D and as $1/(k_0 L)^2$ in 3D.
- In Chap. IV we have presented the measurement of the intensity-intensity correlation in R/T performed at the University of Exeter (UK) by I. Starshinov, A.M Paniagua-Diaz and J. Bertolotti in the framework of a collaboration with our group. The measurements confirms that the correlation in 3D indeed tends towards a negative function of typical size $L$ and of amplitude $1/(k_0 L)^2$ in the diffusive regime, but it also reveals a rich behavior for optical thickness close to unity (single scattering regime $\lambda \ll \ell \sim L$). In this regime, the correlation function presents both a positive and a negative contribution and is sensitive to the angle of incidence. This suggests that unusual scattering sequences contribute to the correlation function in R/T in this regime.
- In Chap. V we have studied the intensity-intensity correlation in R/T numerically and analytically in 2D in the quasi ballistic regime ($\lambda \ll L \lll \ell$), and observed a purely positive contribution not dependent on the angle of incidence. The analytical study suggests the existence and the dominant weight of usually non-considered four fields diagrams in this regime.
- In Chap. VI we have proposed a new imaging modality based on the existence of this intensity-intensity correlation in R/T, named Blind Ghost Imaging, and have presented a numerical proof of concept.

The conclusion of this fist part of the thesis is that the intensity-intensity correlation function in R/T is a rich and instructive observable. The power law decay with $L$ of the amplitude of the correlation for large optical thicknesses makes it usable even for thick scattering sample. From a theoretical point of view, we can stress that the R/T correlation gives a direct access to the non-gaussian correlation whatever the optical thickness (not being blurred by the $C_1$ correlation).

The second part of this thesis was devoted to the study of the statistical dependency of the reflected and the transmitted light.

- In Chap. VIII we have built the analytical joint density probability function of many reflected and many transmitted intensities using diagrammatic techniques, and have supported its expression using numerical simulations.
- In Chap. IX we have used the joint probability density function built in Chap. VIII to quantify analytically and numerically the mutual information (MI) between reflected and transmitted

speckle patterns. We have studied this quantity versus the parameters of the system, the number of reflected and transmitted speckle spots considered and their spacing. We have shown that the MI between reflection and transmission is principally carried by loops of correlation. We have discussed the competing effects between two points and three points loop processes and have shown that they are the cause of the existence of an optimal transverse distance between detectors in transmission and in reflection in order to have a maximum information contained in reflection on the transmission. This optimal distance between detectors is predicted to increase when the optical thickness increases. We have also shown that increasing the number of measured speckle spots in reflection and transmission increases the information contained in reflection on the transmission (as long as the distance between the points is larger than the wavelength). This results is of practical interest for our objective of using the reflected intensity to control the transmitted light.

- In Chap. X we have discussed the conditional average value of the transmitted intensity having some information on the reflected intensity numerically and analytically. We have shown that the change in the transmitted intensity is proportional to the intensity-intensity correlation in R/T configuration, and that it scales linearly with the number of points from which we extract information in reflection. Since the intensity correlation function in R/T is long range, there are possibly many reflected spots available containing information on the chosen transmitted intensity. This have led us to conclusion that regardless of the optical thickness of the scattering sample, one can strongly modify the transmitted intensity factor taking all the reflected information into account.

The conclusion of the second part of this thesis is that information on the transmission can be obtained from measurements limited to reflection, and that this information is principally carried by the long range intensity-intensity correlation function in R/T. Taking advantage on the long range character of this function, we can find ways to use more than one speckle spots to infer the behavior of the transmitted light.

In the future, the first objective is to complete the study of BGI in collaboration with our colleagues from Exeter (UK). This is of practical interest and could additionally motivate additional research on the intensity correlation in R/T. We believe that the reflection/transmission configuration is interesting in many ways (practically and conceptually). It would be interesting to push deeper the analytical study of the correlation in the single scattering regime (using the Radiative Transfer Equation) in order to strengthen the comprehension of the variation of the correlation with the angle of incidence. A full experimental study of the quasi ballistic regime is also needed to corroborate our guess that in this regime, some non usual scattering sequences dominate the correlation in R/T. Concerning the second part of this thesis, we believe a nice analytical follow up of this work would be to manage to take into account both the the short range correlation and the long range correlation in the analytical expression of the joint density probability functions. This could probably open new questions currently out of reach. An experimental study of the MI would be certainly interesting, but also difficult, due to its scaling as $1/(k_0 L)^4$ in 3D. The link between MI in R/T and wavefront shaping in transmission using only reflected information is of great interest both conceptually and practically. A clear numerical and/or experimental study of wavefront shaping in transmission using only reflected information could help us propose a theory for this process.

# Remerciements

Je vais commencer ces lignes par remercier les personnes avec qui j'ai eu la chance de travailler pendant les trois dernières années. Merci à Rémi, qui m'aura dans un premier temps donné l'envie de choisir ce sujet en tant que professeur d'optique à l'ESPCI. Merci ensuite pour le choix de ce sujet de thèse et la confiance mise en moi, j'ai trouvé beaucoup de d'intérêt dans l'étude des corrélations RT et je pense que leur étude m'a fait progresser nettement sur plusieurs points. Merci à Romain qui m'aura tout appris concernant les simulations numériques. Comme je le dis souvent je suis arrivé en ayant peur du numérique et cette peur a très vite disparue grace à ta très grande gentillesse dans ta façon de répondre aux questions. Merci à toi ainsi qu'à Rémi pour les conseils et corrections lors de l'écriture de ce manuscrit et de la préparation de la soutenance que je sais très grandement améliorés grace à vous deux. Merci ensuite à Arthur pour son aide à la fois dans la construction de nombreux résultats de cette thèse mais aussi pour m'avoir permis de progresser dans ma façon de traiter analytiquement un problème. Je tiens aussi à avoir quelques mots pour nos collègues de l'université d'Exeter: Alba, Illia et Jacopo qui ont tant apporté à notre compréhension de ce sujet par leurs résultats expérimentaux. Mes quelques voyages à Exeter pour leur rendre visite ont toujours été très agréables et enrichissants.

J'ai eu la chance durant mon doctorat de rencontrer un grand nombre de personnes avec qui j'ai tissé des liens d'amitié. Commençons par le trio avec qui j'ai passé je pense le plus de temps: Amaury, Maxime et Benoit. Je n'aurai eu de cesse que de vous mettre la pâtée au tennis, football, ping-pong, à agar et malgré cela vous m'avez très gentiment accueilli dans votre bureau. Une grande pensée pour nos innombrables soirées dans les bars du quartier avec Juliette et Diego (deux belles rencontres corses), Fabrice , Laura et Fishtador (les amoureux du jeuqnard). Un grand merci ensuite à Victor, William pour les derniers mois du bureau R229 vécus ensemble ! Merci aux collègues avec qui j'ai partagé les réunions d'équipe du vendredi matin: Clothilde, Florian, Antoine, Dorian, Olivier, Valentina, Valentina.P, Maxime, Mathieu, Pierre. Merci aussi aux copains de l'ESPCI qui m'auront accompagné de l'École, en passant par le M2 à l'IOGS jusqu'à la thèse: Clément, Élodie et Miki. Merci enfin aux afficionados du café du matin: Patricia, Olivier, Yannick, Arnaud, Claire, François, Daria.

Merci aux amis, frères et soeurs de coeur Sebastien, Quentin, Thomas, Antoine, Eric, Mai-lan et Léa. Merci à Justine, avec qui j'ai partagé ces moments. Mes années de thèse garderont ta couleur et j'en suis content. Merci enfin à ma famille, plus particulièrement à mon père Louis, ma mère Lydia et ma soeur Florence pour *tout*.

# Appendices

# Analytical derivation of non gaussian correlations in R/T, T/T and R/R

In this appendix we give the complete formulas of the non gaussian correlation functions in T/T, RR and R/T derived with diffusion theory.

## .1 Reflection/Transmission

In this subsection we give the final result of the derivation of the diagram represented in panel (b) in Fig. III.10 in the diffusive regime. Let us call $C_2$ the non gaussian contribution to the $\widetilde{I}$-$\widetilde{I}$ correlation coming from this diagram. Mathematically, this $C_2$ contribution comes from a connected four fields correlation which reads

$$\langle \delta E_R \delta E_R^* \delta E_T \delta E_T^* \rangle_{C_2} = \int |E(\mathbf{r}_1)|^2 |E(\mathbf{r}_2)|^2 \, \mathrm{L}(\mathbf{r}_2, \boldsymbol{\rho}_2) \, \mathrm{L}(\mathbf{r}_1, \boldsymbol{\rho}_1) \, \mathrm{H}(\boldsymbol{\rho}_1, \boldsymbol{\rho}_2, \boldsymbol{\rho}_3, \boldsymbol{\rho}_4) \\ \mathrm{L}(\mathbf{r}_3, \boldsymbol{\rho}_3) \, \mathrm{L}(\mathbf{r}_4, \boldsymbol{\rho}_4) |\langle \mathrm{G}(\mathbf{r}_R - \mathbf{r}_3) \rangle|^2 |\langle \mathrm{G}(\mathbf{r}_T - \mathbf{r}_4) \rangle|^2 \mathrm{d}\mathbf{r}_1 ... \mathrm{d}\mathbf{r}_4 \mathrm{d}\boldsymbol{\rho}_1 ... \mathrm{d}\boldsymbol{\rho}_4 \quad (1)$$

and is equal to

$$C_2(\mathbf{r}_R, \mathbf{r}_T) = C_2^{\Delta}(\mathbf{r}_R, \mathbf{r}_T) + \frac{C_2^{in}(\mathbf{r}_R, \mathbf{r}_T) + C_2^{out}(\mathbf{r}_R, \mathbf{r}_T)}{2}, \quad (2)$$

where the three contributions come from the three terms labelled in the vertex in Eq. (III.53).

### 3D case

Here we give the final expressions of the different terms entering into Eq. (2) in dimension three.

$$C_2^{\Delta} = \frac{-3}{4k^2\ell^2} \int \frac{\mathrm{J}_0(\frac{q\Delta r}{L}) \, \mathrm{sh}(q\frac{z_0}{L})^2}{q \, \mathrm{sh}[q(1+2\frac{z_0}{L})]^2} \\ \times \left( \mathrm{sh}[q\left(1+\frac{z_0}{L}\right)] \, \mathrm{sh}\left(q\frac{z_0}{L}\right) \frac{27L}{10\ell} + \left(\frac{27}{20} + \frac{5\ell^2}{3L^2}\right) q \, \mathrm{sh}[q\left(1+2\frac{z_0}{L}\right)] \right) \mathrm{d}q, \quad (3)$$

$$C_2^{in} = \frac{-3}{4k^2\ell^2} \frac{15}{2} \int \frac{\mathrm{J}_0(\frac{q\Delta r}{L}) \, \mathrm{sh}(q\frac{z_0}{L})^2}{q^2 \, \mathrm{sh}[q(1+2\frac{z_0}{L})]^2} \\ \times \left( -q \, \mathrm{ch}[q\left(1+\frac{z_0}{L}\right)] + \mathrm{sh}(q) \right) \mathrm{d}q, \quad (4)$$

$$C_2^{out} = \frac{-3}{4k^2\ell^2} \frac{15}{2} \int \frac{\mathrm{J}_0(\frac{q\Delta r}{L}) \, \mathrm{sh}(q\frac{z_0}{L})^2}{q^2 \, \mathrm{sh}[q\left(1+2\frac{z_0}{L}\right)]^2} \\ \times \left( -q \, \mathrm{ch}(q) + [1 + q^2\left(1 + \frac{2z_0}{L} + \frac{2z_0^2}{L^2}\right)] \, \mathrm{sh}(q) \right) \mathrm{d}q, \quad (5)$$

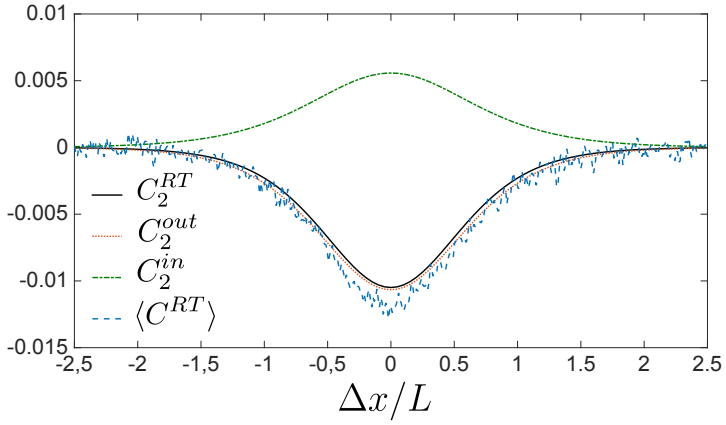


**Figure 1** – Analytical predictions for the $C_2^{RT}$ correlation (black solid line), $C_2^{out}$ correlation (red dotted line) and $C_2^{in}$ correlation (green dash-dotted line) compared with the simulation of $2D$ wave propagation in a disordered medium (blue dashed line). Parameters of the simulations: $k\ell = 10$, $L/\ell = 10$, $\theta_a = 0$.

### 2D case

Here we give the final expressions of the different terms entering into Eq. (2) in dimension two.

$$C_2^{\Delta} = \frac{-L}{\pi k\ell^2} \int \frac{\cos(\frac{q\Delta r}{L})\,\mathrm{sh}(q\frac{z_0}{L})^2}{q^2\,\mathrm{sh}[q\left(1+2\frac{z_0}{L}\right)]^2} \times \left(\mathrm{sh}\left(q\frac{z_0}{L}\right)\mathrm{sh}[q\left(1+\frac{z_0}{L}\right)]\frac{16(1+\frac{\pi}{2})L}{\pi^2(1+\frac{\pi}{4})\ell} + \left(\frac{4(1+\frac{\pi}{2})^2}{\pi^2(1+\frac{\pi}{4})} + \frac{(1+\pi/4)\ell^2}{L^2}\right) q\,\mathrm{sh}[q\left(1+2\frac{z_0}{L}\right)]\right) \mathrm{d}q \tag{6}$$

$$C_2^{in} = \frac{-32L}{\pi k\ell^2}\frac{(1+\frac{\pi}{4})}{\pi^2} \int \frac{\cos(\frac{q\Delta r}{L})\,\mathrm{sh}(q\frac{z_0}{L})^2}{q^3\,\mathrm{sh}[q\left(1+2\frac{z_0}{L}\right)]^2} \times \left(-q\,\mathrm{ch}[q\left(1+\frac{z_0}{L}\right)] + \mathrm{sh}(q)\right) \mathrm{d}q \tag{7}$$

$$C_2^{out} = \frac{-32L}{\pi k\ell^2}\frac{(1+\frac{\pi}{4})}{\pi^2} \int \frac{\cos(\frac{q\Delta r}{L})\,\mathrm{sh}(q\frac{z_0}{L})^2}{q^3\,\mathrm{sh}[q\left(1+2\frac{z_0}{L}\right)]^2} \times \left(-q\,\mathrm{ch}(q) + [1+q^2\left(1+\frac{2z_0}{L}+\frac{2z_0^2}{L^2}\right)]\,\mathrm{sh}(q)\right) \mathrm{d}q, \tag{8}$$

where $z_0$ is the extrapolation length (see Ref. [85] for details). We have represented these different contributions in Fig. 1 in the case of wave propagation through 2D disordered slab. The contribution $C_2^{out}$ is negative, whereas $C_2^{in}$ and $C_2^{\Delta}$ are positive. In addition, $C_2^{in}$ and $C_2^{out}$ do not have the same amplitude. However the sum of all terms, given by Eq. (2), turns out to be well approximated by $C_2^{out}$, as it was done in Ref. [85]. Both expressions are in good agreement with simulation of microscopic wave propagation.

## .2 Transmission/Transmission

In this subsection we give the final results of the derivation of the two diagrams represented in Fig. 2 in the diffusive regime in the T/T configuration. Let us call $C_{2'}$ the non gaussian contribution to the

$\widetilde{I}$-$\widetilde{I}$ correlation coming from the diagram in panel (b) and $C_{2''}$ the one in panel (a) in Fig. 2.

$$\langle \delta E_{T_1} \delta E_{T_2} \delta E^*_{T_1} \delta E^*_{T_2} \rangle_{C_{2'}} = \int |E(\mathbf{r}_1)|^2 |E(\mathbf{r}_2)|^2 \, \mathrm{L}(\mathbf{r}_2, \boldsymbol{\rho}_2) \, \mathrm{L}(\mathbf{r}_1, \boldsymbol{\rho}_1) \, \mathrm{H}(\boldsymbol{\rho}_1, \boldsymbol{\rho}_2, \boldsymbol{\rho}_3, \boldsymbol{\rho}_4) \\ \mathrm{L}(\mathbf{r}_3, \boldsymbol{\rho}_3) \, \mathrm{L}(\mathbf{r}_4, \boldsymbol{\rho}_4) |\langle \mathrm{G}(\mathbf{r}_{T_1} - \mathbf{r}_3) \rangle|^2 |\langle \mathrm{G}(\mathbf{r}_{T_2} - \mathbf{r}_4) \rangle|^2 \mathrm{d}\mathbf{r}_1 ... \mathrm{d}\mathbf{r}_4 \mathrm{d}\boldsymbol{\rho}_1 ... \mathrm{d}\boldsymbol{\rho}_4. \quad (9)$$

$$\langle \delta E_{T_1} \delta E_{T_2} \delta E^*_{T_1} \delta E^*_{T_2} \rangle_{C_{2''}} = \int |E(\mathbf{r}_1)|^2 |E(\mathbf{r}_2)|^2 \, \mathrm{L}(\mathbf{r}_2, \boldsymbol{\rho}_2) \, \mathrm{L}(\mathbf{r}_1, \boldsymbol{\rho}_1) \, \mathrm{H}(\boldsymbol{\rho}_1, \boldsymbol{\rho}_2, \boldsymbol{\rho}_3, \boldsymbol{\rho}_4) \\ \mathrm{L}(\mathbf{r}_3, \boldsymbol{\rho}_3) \, \mathrm{L}(\mathbf{r}_4, \boldsymbol{\rho}_4) \langle \mathrm{G}(\mathbf{r}_{T_1} - \mathbf{r}_3) \rangle \langle \mathrm{G}(\mathbf{r}_{T_2} - \mathbf{r}_3) \rangle^* \langle \mathrm{G}(\mathbf{r}_{T_1} - \mathbf{r}_4) \rangle^* \langle \mathrm{G}(\mathbf{r}_{T_2} - \mathbf{r}_4) \rangle \mathrm{d}\mathbf{r}_1 ... \mathrm{d}\mathbf{r}_4 \mathrm{d}\boldsymbol{\rho}_1 ... \mathrm{d}\boldsymbol{\rho}_4. \quad (10)$$

The only difference between the two diagrams is the exit vertex. In diffusive regime, $C_{2''}$ can be

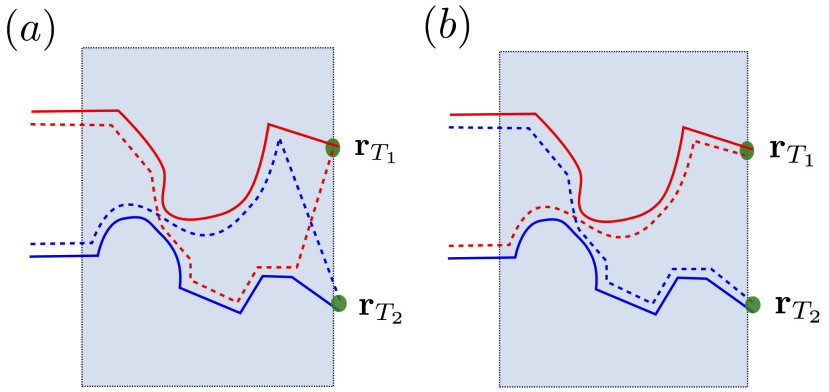


**Figure 2** – Two typical diagrams contributing to the connected four-field correlations. In T/T the diagram depicted in panel (a) is not negligible and we have to consider both.

calculated from $C_{2'}$ easily [65] using:

$$C_2(\mathbf{r}_{T_1}, \mathbf{r}_{T_2}) = C_{2'}(\mathbf{r}_{T_1}, \mathbf{r}_{T_2}) + C_{2''}(\mathbf{r}_{T_1}, \mathbf{r}_{T_2}) = C_{2'}(\mathbf{r}_{T_1}, \mathbf{r}_{T_2}) \, (1 + v_e(\mathbf{r}_{T_1}, \mathbf{r}_{T_2})) \quad (11)$$

with

$$v_e(\mathbf{r}_{T_1}, \mathbf{r}_{T_2}) \propto |\, \mathrm{Im} \, [\langle G(\mathbf{r}_{T_1}, \mathbf{r}_{T_2}) \rangle] \,|^2 \quad (12)$$

the proportionality factor chosen so that $v_e(\mathbf{r}_{T_1}, \mathbf{r}_{T_1}) = 1$.

Consequently we only detail the derivation of $C_{2'}(\mathbf{r}_{T_1}, \mathbf{r}_{T_2})$ in the following. In transmission we follow [34] and neglect the laplacian terms:

$$C_{2'}(\mathbf{r}_{T_1}, \mathbf{r}_{T_2}) = \frac{C^{in}_{2'}(\mathbf{r}_{T_1}, \mathbf{r}_{T_2}) + C^{out}_{2'}(\mathbf{r}_{T_1}, \mathbf{r}_{T_2})}{2}. \quad (13)$$

## 2D case

In 2D we have

$$C^{in}_{2'} = \frac{-L^2}{\pi k_0 \ell z_0^2} \int \frac{\cos(\frac{q\Delta r}{L}) \, \mathrm{sh}(q\frac{z_0}{L})^2}{q^3 \, \mathrm{sh}[q\left(1 + 2\frac{z_0}{L}\right)]^2} \\ \times \left(2q + \mathrm{sh}\left[2q\frac{z_0}{L}\right] - \mathrm{sh}\left(2q\left[1 + \frac{z_0}{L}\right]\right)\right) \mathrm{d}q \quad (14)$$

$$C^{out}_{2'} = \frac{L^2}{\pi k_0 \ell z_0^2} \int \frac{\cos(\frac{q\Delta r}{L}) \, \mathrm{sh}(q\frac{z_0}{L})^2}{q^3 \, \mathrm{sh}[q\left(1 + 2\frac{z_0}{L}\right)]^2} \left(-2q\,(1 + z_0/L) \, \mathrm{ch}\left[\frac{2qz_0}{L}\right] + 2q\frac{z_0}{L} \, \mathrm{ch}\,[2q(1 + z_0/L)]\right. \\ \left. - \left[1 + 2q^2\left(1 + \frac{z_0}{L}\right)^2\right] \mathrm{sh}\left(\frac{2qz_0}{L}\right) + \left[1 + 2q^2\frac{z_0^2}{L^2}\right] \mathrm{sh}\left(2q\left[1 + \frac{z_0}{L}\right]\right)\right) \mathrm{d}q. \quad (15)$$

To have the complete $C_2$ we use Eq. (11).

### 3D case

In 3D we have

$$C_{2'}^{in} = \frac{-3\pi^2 L^2}{k_0^2 \ell L z_0^2} \int \frac{\mathrm{J}_0(\frac{q\Delta r}{L})\,\mathrm{sh}(q\frac{z_0}{L})^2}{q^2\,\mathrm{sh}[q\left(1+2\frac{z_0}{L}\right)]^2} \times \left(2q + \mathrm{sh}\left[2q\frac{z_0}{L}\right] - \mathrm{sh}\left(2q\left[1+\frac{z_0}{L}\right]\right)\right)\mathrm{d}q \tag{16}$$

$$C_{2'}^{out} = \frac{3\pi^2 L^2}{k_0^2 \ell L z_0^2} \int \frac{\mathrm{J}_0(\frac{q\Delta r}{L})\,\mathrm{sh}(q\frac{z_0}{L})^2}{q^2\,\mathrm{sh}[q\left(1+2\frac{z_0}{L}\right)]^2} \left(-2q\,(1+z_0/L)\,\mathrm{ch}\left[\frac{2qz_0}{L}\right] + 2q\frac{z_0}{L}\,\mathrm{ch}\,[2q(1+z_0/L)]\right.$$
$$\left. - \left[1+2q^2\left(1+\frac{z_0}{L}\right)^2\right]\mathrm{sh}\left(\frac{2qz_0}{L}\right) + \left[1+2q^2\frac{z_0^2}{L^2}\right]\mathrm{sh}\left(2q\left[1+\frac{z_0}{L}\right]\right)\right)\mathrm{d}q. \tag{17}$$

To have the complete $C_2$ we use Eq. (11).

### Discussion

Let us here discuss the expressions Eq. (14) and Eq. (16). In Chap. IX, we argued that $C_2^{TT}$ cannot be put in a large optical thickness form as easily as $C_2^{RT}$. We can see this removing the $z_0/L$ terms into the expressions Eq. (14) and Eq. (16) and consider that $\mathrm{sh}(q\frac{z_0}{L})^2 \sim (q\frac{z_0}{L})^2$ exactly like we did for $C_2^{RT}$. Doing so the expressions Eq. (14) and Eq. (16) diverge. If we do not neglect the $z_0/L$ terms in the sh but still do the approximation $\mathrm{sh}(q\frac{z_0}{L})^2 \sim (q\frac{z_0}{L})^2$ into Eq. (14) and Eq. (16) then the integral converges thanks to the extra $\exp[qz_0/L]$ in its denominator. The scaling of the $C_2^{TT}$ thus becomes $C_2^{TT} \sim 1/(k_0 L k_0 \ell)$ in 3D and $C_2^{TT} \sim 1/(k_0\ell)$ in 2D. Note that we neglect the variation of the function inside the integral with $b$ saying this which is not exactly correct.

## .3 Reflection/Reflection

In this subsection we calculate the two diagrams represented in Fig. 3 in the diffusive regime in the R/R configuration. Let us call $C_{2'}$ the non gaussian contribution to the $\widetilde{I}$-$\widetilde{I}$ correlation coming from the diagram in panel (b) and $C_{2''}$ the one in panel (a) in Fig. 3.

$$\langle \delta E_{T_1}\delta E_{R_2}\delta E_{R_1}^*\delta E_{R_2}^*\rangle_{C_{2'}} = \int |E(\mathbf{r}_1)|^2|E(\mathbf{r}_2)|^2\,\mathrm{L}(\mathbf{r}_2,\boldsymbol{\rho}_2)\,\mathrm{L}(\mathbf{r}_1,\boldsymbol{\rho}_1)\,\mathrm{H}(\boldsymbol{\rho}_1,\boldsymbol{\rho}_2,\boldsymbol{\rho}_3,\boldsymbol{\rho}_4)$$
$$\mathrm{L}(\mathbf{r}_3,\boldsymbol{\rho}_3)\,\mathrm{L}(\mathbf{r}_4,\boldsymbol{\rho}_4)|\langle \mathrm{G}(\mathbf{r}_{R_1}-\mathbf{r}_3)\rangle|^2|\langle \mathrm{G}(\mathbf{r}_{R_2}-\mathbf{r}_4)\rangle|^2 \mathrm{d}\mathbf{r}_1...\mathrm{d}\mathbf{r}_4\mathrm{d}\boldsymbol{\rho}_1...\mathrm{d}\boldsymbol{\rho}_4. \tag{18}$$

the other diagrams reads

$$\langle \delta E_{R_1}\delta E_{R_2}\delta E_{R_1}^*\delta E_{R_2}^*\rangle_{C_{2''}} = \int |E(\mathbf{r}_1)|^2|E(\mathbf{r}_2)|^2\,\mathrm{L}(\mathbf{r}_2,\boldsymbol{\rho}_2)\,\mathrm{L}(\mathbf{r}_1,\boldsymbol{\rho}_1)\,\mathrm{H}(\boldsymbol{\rho}_1,\boldsymbol{\rho}_2,\boldsymbol{\rho}_3,\boldsymbol{\rho}_4)$$
$$\mathrm{L}(\mathbf{r}_3,\boldsymbol{\rho}_3)\,\mathrm{L}(\mathbf{r}_4,\boldsymbol{\rho}_4)\langle \mathrm{G}(\mathbf{r}_{R_1}-\mathbf{r}_3)\rangle\langle \mathrm{G}(\mathbf{r}_{R_2}-\mathbf{r}_3)\rangle^*\langle \mathrm{G}(\mathbf{r}_{R_1}-\mathbf{r}_4)\rangle^*\langle \mathrm{G}(\mathbf{r}_{R_2}-\mathbf{r}_4)\rangle \mathrm{d}\mathbf{r}_1...\mathrm{d}\mathbf{r}_4\mathrm{d}\boldsymbol{\rho}_1...\mathrm{d}\boldsymbol{\rho}_4. \tag{19}$$

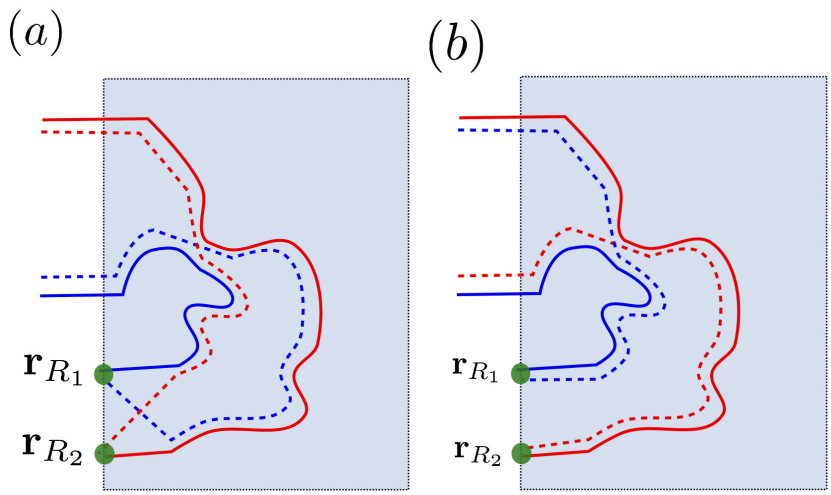


**Figure 3** – Two typical diagrams contributing to the connected four-field correlations. In R/R the diagram depicted in panel (a) is not negligible and we have to consider both.

The only difference between the two diagrams is the exit vertex. In diffusive regime, $C_{2'}$ can be calculated from $C_{2'}$ easily [65] using:

$$C_2(\mathbf{r}_{R_1},\mathbf{r}_{R_2}) = C_{2'}(\mathbf{r}_{R_1},\mathbf{r}_{R_2}) + C_{2''}(\mathbf{r}_{R_1},\mathbf{r}_{R_2}) = C_{2'}(\mathbf{r}_{R_1},\mathbf{r}_{R_2})\,(1+v_e(\mathbf{r}_{R_1},\mathbf{r}_{R_2})) \tag{20}$$

with

$$v_e(\mathbf{r}_{R_1},\mathbf{r}_{R_2}) \propto |\,\mathrm{Im}\,[\langle G(\mathbf{r}_{R_1},\mathbf{r}_{R_2})\rangle]\,|^2 \tag{21}$$

the proportionality factor chosen so that $v_e(\mathbf{r}_{R_1},\mathbf{r}_{R_1}) = 1$.

In reflection, we do not know if the laplacian terms can be neglected and we thus keep them leading to the final expression of $C_2$ in R/R

$$C_2(\mathbf{r}_{R_1},\mathbf{r}_{R_2}) = C_2^{\Delta}(\mathbf{r}_{R_1},\mathbf{r}_{R_2}) + \frac{C_2^{in}(\mathbf{r}_{R_1},\mathbf{r}_{R_2}) + C_2^{out}(\mathbf{r}_{R_1},\mathbf{r}_{R_2})}{2}. \tag{22}$$

### 2D case

The different terms read in 2D:

$$C_{2'}^{\Delta} = \frac{-4}{\pi k_0 \ell}\left[\frac{2(1+z_0/\ell)}{2z_0/\ell}\right]\int \frac{\cos(\frac{q\Delta r}{L})\,\mathrm{sh}(q\frac{z_0}{L})}{2q^3\,\mathrm{sh}[q\left(1+2\frac{z_0}{L}\right)]} \times\left(\frac{L}{z_0}\frac{q\,\mathrm{sh}(q\frac{z_0}{L})}{\mathrm{sh}[q\left(1+2\frac{z_0}{L}\right)]} + \left[\frac{2(1+z_0/\ell)}{2z_0/\ell}\right] q^2\,\mathrm{sh}[q\left(1+\frac{z_0}{L}\right)]\right)\mathrm{d}q \tag{23}$$

$$C_{2'}^{in} = \frac{-1}{\pi k_0 \ell}\left[\frac{2(1+z_0/\ell)}{2z_0/\ell}\right]^2\int \frac{\cos(\frac{q\Delta r}{L})\,\mathrm{sh}(q\frac{z_0}{L})^2}{q^3\,\mathrm{sh}[q\left(1+2\frac{z_0}{L}\right)]^2} \times\left(2q+\mathrm{sh}\left[2q\frac{z_0}{L}\right]-\mathrm{sh}\left(2q\left[1+\frac{z_0}{L}\right]\right)\right)\mathrm{d}q \tag{24}$$

$$C_{2'}^{out} = \frac{1}{\pi k_0 \ell}\left[\frac{2(1+z_0/\ell)}{2z_0/\ell}\right]^2\int \frac{\cos(\frac{q\Delta r}{L})\,\mathrm{sh}(q\frac{z_0}{L})^2}{q^3\,\mathrm{sh}[q\left(1+2\frac{z_0}{L}\right)]^2}\left(-2q\,(1+z_0/L)\,\mathrm{ch}\left[2q(1+\frac{z_0}{L})\right]+2q\frac{z_0}{L}\,\mathrm{ch}\,[2qz_0/L]\right. \left.+\left[1+2q^2\left(1+\frac{z_0}{L}\right)^2\right]\mathrm{sh}\left(2q(1+\frac{z_0}{L})\right)-\left[1+2q^2\frac{z_0^2}{L^2}\right]\mathrm{sh}\,(2qz_0/L)\right)\mathrm{d}q. \tag{25}$$

To have the complete $C_2$ we use Eq. (20).

### 3D case

The different terms read in 3D:

$$C_{2'}^{\Delta} = \frac{-27}{8k_0^2\ell L}\int \frac{\mathrm{J}_0(\frac{q\Delta r}{L})\,\mathrm{sh}(q\frac{z_0}{L})\,\mathrm{sh}[q\left(1+\frac{z_0}{L}\right)]}{q\,\mathrm{sh}[q\left(1+2\frac{z_0}{L}\right)]} \times\left(\frac{\mathrm{sh}(q\frac{z_0}{L})\,\mathrm{sh}[q\left(1+\frac{z_0}{L}\right)]}{\mathrm{sh}[q\left(1+2\frac{z_0}{L}\right)]}+q\right)\mathrm{d}q \tag{26}$$

$$C_{2'}^{in} = \frac{-3}{k_0^2\ell L}\left(\frac{5}{4}\right)^2\int \frac{\mathrm{J}_0(\frac{q\Delta r}{L})\,\mathrm{sh}(q\frac{z_0}{L})^2}{q^2\,\mathrm{sh}[q\left(1+2\frac{z_0}{L}\right)]^2} \times\left(2q+\mathrm{sh}\left[2q\frac{z_0}{L}\right]-\mathrm{sh}\left(2q\left[1+\frac{z_0}{L}\right]\right)\right)\mathrm{d}q \tag{27}$$

$$C_{2'}^{out} = \frac{3}{k_0^2\ell L}\left(\frac{5}{4}\right)^2\int \frac{\mathrm{J}_0(\frac{q\Delta r}{L})\,\mathrm{sh}(q\frac{z_0}{L})^2}{q^2\,\mathrm{sh}[q\left(1+2\frac{z_0}{L}\right)]^2}\Big(-2q\,(1+z_0/L)\,\mathrm{ch}\left[2q(1+\frac{z_0}{L})\right]+2q\frac{z_0}{L}\,\mathrm{ch}\,[2qz_0/L] +\left[1+2q^2\left(1+\frac{z_0}{L}\right)^2\right]\mathrm{sh}\left(2q(1+\frac{z_0}{L})\right)-\left[1+2q^2\frac{z_0^2}{L^2}\right]\mathrm{sh}\,(2qz_0/L)\Big)\mathrm{d}q. \tag{28}$$

To have the complete $C_2$ we use Eq. (20).

# Impact of a non zero average field in the intensity-intensity correlation functions.

As explained in Chap. IV, the measurement of the R/T intensity correlation is performed with a laser illumination oriented with a non-zero angle with respect to the sample surface, that allows us to measure the intensity of the fluctuating part of the fields, $\widetilde{I}_R = |\delta E(\mathbf{r}_R)|^2$ and $\widetilde{I}_T = |\delta E(\mathbf{r}_T)|^2$, only. We want here to discuss what would be the R/T correlation if the mean fields were also measured.

$$\begin{aligned}\langle \delta I_R \delta I_T \rangle - \langle \delta \widetilde{I}_R \delta \widetilde{I}_T \rangle = 2\,\mathrm{Re}\left[\langle E_T \rangle \langle \delta E_T^* \widetilde{I}_R \rangle + \langle E_R \rangle \langle \delta E_R^* \widetilde{I}_T \rangle\right] \\ + 2\,\mathrm{Re}\left[\langle E_R \rangle \langle E_T \rangle^* \langle \delta E_R^* \delta E_T \rangle + \langle E_R \rangle \langle E_T \rangle \langle \delta E_R \delta E_T \rangle^*\right]. \end{aligned} \tag{29}$$

Hence, the R/T correlation built from the total reflected and transmitted fields contains additional interferences between the mean fields and the scattered fields. We illustrate their role in Fig. 4, where we compare $\langle \delta \widetilde{I}_T \delta \widetilde{I}_R \rangle / [\langle \delta \widetilde{I}_T \rangle \langle \delta \widetilde{I}_R \rangle]$ [(a) panel] and $\langle \delta I_T \delta I_R \rangle / [\langle \delta I_T \rangle \langle \delta I_R \rangle]$ [(b) panel] calculated for a 3D disordered slab ($L/\ell = 1$, $k_0\ell = 15$, illumination angle $\theta_a = 45°$). On top of the long-range component of $\langle \delta \widetilde{I}_T \delta \widetilde{I}_R \rangle / [\langle \delta \widetilde{I}_T \rangle \langle \delta \widetilde{I}_R \rangle]$, $\langle \delta I_T \delta I_R \rangle / [\langle \delta I_T \rangle \langle \delta I_R \rangle]$ also exhibits tiny oscillating contributions and additional long-range contribution due to the four terms of Eq. (29). These contributions, negligible in the deep diffusive regime $L \gg \ell$, become important at moderate optical depth $L \sim \ell$. This explains why the positive contribution to the long-range correlation discussed in Chap. IV was not detected in Ref. [85]. At large optical depth the two correlations are equal while it is no more the case in the regime $L \sim \ell$ where interference terms dominate.

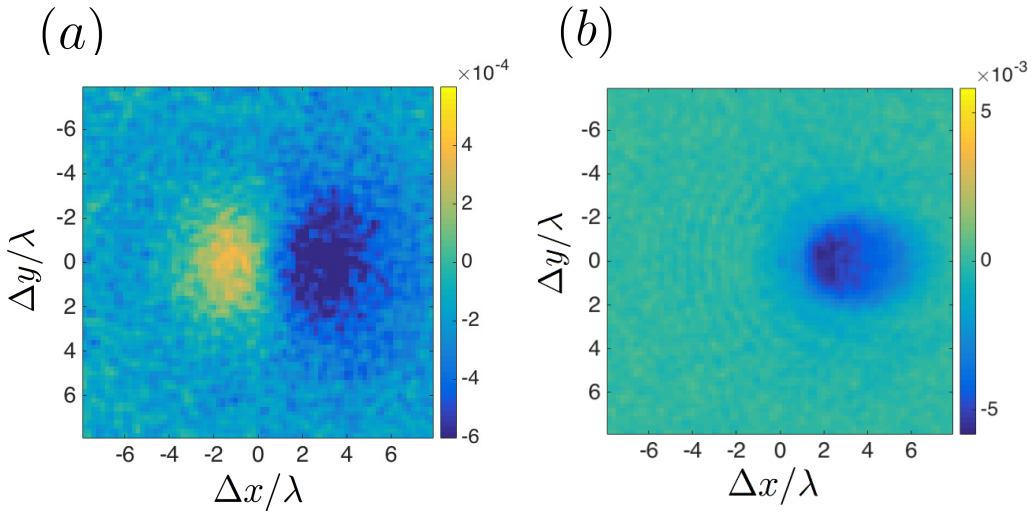


**Figure 4** – Comparaison of two R/T correlation functions calculated from numerical simulation of the wave equation in a 3D slab. (a) Correlation function $\langle \delta \widetilde{I}_T \delta \widetilde{I}_R \rangle / [\langle \delta \widetilde{I}_T \rangle \langle \delta \widetilde{I}_R \rangle]$ built from fluctuating parts of the fields; (b) Correlation function $\langle \delta I_T \delta I_R \rangle / [\langle \delta I_T \rangle \langle \delta I_R \rangle]$ built from the full fields. Parameters: $k_0\ell = 15$, $L/\ell = 1$, $\theta_a = 45°$.

# Coupled-dipole method

When an object interacts with an electromagnetic field it develops a polarization. If one considers a small enough volume inside the object, the induced polarization is uniform within this volume, and hence that small region can be represented by a radiating electric dipole with the appropriate polarizability. Point dipoles are small by definition and the scattering problem for a medium composed of them reduces to the problem of finding the value of the dipoles interacting with each other in the electromagnetic field. This method called coupled dipoles method [25] is the one we use to calculate numerically the intensity in the transmitted and reflected speckle patterns. Repeating the calculations for a large number of configurations of disorder (positions of scatterers) allows us to compute statistics of fields and intensities. The system contains $N$ randomly distributed non-overlapping point scatterers, and is illuminated by a plane wave from the left at normal incidence. We deal with TE-polarized waves with an electric field oriented along the invariance axis of the system (scalar waves). The resonant point scatterers are described by their electric polarizability

$$\alpha(\omega) = -\frac{2\pi^{d-2}\Gamma}{k_0^d(\omega - \omega_0 + i\Gamma/2)} \tag{30}$$

where $\omega_0$ is the resonance frequency, $\Gamma$ the linewidth and $d$ the dimension of the problem. This specific form of the polarizability fulfills the optical theorem (energy conservation) in 2D and 3D scalar. From the polarizability the scattering cross section $\sigma(\omega) = k_0^3|\alpha(\omega)|^2/4$ in 2D ($\sigma(\omega) = k_0^4|\alpha(\omega)|^2/(4\pi)$ in 3D) and the scattering mean-free path $\ell(\omega) = [\rho\sigma(\omega)]^{-1}$ can be deduced, where $\rho = N/(LW^{d-1})$ is the number density of scatterers. In the following, we consider scatterers at resonance ($\omega = \omega_0$) in order to reach large optical thicknesses with a reasonable number of scatterers (typically a few hundreds).

In the coupled dipoles formalism, the exciting field $E_j$ on scatterer number $j$ is written as [25]

$$E_j = E_0\left(\mathbf{r}_j\right) + \alpha\left(\omega\right) k_0^2 \sum_{\substack{k=1 \\ k\neq j}}^{N} G_0\left(\mathbf{r}_j - \mathbf{r}_k\right) E_k \tag{31}$$

where $G_0$ is the free-space Green's function given by $G_0(\mathbf{r} - \mathbf{r}') = (i/4)\,\mathrm{H}_0(k_0|\mathbf{r} - \mathbf{r}'|)$ in 2D and $G_0(\mathbf{r} - \mathbf{r}') = \exp\left[ik_0|\mathbf{r} - \mathbf{r}'|\right]/[4\pi|\mathbf{r} - \mathbf{r}'|]$ in 3D. Equation (31) defines a set of $N$ linear equations that are solved by a standard matrix inversion procedure. Once the exciting field is known on each scatterer, the field $E(\mathbf{r})$ and the intensity at any position $\mathbf{r}$ inside or outside the scattering medium can be calculated by a direct summation, using

$$E(\mathbf{r}) = E_0\left(\mathbf{r}\right) + \alpha\left(\omega\right) k_0^2 \sum_{j=1}^{N} G_0\left(\mathbf{r} - \mathbf{r}_j\right) E_j. \tag{32}$$

# Intensity-intensity correlation in the gaussian approximation for the field

In this appendix we give details about the derivation of the $C_1$ correlation functions in T/T, R/R and R/T.

## .3.1 Field-field correlation in transmission

The easiest and most known geometry to test the analytical derivation of the $C_1$ correlation function is the transmission/transmission (T/T) geometry. In that case we can show with simple arguments that $C_1$ has a unitary value between two identical points. This simply comes from the fact that when $\mathbf{r}_{T1} = \mathbf{r}_{T2}$ we can not distinguish the diagram of the field-field correlation from the one giving the diffuse intensity.

Let us remind that:

$$C_1(\mathbf{r}_{T1}, \mathbf{r}_{T2}) = \frac{|\langle \delta E_{T1} \delta E^*_{T2} \rangle|^2}{\langle \widetilde{I}_{T1} \rangle \langle \widetilde{I}_{T2} \rangle}. \tag{33}$$

We thus have to calculate the field-field correlation in transmission. Let us first have a quick diagrammatic analysis of Fig. II.13. We see that first the two fields propagate with straight lines up to a point close to the boundary of the medium, then they travel with twisting lines up to a point close to transmission where they split and leave with straight lines. The mathematical writing of this scattering sequence is

$$\begin{aligned}
\langle \delta E_{T1} \delta E^*_{T2} \rangle &= \int |\langle E(\mathbf{r}_1) \rangle|^2 \, \mathrm{L}(\mathbf{r}_1, \mathbf{r}_2) \langle G(\mathbf{r}_{T1} - \mathbf{r}_2) \rangle \langle G(\mathbf{r}_{T2} - \mathbf{r}_2) \rangle^* \mathrm{d}\mathbf{r}_1 \mathrm{d}\mathbf{r}_2 \\
&= I_0 \int \exp\left(-\frac{z_1}{\ell}\right) \mathrm{L}(z_1, z_2, \mathbf{q}) e^{i\mathbf{q}.(\mathbf{r}_{t1} - \mathbf{r}_{t2})} \langle G(\mathbf{k}_1) \rangle \langle G(\mathbf{k}_2) \rangle^* \\
&\times e^{i\mathbf{k_1}.(\mathbf{r}_{T1} - \mathbf{r}_2)} e^{-i\mathbf{k_2}.(\mathbf{r}_{T2} - \mathbf{r}_2)} \mathrm{d}\mathbf{r}_1 \mathrm{d}\mathbf{r}_2 \mathrm{d}\mathbf{k}_1/(2\pi)^d \mathrm{d}\mathbf{k}_2/(2\pi)^d \mathrm{d}\mathbf{q}/(2\pi)^{d-1} \\
&= I_0 \int \exp\left(-\frac{z_1}{\ell}\right) \mathrm{L}(z_1, z_2, \mathbf{q} = 0) \frac{e^{ik_{1z}(L-z_2)}}{k_{1z}^2 + kt^2 - k_{eff}^2} \frac{e^{-ik_{2z}(L-z_2)}}{k_{2z}^2 + kt^2 - k_{eff}^{*2}} \\
&\times e^{i\mathbf{k}_T.\mathbf{\Delta R}} \mathrm{d}z_1 \mathrm{d}z_2 \mathrm{d}k_{1z}/(2\pi) \mathrm{d}k_{2z}/(2\pi) \mathrm{d}\mathbf{k}_T/(2\pi)^{d-1} \\
&\simeq \ell I_0 \int \mathrm{L}(0, z_2, \mathbf{q} = 0) \frac{ie^{i\widetilde{k_1}(L-z_2)}}{2\widetilde{k_1}} \frac{ie^{-i\widetilde{k_2}(L-z_2)}}{2\widetilde{k}_2} e^{i\mathbf{k}_T.\mathbf{\Delta R}} \mathrm{d}z_2 \mathrm{d}\mathbf{k}_T/(2\pi)^{d-1}.
\end{aligned} \tag{34}$$

The only approximation done in Eq. (34) is the one done to access the last line, where we disconnected the entrance point of the Ladder from the ballistic intensity. The main difference between this derivation and the one done to access the diffuse intensity in transmission is the work done on the exit vertex. A rough approximation would have been to disconnect the Ladder from the two average

Green's functions and to calculate the integration over all space of $\langle G(\mathbf{r}_{T1}-\mathbf{r}_2)\rangle\langle G(\mathbf{r}_{T2}-\mathbf{r}_2)\rangle^*$ which is proportional to the imaginary part of $\langle G(\mathbf{r}_{T1}-\mathbf{r}_{T2})$. Let us stress here that the disconnecting step is more subtle here than in Eq. III.31 because we have to select one point for the Ladder to stop. Should it be $\mathbf{r}_{T1}$ or $\mathbf{r}_{T2}$? In transmission this does not have a strong impact on the calculation, neither it does in reflection, but in the case of reflection/transmission where should we stop? To avoid this discussion and to have the same formalism in transmission, reflection and transmission/reflection we do not split the Ladder and the exit vertex in the calculation of $C_1$. In Eq. (34) $\widetilde{k_1}$ and $\widetilde{k_2}$ are defined as

$$\widetilde{k_1} = \sqrt{k_0^2 - k_T^2 + i\frac{k_0}{\ell}} = K_{TT} + iK'_{TT} = \widetilde{k_2}^* \tag{35}$$

with $K'_{TT} \geq 0$. To do the integration over $z_2$ we can use the expression of the Ladder

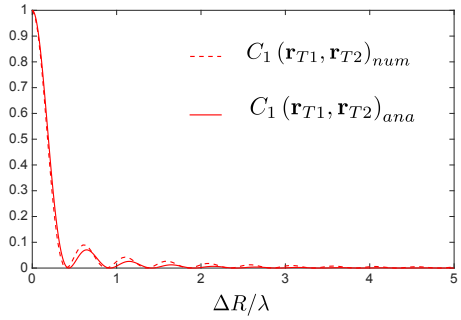


**Figure 5** – Numerical (dashed line) and analytical (solid line) calculation of $C_1(\mathbf{r}_{T1},\mathbf{r}_{T2})$ versus the transverse distance normalized by $\lambda$ for a thick ($b = 10$) and dilute ($k\ell = 10$) system.

$$\begin{aligned}\langle \delta E_{T1}\delta E^*_{T2}\rangle &\simeq \ell I_0 \int \mathrm{L}(0,z_2,\mathbf{q}=0)\frac{e^{-2K'_{TT}(L-z_2)}}{4(K_{TT}^2+K_{TT}'^2)}e^{i\mathbf{k}_T.\mathbf{\Delta R}}\mathrm{d}z_2\mathrm{d}\mathbf{k}_T/(2\pi)^{d-1} \\ &\simeq \frac{d\gamma I_0 z_0}{\ell(L+2z_0)}\int (L+z_0-z_2)\frac{e^{-2K'_{TT}(L-z_2)}}{4(K_{TT}^2+K_{TT}'^2)}e^{i\mathbf{k}_T.\mathbf{\Delta R}}\mathrm{d}z_2\mathrm{d}\mathbf{k}_T/(2\pi)^{d-1} \\ &\simeq \frac{d\gamma I_0 z_0}{\ell(L+2z_0)}\int \mathrm{F}_{TT}(K_{TT},K'_{TT},z_0,L)e^{i\mathbf{k}_T.\mathbf{\Delta R}}\mathrm{d}\mathbf{k}_T/(2\pi)^{d-1}\end{aligned} \tag{36}$$

and end up with a Fourier transform expression of a function $\mathrm{F}_{TT}(K_{TT},K'_{TT},z_0,L)$

$$\begin{aligned}\mathrm{F}_{TT}(K_{TT},K'_{TT},z_0,L) &= \int (L+z_0-z_2)\frac{e^{-2K'_{TT}(L-z_2)}}{4(K_{TT}^2+K_{TT}'^2)}\mathrm{d}z_2 \\ &\simeq \frac{1+2K'_{TT}z_0}{4K_{TT}'^2\left(4[K_{TT}^2+K_{TT}'^2]\right)}.\end{aligned} \tag{37}$$

Keeping in mind that the normalizing factor is defined according to

$$\langle|\delta E_T|^2\rangle \simeq \frac{d\gamma I_0 z_0}{\ell(L+2z_0)}\int \mathrm{F}_{TT}(K_{TT},K'_{TT},z_0,L)\mathrm{d}\mathbf{k}_T/(2\pi)^{d-1} \tag{38}$$

the $C_1$ correlation in transmission can be calculated the following way

$$C_1(\mathbf{r}_{T1},\mathbf{r}_{T2}) = \frac{|\int \mathrm{F}_{TT}(K_{TT},K'_{TT},z_0,L)e^{i\mathbf{k}_T.\mathbf{\Delta R}}\mathrm{d}\mathbf{k}_T/(2\pi)^{d-1}|^2}{\left(\int \mathrm{F}_{TT}(K_{TT},K'_{TT},z_0,L)\mathrm{d}\mathbf{k}_T/(2\pi)^{d-1}\right)^2}. \tag{39}$$

In Fig. 5 we plot the numerically and analytically (using Eq. (39) ) calculated $C_1$ correlation in transmission of a thick ($b = 10$) and dilute ($k\ell = 10$) complex medium versus the transverse distance normalized by the wavelength. We see a good agreement between numerics and analytics. The $C_1$ correlation in transmission is an oscillating function whose value is unity at zero distance between the points. We see that the typical oscillating distance is approximatively $\lambda/2$. We believe the small difference between numerics and analytics is due to the fact that we use bulk (calculated for an infinite medium) average Green's functions in our calculation. Those average Green's function should be a good approximation of the Green's function for points inside the medium. Nonetheless we can see in Fig. II.13 that for $C_1$ correlation the average Green's functions connect points close to the boundary to one point at the boundary and thus should differ from bulk Green's functions.

## .3.2 Field-field correlation in reflection

Let us go quickly through the exact same calculation in reflection. In that case

$$C_1(\mathbf{r}_{R1}, \mathbf{r}_{R2}) = \frac{|\langle \delta E_{R1} \delta E^*_{R2} \rangle|^2}{\langle \widetilde{I}_{R1} \rangle \langle \widetilde{I}_{R2} \rangle}. \tag{40}$$

The field-field correlation writes

$$\begin{aligned}
\langle \delta E_{R1} \delta E^*_{R2} \rangle &= \int |\langle E(\mathbf{r}_1) \rangle|^2 \, \mathrm{L}(\mathbf{r}_1, \mathbf{r}_2) \langle G(\mathbf{r}_{R1} - \mathbf{r}_2) \rangle \langle G(\mathbf{r}_{R2} - \mathbf{r}_2) \rangle^* \mathrm{d}\mathbf{r}_1 \mathrm{d}\mathbf{r}_2 \qquad (41) \\
&= I_0 \int \exp\left(-\frac{z_1}{\ell}\right) \mathrm{L}(z_1, z_2, \mathbf{q}) e^{i\mathbf{q}.(\mathbf{r}_{t1} - \mathbf{r}_{t2})} \langle G(\mathbf{k}_1) \rangle \langle G(\mathbf{k}_2) \rangle^* \\
&\times e^{i\mathbf{k_1}.(\mathbf{r}_{R1} - \mathbf{r}_2)} e^{-i\mathbf{k_2}.(\mathbf{r}_{R2} - \mathbf{r}_2)} \mathrm{d}\mathbf{r}_1 \mathrm{d}\mathbf{r}_2 \mathrm{d}\mathbf{k}_1/(2\pi)^d \mathrm{d}\mathbf{k}_2/(2\pi)^d \mathrm{d}\mathbf{q}/(2\pi)^{d-1} \\
&= I_0 \int \exp\left(-\frac{z_1}{\ell}\right) \mathrm{L}(z_1, z_2, \mathbf{q} = 0) \frac{e^{-ik_{1z} z_2}}{k_{1z}^2 + kt^2 - k_{eff}^2} \frac{e^{ik_{2z} z_2}}{k_{2z}^2 + kt^2 - k_{eff}^{*2}} \\
&\times e^{i\mathbf{k}_T.\mathbf{\Delta R}} \mathrm{d}z_1 \mathrm{d}z_2 \mathrm{d}k_{1z}/(2\pi) \mathrm{d}k_{2z}/(2\pi) \mathrm{d}\mathbf{k}_T/(2\pi)^{d-1} \\
&\simeq \ell I_0 \int \mathrm{L}(0, z_2, \mathbf{q} = 0) \frac{i e^{i\widetilde{k_1}(L - z_2)}}{2\widetilde{k_1}} \frac{i e^{-i\widetilde{k_2}(L - z_2)}}{2\widetilde{k}_2} e^{i\mathbf{k}_T.\mathbf{\Delta R}} \mathrm{d}z_2 \mathrm{d}\mathbf{k}_T/(2\pi)^{d-1}. \qquad (42)
\end{aligned}$$

In Eq. (41) $\widetilde{k_1}$ and $\widetilde{k_2}$ are defined as

$$\widetilde{k_1} = \sqrt{k_0^2 - k_T^2 + i\frac{k_0}{\ell}} = K_{RR} + iK'_{RR} = \widetilde{k_2}^* \tag{43}$$

with $K'_{RR} \leq 0$. We can now do the integration over $z_2$

$$\begin{aligned}
\langle \delta E_{R1} \delta E^*_{R2} \rangle &\simeq \ell I_0 \int \mathrm{L}(0, z_2, \mathbf{q} = 0) \frac{e^{2K'_{RR} z_2}}{4(K_{RR}^2 + K_{RR}'^2)} e^{i\mathbf{k}_T.\mathbf{\Delta R}} \mathrm{d}z_2 \mathrm{d}\mathbf{k}_T/(2\pi)^{d-1} \qquad (44) \\
&\simeq \frac{d\gamma I_0 z_0}{\ell(L + 2z_0)} \int (L + z_0 - z_2) \frac{e^{2K'_{RR} z_2}}{4(K_{RR}^2 + K_{RR}'^2)} e^{i\mathbf{k}_T.\mathbf{\Delta R}} \mathrm{d}z_2 \mathrm{d}\mathbf{k}_T/(2\pi)^{d-1} \\
&\simeq \frac{d\gamma I_0 z_0}{\ell(L + 2z_0)} \int \mathrm{F}_{RR}(K_{RR}, K'_{RR}, z_0, L) e^{i\mathbf{k}_T.\mathbf{\Delta R}} \mathrm{d}\mathbf{k}_T/(2\pi)^{d-1}
\end{aligned}$$

and end up with a Fourier transform expression of $F_{RR}$

$$\mathrm{F}_{RR}(K_{RR}, K'_{RR}, z_0, L) = \int (L + z_0 - z_2) \frac{e^{2K'_{RR} z_2}}{4(K_{RR}^2 + K_{RR}'^2)} \mathrm{d}z_2 \simeq \frac{2K'_{RR} L}{4K_{RR}'^2 \left(4[K_{RR}^2 + K_{RR}'^2]\right)}. \tag{45}$$

The last equality of Eq. (45) is the limit of $\mathrm{F}_{RR}$ at large optical thickness. Taking into account that the normalization factor writes:

$$\langle |\delta E_R|^2 \rangle \simeq \frac{d\gamma I_0 z_0}{\ell(L + 2z_0)} \int \mathrm{F}_{RR}(K_{RR}, K'_{RR}, z_0, L) \mathrm{d}\mathbf{k}_T / (2\pi)^{d-1} \tag{46}$$

we can calculate the $C_1$ correlation in reflection the following way:

$$C_1(\mathbf{r}_{R1}, \mathbf{r}_{R2}) = \frac{|\int \mathrm{F}_{RR}(K_{RR}, K'_{RR}, z_0, L) e^{i\mathbf{k}_T \cdot \mathbf{\Delta R}} \mathrm{d}\mathbf{k}_T / (2\pi)^{d-1}|^2}{\left(\int \mathrm{F}_{RR}(K_{RR}, K'_{RR}, z_0, L) \mathrm{d}\mathbf{k}_T / (2\pi)^{d-1}\right)^2}. \tag{47}$$

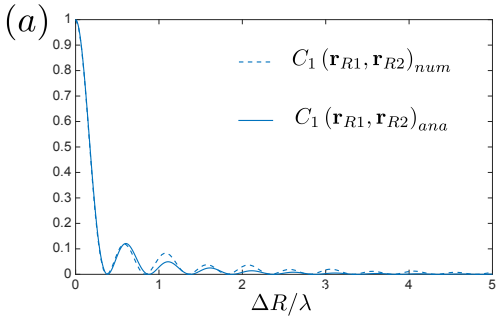


**Figure 6** – Numerical (blue dashed line) and analytical (blue solid line) calculation of $C_1$ in reflection of a thick ($b = 10$) and dilute ($k\ell = 10$) sample.

In panel (a) of Fig. 6 we plot the numerically and analytically (using Eq. (47)) calculated $C_1$ correlation in reflection of a thick ($b = 10$) and dilute ($k\ell = 10$) complex medium versus the transverse distance normalized by the wavelength. We see a good agreement between numerics and analytics. The $C_1$ correlation in reflection is an oscillating function whose value is unity at zero distance between the points. We see that the typical oscillating distance is approximatively $\lambda/2$.

## .3.3 Large optical thickness scaling of $C_1$ in reflection/transmission

In this subsection we give details about the large optical thickness scaling of $C_1$ in reflection/transmission. Let us recall the expression of $C_1$ valid in both 2D and 3D geometries:

$$C_1(\Delta R = 0) \propto \frac{L}{\ell} \left| \frac{d\gamma I_0 z_0}{\ell(L + 2z_0)} \int \mathrm{F}_{RT}(K, K') \frac{\mathrm{d}\mathbf{k}_T}{(2\pi)^{d-1}} \right|^2, \tag{48}$$

with

$$\mathrm{F}_{RT}(K, K') = \frac{e^{-(iK+K')L} \left(-1 + 2iKz_0 + e^{2iKL}[1 - 2iK(L + z_0)]\right)}{4(K^2 + K'^2)4K^2}. \tag{49}$$

In this subsection we do not care about numerical constant, we only look for the scaling of the quantity given in Eq. (48).

### 2D case

In 2D we can rewrite Eq. (48) into

$$C_1(\Delta R=0) \propto \frac{k_0^2}{L\ell^3} \underbrace{\left| \int \mathrm{F}_{RT}(K,K') \frac{\mathrm{d}\mathbf{k}_T}{(2\pi)^{d-1}} \right|^2}_{A}. \tag{50}$$

The term called A into Eq. (50) writes

$$\begin{aligned} A =& \left| \int_0^\infty \frac{e^{-(iK+K')L}\left[-1+2iKz_0+e^{2iKL}(1-2iK(L+z_0))\right]}{2(K^2+K'^2)4K^2} \frac{\mathrm{d}k_T}{2\pi} \right|^2 \\ \sim & e^{-L/\ell} \frac{k_0^2 L^2}{k_0^8} \left| \int_0^{k_0} e^{-i(\sqrt{k_0^2-k_T^2}L)} \frac{\mathrm{d}k_T}{2\pi} \right|^2. \end{aligned} \tag{51}$$

Using the fact that

$$\begin{aligned} \left| \int_0^{k_0} e^{-i(\sqrt{k_0^2-k_T^2}L)} \frac{\mathrm{d}k_T}{2\pi} \right|^2 &\sim k_0^2 \left| \int_0^1 e^{-i(k_0 L\sqrt{1-q^2})} \frac{\mathrm{d}q}{2\pi} \right|^2 \\ &\sim \frac{k_0^2}{k_0 L}, \end{aligned} \tag{52}$$

we can give the final expression of the scaling of the value at zero transverse distance of $C_1$ in R/T:

$$C_1(\Delta R=0) \sim e^{-L/\ell} \frac{L}{\ell} \frac{1}{k_0^2\ell^2} \frac{1}{k_0 L}. \tag{53}$$

### 3D case

In 3D we can rewrite Eq. (48) into

$$C_1(\Delta R=0) \propto \frac{1}{L\ell^3} \underbrace{\left| \int \mathrm{F}_{RT}(K,K') \frac{\mathrm{d}\mathbf{k_T}}{(2\pi)^{d-1}} \right|^2}_{A}. \tag{54}$$

The term called A into Eq. (54) writes

$$\begin{aligned} A =& \left| \int_0^\infty \int_\pi^\pi \frac{e^{-(iK+K')L}\left[-1+2iKz_0+e^{2iKL}(1-2iK(L+z_0))\right]}{2(K^2+K'^2)4K^2} k_T \frac{\mathrm{d}k_T}{2\pi} \right|^2 \\ \sim & \frac{L^2}{k_0^2} \left| \int_0^1 e^{-i(k_0 L\sqrt{1-q^2})} q \frac{\mathrm{d}q}{2\pi} \right|^2 \\ \sim & \frac{1}{k_0^4} e^{-L/\ell}. \end{aligned} \tag{55}$$

We can give the final expression of the scaling of the value at zero transverse distance of $C_1$ in R/T:

$$C_1(\Delta R=0) \sim e^{-L/\ell} \frac{L}{\ell} \frac{1}{k_0^2\ell^2} \frac{1}{k_0^2 L^2}. \tag{56}$$

## Discussion

Both the 2D and the 3D scalings of the value at zero transverse distance of $C_1$ in R/T are proportional to $e^{-L/\ell}$. In the diffusive regime this is the important term making the $C_1$ correlation completely negligible in comparison with non gaussian correlations scaling as $1/(k_0 L)$ in 2D and as $1/(k_0 L)^2$ in 3D.

# Four-fields vertex

In this appendix we discuss the Born approximation for the four-fields vertex and its difference from the full four-fields vertex. We do not enter the equation for the fourth order moment of the field (equivalent of Bethe-Salpeter equation). We rather discuss the impact of the choice of the vertex in the different diagrams one can build.

## .4 First order Born approximation for the four-fields vertex

We start with the usual approximation for the four-fields vertex: the fields can only be scattered in pairs by the disorder. We do not consider the possibility that three or four fields are scattered by the same impurity.

### .4.1 Four-fields vertex in the Born approximation

In Fig. 7 we represent the vertex in the Born approximation. This vertex is branched on the incident

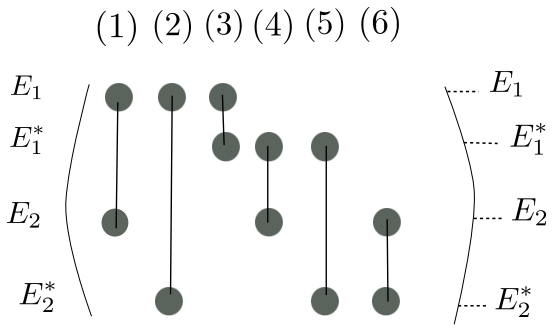


**Figure 7** – Four-fields vertex in the Born approximation. The vertex contains six different operators corresponding to the common scattering of two fields.

average fields and iterated until the exit of the four fields from the sample. It contains 6 operators and is branched with average Green's functions (dotted lines). If you apply the first operator to the four fields coming then $E_1$ and $E_2$ encounters a common scattering event while nothing happens to $E_1^*$ and $E_2^*$. If you now reapply the vertex and use for instance the sixth operator, then $E_2$ and $E_2^*$ encounters a common scattering event. Between the first and the second scattering event, the fields propagates with average Green's functions. One can observe that this procedure creates many different scattering sequences, but only a few have non negligible value. In the next subsections we discuss how the usual diagrams are created with the use of this vertex.

## .4.2 Average intensity and $C_1$

Let us recover the two easiest four-fields scattering sequences using this vertex: the one leading to the product of the average intensities and the one leading to the square modulus of the field-field correlation responsible for the $C_1$ correlation.

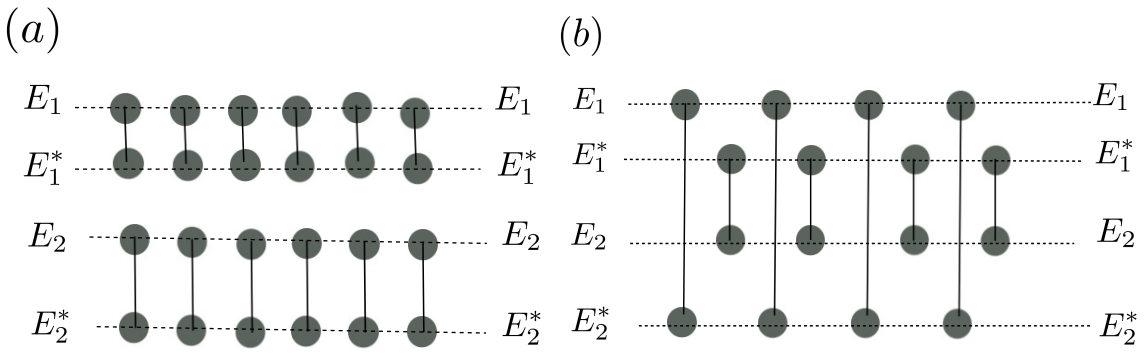


**Figure 8** – Panel (a): repeated application of the operators 3 and 6 of the vertex represented In Fig. 7. Panel (b): repeated application of the operators 2 and 4 of the vertex represented In Fig. 7. We recognize in panel (a) the four-fields diagram responsible for the product of the average intensities. We recognize in panel (b) the four-fields diagram responsible for the squared modulus of the field-field correlation.

In Fig. 8 we represent two scattering sequences obtained from the repeated application of the vertex represented in Fig. 7. In panel (a) we applied a large number of times the third and sixth operators of the vertex. We recognize in this figure two ladder diagrams giving rise to the independent propagation of $\langle|\delta E_1|^2\rangle$ and $\langle|\delta E_2|^2\rangle$. In panel (b) we represent the scattering sequences obtained from the application of a large number of times the second and the fourth operators. We recognize in this figure two ladder diagrams giving rise to the modulus squared of the field-field correlation $|\langle\delta E_2\delta E_1^*\rangle|^2$. We can keep in mind that when the fields arrived at the end of the propagation in the same configuration that the one represented in panel (b) in Fig. 8 ($E_1$ with $E_2^*$ and $E_1^*$ with $E_2$) then they encounters the same exit vertex as the one in the $C_1$ correlation. This vertex gives the diagrams a short-range character. Whereas when the fields arrived at the end of the propagation in the same configuration that the one represented in panel (a) in Fig. 8 ($E_1$ with $E_1^*$ and $E_2^*$ with $E_2$) then they encounters the same exit vertex that the one in average intensity diagrams. This vertex gives the diagrams a long-range character.

## .4.3 The $C_2$ correlation

Let us now discuss how we can obtain the the two different $C_2$ diagrams from the vertex represented in Fig. 7. The first possibility to create a $C_2$ diagram is the following. One first applies the second and the fourth operators of the vertex represented in Fig. 7 a large number of times creating two ladder diagrams ($E_1$ with $E_2^*$ and $E_1^*$ with $E_2$). At a certain point, the pairs of fields mix in order to continue their propagation in ladder diagrams ($E_1$ with $E_1^*$ and $E_2^*$ with $E_2$). There are three possibilities to do the mixing (using the vertex given in Fig. 7). The first one is simply to propagate with average Green's functions (panel (a) in Fig. 9), while for the second and the third possibilities two fields encounter a common scattering event during the propagation (first and fifth operator of the vertex represented in Fig. 7). We recognize at the end of the propagation the same exit vertex as for the average intensities giving to these diagrams represented in Fig. 9 a long-range character.

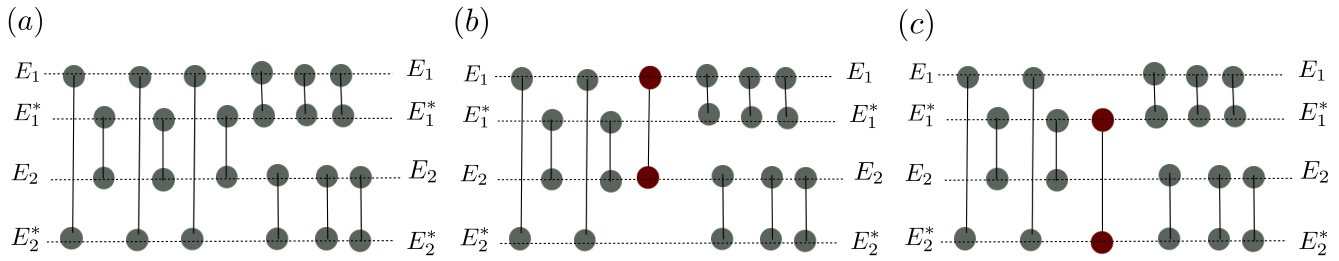


**Figure 9** – In panel (a) we apply repeatedly the second and fourth operators of the vertex. At a certain point we start to apply a large number of times the third and sixth operators of the vertex. This diagram is the $C_2$ diagram with the $H_A$ component of the Hikami box. In panels (b,c) we apply repeatedly the second and fourth operators of the vertex. At a certain point we start to apply a large number of times the third and sixth operators of the vertex. In between the two propagations with ladder diagrams, we apply the first or the fifth operator of the vertex. These diagrams are the $C_2$ diagram with the $H_B$ and $H_C$ components of the Hikami box.

The second possibility to create a $C_2$ diagram is the following. One first apply the third and the sixth operators a large number of times creating two ladder diagrams ($E_1$ with $E_1^*$ and $E_2^*$ with $E_2$). At a certain points, the pairs of fields mix in order to continue their propagation in ladder diagrams ($E_1$ with $E_2^*$ and $E_1^*$ with $E_2$). There are three possibilities to do the mixing (using the vertex given in Fig. 7). The first one is simply to propagate with average Green's functions (panel (a) in Fig. 10), while for the second and the third possibilities two fields encounter a common scattering event during the propagation (first and fifth operator of the vertex represented in Fig. 7). We recognize at the end of the propagation the same exit vertex as for the $C_1$ correlation giving to these diagrams represented in Fig. 10 a short-range character.

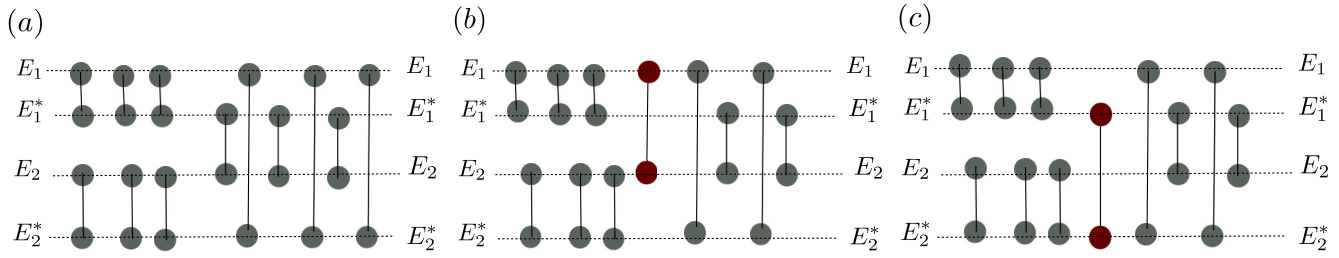


**Figure 10** – In panel (a) we apply repeatedly the third and sixth operators of the vertex. At a certain point we start to apply a large number of times the second and the fourth operators of the vertex. This diagram is the $C_2$ diagram with the $H_A$ component of the Hikami box and the short-range exit vertex. In panels (b,c) we apply repeatedly the third and sixth operators of the vertex. At a certain point we start to apply a large number of times the second and the fourth operators of the vertex. In between the two propagations with ladder diagrams, we apply the first or the fifth operator of the vertex. These diagrams are the $C_2$ diagram with the $H_B$ and $H_C$ components of the Hikami box and the short-range exit vertex.

## .4.4 The $C_0$ correlation

In this subsection we discuss the $C_0$ diagrams. First we choose the following definition for the $C_0$ diagrams: The $C_0$ diagrams are all the diagrams connecting two ladders with one scattering event (either in entrance or in exit of the propagation).

### Entrance crossing

Following the reasoning in the last subsection we discuss how to obtain the $C_0$ diagrams with an extra scattering event in entrance of the propagation using the vertex represented in Fig. 7. In Fig. 11 we represent the first possibility to create a $C_0$ diagram with the extra scattering event in entrance of the sample. These diagrams can be obtained with the vertex represented in Fig. 7 using first the fourth operator [panel (a)], or the second operator [panel (b)], or the first operator [panel (c)], or the fifth operator [panel (d)] before a repeated application of the operators three and six of the vertex represented in Fig. 7. The pairing of the two ladders gives to this diagram a long-range character. This diagram is the original $C_0$ diagram considered in [60, 91] and this is the one derived in the R/T configuration in Chap. IV.

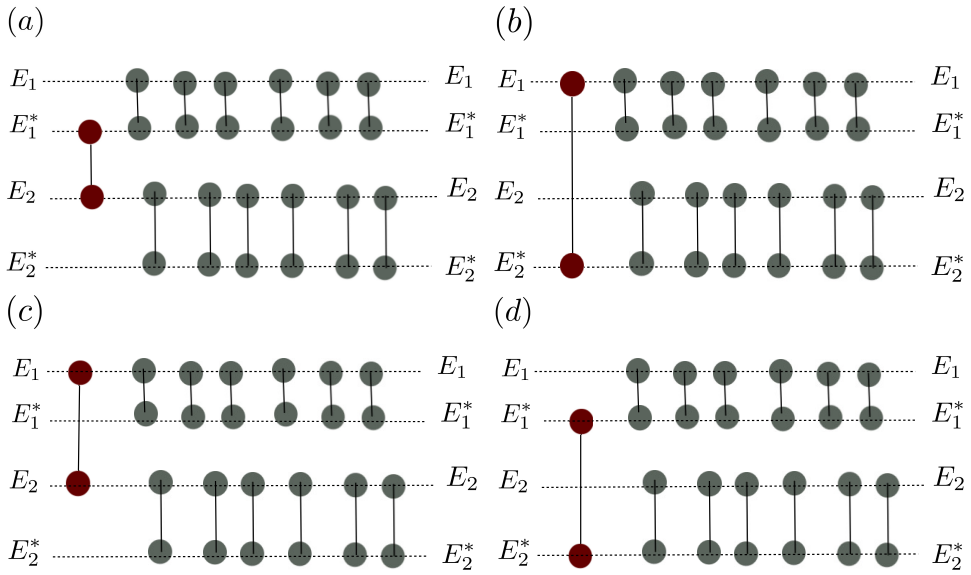


**Figure 11** – Four different diagrams corresponding to the first $C_0$ diagram with the extra scattering event in entrance of the medium. The sum of the four diagrams represented gives the diagram considered in Chap. IV. The extra scattering event connects two ladders and the pairing at the exit gives to this diagram a long-range character.

In Fig. 12 we represent the second possibility to create a $C_0$ diagram with the extra scattering event in entrance of the sample. These diagrams can be obtained with the vertex represented in Fig. 7 using first the third operator [panel (a)], or the sixth operator [panel (b)], or the fifth operator [panel (c)], or the first operator [panel (d)] before a repeated application of the operators two and four of the vertex represented in Fig. 7. The pairing of the two ladders gives to this diagram a short-range character.

### Exit crossing

Now the consider the $C_0$ diagrams with the extra scattering event in exit of the propagation. This possibility gives rise to two different diagrams. In Fig. 13 we represent the first possibility to create a $C_0$ diagram with the extra scattering event in exit of the sample. These diagrams can be obtained with the vertex represented in Fig. 7 using repeatedly the second and the fourth operators of the vertex represented in Fig. 7 before applying first the third operator [panel (a)], or the sixth operator [panel (b)], or the first operator [panel (c)], or the fifth operator [panel (d)]. The extra scattering event gives a short-range character to this diagram.

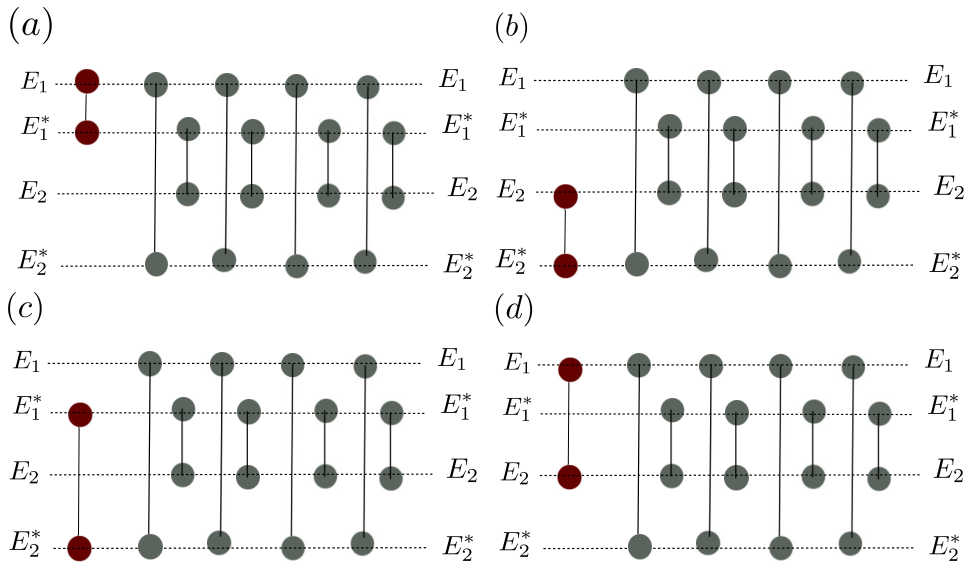


**Figure 12** – Four different diagrams corresponding to the second $C_0$ diagram with the extra scattering event in entrance of the medium. The extra scattering event connects two ladders and the pairing at the exit gives to this diagram a short-range character.

In Fig. 14 we represent the second possibility to create a $C_0$ diagram with the extra scattering event in exit of the sample. These diagrams can be obtained with the vertex represented in Fig. 7 using repeatedly the third and the sixth operators of the vertex represented in Fig. 7 before applying first the fourth operator [panel (a)], or the second operator [panel (b)], or the first operator [panel (c)], or the fifth operator [panel (d)]. The extra scattering event gives a short-range character to this diagram.

## .5 The complete four-fields vertex

Let us now discuss the full four-fields vertex. In Fig. 15 we represent the vertex beyond its usual Born approximation. In addition to the possibilities that two fields encounter a common scattering event, one adds to the vertex the possibility that three and four fields encounter a common scattering event. Those new possibilities can to be taken into account to modify the value of the existing diagrams [121, 39], but they also create new topologies of diagrams as pointed out in ref. [39]). These diagrams should be sub-leading in the diffusive regime because never observed for now.

The scattering sequence we specify in Fig. 16 corresponds to the unique application of the operator of the common scattering of four fields contained in the vertex given in Fig. 15. This scattering sequence is studied in detail in Chap. V and seems to be the dominant term of the non-gaussian correlation functions in T/T, R/R and R/T in the quasi-ballistic regime ($\lambda \ll L \ll \ell$).

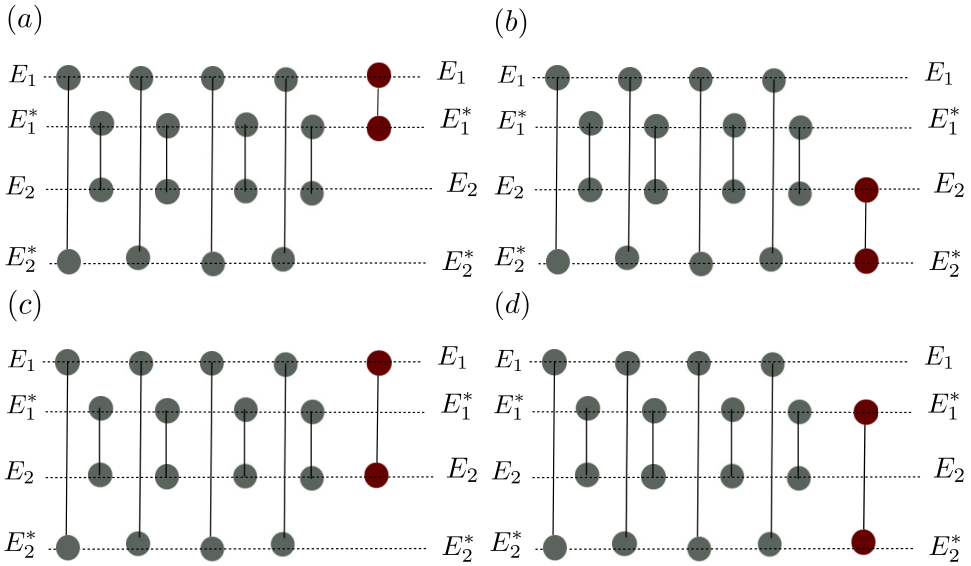


**Figure 13** – Four different diagrams corresponding to the first $C_0$ diagram with the extra scattering event in exit of the medium. The extra scattering event connects two ladders and gives to this diagram a short-range character.

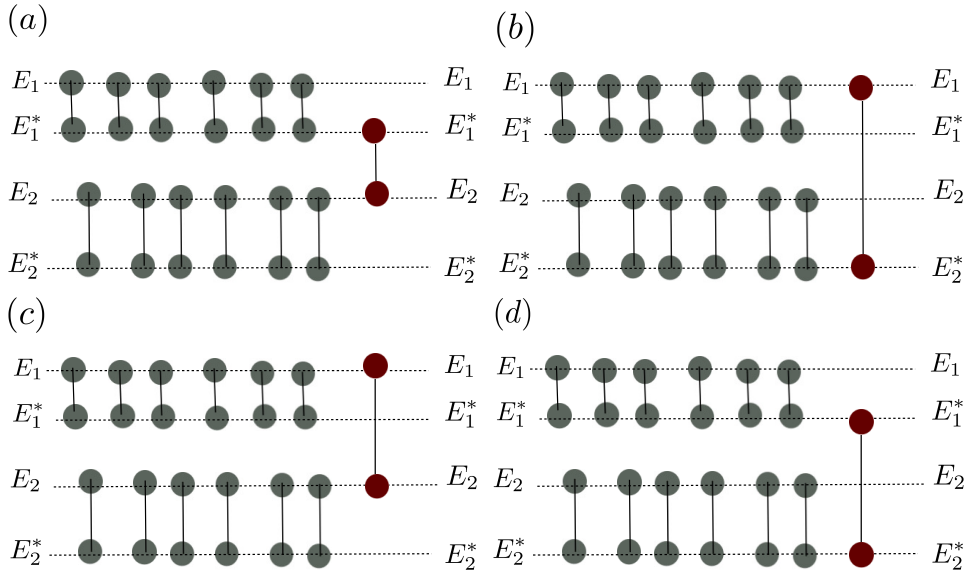


**Figure 14** – Four different diagrams corresponding to the second $C_0$ diagram with the extra scattering event in exit of the medium. The extra scattering event connects two ladders and gives to this diagram a short-range character.

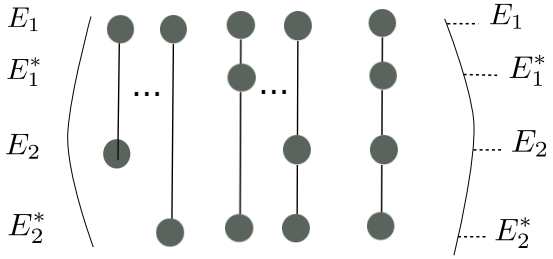


**Figure 15** – Scheme of the full four-fields vertex. Two, three and four fields can be scattered simultaneously by the disorder.

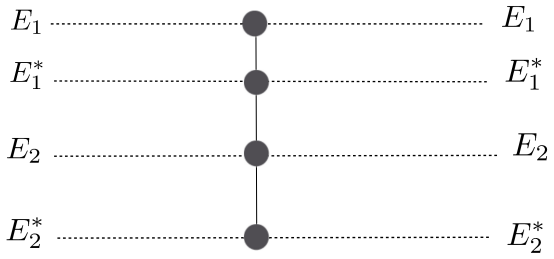


**Figure 16** – Diagram responsible for the dominant contribution of the non gaussian correlations in T/T, R/R and R/T in the quasi-ballistic regime.

# Bibliography


[1] M. Born and E. Wolf, *Principles of optics: electromagnetic theory of propagation, interference and diffraction of light*, Elsevier (2013).

[2] V. Parigi, E. Perros, G. Binard, C. Bourdillon, A. Maître, R. Carminati, V. Krachmalnicoff, and Y. D. Wilde, *Opt. Express* **24**, 7019–7027 (2016).

[3] M. Fink, D. Cassereau, A. Derode, C. Prada, P. Roux, M. Tanter, J.-L. Thomas, and F. Wu, *Rep. Prog. Phys.* **63**, 1933 (2000).

[4] A. P. Mosk, A. Lagendijk, G. Lerosey, and M. Fink, *Nat. Photonics* **6**, 283–292 (2012).

[5] A. Derode, P. Roux, and M. Fink, *Phys. Rev. Lett.* **75**, 4206 (1995).

[6] G. Lerosey, J. De Rosny, A. Tourin, A. Derode, G. Montaldo, and M. Fink, *Phys. Rev. Lett.* **92**, 193904 (2004).

[7] M. Lanoy, R. Pierrat, F. Lemoult, M. Fink, V. Leroy, and A. Tourin, *Phys. Rev. B* **91**, 224202 (2015).

[8] V. Bacot, M. Labousse, A. Eddi, M. Fink, and E. Fort, *Nat. Phys* **12**, 972–977 (2016).

[9] I. M. Vellekoop and A. Mosk, *Opt. Lett.* **32**, 2309–2311 (2007).

[10] S. Popoff, G. Lerosey, R. Carminati, M. Fink, A. Boccara, and S. Gigan, *Phys. Rev. Lett.* **104**, 100601 (2010).

[11] S. Rotter and S. Gigan, *Rev. Mod. Phys.* **89**, 015005 (2017).

[12] H. P. Paudel, C. Stockbridge, J. Mertz, and T. Bifano, *Opt. Express* **21**, 17299–17308 (2013).

[13] D. Andreoli, G. Volpe, S. Popoff, O. Katz, S. Grésillon, and S. Gigan, *Sci. Rep.* **5** (2015).

[14] M. Mounaix, D. Andreoli, H. Defienne, G. Volpe, O. Katz, S. Grésillon, and S. Gigan, *Phys. Rev. Lett.* **116**, 253901 (2016).

[15] Z. Shi and A. Z. Genack, *Phys. Rev. Lett.* **108**, 043901 (2012).

[16] M. Kim, Y. Choi, C. Yoon, W. Choi, J. Kim, Q.-H. Park, and W. Choi, *Nat. Photonics* **6**, 581–585 (2012).

[17] M. Davy, Z. Shi, J. Wang, and A. Z. Genack, *Opt. Express.* **21**, 10367–10375 (2013).

[18] B. Gérardin, J. Laurent, A. Derode, C. Prada, and A. Aubry, *Phys. Rev. Lett.* **113**, 173901 (2014).

[19] R. Sarma, A. G. Yamilov, S. Petrenko, Y. Bromberg, and H. Cao, *Phys. Rev. Lett.* **117**, 086803 (2016).

[20] Y. Choi, T. R. Hillman, W. Choi, N. Lue, R. R. Dasari, P. T. So, W. Choi, and Z. Yaqoob, *Phys. Rev. Lett.* **111**, 243901 (2013).

[21] S. Kang, S. Jeong, W. Choi, H. Ko, T. D. Yang, J. H. Joo, J.-S. Lee, Y.-S. Lim, Q.-H. Park, and W. Choi, *Nat. Photonics* **9**, 253–258 (2015).

[22] A. Badon, D. Li, G. Lerosey, A. C. Boccara, M. Fink, and A. Aubry, *Sci. Adv.* **2**, e1600370 (2016).

[23] A. Lagendijk and B. A. Van Tiggelen, *Phys. Rep.* **270**, 143–215 (1996).

[24] J. W. Goodman, Speckle phenomena in optics: theory and applications (2007).

[25] M. Lax, *Physical Review* **85**, 621 (1952).

[26] M. C. W. van Rossum and T. M. Nieuwenhuizen, *Rev. Mod. Phys.* **71**, 313 (1999).

[27] U. Frisch, in *"Probabilistic Methods in Applied Mathematics"*, Academic Press, New York (1968).

[28] B. Shapiro, *Phys. Rev. Lett.* **57**, 2168 (1986).

[29] E. Kogan and M. Kaveh, *Phys. Rev. B* **51**, 16400–16402 (1995).

[30] E. Kogan, M. Kaveh, R. Baumgartner, and R. Berkovits, *Phys. Rev. B* **48**, 9404–9410 (1993).

[31] T. M. Nieuwenhuizen and M. C. W. van Rossum, *Phys. Rev. Lett.* **74**, 2674–2677 (1995).

[32] R. Dashen, *Journal of Mathematical Physics* **20**, 894–920 (1979).

[33] V. Emiliani, F. Intonti, M. Cazayous, D. S. Wiersma, M. Colocci, F. Aliev, and A. Lagendijk, *Phys. Rev. Lett.* **90**, 250801 (2003).

[34] E. Akkermans and G. Montambeaux, *Mesoscopic physics of electrons and photons*, Cambridge University Press (2007).

[35] N. Garcia and A. Genack, *Phys. Rev. Lett.* **63**, 1678 (1989).

[36] S. Feng, C. Kane, P. A. Lee, and A. D. Stone, *Phys. Rev. Lett.* **61**, 834 (1988).

[37] R. Berkovits and S. Feng, *Phys. Rep.* **238**, 135 – 172 (1994).

[38] C. Kane, R. Serota, and P. Lee, *Phys. Rev. B* **37**, 6701 (1988).

[39] D. Rogozkin, *JETP Lett.* **84**, 916–939 (1997).

[40] J.-L. Lacoume, P.-O. Amblard, and P. Comon, *Statistiques d'ordre supérieur pour le traitement du signal*, Masson (1997).

[41] G. Bergman, *Phys. Rep* **107**, 1 (1984).

[42] P. A. Lee and A. D. Stone, *Phys. Rev. Lett.* **55**, 1622 (1985).

[43] B. Altshuler, *JETP Lett.* **41**, 648–651 (1985).

[44] B. L. Altshuler, P. A. Lee, and W. R. Webb, *Mesoscopic phenomena in solids*, volume 30, Elsevier (2012).

[45] I. Freund, M. Rosenbluh, and S. Feng, *Phys. Rev. Lett.* **61**, 2328 (1988).

[46] R. Berkovits, M. Kaveh, and S. Feng, *Phys. Rev. B* **40**, 737 (1989).

[47] J. Bertolotti, E. G. van Putten, C. Blum, A. Lagendijk, W. L. Vos, and A. P. Mosk, *Nature* **491**, 232–234 (2012).

[48] M. P. Van Albada and A. Lagendijk, *Phys. Rev. Lett.* **55**, 2692 (1985).

[49] P.-E. Wolf and G. Maret, *Phys. Rev. Lett.* **55**, 2696 (1985).

[50] E. Akkermans, P. Wolf, and R. Maynard, *Phys. Rev. Lett.* **56**, 1471 (1986).

[51] F. Scheffold and G. Maret, *Phys. Rev. Lett.* **81**, 5800 (1998).

[52] A. Yamilov, *Phys. Rev. B* **78**, 045104 (2008).

[53] S. Feng, C. Kane, P. A. Lee, and A. D. Stone, *Phys. Rev. Lett.* **61**, 834–837 (1988).

[54] M. J. Stephen and G. Cwilich, *Phys. Rev. Lett.* **59**, 285 (1987).

[55] A. Zyuzin and B. Spivak, *JETP Lett.* **66**, 560–566 (1987).

[56] R. Pnini and B. Shapiro, *Phys. Rev. B* **39**, 6986 (1989).

[57] M. Van Albada, J. De Boer, and A. Lagendijk, *Phys. Rev. Lett.* **64**, 2787 (1990).

[58] J. F. de Boer, M. P. van Albada, and A. Lagendijk, *Phys. Rev. B* **45**, 658 (1992).

[59] A. Z. Genack, N. Garcia, and W. Polkosnik, *Phys. Rev. Lett.* **65**, 2129–2132 (1990).

[60] B. Shapiro, *Phys. Rev. Lett.* **83**, 4733–4735 (1999).

[61] B. A. van Tiggelen and S. E. Skipetrov, *Phys. Rev. E* **73**, 045601 (2006).

[62] S. E. Skipetrov and R. Maynard, *Phys. Rev. B* **62**, 886–891 (2000).

[63] A. Cazé, R. Pierrat, and R. Carminati, *Phys. Rev. A* **82**, 043823 (2010).

[64] P. Sebbah, R. Pnini, and A. Genack, *Phys. Rev. E* **62**, 7348 (2000).

[65] P. Sebbah, B. Hu, A. Genack, R. Pnini, and B. Shapiro, *Phys. Rev. Lett.* **88**, 123901 (2002).

[66] A. Chabanov, N. Tregoures, B. Van Tiggelen, and A. Genack, *Phys. Rev. Lett.* **92**, 173901 (2004).

[67] P. A. Mello and N. Kumar, *Quantum transport in mesoscopic systems: complexity and statistical fluctuations, a maximum-entropy viewpoint*, 4, Oxford University Press on Demand (2004).

[68] C. W. J. Beenakker, *Rev. Mod. Phys.* **69**, 731–808 (1997).

[69] P. A. Mello, E. Akkermans, and B. Shapiro, *Phys. Rev. Lett.* **61**, 459 (1988).

[70] A. García-Martín, F. Scheffold, M. Nieto-Vesperinas, and J. Sáenz, *Phys. Rev. Lett.* **88**, 143901 (2002).

[71] D. Rogozkin and M. Y. Cherkasov, *Phys. Rev. B* **51**, 12256 (1995).

[72] S. Hikami, *Phys. Rev. B* **24**, 2671 (1981).

[73] T. M. Nieuwenhuizen and M. Van Rossum, *Phys. Lett. A* **177**, 102–106 (1993).

[74] D. B. Rogozkin and M. Y. Cherkasov, *Phys. Lett. A* **214**, 292 (1996).

[75] D. Rogozkin and M. Y. Cherkasov, *JETP Lett.* **58**, 585–585 (1993).

[76] D. Rogozkin, *Phys. Lett. A* **236**, 159–166 (1997).

[77] D. Rogozkin, *JETP Lett.* **69**, 117–122 (1999).

[78] E. Bascones, M. Calderón, D. Castelo, T. López, and J. Sáenz, *Phys. Rev. B* **55**, R11911 (1997).

[79] J. Sáenz, L. Froufe-Pérez, and A. GarcíA-Martín, *Wave Scattering in Complex Media: From Theory to Applications: Proceedings of the NATO Advanced Study Institute on Wave Scattering in Complex Media: From Theory to Applications Cargèse, Corsica, France 10–22 June 2002* **107**, 175 (2003).

[80] L. Froufe-Pérez, A. Garcia-Martin, G. Cwilich, and J. Saenz, *Physica A* **386**, 625 – 632 (2007).

[81] J. W. Goodman, *Introduction to Fourier optics*, Roberts and Company Publishers (2005).

[82] A. Ishimaru, *Wave Propagation and Scattering in Random Media*, IEEE Press, Oxford (1997).

[83] Y. Lai, S.-K. Cheung, and Z.-Q. Zhang, *Phys. Rev. E* **72**, 036606 (2005).

[84] E. Akkermans and G. Montambaux, *Mesoscopic Physics of Electrons and Photons*, Cambridge University Press (2007).

[85] N. Fayard, A. Cazé, R. Pierrat, and R. Carminati, *Phys. Rev. A* **92**, 033827 (2015).

[86] I. Starshynov, A. Paniagua-Diaz, N. Fayard, A. Goetschy, R. Pierrat, R. Carminati, and J. Bertolotti, *arXiv:1707.03622* (2017).

[87] T. Strudley, T. Zehender, C. Blejean, E. P. Bakkers, and O. L. Muskens, *Nat. Photonics* **7**, 413–418 (2013).

[88] W. K. Hildebrand, A. Strybulevych, S. E. Skipetrov, B. A. van Tiggelen, and J. H. Page, *Phys. Rev. Lett.* **112**, 073902 (2014).

[89] R. Sarma, A. Yamilov, P. Neupane, B. Shapiro, and H. Cao, *Phys. Rev. B* **90**, 014203 (2014).

[90] R. Sarma, A. Yamilov, P. Neupane, and H. Cao, *Phys. Rev. B* **92**, 180203 (2015).

[91] S. E. Skipetrov and R. Maynard, *Phys. Rev. B* **62**, 886–891 (2000).

[92] I. Freund, M. Rosenbluh, and S. Feng, *Phys. Rev. Lett.* **61**, 2328–2331 (1988).

[93] K. Vynck, R. Pierrat, and R. Carminati, *Phys. Rev. A* **89**, 013842 (2014).

[94] E. Gorodnichev, A. Kuzovlev, and D. Rogozkin, *J. Opt. Soc. Am. A* **33**, 95–106 (2016).

[95] L. Roux, P. Mareschal, N. Vukadinovic, J. B. Thibaud, and J. J. Greffet, *J. Opt. Soc. Am. A* **18**, 374 (2001).

[96] F. Ferri, D. Magatti, A. Gatti, M. Bache, E. Brambilla, and L. A. Lugiato, *Phys. Rev. Lett.* **94**, 183602 (2005).

[97] B. I. Erkmen and J. H. Shapiro, *Phys. Rev. A* **77**, 043809 (2008).

[98] J. H. Shapiro, *Phys. Rev. A* **78**, 061802 (2008).

[99] Y. Bromberg, O. Katz, and Y. Silberberg, *Phys. Rev. A* **79**, 053840 (2009).

[100] R. Meyers, K. S. Deacon, and Y. Shih, *Phys. Rev. A* **77**, 041801 (2008).

[101] N. D. Hardy and J. H. Shapiro, *Phys. Rev. A* **84**, 063824 (2011).

[102] M. Bina, D. Magatti, M. Molteni, A. Gatti, L. Lugiato, and F. Ferri, *Phys. Rev. Lett.* **110**, 083901 (2013).

[103] W. Gong and S. Han, *Opt. Lett.* **36**, 394–396 (2011).

[104] F. Ferri, D. Magatti, L. Lugiato, and A. Gatti, *Phys. Rev. Lett.* **104**, 253603 (2010).

[105] T. M. Cover and J. A. Thomas, *Elements of information theory*, John Wiley & Sons (2012).

[106] G. Saporta, *Probabilités, analyse des données et statistique*, Editions Technip (2006).

[107] O. S. Ojambati, J. T. Hosmer-Quint, K.-J. Gorter, A. P. Mosk, and W. L. Vos, *Phys. Rev. A* **94**, 043834 (2016).

[108] N. Shnerb and M. Kaveh, *Phys. Rev. B* **43**, 1279 (1991).

[109] A. Genack and N. Garcia, *Europhys. Lett.* **21**, 753 (1993).

[110] S. M. Flatté, D. R. Bernstein, and R. Dashen, *The Physics of fluids* **26**, 1701–1713 (1983).

[111] E. Kogan, M. Kaveh, R. Baumgartner, and R. Berkovits, *Phys. Rev. B* **48**, 9404 (1993).

[112] T. M. Nieuwenhuizen and M. Van Rossum, *Phys. Rev. Lett.* **74**, 2674 (1995).

[113] E. Kogan and M. Kaveh, *Phys. Rev. B* **52**, R3813 (1995).

[114] J. F. de Boer, M. Van Rossum, M. P. van Albada, T. M. Nieuwenhuizen, and A. Lagendijk, *Phys. Rev. Lett.* **73**, 2567 (1994).

[115] M. Stoytchev and A. Genack, *Phys. Rev. Lett.* **79**, 309 (1997).

[116] N. Fayard, A. Goetschy, R. Pierrat, and R. Carminati, *arXiv:1710.03549* (2017).

[117] R. M. Gray *et al.*, *Foundations and Trends® in Communications and Information Theory* **2**, 155–239 (2006).

[118] R. Moddemeijer, *Signal Process.* **16**, 233–248 (1989).

[119] A. Kraskov, H. Stögbauer, and P. Grassberger, *Phys. Rev. E* **69**, 066138 (2004).

[120] C. W. Hsu, S. F. Liew, A. Goetschy, H. Cao, and A. D. Stone, *Nat. Phys.* (2017).

[121] M. Van Rossum and T. M. Nieuwenhuizen, *Phys. Lett. A* **177**, 452–458 (1993).

## Résumé

Les nuages, le lait, le papier, les tissus biologiques appartiennent tous à une même classe de milieux que l'on nomme diffusants de part leur habilité à transformer une onde incidente collimatée en un faisceau diffus. L'imagerie, ou le transfert d'information à travers ces milieux est *a priori* plus difficile qu'en milieu homogène. Les méthodes actuelles d'imagerie en milieu diffusant nécessitent souvent une caméra se situant en transmission du milieu considéré afin d'y mesurer la lumière diffusée. La présence de cette caméra est considérée comme une faille de ces méthodes car la transmission de ces milieux est dans la plupart des cas hors d'atteinte par l'opérateur. Dans cette thèse nous posons la question du lien qui existe entre la lumière réfléchie et la lumière transmise en milieux fortement diffusant. Nous traitons ce problème de manière statistique et nous intéressons à la dépendance statistique qui existe entre la lumière réfléchie et la lumière transmise. Nous verrons que ce lien statistique persiste même pour des milieux fortement diffusants, pouvant donc en principe être a la base de nouvelles méthodes d'imagerie ou de contrôle du front d'onde en milieux diffusants n'utilisant que des informations réfléchies par le milieu.

## Mots Clés

Optiques, Milieux dilués, Corrélations mésoscopiques, Théorie de l'information, Imagerie.

## Abstract

Clouds, milk, paper or biological tissues are called scattering media for light. Indeed when a plane wave encounters one of these media, the light is scattered and loses its preferential direction. Consequently, imaging through a complex medium is more difficult than in a homogeneous one. The existing methods rely on a CCD camera measuring the transmitted light. Nonetheless, in practical cases the transmitted side of the sample is out of reach of the operator. In this thesis we interest ourselves to the link that exists between the reflected light and the transmitted light for thick scattering media. From a statistical point of view, this link is equivalent to the statistical dependency between the reflected light and the transmitted light. We show that the statistical dependency persists even for very thick media allowing us to propose new imaging modalities based on it. This statistical dependency between the reflected and the transmitted light is a very rich function of the parameters of the system, and may allow us to control the transmitted light using reflected informations only.

## Keywords

Optics, Scattering media, Mesoscopic correlations, Information theory, Imaging.